Experimental Study of Passive Ramps for Control of Shock–Boundary Layer Interactions

by

Andrew P. Lapsa

A dissertation submitted in partial fulfillment
of the requirements for the degree of
Doctor of Philosophy
(Aerospace Engineering)
in The University of Michigan
2009

Doctoral Committee:

Professor Werner J. A. Dahm, Chair
Professor David R. Dowling
Professor James F. Driscoll
Assistant Professor Matthias Ihme

To my loving wife, Katie.

ACKNOWLEDGEMENTS

This work results from the guidance, trust, and support bestowed upon me by countless individuals. By far the most tangible contributions are from my advisor, Professor Dahm, who has entrusted me with several compelling projects. His technical guidance, physical understanding, and creativity have helped to mold my analytical mind in a way I could have only hoped. I am exceedingly grateful for his mentorship, especially in the face of his many competing priorities.

Disproportionate thanks is also owed to Professor Driscoll, who advised me as his own and provided me opportunities when others did not exist. My hope is that his projects have benefitted from my involvement. These words are not written without his unnecessary generosity.

I have also benefitted from enlightening discussions with Professor Ihme on this and other topics. Professor Dowling has also played a critical role in my work, particularly in helping to uncover the mysteriously powerful role of acoustics. No doubt this work has benefitted from these and other contributions from all my committee members.

When sources were otherwise exhausted, Denise Phelps ensured my studies were not interrupted. I am enormously thankful to her for enabling this work to be completed in a continuous and timely fashion.

Experimental works are not possible without the support of exemplary technical support, and this is no exception. Eric Kirk went far beyond his job description to

help make the facility operational. Dave Mclean's assistance with electrical components was not only helpful, but essential. Tom Griffin had the unenviable task of coordinating "building integration," and he did this willingly, graciously, and effectively. I am also grateful for the exceptional skill of Terry Larrow, for without it the many reasonable and unreasonable tasks I have asked of him could never have been completed.

The technical caliber of my peers is first-rate, and my education has unquestionably benefitted from many an illuminating discussion with them. Particular thanks is due to Sulabh Dhanuka, Peter Hamlington, Danny Micka, Zac Nagel, Alex Schumaker, and Adam Steinberg. Thanks also goes to this group, as well as to Erin Farbar, Hyce Schumaker, Liza Rosenmann, Steve Walton, The Beautiful Game, and many others for making my time in Michigan enjoyable. Without them, my personal and academic success would be in doubt. Edwin Kang's assistance with data collection was also most welcome during an otherwise monotonous stretch.

My every opportunity is a direct result of the inspiring determination of my grandparents and parents. Their dedication to each other and to their children, the ideals they've promoted, and most importantly their example, have left me with only open doors. May they have also given me the wisdom to choose the right ones.

Finally, I am indescribably grateful for the love of my beautiful wife Katie. Unquestionably, the dinner dates of her childhood dreams were not set in engineering laboratories or cluttered offices, and yet she has not wavered in her support of me. To the contrary, the timely completion of this work is due preeminently to her tireless efforts. Her work ethic exceeds my own, her smile is transcendent, her wit delightful. She is a true source of inspiration and a best friend; it is an honor to share and grow in life with her. Let this be only the beginning.

TABLE OF CONTENTS

LIST OF FIGURES

Figure

LIST OF TABLES

Table

LIST OF APPENDICES

Appendix

NOMENCLATURE

Symbol	Description
A_p	Half-angle of passive micro-ramp geometries
a_{ij}	Anisotropy tensor
b_{ij}	Normalized anisotropy tensor
C	§ 3.3.3–3.3.5: $C = 5.0$, universal constant of integration
C'	§ 3.3.3–3.3.5: Non-universal constant of integration
C_i	Shock-wave trajectory
C_f	$\equiv 2u_\tau^2 \rho_w / (\rho_\infty u_\infty^2)$, Coefficient of friction
c	Side-length of passive micro-ramp geometries
D^*	Effective diameter of diffuser
d	§ 2.1.1: Diameter of cells in honeycomb mesh
d_p	Diameter of seed particles
F	Forces describing vortex-vortex interaction
H	Incompressible shape factor
H^*	Shape factor modified using finite integration limits
h	Height of passive micro-ramp geometries
I	Intersection point between incident and reflected shock waves
II	Second invariant of b_{ij}
III	Third invariant of b_{ij}

Kn	Knudsen number
k	$\equiv \frac{1}{2}\left(\overline{u'^2} + \overline{v'^2} + \overline{w'^2}\right)$, Turbulence kinetic energy
L	§ 2.1.1: Length of cells in honeycomb mesh;
	§ 2.1.4: Length of diffuser
L_0	Upstream penetration distance of SBLI
M	Mach number
N	Number of samples
p	Static pressure
p_0	Stagnation pressure
Re_δ	Reynolds number based on boundary layer height
Re_θ	Reynolds number based on momentum thickness
St	Stokes number
S_{ij}	Strain rate tensor
s	Centerline spacing micro-ramp array elements
T	Static temperature
T_0	Stagnation temperature
Δt	Actual interframe time
Δt_0	Target interframe time
u	Local streamwise velocity component
u_∞	Incoming free-stream velocity
u_τ	$\equiv \sqrt{\tau_w/\rho_w}$, Friction velocity
u_n	Shock-normal velocity component
u^+	$\equiv \overline{u}/u_\tau$, Inner velocity scaling
u^*	Van Driest transformation of velocity
v	Local wall-normal velocity component

W	Coles wake parameter
w	Local spanwise velocity component
x	Streamwise dimension
x_R	Streamwise location of micro-ramp array
y	Wall-normal dimension
y^+	$\equiv yu_\tau/\nu$, Wall-normal dimension scaled by inner variables
z	Spanwise dimension

Greek

α	Camera angle with respect to the object plane normal;
	§ 2.1.4: Effective diffuser angle
β	Flow deflection angle by micro-ramps
Γ	Circulation
γ	Specific heat ratio
δ	Local boundary layer thickness
δ_0	Reference boundary layer thickness at SBLI location
δ^*	Displacement thickness
$\langle\delta^*\rangle$	Net displacement thickness, using finite integration limits
δ_{ij}	Kronecker delta tensor
ε	Dissipation rate due to turbulent fluctuations
ε^*	Isotropic approximation to ε
$\varepsilon^\dagger$	Isotropic/incompressible approximation to ε
η	System of compression/expansion waves;
	§ 3.3: $\equiv y/\delta$, normalized wall-normal dimension
θ	Free stream deflection angle;

	Momentum thickness
κ	von Kármán constant
λ_ν	Dissipative length scale
μ	Dynamic viscosity
ν	Kinematic viscosity
ρ	Density
ρ_p	Density of seed particles
σ	Statistical variance
τ_f	Fluid-dynamic timescale
τ_p	Timescale for particle lag
τ_w	Wall shear stress
Φ	Total turbulence kinetic energy dissipation rate
ω	Vorticity

Mathematical

$\overline{(\cdot)}$	Ensemble averaged quantity
$(\cdot)'$	Fluctuating quantity from Reynolds decomposition
$\sim$	Proportional to

Initializations & Acronyms

DNS	Direct numerical simulation
LES	Large eddy simulation
RANS	Reynolds-averaged Navier-Stokes
SBLI	Shock/boundary layer interactions
SPIV	Stereo particle image velocimetry

CHAPTER I

Introduction

The formation of shock waves, and their subsequent interactions with boundary layers, is pervasive in modern aerospace applications. Rocket nozzles, ramjets, supersonic airframes, and rotor blades are only a few relevant examples. The effects of the shock wave–boundary layer interactions (SBLI) are often detrimental to vehicle or component performance. On transonic airfoils, for example, the normal shock formed above the wing can lead to boundary layer separation, and in supersonic inlets the interaction between the boundary layer and oblique shock waves generated at the leading edges of the inlet substantially thicken the boundary layer, affecting the flow rate to the engine. Additionally, SBLI are inherently unsteady processes that ultimately result in dynamic loading of vehicle components. Left uncontrolled, SBLI prove to be detrimental or prohibitive in many applications. Despite approximately sixty years of continuous research, the complexity of the topic continues to challenge researchers and designers alike.

The present state of the field, however, provides a new and promising vantage from which to approach the SBLI problem. Ever-increased computing power is enabling computational methods to be developed that model high Reynolds number unsteady flows with increasing fidelity. Simultaneously, experimental techniques are being

developed and refined at a similarly impressive rate, allowing for the non-intrusive instantaneous field measurements necessary to provide both new insight into the physics and validation data for new computational models. This unique juncture is highlighted in a review of SBLI research by Dolling (2001), in which he states:

> "Computational abilities are now beginning to resolve these flows. Validation of such codes, and their extension to progressively more complex flow situations, such as unsteady or transient flows, will hinge critically on new, closely coupled experimental and computational studies."

Recognizing this, the United States Air Force (USAF) and the National Aeronautics and Space Administration (NASA), among other organizations, have placed renewed emphasis on the study of SBLI in order to realize the vision of high efficiency supersonic flight for unparalleled global reach capabilities (Croker et al., 2007). In particular, high efficiency mixed compression inlets are a key enabling technology for their Long Range Strike (LRS) objectives; the thrust efficiency of a supersonic aircraft depends crucially on its air intakes.

The present work is part of a greater collaborative effort to enhance the understanding, prediction, and ability to control SBLI. It uses high-fidelity non-intrusive stereo particle image velocimetry (SPIV) measurements of incident oblique SBLI to evaluate the effectiveness of micro-ramp geometries that are intended to provide passive control of SBLI. Based on insights gained from these measurements, a fundamentally new design is proposed for such ramps and is shown herein to demonstrate considerably greater potential for achieving effective SBLI control than existing ramp concepts. Furthermore, the highly-resolved field data contained herein also provide means for validation of computational models of compressible boundary layers, uncontrolled SBLI, and SBLI involving micro-ramp control.

1.1 Oblique shock–boundary layer interactions

Owing to the complexities of SBLI, and to their ubiquity in aerospace applications, many prior investigations have been directed at this subject. Chapman et al. (1958), Green (1970), Delery and Marvin (1986) and Delery (2001) together provide the historical perspective and physical understanding necessary to appreciate the topic. In particular, the reviews by Delery and Marvin (1986) and Delery (2001) give excellent descriptions of the essential elements of the physical nature of SBLI. A brief description of the physics derived from those and other sources is given in this section.

Shock wave–boundary layer interactions can typically be categorized as one of three types: an incident oblique SBLI, a SBLI formed by a compression ramp, or as the interaction between a boundary layer and a normal shock. The present study involves only the first, however it should be noted that essentially the same physical mechanisms govern the boundary layer response in all three. For example, Green (1970) noted that a compression ramp of angle 2θ produces the same series of interactions as a reflected oblique interaction produced by a flow deflection of θ. In the present case an oblique shock is formed by a deflection of the free stream, and that shock impinges on a boundary layer formed along a rigid wall. The necessity for the downstream flow direction to be parallel to the wall requires that a second reflected shock be formed at the incident shock impingement point. Figure 1.1 shows the basic incident shock reflection, with the bulk flow becoming divided into three thermodynamic states determined by the inviscid oblique shock relations. Table 1.1 gives these state quantities for the cases considered in this study. The effects of viscosity become significant in the boundary layer and result in a complicated inter-

action between it and the shock waves. This structure is discussed in some detail in § 1.1.1–1.1.4.

1.1.1 Mean two-dimensional incident oblique SBLI

The structure of a two dimensional interaction produced by a relatively weak incident shock is shown in a time-averaged sense in Fig. 1.2. As the incident oblique shock, C_1, enters the boundary layer, which has height δ_0, and approaches the wall, it curls in response to the progressively decreasing local Mach number. The magnitude of the pressure rise produced across the shock wave correspondingly diminishes until eventually the sonic line is reached; there, the shock ceases. Below the sonic line is a layer of subsonic fluid through which the shock-induced pressure rise can be transmitted. At the wall, the streamwise pressure distribution thus becomes spread over a finite length, as shown in Fig. 1.3. Owing to this adverse pressure gradient the subsonic layer is thickened, which in turn deflects the supersonic flow above it. This deflection of the outer flow requires the formation of a system of compression waves, η_1, which eventually coalesce to form the reflected shock, C_2. The η_1 compression waves are refracted as they traverse the supersonic portion of the boundary layer, forming the η_2 wave system. These in turn reflect from the sonic line and produce an expansion fan, η_3, which propagates until eventually it interacts with the reflected shock C_2. Thus the interaction becomes highly non-localized, and the reflected shock properties predicted by the fully inviscid solution are only realized after the interaction between the reflected shock, C_2, and the expansion, η_3, is complete.

The interaction structure, and in particular the upstream interaction length L_0, depends strongly on the incoming conditions. Consider the interaction to be com-

prised of three layers: an inviscid irrotational region outside the boundary layer, a rotational region comprising the majority of the boundary layer where viscous forces are still negligible in comparison to the pressure and inertial forces (the classical "outer layer"), and an inner-most viscous region in which viscous forces are significant or even dominate (the classical "inner layer"). The interplay between these layers is fundamental to the resulting interaction structure, with their relative sizes and roles being Reynolds number dependent. At low or moderate Reynolds number, the upstream interaction length L_0/δ_0 increases with Reynolds number. This is consistent with the theory of a free interaction between the intermediate "inviscid" rotational layer and the inner viscid layer, as was first described by Chapman et al. (1958). For Reynolds numbers $Re_{\delta_0} \gtrsim 10^5$, the energy transfer between the two layers is enhanced and this trend reverses. A full discussion is deferred to Delery and Marvin (1986).

When the incident shock becomes strong enough, the adverse pressure gradient in the subsonic region can cause the flow to locally reverse, as shown in Fig. 1.4. In this case, the compression waves formed as a result of the thickened subsonic region are more highly concentrated and coalesce to form the reflected shock, C_2, upstream of the incident shock wave, C_1. The reflected shock then intersects the incident shock at I. Due to the change in the upstream flow state, the reflected shock turns as it moves through the intersection and continues to propagate as C_4. The continuation of the incident shock, C_3, curls toward the wall as before, with its reflection from the sonic line again manifesting as an expansion fan. Downstream of the separation, the flow velocity is necessarily returned to the direction parallel to the wall by an additional system of compression waves. The wall pressure distribution through the interaction is now divided into two regions of rising pressure; the first produced by the upstream

system of compression waves, and the second produced by the downstream system of compression waves. This is shown in Fig. 1.5. As before, the upstream portion of the interaction is essentially a free interaction process, leading to the major consequence that, provided separation exists, the upstream pressure rise Δp_1 is independent of downstream conditions; namely the incident shock strength. Thus for increasingly strong incident shocks, the pressure rise due to the downstream compression waves becomes increasingly large.

Of obvious importance is the ability to predict the defining dimensions of the interaction structure, and this topic has appropriately received considerable attention. Many purely empirical correlations have been proposed, with studies by Settles et al. (1976), Roshko and Thomke (1976), and Settles et al. (1981) being prominent among them. General formulations, however, are left outstanding. Instead, consensus can be drawn around several broad statements. Specifically relevant to the present study, for fixed Reynolds number Re_{δ_0}:

- L_0/δ_0 increases with θ for fixed M_0,
- L_0/δ_0 decreases with M_0 for fixed θ,
- The "incompressible" shape factor H is the appropriate characterization of the incoming boundary layer for scaling of the upstream interaction length L_0 (Hayakawa and Squire, 1982; Delery and Marvin, 1986).

The difficulty in forming general quantitative relations stems, among other reasons, from geometrical effects which are essentially always significant in incident oblique SBLI. In addition, the temporal and spatial fluctuations of the interaction, which are due both to turbulence and to large-scale effects, are of at least equal importance as the mean fields in practical applications. Much of the recent research has therefore

turned to these topics in hopes of both understanding the physical mechanisms and guiding the development of computational models.

1.1.2 Unsteady and turbulent properties of SBLI

The highly unsteady nature of SBLI produces large fluctuations in pressure loads and heat transfer rates, which are of paramount importance since they can lead to structural damage or rapid fatigue rates (Brusniak and Dolling, 1996). The fluctuations arise from two sources: the interaction between the shock wave and the free stream turbulence, and the instabilities in the shock foot. The former produces comparatively minor fluctuations but is nonetheless of interest since it is a known source of turbulence amplification. As would be expected, these fluctuations occur at frequencies that are consistent with typical turbulence time scales and are the source of turbulence generated "shock jitter." The topic is reviewed in detail by Andreopoulos et al. (2000).

Of even greater importance to practical applications are the fluctuations of the SBLI region, which occur on much larger spatial scales and at frequencies at least one order of magnitude lower than those associated with typical boundary layer turbulence. The governing mechanism has evaded researchers, who have investigated the issue predominantly through SBLI formed by compression ramps (Dolling and Murphy, 1983; Andreopoulos and Muck, 1987; Smits and Muck, 1987; Selig et al., 1989; Thomas et al., 1994; Ganapathisubramani et al., 2007), although the same physical mechanisms are at work in incident oblique SBLI. The debate centers around the source of the low-frequency oscillations in the shock foot, which in turn lead to low-frequency oscillations emanating from the SBLI region by means of the reflected

shock. Andreopoulos and Muck (1987), for example, argue that the oscillations of the shock formed by the compression ramp correlate with the burst frequency of the incoming boundary layer. However Thomas et al. (1994) show that the oscillations resulting from this mechanism are of lower amplitude than the preeminent oscillations of the shock and that, not surprisingly, the higher amplitude lower frequency oscillations correlate directly with the overall oscillations of the entire interaction region. This correlation between the low frequency oscillation of the compression ramp interaction was later observed by Dupont et al. (2006) in an incident oblique SBLI. In a series of studies, Ünalmis and Dolling (1998), Beresh et al. (2002), and Hou et al. (2003) found correlations between velocity fluctuations in the lower portion of the upstream boundary layer and the shock foot region, but other aspects of their findings were contradictory and prevented a definitive conclusion.

The order-of-magnitude difference between typical boundary layer fluctuation frequencies and the large scale SBLI fluctuations might suggest that structures at least one order of magnitude larger than the boundary layer are required. Ganapathisubramani et al. (2007) proposes that long vortical structures formed in the incoming boundary layer dictate the oscillation frequency of the SBLI, noting findings by the same authors that such vortical structures can be as long as 8δ in compressible boundary layers (Ganapathisubramani et al. 2006). Although such vortical formations have been observed by other authors in subsonic and supersonic boundary layers, agreement on their wall-normal locations and streamwise extent is far from consensus; Smith and Smits (1995) report no apparent structures, and in a DNS study of a Mach 2 boundary layer Pirozzoli et al. (2008) report structures of only five to six dissipative length scales. Most recently, Humble et al. (2009) identified streamwise-elongated regions of relatively low- and high-speed fluid, and identified

an apparent statistical link between these and the motions of the the interaction region. But the recency of these findings, as well as the lack of consensus regarding the prevalence of the streamwise vortical structures, leave this description of the cause for low frequency oscillations in the shock foot open for debate.

A yet different description is offered by Pirozzoli and Grasso (2006), who used direct numerical simulation (DNS) to study the incident oblique SBLI. They propose that the large-scale, low-frequency oscillations in the shock foot are a result of an acoustic resonance mechanism in which vortices are shed at the separation point, propagate downstream, and produce pressure waves as they interact with the incident shock. The pressure waves propagate upstream through the subsonic inner layer and excite the mixing layer that produces the vortices. The mechanism is similar to those observed in screeching jets and supersonic cavity flows, and the vortex shedding mechanism was visualized in particle image velocimetry (PIV) measurements by Dupont et al. (2008). Note also that this description of the instability mechanism is not inconsistent with the observations of Thomas et al. (1994) and Dupont et al. (2006); the reflected shock oscillations are closely correlated with the overall oscillations of the shock foot.

1.1.3 Experimental investigations of incident oblique SBLI

The studies discussed in § 1.1.2 almost exclusively involve SBLI produced by compression ramps. The incident oblique SBLI configuration has been studied considerably less, and provides an experimental challenge because of the propensity for reverse flow, high turbulence intensity, the presence of shock waves, and often substantial three-dimensional effects. Mean velocity profiles were measured by Chap-

man et al. (1958) and Green (1970), however those studies were based on pitot-probe or hot-wire measurements and were therefore unable to accurately resolve recirculation. Rose and Johnson (1975) and Modarress and Johnson (1976) presented the first non-intrusive velocity and fluctuation measurements of incident SBLI using line-of-site laser velocimetry. Non-intrusive measurements were not repeated until Meyer et al. (1997), who used laser doppler velocimetry (LDV) to construct rough velocity and fluctuation profiles at various downstream distances through an incident oblique SBLI formed by $\theta = 5$-deg, 7-deg, and 10-deg deflections of a $M = 2.9$ free stream. Together, Bookey et al. (2005a, 2005b) and Wu et al. (2005) present corresponding experimental and computational data for a 24-deg compression ramp, as well as data for an incident shock formed by a 12-deg reflection of a $M = 2.9$ free stream. Those experimental studies used pitot probe measurements of the mean velocity, pressure measurements as indicators of the fluctuations, and filtered Rayleigh scattering (FRS) to form an *ad hoc* interpretation of the intermittency. The experimental measurements were compared to a large eddy simulation (LES) and direct numerical simulation (DNS), but showed only relatively poor agreement.

Dupont et al. (2006) used high-speed wall pressure measurements to provide essentially the only detailed investigation of the unsteady behavior of incident oblique SBLI. As in compression ramp SBLI, very low-frequency oscillations on the order of $\mathcal{O}(300)$ Hz were observed at the shock foot. Through an extensive discussion they conclude that the established relevant length and velocity scales L_0 and u_∞ are insufficient to describe the SBLI organization in a manner sufficient to allow frequency scalings to be derived.

Non-intrusive field measurements of the interactions will be unquestionably valuable in uncovering this detailed structure. To date, such measurements of incident

oblique SBLI are relatively few. Humble et al. (2007) presented particle image velocimetry (PIV) measurements from a $M = 2.1$ flow with a single flow deflection angle of $\theta = 8.0$-deg. Quantitative mean streamwise velocity ($\overline{u}$) and fluctuation ($\overline{u'^2}$, $\overline{v'^2}$, $\overline{u'v'}$) measurements from the incoming boundary layer were presented. Visualizations of the streamwise velocity and fluctuation fields through the interaction region were shown for the first time, however detailed quantitative profiles of these and other velocity components were not given. Dupont et al. (2008) presented similar quantities from a $M = 2.3$ undisturbed boundary layer upstream of the interaction. As mentioned in § 1.1.2, they additionally provided visualizations of coherent vortical structures being shed from the reflected shock anchor point. Finally, Humble et al. (2009) performed tomographic PIV on a similar SBLI as in their 2007 study, with emphasis on identifying a statistical link between incoming boundary layer behavior and large-scale motions of the interaction. However, none of those studies provide statistically converged results for the full three-dimensional velocity vector and associated full Reynolds stress tensor. Nor do they provide quantitative accounts of the gradient quantities and higher-order statistics, which are necessary for understanding additional key aspects of the interaction, and for rigorous evaluation of computational models.

1.1.4 Computational efforts

The difficulty in forming general yet accurate predictive tools for even canonical SBLI configurations, and the presence of a diverse range of geometrical effects, makes the prospect of computational fluid dynamics (CFD) simulations both appealing and necessary for the development of practical applications. But the compress-

ibility effects, unsteady nature, and large range of scales (owing to high Reynolds numbers) typically associated with these high-speed flows pose significant challenges. Compressible turbulent boundary layers alone, for example, are an active topic of research. Guarini et al. (2000), Maeder et al. (2001), Pirozzoli et al. (2004), Pirozzoli et al. (2008), and Ringuette et al. (2008) exemplify the recency of this through their direct numerical simulations (DNS) of turbulent boundary layers formed with free stream Mach numbers ranging from $2 \leq M \leq 6$.

Naturally, the shock–boundary layer interaction provides an even more formidable challenge. The computational resources required for high-fidelity time-resolved solutions, as would be provided by DNS or large eddy simulation (LES), are presently overwhelming for the majority of engineering simulations. Reynolds-averaged Navier-Stokes (RANS) approaches therefore constitute the majority of simulations. Many of the myriad RANS studies of SBLI flows are reviewed by Gatski and Erlebacher (2002), and the subsequent work by Gerolymos et al. (2004) is additionally notable for its direct comparison of several RANS models in oblique SBLI flows. But the vast majority of these make use of the Boussinesq "gradient transport" hypothesis, in which the RANS equations are closed by linearly relating the Reynolds stress components to the mean strain rate tensor via an "eddy viscosity." The discrepancies with existing data are large and the errors fundamental, particularly in non-equilibrium flows where the turbulence undergoes rapid straining. Nonlinear eddy viscosity models help to address some of these shortcomings, with Sinha et al. (2003) and Sinha et al. (2005) providing notable examples applied to the case of SBLI. While these nonlinear adaptations are made largely on an *ad hoc* basis, new physically-derived nonlinear models are being developed and show promise in non-equilibrium flows like SBLI (Hamlington and Dahm 2007, 2008, 2009). The shock-boundary layer

interaction forms a quintessential scenario on which to test these non-equilibrium approaches, however the highly-resolved measurements of velocity and higher-order turbulence and gradient statistics necessary for rigorous evaluation of the new models were until now unavailable.

Even an ideal mean-field solution from a RANS simulation, however, fails to capture the fluctuating behavior of SBLI and the large dynamic loads that follow from them. Direct numerical simulation (DNS), which solves the Navier-Stokes equations directly at all relevant scales of the flow, certainly has the potential to capture these physics. The enormous computational expense required, however, prevent simulations of this type from being feasible for practical applications, and has furthermore limited DNS simulations to only a few studies of canonical SBLI configurations. Adams (2000) and Wu and Martin (2007) are notable examples of DNS simulations of compression ramps, while Pirozzoli and Grasso (2006) and Robinet (2007) provide essentially the only studies of incident oblique SBLI using DNS. The simulation by Robinet (2007) is notable for its full consideration of three-dimensional effects, and is the only DNS study with non-periodic side-wall boundary conditions. Robinet then uses a linearized global stability analysis to show that the interaction becomes globally unstable for sufficiently strong incident shock waves, ultimately producing the complex features observed in the surface visualizations from innumerable experiments. Yet even in these DNS studies a degree of numerical modeling is required due to the stringent constraints around affordable grid sizes. As such, and as noted repeatedly by the above authors, these simulations are lacking the high-fidelity experimental data required to evaluate their accuracy.

Owing again to the necessary limitations on grid sizes, an additional disadvantage of DNS studies of SBLI is the present inability to resolve large-scale three-

dimensionality at realistic Reynolds numbers, since periodic sidewall boundary conditions are required to limit the computational costs. The very low Reynolds number simulation of Robinet (2007) is the notable exception. It appears that DNS may never be suitable as a design tool for practical conditions and instead will be used for fundamental studies of specific canonical test cases.

Large eddy simulation (LES) is proving to be an attractive alternative to both RANS and DNS; it solves for the time-resolved solutions, but saves considerable computational cost by directly solving for only the non-similar outer scales of the flow while modeling the universal inner "sub-grid" scales. Early LES simulations of SBLI have been reviewed by Knight et al. (2003). The studies by Rizzetta et al. (2001) and Loginov et al. (2006) are notable examples of simulations involving compression ramp SBLI, with Garnier et al. (2002) and Teramoto (2005) performing essentially the only LES studies of incident oblique SBLI. As with DNS, the present computational requirements for LES severely limit its use for studying SBLI. Furthermore, the models used to represent the sub-grid scales of the flow are still very much an open research topic. LES simulations therefore also will benefit from highly-resolved experimental data for the mean, fluctuation, and gradient quantities through the SBLI interactions for validation purposes.

RANS, DNS, and LES all play important roles in the design and research communities, however the challenges presented by SBLI render none of them independently sufficient for design purposes or even for insight to basic physical understanding. The high local strain rates, unsteady nature, and potential for reversed flow lead to considerable errors in the current RANS models. The high Reynolds numbers and resulting large range of turbulence scales make DNS impractical for all but low Reynolds number test cases. A combination of these factors also present challenges

to LES, the models for which remain a research topic even outside of SBLI. Of critical importance for the validation of each technique in flows involving SBLI is the availability of high-fidelity experimental data of the quantities on which the models are based, including the velocity, higher-order fluctuations, and gradient quantities. Such field data has until now been unavailable.

1.2 Techniques for Passive SBLI Control

Previous studies of the uncontrolled SBLI show dramatic thickening of the boundary layer in the interaction location and furthermore demonstrate substantial oscillations. In most applications these effects are detrimental or even prohibitive; the former can compromise aerodynamic integrity or affect the air flow rate to an engine while the latter can lead to rapid fatigue of vehicle components. Techniques are therefore required to control the interaction, with the ultimate goals being to reduce the separation and overall thickening of the boundary layer and increase the stability of the interaction, both without significantly increasing the overall drag or total pressure loss in the system. Myriad techniques have been proposed for this purpose, with essentially all of them aiming to transport high-velocity fluid from the free stream to the near-wall region in order to stabilize the interaction region and prevent shock-induced boundary layer separation.

For laminar boundary layers, relatively simple tripping devices trigger the onset of turbulence so that the resulting lower shape factor replaces the laminar profile. In already turbulent boundary layers, such as in typical supersonic inlets, bleed is the most widely used technique. In this approach, the low-momentum fluid in the incoming boundary layer is bled via suction through the wall so that only higher-

momentum fluid remains at the interaction location. Hamed and Shang (1991) provide a review of numerous studies involving bleed, which essentially all demonstrate the anticipated result that the boundary layer thickening and separation are reduced and the overall stability of the interaction is improved. As expected, the efficiency of supersonic inlets using boundary layer bleed is increased over similar inlets without bleed (e.g. Yanta et al. 1990).

While boundary layer bleed sufficiently demonstrates the utility of transferring high momentum gas from the free stream to the near wall region for controlling SBLI, the gains come at a direct cost. The work done to initially compress the bleed air is lost when the air is removed from the system, and thus a direct and substantial loss in overall thermodynamic efficiency is incurred. Much attention has therefore been paid toward identifying alternative passive and active techniques that replace or supplement boundary layer bleed systems, while still achieving the desired momentum transfer from the outer stream to the near-wall region. Swept grooves, passive porous surfaces, vortex generators (Lin and Howard, 1989), passive cavities (Raghunathan, 1989), perforated plates (Bur et al., 1998), aeroelastic mesoflaps (Gefroh et al., 2002), streamwise slots (Smith and Babinsky, 2004), piezoelectric actuators (Couldrick et al., 2005), and small-scale cross-flowing jets (Kumar and Alvi, 2006) are only some of the many techniques investigated for preventing separation of boundary layers subjected to adverse pressure gradients.

Among these, passive streamwise vortex generators have demonstrated particular potential, in part due to their simplicity and independence from the requirement of external power sources. As the streamwise vortices move downstream of the generator, they preferentially entrain high-momentum fluid from the free stream and transport it to the near-wall region. Vane-like passive vortex generators were initially

investigated by Donaldson (1950) and Lina and Reed (1950) to prevent separation on supercritical airfoils, and have since been used to prevent separation on many airfoil and airframe designs. A number of alternative vortex generator designs have also been proposed, notable among them being sub-boundary layer scale features in the form of long angled bumps (Kuethe, 1971, 1973) and ramp-like wedges (Wheeler, 1984, 1991). In the experimental study by Lin and Howard (1989), which involved subsonic flows with adverse pressure gradients, the so-called "Wheeler doublets" reduce separation with equal effectiveness as similarly dimensioned vane-type vortex generators, but with significantly less parasitic drag. The ramp-like structures have the additional advantage of being considerably more robust as compared to the thin micro-vane design. The many concepts since conceived for passive vortex generation are reviewed by Lin (2002).

McCormick (1993) was one of the first to investigate ramp-type vortex generators in a transonic application. At about the same time Barter and Dolling (1993) investigated the effect of Wheeler dublets on the stability of compression ramp SBLI with illuminating results: the shock motion and upstream influence were reduced by 60% and the RMS pressure fluctuations by 23%. More modernly, the ramp-like Wheeler dublet vortex generators have been kept to sub-boundary layer scales and extended to applications involving incident oblique shock–boundary layer interactions. The design has additionally evolved (or, more aptly, devolved) into a singular triangular ramp-like structure whose dimensions were optimized according to RANS simulations by Anderson et al. (2006) and subsequently termed "standard micro-ramps." Holden and Babinsky (2007) and Ford and Babinsky (2007) performed experimental studies of the effects of standard micro-ramps ranging in height from $0.25\delta_0$ to $0.75\delta_0$ using pitot probe measurements, Schlieren imaging, and oil streak visualiza-

tions. Their findings showed that the boundary layer is significantly less susceptible to separations within the immediate region of influence of the ramps, but this region is confined to the direct wake of the ramps. Lee et al. (2007) used RANS and LES simulations to study the effects of the same standard micro-ramp designs in a Mach 3 flow and similarly found localized advantages but an overall inability to completely eliminate the separation bubble. Recognizing the localized effects, Galbraith et al. (2009) performed RANS simulations of a two row staggered array of standard micro-ramps; while this arrangement showed a further reduction in the level of separation at the shock foot, the separation was still not entirely eliminated.

The transfer of high momentum fluid to the near-wall region has repeatedly demonstrated advantageous effects for SBLI control. Owing to their stark simplicity and physically robust nature, micro-ramp features remain an attractive approach for passive shock–boundary layer control. Several studies, however, show that the effects from current designs are confined to the highly localized region directly in their wake. New micro-ramp designs that offer less confined influence are therefore of potentially great interest. One such concept is offered herein.

1.3 Present work

The present study is designed to address several of the existing voids illuminated in § 1.1 and § 1.2. Specifically, non-intrusive field measurements of all three velocity components visualize the incident oblique SBLI structure with high fidelity. As alluded to by Dupont et al. (2006), such new detailed accounts of the structure are needed to supply new insight that might help in approaching a definitive determination of the cause for the prevalent low-frequency oscillations. Additionally, the data

presented herein includes not only velocity and fluctuation field data, but also the higher order fluctuation and gradient statistics that are needed for rigorous evaluation of computational models and simulations. The results are particularly well suited for evaluation of new non-equilibrium RANS codes presently under development. Furthermore, and possibly most substantially, the work provides a thorough quantitative investigation into the effectiveness of the standard micro-ramp passive vortex generator design. After confirming the inferences of previous authors, a new design that preserves the appealing aspects of the standard design but produces stronger streamwise vortices and wider regions of influence, is proposed and evaluated.

Chapter II describes the custom facility designed specifically for the present study of incident oblique shock–boundary layer interactions using non-invasive measurement techniques. A Mach 2.75 free stream is created in a vacuum driven wind tunnel and flow deflection angles of $\theta = 7.75$-deg, 10.0-deg, and 12.0-deg create oblique shock waves of varying strengths. Liberal optical access enables velocity field visualizations in planes oriented in both the streamwise and spanwise directions. The boundary layer Reynolds number is also considered so that the interaction is in the near-LES accessible regime; the Reynolds number based on momentum thickness at the SBLI location is measured to be $Re_\theta = 9,600$.

The non-intrusive stereo particle image velocimetry (SPIV) technique is used to measure velocity fields throughout the interaction regions. The technique enables instantaneous field measurements of all three velocity components (u, v, w) and six of the nine gradient quantities ($\partial u_i/\partial x_j$). Ensemble averages over hundreds or thousands of statistically independent realizations allow measurements of the mean fields and, together with the instantaneous fields, the fluctuation components can be computed. Specifically, the present work presents all nine components of the Reynolds

stress tensor $\overline{u_i' u_j'}$, which in turn enables computation of the turbulence kinetic energy $\overline{k}$ and all nine components of the anisotropy tensor $\overline{b}_{ij}$, three of the six unique components of the strain rate tensor $\overline{S}_{ij}$, one component of the vorticity vector $\overline{\omega}$, and six of the nine components of the kinetic energy dissipation rate tensor ε. Chapter III evaluates this capability for the present study through measurements of the boundary layer at two undisturbed locations upstream of the interaction location. The results are among the first of their kind in compressible boundary layers, and provide highly resolved statistical quantities suitable for evaluation of DNS simulations such as those described in § 1.1.4.

Chapter IV examines uncontrolled incident oblique SBLI produced by the three deflection angles, providing high fidelity velocity, fluctuation, and gradient data throughout the interaction region. Among other original findings, the effect of the SBLI on the turbulence anisotropy is quantified, making significant implications for computational models. Also, instantaneous visualizations of the gradient fields identify a highly unstable layer of extremely high shear in the upstream portion of the interaction; the unsteadiness of this layer is almost certainly tied to the overall instability of the interaction.

Passive control effects on SBLI are evaluated in Chapters V and VI; the effects of the standard micro-ramp design are quantified in Chapter V, and a new micro-ramp design is proposed and evaluated in Chapter VI. Field visualizations oriented in spanwise planes normal to the free stream velocity are used to quantify the vorticity produced by each of the passive techniques. Visualizations of various statistics in both the spanwise and streamwise planes combine to provide unprecedented insight and clarity into the effects of such techniques on the SBLI structure. Boundary layer integral relations measured as a function of the spanwise dimension further quantify

potential advantages. In short, the newly proposed design for passive control offers a two-fold increase in the maximum vorticity generated, a two-fold increase in the spanwise region of influence of each feature, and nearly a two fold improvement in the wall-normal location of the streamwise vortices as compared to the standard micro-ramp design. The resulting effects on the flow field through the SBLI are similarly encouraging.

Chapter VI provides a summary of the major conclusions.

	$\theta = 7.75$-deg	$\theta = 10.0$-deg	$\theta = 12.0$-deg
T_0 (K)	295	295	295
M_1	2.75	2.75	2.75
M_2	2.40	2.30	2.21
M_3	2.09	1.91	1.75
T_1 (K)	117.4	117.4	117.4
T_2/T_1	1.168	1.222	1.272
T_3/T_1	1.342	1.453	1.556
p_1 (atm)	0.040	0.040	0.040
p_2/p_1	1.697	1.956	2.210
p_3/p_1	2.727	3.512	4.341
p_{0_1} (atm)	1.0	1.0	1.0
p_{0_2}/p_{0_1}	0.985	0.970	0.951
p_{0_3}/p_{0_1}	0.974	0.951	0.922

Table 1.1: Inviscid state quantities computed for the three flow deflection angles θ. Pre-shock quantities are denoted by the subscript 1, quantities between the incident and reflected shock are denoted by the subscript 2, and downstream quantities are denoted by the subscript 3. The subscript '0' denotes a stagnation quantity.

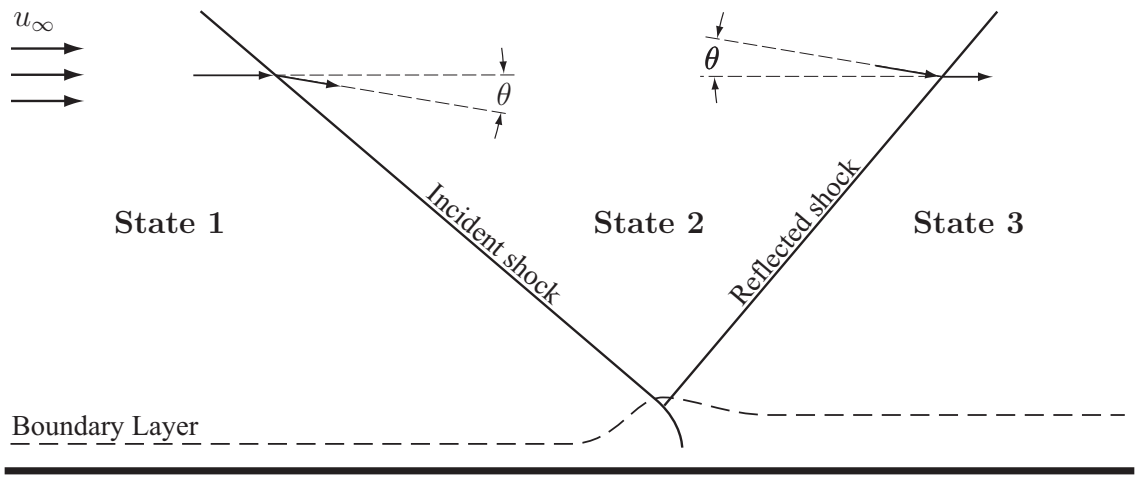

Figure 1.1: Incident oblique shock wave reflecting off a rigid wall. Effects of the shock–boundary layer interaction are indicated roughly by the dashed line.

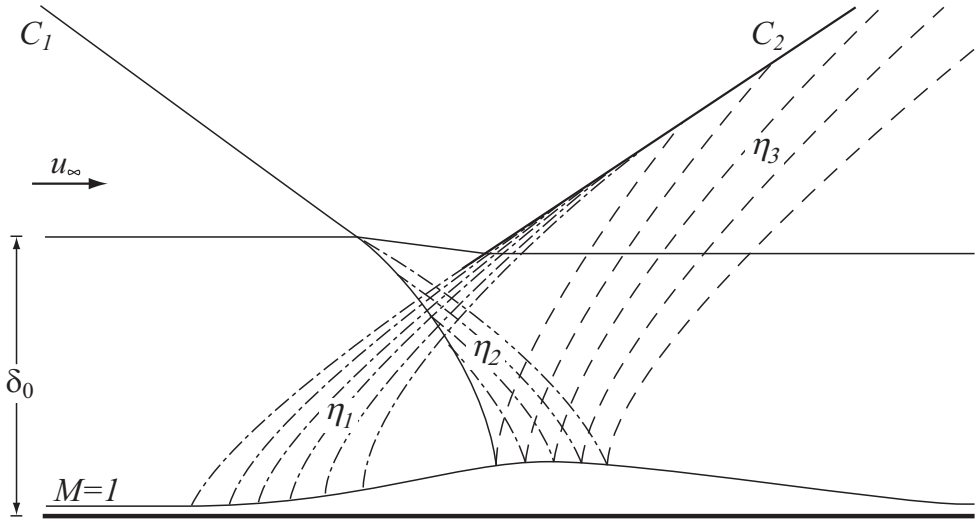

Figure 1.2: Incident oblique shock–boundary layer interaction structure with a weak incident wave and no mean boundary layer separation.

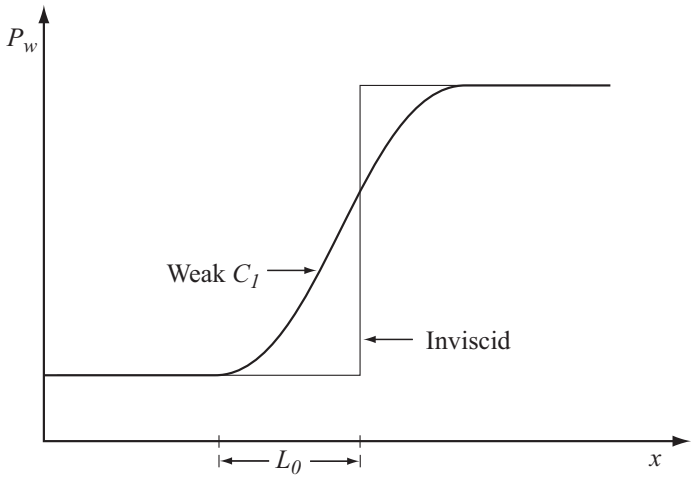

Figure 1.3: Wall pressure distribution for a weak incident oblique SBLI with no mean boundary layer separation in comparison with the discontinuous distribution from a hypothetical purely inviscid interaction.

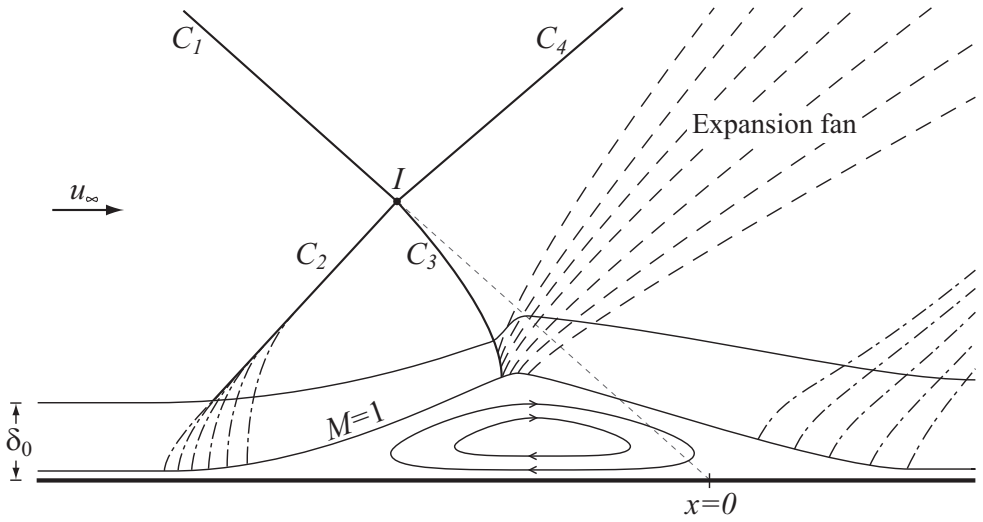

Figure 1.4: Incident oblique shock–boundary layer interaction structure with a strong incident wave and mean boundary layer separation, showing also the inviscid impingement point $x = x_0 = 0$.

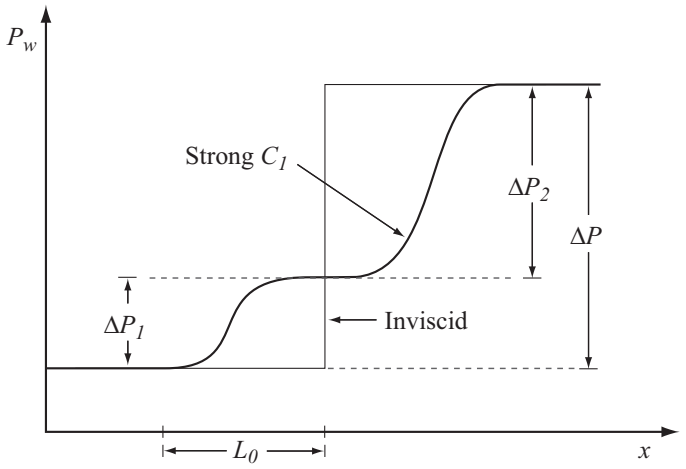

Figure 1.5: Wall pressure distribution for a strong incident oblique SBLI with mean boundary layer separation in comparison with the discontinuous distribution from a hypothetical purely inviscid interaction.

CHAPTER II

Experimental Facilities and Diagnostic

The present study is directed at illuminating the dominant physical mechanisms that govern shock–boundary layer interactions (SBLI) through quantitative accounts of the flow structure and turbulence statistics, as well as evaluating the effectiveness of selected passive control methods. Fig. 2.1 shows a schematic of the experimental approach. Supersonic flow at a fixed design Mach number is induced by a one-sided converging-diverging nozzle. Velocity data are collected in two dimensional planes oriented in both the streamwise and spanwise directions. Data in spanwise planes located immediately downstream of the nozzle provide inlet boundary conditions to support modeling efforts, while high-resolution velocity data throughout the interaction region provide high-fidelity accounts of the interaction region. Figure 2.1 also indicates the coordinate definitions used throughout. The x-coordinate is aligned with the streamwise direction, the y-coordinate is aligned with the wall-normal direction, and the z-coordinate is aligned with the spanwise direction. The origin is located along the centerline of the bottom wall boundary of the tunnel, with $x = 0$ being defined as the inviscid shock-impingement location.

A vacuum-driven supersonic wind tunnel facility designed specifically for this purpose has been implemented in the LTC laboratory. Non-intrusive optical diagnosis

of the SBLI region, by means of stereo particle image velocimetry (SPIV), provides instantaneous and mean velocity data containing all three components of velocity in the two-dimensional planes described above. The key elements of the SBLI wind tunnel facility as well as the SPIV diagnostic technique are described in this chapter.

2.1 Supersonic SBLI Wind Tunnel

The vacuum-driven, or "suck down" wind tunnel facility is shown pictorially in Fig. 2.2 and schematically in Fig. 2.3. The tunnel is driven by off-site vacuum tanks which allow for approximately ten minutes of continuous run time. In contrast to tunnels driven by high pressure sources, the suck-down design ensures constant stagnation pressure and temperature, and thus constant Mach number, throughout the entire course of the run. Interchangeable nozzles enable the tunnel to run at multiple Mach numbers, and interchangeable shock generating wedges produce several shock strengths. Optical access on three sides of the test section enables use of the SPIV diagnostic in planes oriented in both the streamwise and spanwise directions. The constituent modular sections, which include a bell mouth, flow conditioner, subsonic converging nozzle, supersonic diverging nozzle, test section, and diffuser, are discussed individually in Sections 2.1.1–2.1.4. The nozzle and test section can be reconstructed for modeling or experimental purposes through the full account of critical dimensions given in Appendix A.

2.1.1 Flow Conditioning Section

Ambient air enters the 2.25×10.0-in flow conditioning section via a rectangular bell mouth, which has a 2.25-in radius of curvature on all four sides. Fig. 2.4 shows the bell mouth connected to the flow conditioning section with the side wall removed. The flow conditioning section includes three honeycomb meshes on its interior to reduce large scale turbulent structures. The first is located immediately downstream of the bell mouth and has cell length $L = 1.80$-in and diameter $d = 0.10$-in, giving $L/d \approx 15.8$. The second and third meshes are located 16.5-in and 18.0-in downstream of the bell mouth, and each of these have cell length $L = 0.75$-in and diameter $d = 0.06$-in, giving $L/d \approx 12.5$. There is a 5.25-in distance between the third mesh and the downstream exit of the flow conditioning section.

2.1.2 Converging-Diverging Nozzle

Immediately downstream of the flow conditioning section the flow enters a one-sided converging-diverging nozzle that accelerates the flow to the design Mach number. This is shown in Fig. 2.5, also with the sidewall removed. The advantages of the one-sided nozzle design are two-fold. First, the straight bottom-wall boundary forms a flat plate compressible boundary layer with reduced pressure gradient effects so that the resulting velocity profiles closely resemble the classic zero-pressure gradient profile. Second, it enables trivial reconfiguration of the nozzle allowing for several different free stream Mach numbers to be generated. The converging-diverging nozzle is broken into two parts: a subsonic portion which provides pure convergence, and a "supersonic" portion which provides the remaining convergence to the design

throat size before also providing the supersonic diverging contour. The contour for the supersonic portion of the nozzle was determined using the nozzle code NOZCS with additional consideration of the displacement thickness. A sampling of the nozzle coordinates is given in Table A.2. Because of the one-sided nozzle design, only this supersonic portion needs to be replaced in order to convert between different design Mach numbers. Two such nozzles have been fabricated: one to provide $M = 2.00$ free-stream flow, and one to provide $M = 2.75$ free-stream flow. This study involves only flows with the $M = 2.75$ free stream.

2.1.3 Test Section

Regardless of the design Mach number, the supersonic nozzle opens into a 2.25×2.75-in test section. To generate the SBLI of interest to this study, a strut and wedge assembly is used to produce an oblique shock wave that propagates across the test section and interacts with the opposite-wall boundary layer. The strut and wedge assembly is installed along the top wall of the test section, and is shown in Fig. 2.7. The leading edge of the 0.90-in tall and 0.125-in wide strut is located 33.9-in downstream of the nozzle entrance, and is mounted on the centerline of the upper boundary of the test section. This downstream location is chosen to balance several competing interests: to allow for sufficient boundary layer growth so that 1) sufficient resolution of the inner boundary layer structure is achieved using the SPIV technique and 2) a zero-pressure gradient profile is approached while 3) limiting the boundary layer Reynolds number in order to accommodate computational efforts.

The strut leading edge provides a convenient fixed location from which other relevant dimensions are defined. The leading and trailing edges of this strut form

sharp edges which spread at half-angles of 3.6-deg, thus generating only a relatively weak and shallow oblique shock wave whose influence does not enter the region of study. Any of three clear acrylic wedges, which span 1.25-in in the spanwise direction, can be fixed to the strut. These provide flow deflection angles of $\theta = 7.75$, 10.0, or 12.0-deg, which in turn produce oblique shock waves with $p_3/p_1 = 2.73$, $p_3/p_1 = 3.51$, and $p_3/p_1 = 4.34$, respectively, with the $M = 2.75$ incoming free stream. These oblique shock waves propagate across the test section and impinge on the boundary layer formed along the opposite wall of the test section, producing the interactions that are the topic of this study.

At the interaction location the flat plate boundary layer height is $\delta_0 = 10.0\,\mathrm{mm}$, as measured in §3.4.2. The strut fixes the wedge 0.90-in from the test section top wall and thus it resides sufficiently outside of the top-wall boundary layer. This ensures a steady shock whose anchor point does not "jitter" due to the considerable turbulence present within the boundary layer. Furthermore, the effect of the side-wall boundary layers on the impinging shock is removed since the wedge spans only 1.25-in of the 2.25-in full-span width.

Three dovetail slots are located on the bottom boundary of the test section at distances of 5.95-in, 3.79-in, and 1.62-in upstream of the leading edge of the strut. Interchangeable inserts are placed into these slots. The insert surfaces can be either blank or can have any number of geometries formed on them. This system of interchangeable dovetail inserts thus provides a relatively trivial and low cost method for investigating the effects of various passive boundary layer control devices. This study focuses on SBLI without passive control as well as SBLI with two passive control designs, herein termed "standard" micro-ramps (Fig. 2.8*a*) and "inverse" micro-ramps (Fig. 2.8*b*). Those designs are described in detail in Chapters V and VI, respectively.

Optical access is provided along the entirety of the test section by windows that form the side walls. These allow the PIV cameras to image the interaction region while being arranged in their stereo positions. They furthermore provide access for the laser sheets to enter the test section in the direction normal to the free stream velocity and thus they illuminate spanwise-oriented planes. An additional window is mounted flush along the lower boundary to enable imaging of the streamwise planes.

2.1.4 Diffuser

The downstream exit of the tunnel consists of a diffuser section which takes the cross-sectional area of the tunnel from rectangular to round. The diffuser section provides a stable setting in which a normal shock can reside, thus bringing the flow velocity from supersonic to subsonic. The effective diffuser angle of $\alpha = 2.0°$ is computed as

$$\alpha = \tan^{-1}\left(\frac{D_{out} - D^*_{in}}{L}\right), \tag{2.1}$$

where

$$D^*_{in} \equiv 2\left(\frac{A_{in}}{\pi}\right)^{1/2}. \tag{2.2}$$

The flow exits the diffuser into a 6-in diameter vacuum line, which later expands to 8-in diameter. A 6-in ball valve is used to open the test section to the vacuum.

2.2 Stereoscopic Particle Image Velocimetry

Stereoscopic particle image velocimetry (SPIV) produces a single-color cross-correlation PIV measurement. Two interline transfer CCD cameras with 1280 ×

1024 pixel resolution and two Nd:YAG lasers are coordinated by a computer with an onboard programmable timing unit. Each individual particle image is a single-color, double-frame, single-exposure PIV image acquired at an angle to the light-sheet normal, thus allowing two cameras oriented in a stereo configuration to determine the two in-plane velocity components and the one out-of-plane velocity component over the measurement field-of-view. The 532 nm light sheets formed by the Nd:YAG lasers illuminate the particles.

Except in the case of the spanwise imaging planes, where the out-of-plane velocity component is approximately 600 m/s, the methodology used here is unremarkable compared to typical SPIV measurements. The special treatment required in the spanwise planes, as well as other elements essential to the technique such as the light sheet generation, seed particles, seed density, and particle imaging, are discussed in § 2.2.1–2.2.5.

2.2.1 Light Sheet Generation

To illuminate the seed particles in the field-of-view, a pair of light sheets are created using two frequency-doubled Nd:YAG lasers (one Spectra-Physics Quanta-Ray Pro-250 and one Spectra-Physics GCR-3). The lasers are sequentially triggered to create the double pulse of the 532 nm sheets, each with total energy of approximately 200 mJ. The flashlamps and Q-switches are triggered by TTL signals at 10 Hz with a pulse duration of 10 ns. The interframe time Δt between pulses is controlled by a PC-based programmable timing unit (PTU) controlled by the LaVision DaVis 7.2 PIV acquisition software.

Both lasers have a 100 ns intrinsic delay between the rising edge of the trigger

pulse and the actual peak in laser energy. This additional delay is significant for the flow conditions used in the present study, and causes the actual interframe time Δt, determined by the peak-to-peak in laser energy, to differ from the target interframe time Δt_0, determined by the trigger pulses. Furthermore two different PTUs (one internal and one external) were used throughout the course of this study, with the laser response being unique to each. Thus quantification of Δt as a function of Δt_0 is required. This is done using a ThorLabs DET10A/M high-speed photodetector connected to a LeCroy WaveRunner 6030 350 MHz oscilloscope. Results for both the internal and external PTU's are shown in Fig. 2.9. The ratio $\Delta t_0/\Delta t$ is used to correctly interpret the measured velocity data.

The laser paths are shown schematically in Fig. 2.10. Two spherical lenses are used as telescoping optics to expand the beam generated by Laser 2 until the beams generated by both lasers have equal width. After being joined by a beam splitter, the initially separate laser pulse pair is directed along one of two common paths. For imaging of spanwise planes, the sheet path is directed normal to the test section centerline and enters the section through the windows that form the side walls. This is shown by the solid green line in Fig. 2.10. For imaging of streamwise planes, the pulse pair is directed under the test section along its centerline until it is reflected vertically through the window in the floor of the test section. This is shown by the dashed green line in Fig. 2.10. In each case, two cylindrical lenses are used to form the sheets. The first expands the beam vertically, while the second focuses the beam in the horizontal direction.

2.2.2 Laser Sheet Thickness

To limit out-of-plane particle loss from Frame 1 to Frame 2, the laser sheet thickness must be large in comparison to the out-of-plane particle displacement. In most typical applications this requirement is automatically satisfied since the full-width at half-maximum of a typical 532 nm Gaussian beam waist is approximately 250 nm. For the spanwise planes in the present work, however, the nominal flow direction is oriented normal to the laser sheet and thus the out-of-plane velocity component is approximately 600 m/s. Current state-of-the-practice camera hardware limits the inter-frame time to a minimum of approximately 500 ns, giving typical out-of-plane particle displacements of approximately 300 μm. The sheet thickness must therefore be made considerably thicker than the minimum Gaussian beam waist. Note, however, that an increasingly thick sheet introduces volumetric effects not accounted for by two-camera SPIV algorithms. Thus a tacit optimization process, in which the sheet thickness is adjusted in conjunction with the camera aperture, camera angle, Scheimpflug angle, laser intensity and other aspects of the arrangement, takes place in order to minimize both particle loss and volumetric effects. These aspects of the experimentation are discussed in §2.2.5.

After performing this optimization, the thickened laser sheets used for imaging the spanwise planes were measured at the center of the field-of-view by traversing a knife edge across the sheet and collecting the transmitted light with a Scientech Vector S310 photodiode detector. Typical results are shown in Fig. 2.11. An error function was fit to the data using nonlinear least-squares differences (Fig. 2.11*a*), and then differentiated to obtain the resulting sheet-normal Gaussian intensity profile (2.11*b*). The full-width at half-maximum, shown by dashed lines in Fig. 2.11*b*, is found to be 450 μm, nearly double the width of the Gaussian waist.

Finally, to ensure uniform sheet thickness across the entire field of view, the originally circular beam is significantly overexpanded by the sheet forming optics such that only the central 15% is used to illuminate the field of view.

2.2.3 SPIV Seed

To seed the flow in this study, an oil aerosol is generated using a TDA-4B portable Laskin nozzle aerosol generator from ATI Techniques. The generator consists of an array of six Laskin nozzles that create polydispersed sub-micron particles. Using a Poly-Alpha Olefin (PAO) oil with density $819\,\mathrm{kg/m^3}$, also provided by ATI Techniques, the mean particle diameter created by the generator is specified to be $0.281\,\mu\mathrm{m}$. Three valves enable any number of the nozzles to be operated simultaneously, thereby allowing for a wide range of aerosol concentrations.

Inherent in any PIV measurement within confined duct flows is the propensity for the seed particles to accumulate on the walls and windows of the duct. This well-known issue is not merely an annoyance; it results in limited run times and thus limits sample sizes. To mitigate this effect, seed is selectively introduced to the flow such that only about one-and-a-half times the measured field of view is seeded with particles. This extends run time and sample size by a factor of approximately five.

2.2.4 Particle Stokes Number Criterion

The SPIV technique measures the displacement field of particles seeded into the flow. The accuracy with which the seed particles track the fluid motion can be expressed in terms of a particle Stokes number (e.g. Samimy and Lele, 1991; Clemens

and Mungal, 1991; Melling, 1997; Raffel et al., 1998), defined as

$$St \equiv \frac{\tau_p}{\tau_f}, \tag{2.3}$$

where τ_p and τ_f are the characteristic particle and flow time scales, respectively. The characteristic particle time scale is derived from Stokes law for spherical particles as

$$\tau_p = \frac{\rho_p d_p^2}{18\mu}, \tag{2.4}$$

where ρ_p and d_p are the particle mass density and mean diameter and μ is the dynamic viscosity of the surrounding fluid. The characteristic flow time scale for a turbulent shear flow is defined from the local outer length scale $\delta(x)$, in this case the local full width of the boundary layer, and the local outer velocity scale u_∞, in this case the local free stream velocity, so that

$$\tau_f = \frac{\delta(x)}{u_\infty}. \tag{2.5}$$

Clemens and Mungal (1991) have shown that particle slip is negligible if the particle Stokes number $St < 0.5$ for typical incompressible flows. Samimy and Lele (1991) showed computationally that in compressible flows, $St < 0.25$ particles could adequately track the large scale motions but that for $St > 0.05$ they were not capable of tracking the smallest scales. Samimy and Elliott (1990) showed experimentally that particle slip is negligible if the Stokes number $St < 0.1$ in supersonic flows.

In this study an oil aerosol is generated with the mean particle diameter being $0.28\,\mu$m, giving a particle relaxation time of $\tau_p \approx 0.44\,\mu$s. For the $M = 2.75$ free stream, the characteristic flow time scale is $\tau_f \approx 17\,\mu$s giving a particle Stokes number of $St \approx 0.026$. This readily meets the criterion noted above. The particle size was independently verified by assessing the relaxation distance as the particle passes through a shock. This assessment is described in detail in § 3.1.

2.2.5 Particle Imaging

The particle images are recorded by two SensiCam PCO interline transfer CCD cameras. The CCD has a 1024×1280 ($h \times w$) pixel array and a physical chip size of 6.8×8.6 mm. The 12-bit signal depth provides sufficient signal dynamic range, and electronic Peltier cooling ensures low noise.

Each camera is equipped with a Sigma 70-300 f /4-5.6 APO macro lens to allow up to 1:1 imaging at a minimum focal length of 40.1 cm. For each camera, particle images from the first laser pulse are recorded onto the first frame and then immediately shifted under the submask. The particle images from the second laser pulse are then stored on the second frame after the time separation Δt.

The cameras are quoted for operation at interframe times as low as 200 ns, however reliable operation ceases for $\Delta t \lesssim 800$ ns. Below this level, the pixels near the horizontally outer boundaries are unsuccessfully transferred under the submask resulting in low or zero signal levels at those locations. As the interframe times are decreased, the affected regions grow in size. Due to the large out-of-plane velocity component, the spanwise planes in the present study require interframe times below 550 ns. Because of this, only the central third of the CCD can be used for imaging those planes; in those cases the CCD has a 1024×425 ($h \times w$) effective pixel array. For imaging streamwise planes, where the out-of-plane velocity is much lower and the interrogation windows are somewhat larger, longer interframe times ($\Delta t \approx 900$ ns) are used and thus the particle images are comprised by the entire CCD array.

The two cameras are arranged differently for imaging of streamwise and spanwise planes, as shown in Fig. 2.12. Imaging of spanwise planes is done using the forward/forward camera configuration, in which both cameras image the particles in forward scattering mode. For imaging of the streamwise planes, the laser sheet enters

the test section through its floor and as a result both cameras image the particles in side-scattering mode.

In both cases the cameras are in an axisymmetric angular-displacement configuration, with each satisfying the Scheimpflug condition for stereoscopic imaging (Prasad and Jensen 1995). This criterion requires that the object plane, the lens plane, and the image plane must all meet at a common point and satisfies a necessary condition for achieving uniform focus across the field-of-view despite the angled vantage of the cameras. The Scheimpflug criterion is met by adding an angular rotation mount between the camera and the camera lens.

Also in both cases, the cameras are oriented at an angle of $\alpha = 33°$ with respect to the object plane normal. Note that the minimum out-of-plane displacement errors occur for $\alpha = 45°$, while the minimum in-plane displacement errors occur at $\alpha \approx 20°$ (Lawson and Wu 1997). Since these two are diametrically opposed, a trade-off between the two is necessary. The angle of $\alpha = 33°$ was found to optimize the performance of the system used in the present study, and is in good agreement with the findings of Lawson and Wu (1997), who indicate the optimum camera angle to be near the range $20° \lesssim \alpha \lesssim 30°$.

The small field-of-view of the measurements, coupled with the long focal length of the camera lens, dictates that a small aperture setting together with the Scheimpflug criterion must be used to create particle images that are focused across the full extent of the field-of-view. The small aperture has the additional advantage of reducing image aberrations such as coma and astigmatism. In the present work all images were captured using an aperture setting of $f22$.

The LaVision DaVis 7.2 software package is used to compute the spatial cross correlation and resulting velocity components using a multi-pass algorithm with in-

terrogation boxes decreasing from 64×64 pixels to 32×32 pixels and 50% overlap. The interrogation volumes are therefore roughly cubical with $480\,\mu$m sides, producing $240\,\mu$m vector spacing. In both streamwise and spanwise imaging planes, over 97% of vectors have acceptable correlations. A 3×3 median filter acts effectively as a low pass filter to remove high frequency noise.

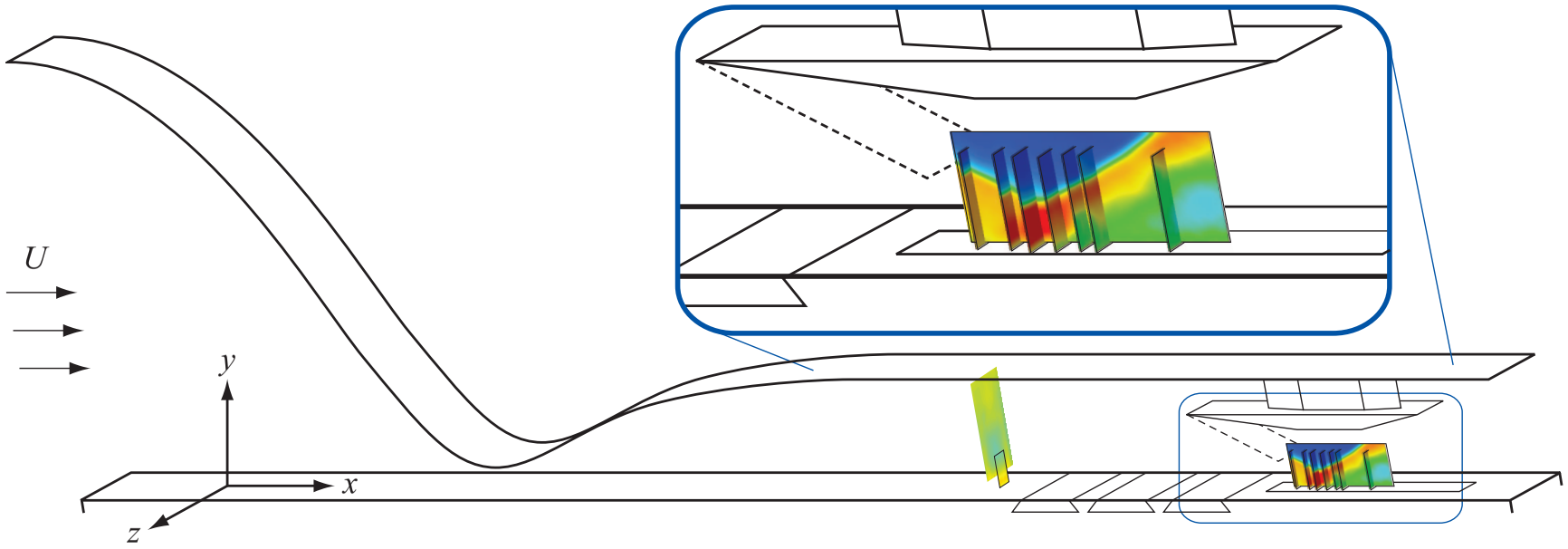

Figure 2.1: Conceptual drawing for wind tunnel and data sampling facility.

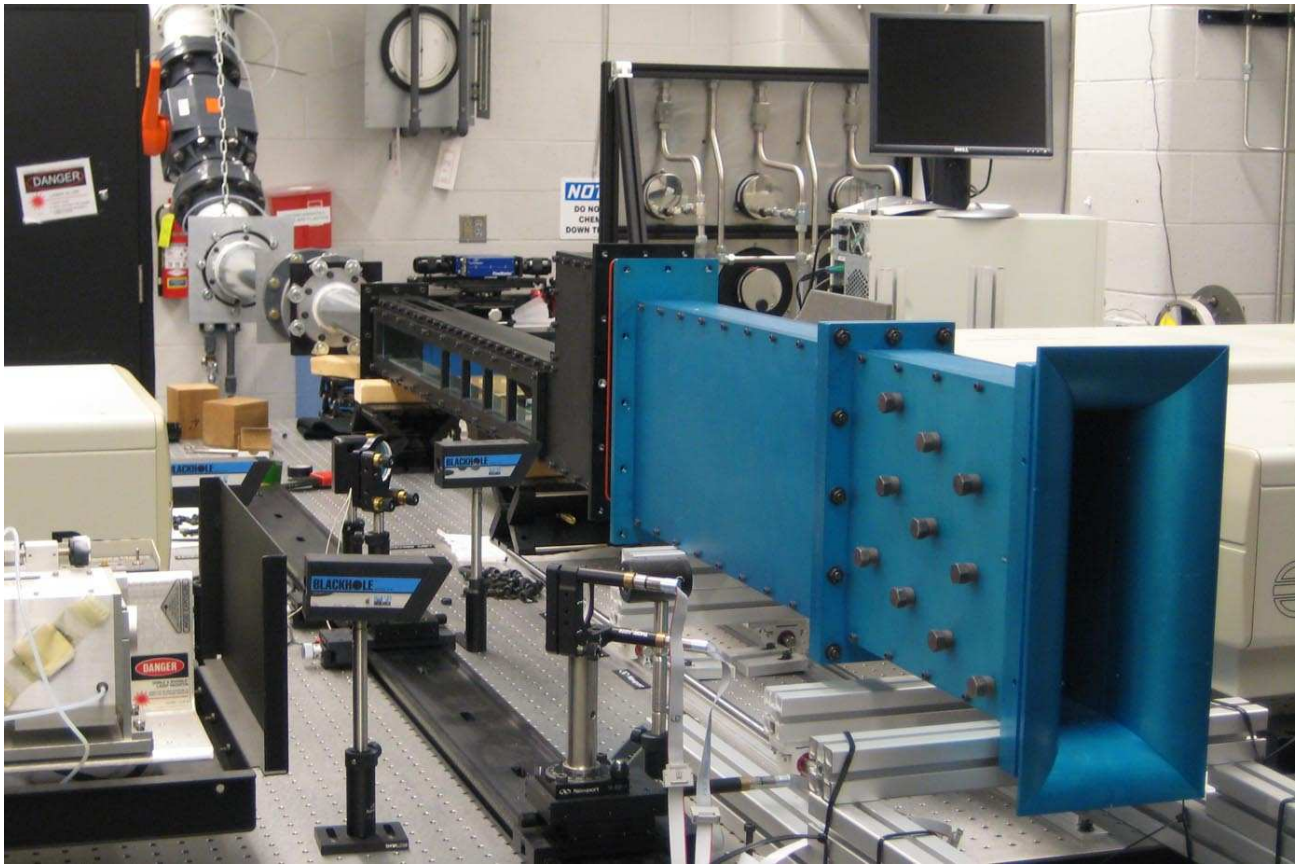

Figure 2.2: Supersonic wind tunnel facility installed in LTC laboratory.

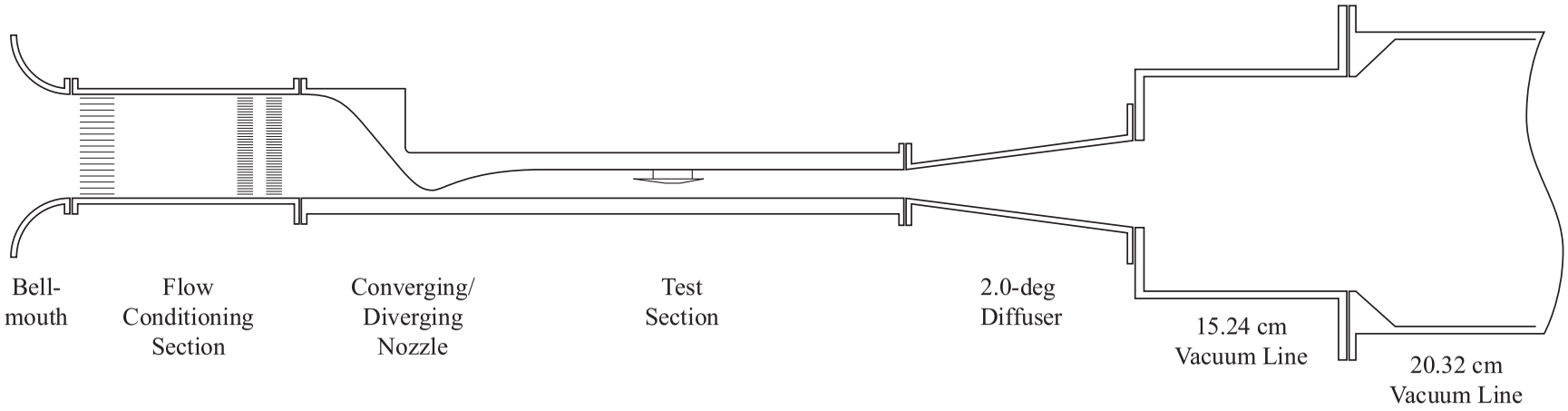

Figure 2.3: Schematic of modular supersonic wind tunnel facility.

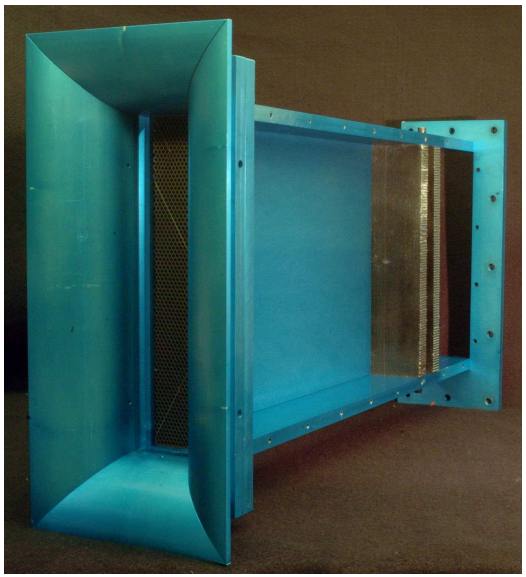

(a)

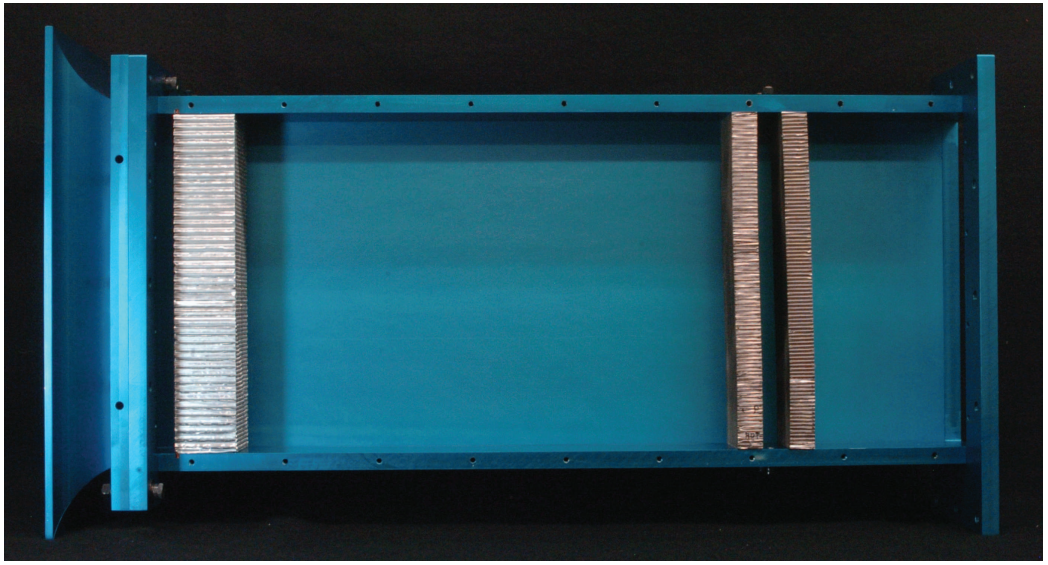

(b)

Figure 2.4: Flow conditioning section with sidewall removed, showing the bell-mouth at the tunnel entrance and honeycomb meshes with decreasing cell size used to reduce the large scale turbulence levels.

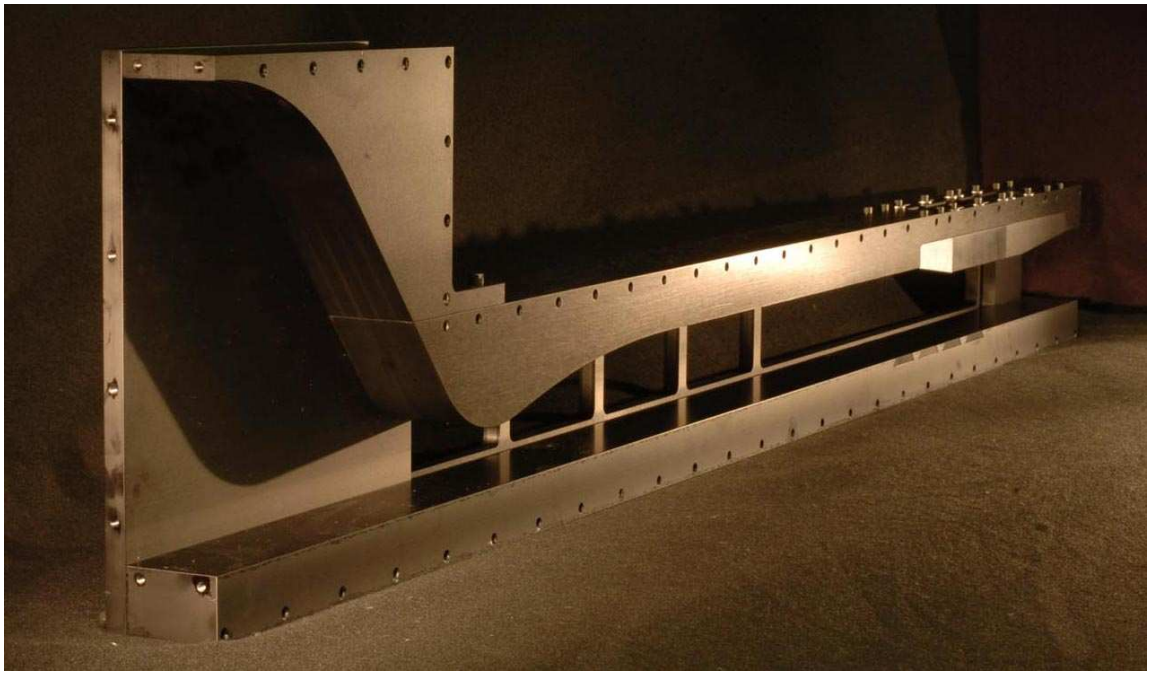

Figure 2.5: Side-view image of the converging-diverging nozzle and test section, with side wall removed.

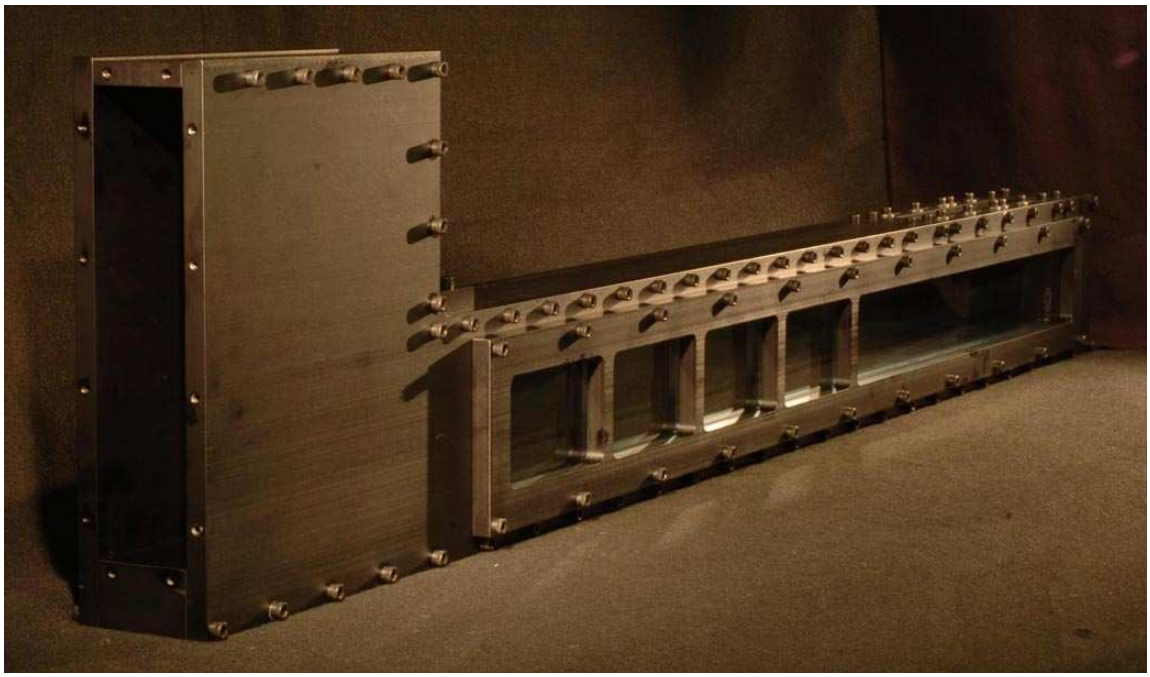

Figure 2.6: Side-view image of the test section with side windows installed.

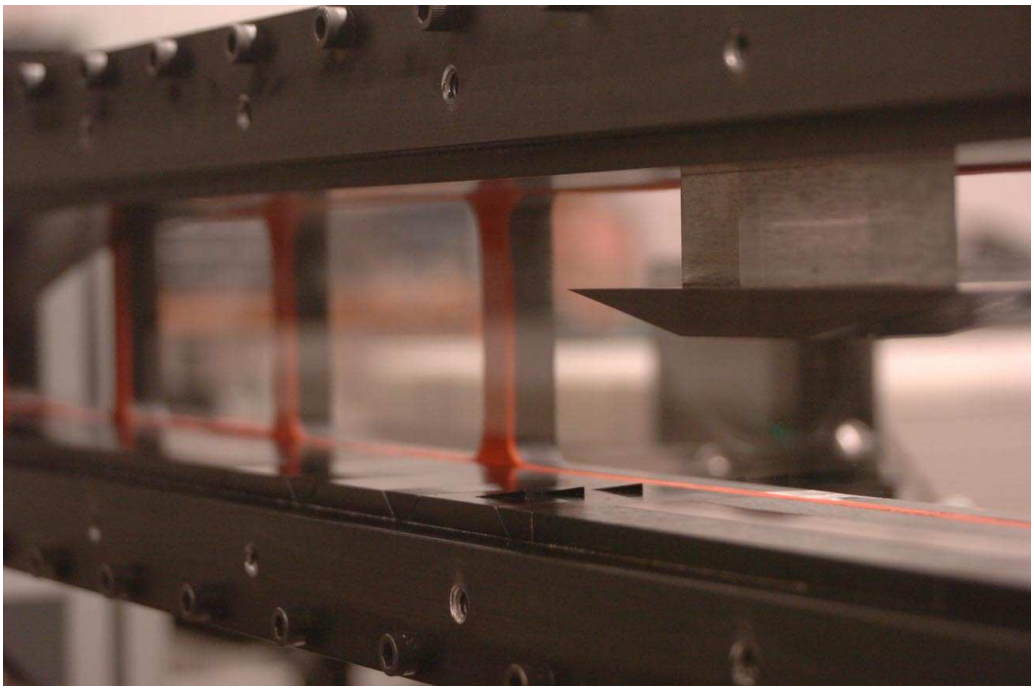

Figure 2.7: The strut/wedge assembly is shown mounted to the top wall of the test section. A dovetail insert containing an array of three "standard" micro-ramps can be seen installed on the bottom wall of the test section.

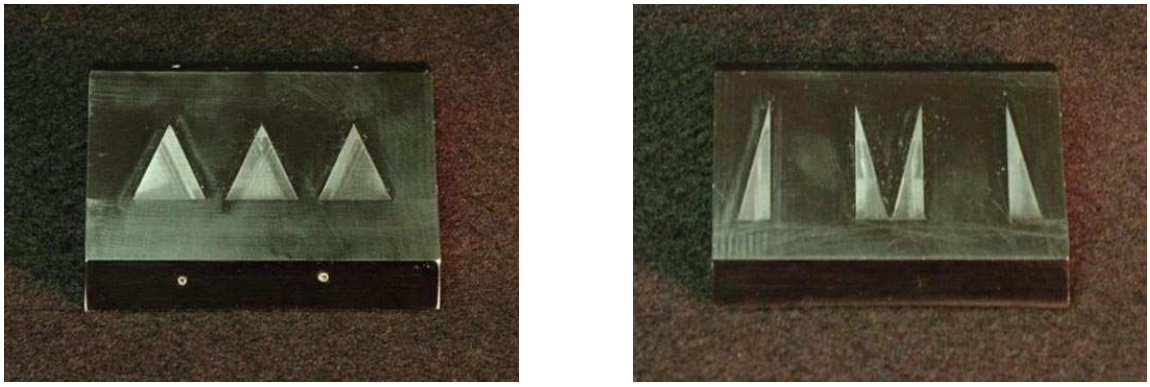

(a) (b)

Figure 2.8: Figure shows *(a)* "standard" micro-ramps and *(b)* "inverse" micro-ramps fabricated on interchangeable dovetail inserts.

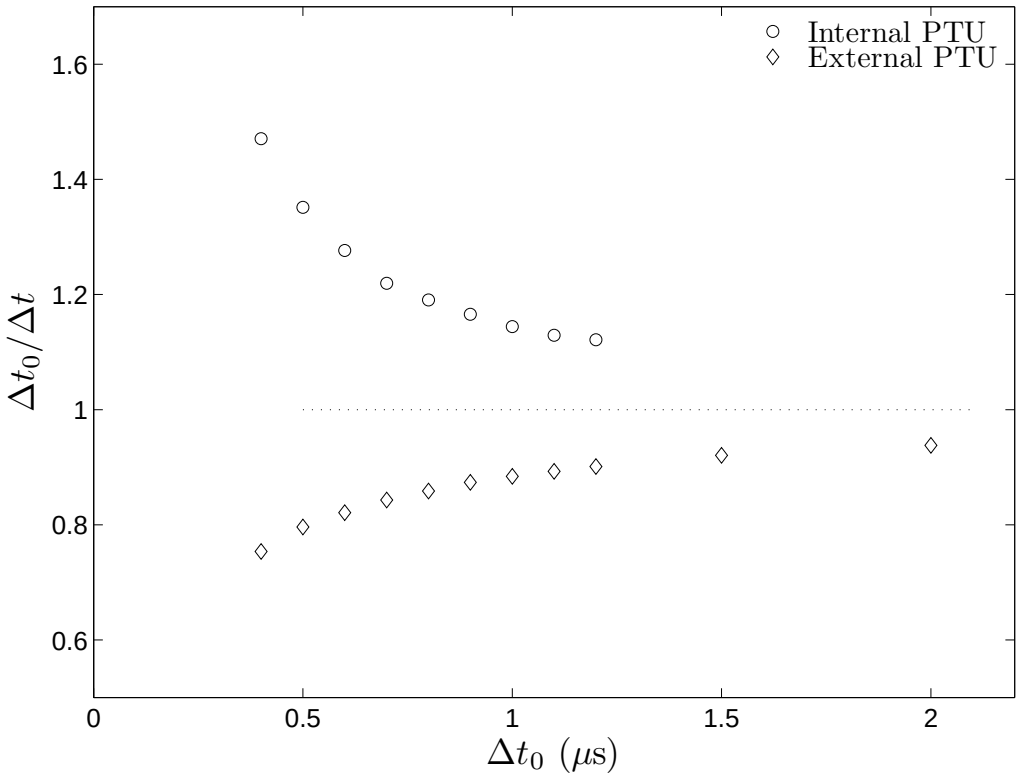

Figure 2.9: The target interframe time Δt_0 and actual interframe time Δt are shown for the two programmable timing units (PTU) used in the present study. The ratio $\Delta t_0/\Delta t$ provides a necessary correction to properly interpret the velocity data.

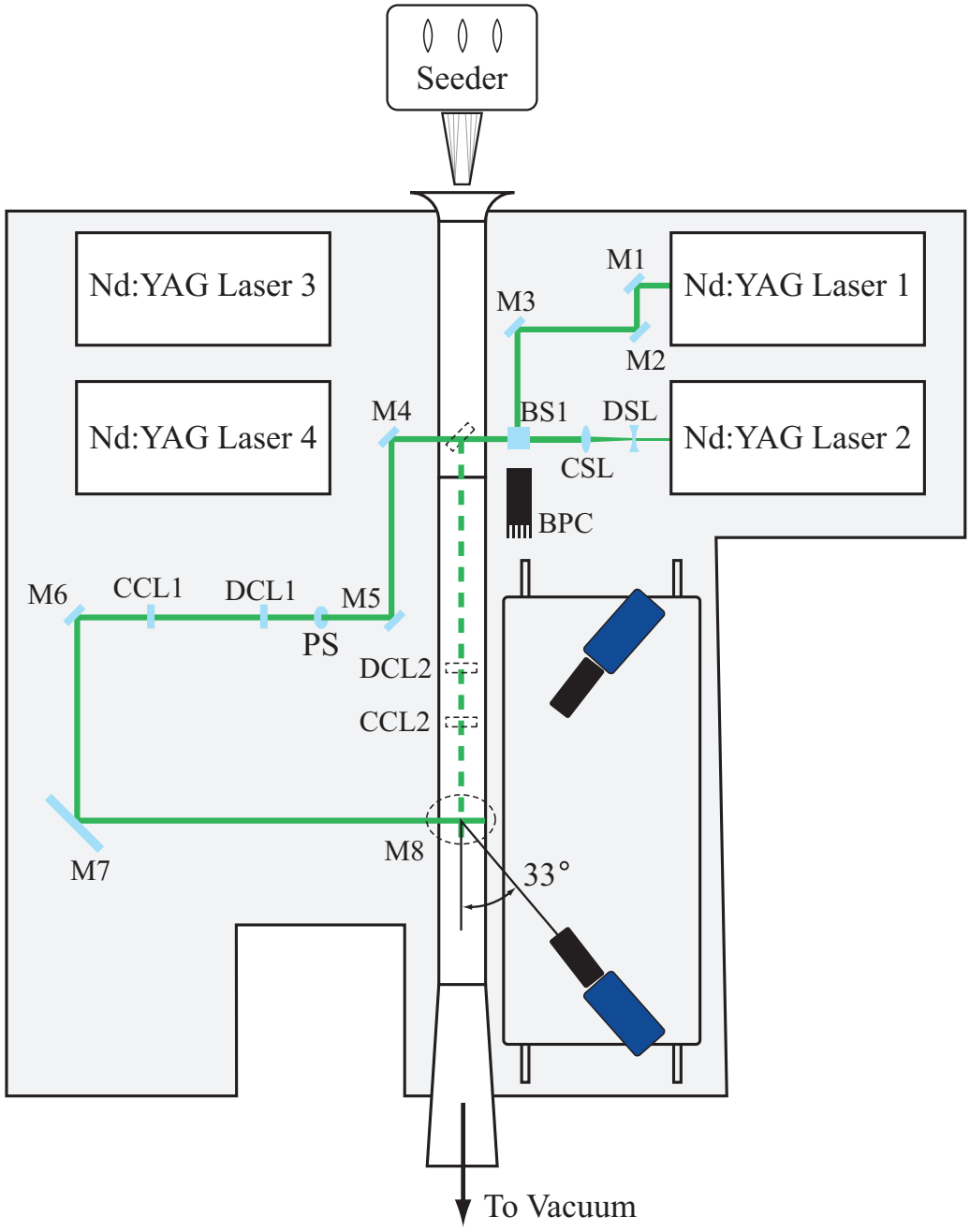

Figure 2.10: Schematic of laser beam path, showing the beam path for spanwise image planes *(solid line)* and for the streamwise image planes *(dashed line)*.

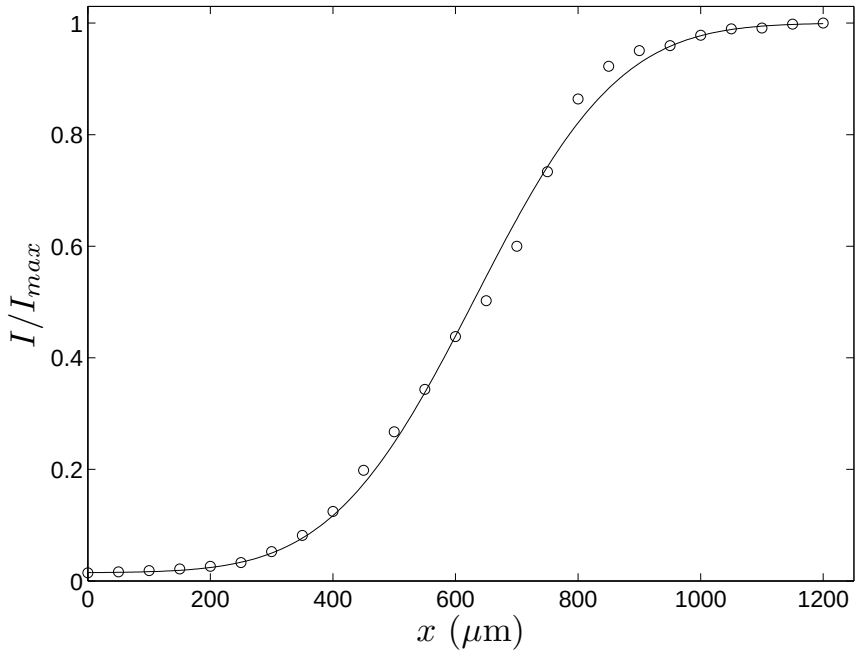

(a)

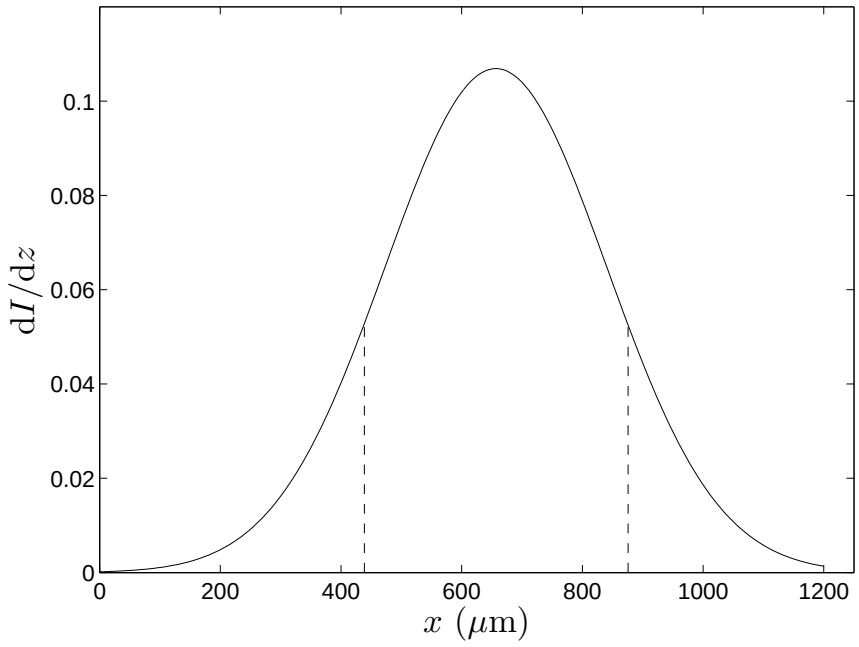

(b)

Figure 2.11: Laser intensity *(a)* measured using a knife edge cuttoff (*symbols*), shown with an error function fit (*line*), and *(b)* the corresponding derivative that indicates the sheet intensity profile.

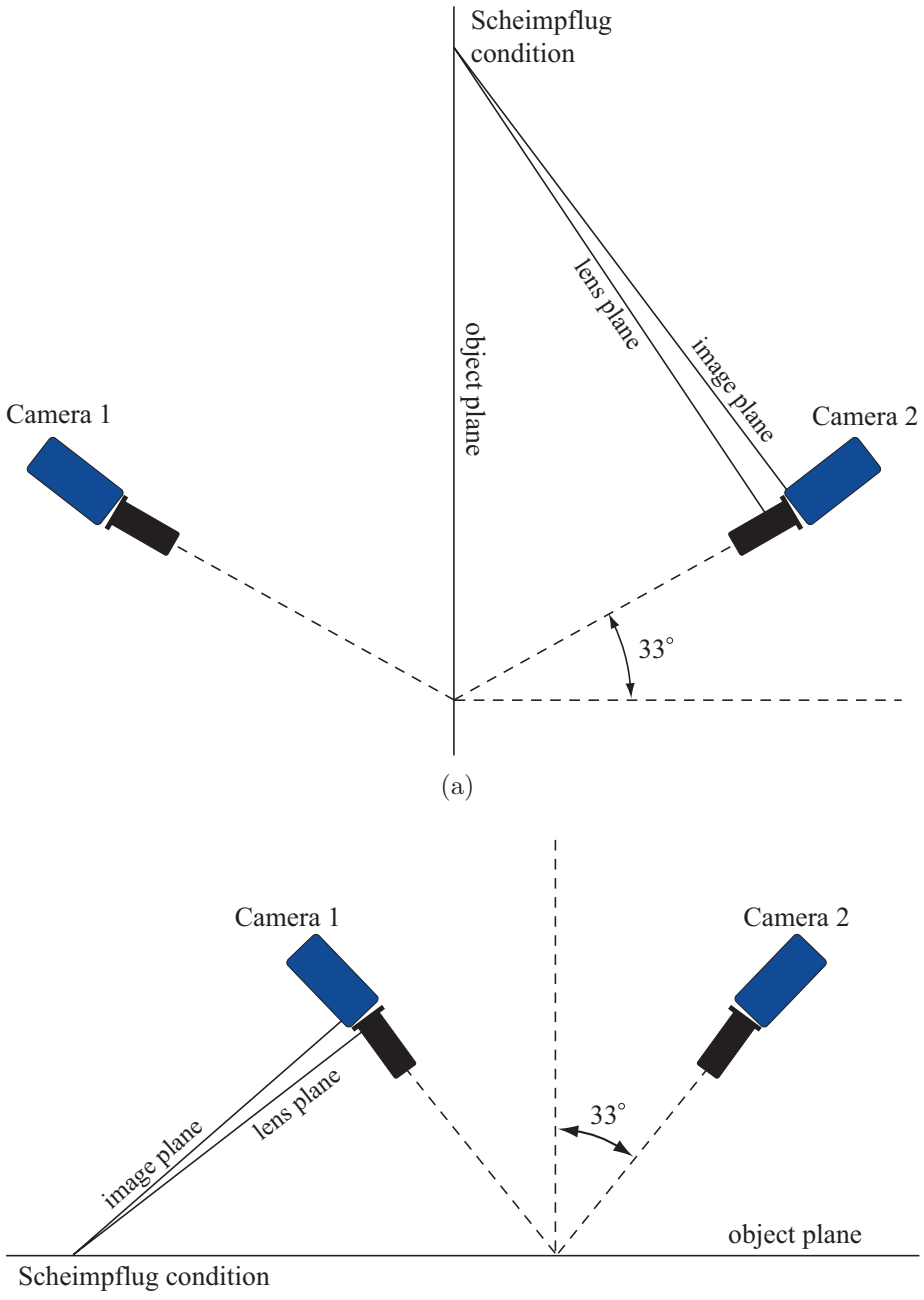

Figure 2.12: Camera configuration used for imaging *(a)* spanwise planes in forward/forward scattering mode and *(b)* streamwise planes in side/side scattering mode.

CHAPTER III

Assessment of Technique and Undisturbed Boundary Layer

This chapter provides an assessment of the SPIV technique that is used in the present study, reviews the existing theory of the compressible boundary layer structure, and compares the present data to that theory.

The experimental assessment consists of three parts. First, an independent deduction of the seed particle size by measurement of the particle response through a shock wave confirms that the particle Stokes number criterion is satisfied. Next the repeatability of the experimental approach is quantified by comparing profiles obtained from two entirely independent measurements at the same downstream location. Finally, the mean and fluctuation velocity data is scaled by inner and outer variables and compared to theoretical predictions for the boundary layer structure.

The fidelity of the data quantifies the degree to which the present boundary layer asymptotically approaches a classic zero pressure gradient profile from its initially disturbed state at the nozzle exit. This evolution is observed in both the mean velocity and Reynolds stress profiles.

3.1 Particle Sizing

As discussed in § 2.2.4, the seed particle size is critical to the accuracy of the PIV technique. This section provides an assessment of the particle lag through a sudden flow discontinuity, namely the oblique shock wave, thus providing an independent measurement of the effective particle size. The discussion is parallel to that of Humble et al. (2007).

A modified Stokes drag law that is valid for spherical particles is given by Scarano (2008) as

$$\tau_p = d_p^2 \frac{\rho_p}{18\mu} \left(1 + 2.7 Kn_d\right), \tag{3.1}$$

where τ_p is the particle relaxation time, Kn_d is the Knudsen number based on the particle diameter d_p, and μ is the surrounding fluid viscosity. Zucrow and Hoffman (1976) show that the Knudsen number can be expressed as

$$Kn_d = 1.26\sqrt{\gamma \left(\frac{M_{\Delta u}}{Re_{d_p}}\right)}. \tag{3.2}$$

The measured particle relaxation time is plotted in Fig. 3.1. The velocity component normal to the shock, u_n, is plotted as a function of distance in the shock-normal direction, n. As the particle passes through the shock its velocity falls from its pre-shock value, u_{n_1}, to its post-shock value, u_{n_2}. The particle relaxation time is the time constant determined from an exponential fit to the particle response, and is found to be $\tau_p = 5.5\,\mu$s. Using this value and solving Equation 3.1 for the particle diameter gives $d_p = 0.57\mu$m. This measurement is not dissimilar to the size quoted by the vendor of the aerosol generator, with at least a portion of the discrepancy resulting from the shock jitter associated with the free stream turbulence. This confirms that the particle Stokes number criterion discussed in § 2.2.4 is readily satisfied.

3.2 Experimental repeatability

The repeatability of the experimental technique is investigated by making two independent measurements of spanwise-oriented planes located at the same downstream location. Each of these visualizations is comprised of an ensemble average of 1350 instantaneous velocity fields and involves completely independent positioning of the laser sheets, camera positioning, calibration, and all other aspects of data acquisition.

Figures 3.2–3.7 show results from the $x/\delta_0 = -2.5$ location with the 7.75-deg flow deflection angle such that the shock resides immediately above the as-yet undisturbed boundary layer. The two independent sets of measurements from the planes oriented in the spanwise direction are marked with squares and circles. Figure 3.2 shows results for the mean streamwise velocity component, and the difference between the two independent spanwise sets is practically indiscernible. Figure 3.2 also includes measurements at the corresponding location from the streamwise-oriented plane, and thus compares the relative error of in-plane and out-of-plane measurements. The 4.5% discrepancy agrees directly with the analysis by Lawson and Wu (1997). Figures 3.3 show the mean vertical velocity component, with the difference between each independent set again being practically indiscernible. Note the clear evidence of the impinging shock, which at this downstream location resides at $y/\delta_0 \approx 1.1$. Immediately above this point, both the streamwise and wall-normal velocity components sharply decrease to the post-shock velocity value.

Higher-order statistical quantities requiring greater sample sizes for acceptable convergence, such as fluctuation and gradient quantities, also show excellent agreement; Figs. 3.4, 3.5, and 3.6 show the mean turbulence kinetic energy $\overline{k}$, the Reynolds

shear stress $\overline{u'v'}$, and the normal strain rate $\overline{S}_{yy}$, respectively. In these, the level of statistical convergence is indicated by showing the $\pm 2\sigma/\sqrt{N}$ error bars, indicating the 95% confidence interval around the mean. The normal strain rate, which is an exceptional marker of the shock location, also shows clearly that the shock resides immediately above the boundary layer. Even the second-order fluctuation gradients, which are required for computation of the turbulence kinetic energy dissipation rate, show good agreement when comparing the two independent sets, as shown in Fig. 3.7.

3.3 Boundary layer structure

The inner boundary layer structure is well understood for both incompressible and compressible flows. The outer wake-like region, which comprises the overwhelming majority of the boundary layer, has a somewhat less concrete theoretical description but is nonetheless well characterized. When scaled correctly, both of these regions have a self-similar nature. In this section these inner and outer variable scalings are described, as well as the logarithmic layer that exists between the inner and outer layers. The effect of compressibility then is considered through discussion of the Van Driest (1951) transformation. Finally, the effect of a pressure gradient on the self-similar boundary layer structure is discussed.

3.3.1 Dimensional reasoning

The mean steady incompressible momentum equation can be written as

$$\rho\overline{u}_j\frac{\partial\overline{u}_i}{\partial x_j} = -\frac{\partial\overline{p}}{\partial x_i} + \frac{\partial}{\partial x_j}\left(\mu\left(\frac{\partial\overline{u}_i}{\partial x_j} + \frac{\partial\overline{u}_j}{\partial x_i}\right) - \rho\overline{u_i'u_j'}\right). \tag{3.3}$$

In a two-dimensional boundary layer with zero pressure gradient, and with $\overline{u} \gg \overline{v}$ and $\partial/\partial y \gg \partial/\partial x$, Equation 3.3 becomes

$$\overline{u}\frac{\partial\overline{u}}{\partial x} + \overline{v}\frac{\partial\overline{u}}{\partial y} = \frac{1}{\rho}\frac{\partial}{\partial y}\left(\mu\frac{\partial\overline{u}}{\partial y} - \rho\overline{u'v'}\right). \tag{3.4}$$

In the inner-most region of the boundary layer, the condition for zero slip at the wall requires that $\overline{u}$, $\overline{v}$, $\overline{w}$, u', v', and w' must all approach zero as the wall is approached. In this limit viscous shear forces would be expected to dominate, and with this logic Prandtl reasoned that in the region nearest to the wall

$$\overline{u} = f\left(\tau_w, \rho, \nu, y\right). \tag{3.5}$$

This scaling is known as "the law of the wall." The only quantities containing units of mass are ρ and τ_w, and these are therefore combined to define the friction velocity $u_\tau \equiv \sqrt{\tau_w/\rho_w}$, which can be used to nondimensionalize the equation. Thus $\overline{u} = f(\tau_w, u_\tau, y)$, out of which only two non-dimensional quantities can exist, so that

$$\left(\frac{\overline{u}}{u_\tau}\right) = f\left(\frac{yu_\tau}{\nu}\right). \tag{3.6}$$

In the outer-most region of the turbulent boundary layer, inertial forces dominate the viscous effects and the boundary layer assumes a wake-like velocity deficit. Kármán therefore deduced that this velocity deficit, independent of viscosity, can be represented by

$$u_\infty - \overline{u} = F\left(\tau_w, \rho, y, \delta, \frac{dp_\infty}{dx}\right). \tag{3.7}$$

This scaling is known as the "velocity deficit law," the dimensionless form of which must have the form

$$\frac{u_\infty - \overline{u}}{u_\tau} = F\left(\frac{y}{\delta}, \frac{\delta}{\tau_w}\frac{dp_\infty}{dx}\right). \tag{3.8}$$

Between the inner and outer regions of the boundary layer the velocity profiles must merge in a continuous fashion. Thus, in this intermediate region the functions f and F, as well as the derivatives of those functions, must be equal. This constraint gives rise to the logarithmic overlap region. Each of these three layers, as well as a composite empirical formulation, are described in § 3.3.2–3.3.5.

3.3.2 The inner viscous sublayer

In the region nearest the wall, the viscous forces dominate and Equation 3.6 applies. Then, defining $u^+ \equiv \overline{u}/u_\tau$ and $y^+ \equiv yu_\tau/\nu$, we have simply

$$u^+ = f(y^+). \tag{3.9}$$

In the region very near to the wall, where mean velocities and their fluctuations approach zero, Equation 3.4 becomes

$$\mu\frac{\partial^2\overline{u}}{\partial y} = 0, \tag{3.10}$$

and in particular

$$\mu\frac{\partial\overline{u}}{\partial y} = \tau_w. \tag{3.11}$$

Integrating again, we have

$$\overline{u} = \frac{\tau_w}{\mu}y = \frac{u_\tau^2}{\nu}y. \tag{3.12}$$

Recalling Equation 3.9 and the definitions for u^+ and y^+, we find that $f(y^+) = y^+$ and, finally, for the inner most region of the boundary layer

$$u^+ = y^+. \tag{3.13}$$

This innermost region is termed the viscous sublayer.

3.3.3 The logarithmic layer

Between the viscous sublayer and the outer-most wake-like region, inertial forces play a critical role but yet they do not dominate completely over the viscous forces. In this region where $\nu/u_\tau \ll y \ll \delta$, Equations 3.6 and 3.8 are simultaneously valid. In this case,

$$\overline{u} = u_\tau f\left(y^+\right) \qquad \text{and} \qquad \overline{u} = u_\infty - u_\tau F(\eta), \tag{3.14}$$

where we have defined $\eta \equiv y/\delta$, and furthermore

$$\frac{\partial \overline{u}}{\partial y} = \frac{u_\tau^2}{\nu} f'\left(y^+\right) \qquad \text{and} \qquad \frac{\partial \overline{u}}{\partial y} = -\frac{u_\tau}{\delta} F'\left(\eta\right). \tag{3.15}$$

Combining the constituent relations of Equation 3.15, we have $y^+ f'(y^+) = -\eta F'(\eta)$. Since the two sides are functions of independent variables only, the relation must equal a constant, so that

$$f(y^+) = \frac{1}{\kappa} \ln y^+ + C \qquad \text{and} \tag{3.16a}$$

$$F(\eta) = -\frac{1}{\kappa} \ln \eta + C', \tag{3.16b}$$

where κ is the von Kármán constant and C and C' are constants of integration. As discussed by Coles and Hirst (1968), the near-universal constants κ and C are generally accepted to be $\kappa = 0.41$ and $C = 5.0$. The non-universal constant C' is a

function of the pressure gradient, and in the present study varies from $3.7 \leq C' \leq 4.6$. Equation 3.16 is known as the "log law". The range of scales at which this region is valid is a strong function of the Reynolds number; the logarithmic layer applies for an increasingly large range for increasingly large Reynolds number. In the present study, the relatively low Reynolds number of $6,600 < Re_\theta < 9,600$ implies a relatively small logarithmic overlap region.

3.3.4 The outer wake-like region

Equations 3.14 and 3.16b combine to give, for the outer region of a zero pressure gradient boundary layer,

$$\frac{\overline{u} - u_\infty}{u_\tau} = \frac{1}{\kappa} \ln \eta + C'. \tag{3.17}$$

Coles (1953) recognized that the scaling in the outer region must agree with that in the logarithmic region, and accomplished this by adding an empirical term to Equation 3.16a. Doing this and combining the result with Equation 3.6, Coles proposed that

$$\frac{\overline{u}}{u_\tau} = \frac{1}{\kappa} \ln \left(\frac{y u_\tau}{\nu} \right) + C + \frac{\Pi}{\kappa} W(\eta), \tag{3.18}$$

where Π is Coles' wake parameter and $W(\eta)$ is Coles' wake function $W(\eta) = 2 \sin^2 \left(\frac{\pi}{2} \eta \right)$ such that $\int_0^1 \eta dW = 1$ and $W(1) = 2$. In this way the empirical term contributes nothing when η is small, but contributes the appropriate correction in the wake-like region. The new empirical term can be related to u_τ and δ by setting $\overline{u} = u_\infty$ at $y = \delta$. Equation 3.18 then becomes

$$\frac{u_\infty}{u_\tau} = \frac{1}{\kappa} \ln \left(\frac{\delta u_\tau}{\nu} \right) + C + \frac{\Pi}{\kappa} W(1). \tag{3.19}$$

By subtracting Equation 3.18 from Equation 3.19, the velocity-deficit form of Equation 3.17 is recovered, giving finally

$$\frac{(u_\infty - \overline{u})}{u_\tau} = -\frac{1}{\kappa}\ln(\eta) + \frac{\Pi}{\kappa}(2 - W). \tag{3.20}$$

For incompressible flat-plate flows with zero pressure gradient and $Re_\theta > 5,000$, it has been demonstrated that $\Pi \approx 0.60$; however it has also been shown that Π varies with boundary layer history and with Mach number. This functionality is discussed in more detail in §3.3.7.

3.3.5 The Spalding composite fit

Spalding (1961) proposed a single empirical composite expression for the entire wall-region, including the linear sublayer, log layer, and the intermediate buffer region that joins the two otherwise discontinuous functions:

$$y^+ = u^+ + e^{-\kappa C}\left(e^{\kappa u^+} - 1 - \kappa u^+ - \frac{1}{2}\left(\kappa u^+\right)^2 - \frac{1}{6}\left(\kappa u^+\right)^3\right). \tag{3.21}$$

3.3.6 The effect of compressibility

Owing to the non-uniform temperature, and therefore non-uniform density and molecular transport properties, compressible boundary layers cannot be directly scaled in the same way as in § 3.3.2–3.3.5. Van Driest (1951) generalized the non-wake portion of Equation 3.18 for compressible boundary layers by defining a generalized velocity

$$u^* = u_\infty \frac{1}{A}\sin^{-1}\left[\frac{2A^2(u/u_\infty) - B}{(B^2 + 4A^2)^{1/2}}\right] \tag{3.22}$$

where

$$A^2 = \frac{[(\gamma - 1)/2]M_\infty^2}{T_w/T_\infty}$$

and

$$B = \frac{1 + [(\gamma - 1)/2]M_\infty^2}{T_w/T_\infty} - 1.$$

Maise and McDonald (1968) combined the Van Driest correction with the Coles law of the wake, giving

$$\frac{(u_\infty^* - u*)}{u_{\tau_w}} = -2.5 \ln\left(\frac{y}{\delta}\right) + \frac{\Pi}{\kappa}(2 - W). \tag{3.23}$$

Here, $u_{\tau_w} = \sqrt{\tau_w/\overline{\rho}_w}$ where $\overline{\rho}_w$ is the gas density at the wall. The density ratio $\overline{\rho}_w/\overline{\rho}_\infty$ is not measured directly in the present work, but can be estimated by values reported in previous works. Spina et al. (1994) compiled several experimental values for $\overline{\rho}_w/\overline{\rho}_\infty$ in flat plate boundary layers at various Mach numbers, and based on an interpolation of these values $\overline{\rho}_w/\overline{\rho}_\infty \approx 0.37$ is used in the present work.

Equation 3.23 thus can be used to compare experimental data in a compressible boundary layer to the well-established incompressible theory for both the inner and outer regions of the boundary layer. Such a comparison also provides a way to indirectly measure the wall shear τ_w and the Coles wake parameter Π.

3.3.7 The effect of the pressure gradient

The preceding relations are based on the assumption of a zero pressure gradient. While the scalings for the inner-most regions of the boundary layer are independent of the pressure gradient, except by the extent to which τ_w is affected, Equation 3.8 makes obvious the fact that the wake-like region is dependent on the pressure gradient. For weak pressure gradients this effect can be accounted for by adjusting of the empirical constant Π, which adds to the simplistic appeal of Coles' wake function.

Figures 3.8 and 3.9 show the Spalding composite fit together with the wake-like scaling of Equation 3.20 for a range of Π values scaled against inner and outer variables, respectively. For a fully relaxed and steady flat plate boundary layer, it is generally accepted that $\Pi \approx 0.60$ (Erm et al. 1985). Π values less than this are representative of flows with favorable pressure gradients, while Π values greater than this are representative of flows with adverse pressure gradients.

For strong adverse pressure gradients, u_τ approaches zero and Π approaches infinity. In this limit, and specifically for $\tau_{max} \gtrsim 1.5\tau_w$, the near-wall variables become irrelevant for scaling purposes. White (1991) discusses several empirical formulations that exist to describe flows with these moderate equilibrium pressure gradients. In the present work the pressure gradients present in the SBLI region are both highly localized and highly unsteady, and therefore leave the existing relations with minimal utility.

3.4 Measured undisturbed boundary layer profiles

The self-similar nature of the boundary layer that was discussed in §3.3 is demonstrated in this section using the present data from two different spanwise planes, each located upstream of the SBLI region. The first is located immediately downstream of the converging–diverging nozzle while the second is located immediately upstream of the SBLI region. Measured and approximated quantities used for the scalings in the present and subsequent chapters are given in Table 3.1. Through these scaling comparisons, the incoming boundary layer as well as its evolution can be sufficiently quantified for use as computational inlet boundary conditions. The comparisons also

provide an indirect measurement of the wall shear-stress τ_w, a determination of the Coles wake parameter Π, a concrete definition of the boundary layer thickness δ, and ultimately an additional validation of the present data. These measurements, as well as other pertinent characterizations of the boundary layer, are summarized in Table 3.2.

By scaling the velocity profiles with inner variables, it is shown that the entire wake-like region of the boundary layer is fully resolved, with the data point nearest to the wall extending through the logarithmic layer and into the buffer region. As discussed in §3.3.7, this resolution enables full quantification of the effects of weak and mild pressure gradients. For strong pressure gradients, the inner variables become irrelevant. Therefore the present resolution is sufficient to fully capture the dominant effects of the incident oblique shock on the boundary layer.

3.4.1 Incoming boundary layer ($x/\delta_0 = -18.2$)

Figures 3.10 and 3.11 show results from the boundary layer at the tunnel inlet, located immediately downstream of the converging-diverging nozzle at $x/\delta_0 = -18.2$. Figure 3.10 shows the velocity data scaled by inner variables, while Fig. 3.11 shows the data scaled by outer variables.

Figure 3.10 compares the theoretical predictions for the linear sublayer, the logarithmic layer, the Spalding fit of the buffer layer, and the Coles wake with the experimental data. The match enables the indirect measurement of the wall shear stress τ_w and the wake parameter Π, and for this location we find $\tau_w = 42.8\,\mathrm{N/m^2}$ and $\Pi = 0.91$. Note that due to the relatively small Reynolds number at this measurement location ($Re_\theta = 6,600$), the logarithmic layer is almost non-existent.

Figure 3.11 demonstrates excellent agreement with Equation 3.23 in the wake region using the same values for τ_w and Π. Note that the departure of the data from the "law-of-the-wake," which occurs at $y/\delta \lesssim 0.15$, is a necessary one as the boundary layer enters the log- and buffer-layers.

Recall from § 3.3.7 that $\Pi \approx 0.6$ for a fully developed flat plate boundary layer with zero pressure gradient. At this $x/\delta_0 = -18.2$ location, the local value of the wake parameter is $\Pi = 0.91$, with the difference being an artifact of the pressure gradient acting on the boundary layer as it traverses the nozzle.

Finally, since the magnitude of the boundary layer thickness δ acts to translate the experimental data in Figure 3.11, scaling by outer variables enables indirect measurement of an unambiguous definition of the boundary layer thickness, giving $\delta = 6.3\,\text{mm}$ for this location.

3.4.2 Boundary layer at shock/boundary layer interaction location

Figures 3.12 and 3.13 show similarly scaled boundary layer profiles immediately upstream of the shock-boundary layer interaction region ($x/\delta_0 = -2.5$). In dimensional space, this location is 15.7 cm downstream of the plane discussed in §3.4.1. Here, the incident shock-wave resides just above the boundary layer at $y/\delta \approx 1.1$. At this location, which is used to determine the reference values at the interaction location, the boundary layer height and Reynolds number are measured to be $\delta = \delta_0 = 10.0\,\text{mm}$ and $Re_\theta = 9,600$. Additionally, at this location Π and τ_w are found to be $\Pi = 0.72$ and $\tau_w = 41.8\,\text{N/m}^2$. For both the inner and outer scalings, the agreement between theory and experiment again is excellent.

3.4.3 Boundary Layer Evolution

Note that from $x/\delta_0 = -18.2$ to $x/\delta_0 = -2.5$ the wake parameter Π decreases from $\Pi = 0.91$ to $\Pi = 0.72$. This is directly related to the evolution of the boundary layer as it asymptotically approaches a classic steady zero pressure gradient boundary layer, for which $\Pi \approx 0.60$. This evolution is shown in Figs. 3.14 and 3.15, which show data from both upstream locations, again scaled by inner and outer variables respectively, as well as the theoretical profile for a classic fully developed flat plate boundary layer with zero pressure gradient. Also noteworthy is the small but certain decrease in the wall shear stress, which is consistent with the thickening boundary layer and is discussed in §3.4.4.

3.4.4 The friction coefficient

From the inner and outer variable scalings, we indirectly measure the shear stress at the wall in each location. These can be compared to typical values in boundary layers via the friction coefficient $C_f \equiv 2u_\tau^2\rho_w/(\rho_\infty u_\infty^2)$ where, recalling from §3.3.1, $u_\tau = \sqrt{\tau_w/\rho_w}$. As before, based on the compilation of Spina et al. (1994), we assume $\rho_w/\rho_\infty \approx 0.37$. Based on this, we find $u_\tau = 31.3\,\mathrm{m/s}$ and $u_\tau = 30.9\,\mathrm{m/s}$ at the inlet and SBLI region, respectively. Then, from the definition of the friction coefficient, we find $C_f = 0.00190$ and $C_f = 0.00185$, respectively. These values are shown in Fig 3.16 together with the experimental results from Coles (1954), the DNS results of Guarini et al. (2000), and the skin friction correlation offered by Bardina et al. (1980).

3.5 The Reynolds stresses

All six Reynolds stresses $\overline{u_i' u_j'}$ are measured at both the tunnel inlet location ($x/\delta_0 = -18.2$) and the SBLI location ($x/\delta_0 = -2.5$). These are shown in Figs. 3.17–3.22, with Figs. 3.17–3.20 showing the on-diagonal normal components $\overline{u'^2}$, $\overline{v'^2}$, and $\overline{w'^2}$ and Figs. 3.21 and 3.22 showing the off-diagonal shear components $\overline{u'v'}$, $\overline{u'w'}$, and $\overline{v'w'}$. Qualitatively, the components behave as expected. Looking first at the outer scalings in Figs. 3.17 and 3.19, the streamwise fluctuation component $\overline{u'^2}$ is easily the largest of the three, while the wall-normal component is the smallest and tends to zero at the wall the fastest. At small y/δ values the wall-parallel components increase sharply. This behavior is well documented, and can be seen in more detail in Figs. 3.18 and 3.20, which show the on-diagonal Reynolds stresses normalized by the inner variables. The behavior of the fluctuations in the inner layer is not dissimilar in trend or magnitude to those in the DNS results of Kim et al. (1987), Spalart (1988), or Pirozzoli et al. (2004). Furthermore, this sharp increase in the fluctuations is known to occur at progressively smaller y/δ values for increasing Reynolds numbers. This is also observed. In Figure 3.17, with $Re_\theta = 6,600$, the sudden increase in $\overline{u'^2}$ occurs at $y/\delta \approx 0.13$ while in Fig. 3.19, where $Re_\theta = 9,600$, the sudden increase occurs at $y/\delta \approx 0.10$.

Somewhat more quantitative evaluation might be achieved by first accounting for the effect of compressibility and then comparing to Reynolds stresses reported for incompressible boundary layers. Guarini et al. (2000) provides a concise summary of the effects of weak compressibility on the Reynolds stresses. The weak compressibility hypothesis, which assumes the turbulence Mach number is small and thus the local dilatation is also small, states that the effect of compressibility is predom-

inantly manifested in the varying fluid properties across the boundary layer. This is the basis for the Van Driest (1951) transformation. Morkovin (1962) stipulates that weak compressibility assumptions are valid for $M \lesssim 5$ free stream, and he further hypothesizes that in this regime the normal Reynolds stresses, when normalized by the local mean density ratio, will scale with the incompressible normal stresses. Morkovin's hypothesis has been supported with reasonable success by the DNS results of Guarini et al. (2000), Pirozzoli et al. (2004), and Pirozzoli et al. (2008), and with the experimental data of Eléna and Lacharme (1988).

To provide this comparison using Morkovin's hypothesis, knowledge of the local mean density is required. While this has not been measured directly, we can approximate the density profile by assuming a temperature profile through the boundary layer. If, in addition, a zero pressure gradient is assumed, the relation of the temperature profile to the density profile is trivial via the ideal gas assumption.

Fernholz and Finley (1980) discuss a number of solutions to the energy-equation that are commonly used to describe the temperature distribution in compressible boundary layers. Dussauge et al. (1996) suggests the linear stagnation temperature profile, given by

$$\frac{\overline{T}_0 - T_w}{T_{0_\infty} - T_w} \equiv \Theta = \frac{\overline{u}}{u_\infty}, \tag{3.24}$$

is the correct profile for fully developed zero pressure gradient flat plate boundary layers. After also assuming isentropic conditions, Equation 3.24 can be solved for the static temperature as a function of the local mean velocity, giving

$$\overline{T} = \frac{\overline{u}}{u_\infty} T_{0_\infty} + \left(\frac{u_\infty - \overline{u}}{u_\infty} \right) \frac{T_w}{T_\infty} T_\infty - \frac{\gamma - 1}{\gamma R} \frac{\overline{u}^2}{2}. \tag{3.25}$$

Again referring to the compilation of state quantities in supersonic boundary layers from Spina et al. (1994) we use $T_w/T_\infty \approx 2.8$ in the present work. Assuming a zero

pressure gradient boundary layer, the local mean density is then

$$\frac{\overline{\rho}}{\rho_\infty} = \frac{T_\infty}{\overline{T}}. \tag{3.26}$$

Figure 3.23 shows the Reynolds stresses from the present data, scaled with the density relation from Equations 3.25 and 3.26, compared to the incompressible DNS results of Spalart (1988). The discrepancy is notable, however recall the considerably liberal assumptions used to define the local mean density, which in turn is used to scale the present data; the equilibrium, zero pressure gradient, and isentropic assumptions are all used despite being known to hold at best approximately. The intention of Fig. 3.23 is therefore not to rigorously compare the experimental results with the incompressible DNS data, but to instead demonstrate the nature of the relaxation of the Reynolds stress as the boundary layer approaches the form of a classic flat plate profile.

Measured Quantities			Approximated Quantities	
	$x/\delta_0 = -18.2$	$x/\delta_0 = -2.5$	Throughout	
y_{min} (mm)	0.36	0.38	μ_∞ (N-s/m^2)	8.21×10^{-6}
Δy (mm)	0.24	0.25	μ_w (N-s/m^2)	1.10×10^{-5}
y^+_{min}	39.6	39.7	ρ_∞ (kg/m^3)	0.12
Δy^+	26.5	26.4	ρ_w (kg/m^3)	0.04
u_∞ (m/s)	613	613	ν_∞ (m^2/s)	6.85×10^{-5}
u_τ (m/s)	31.3	30.9	ν_w (m^2/s)	2.74×10^{-4}

Table 3.1: Measured and approximated quantities used for calculation and normalization of various statistical quantities.

	$x/\delta_0 = -18.2$	$x/\delta_0 = -2.5$
δ (mm)	6.3	10.0
δ^* (mm)	1.03	1.47
θ (mm)	0.74	1.08
H	1.40	1.36
Re/L (m^{-1})	8.9×10^6	8.9×10^6
Re_δ	56,000	89,000
Re_{δ^*}	9,200	13,100
Re_θ	6,600	9,600
τ_w (N/m^2)	42.8	41.8
Π	0.91	0.72

Table 3.2: Boundary layer quantities at the two upstream locations, showing the boundary layer thickness δ, displacement thickness δ^*, momentum thickness θ, shape factor H, associated Reynolds numbers, wall shear stress τ_w, and wake parameter Π.

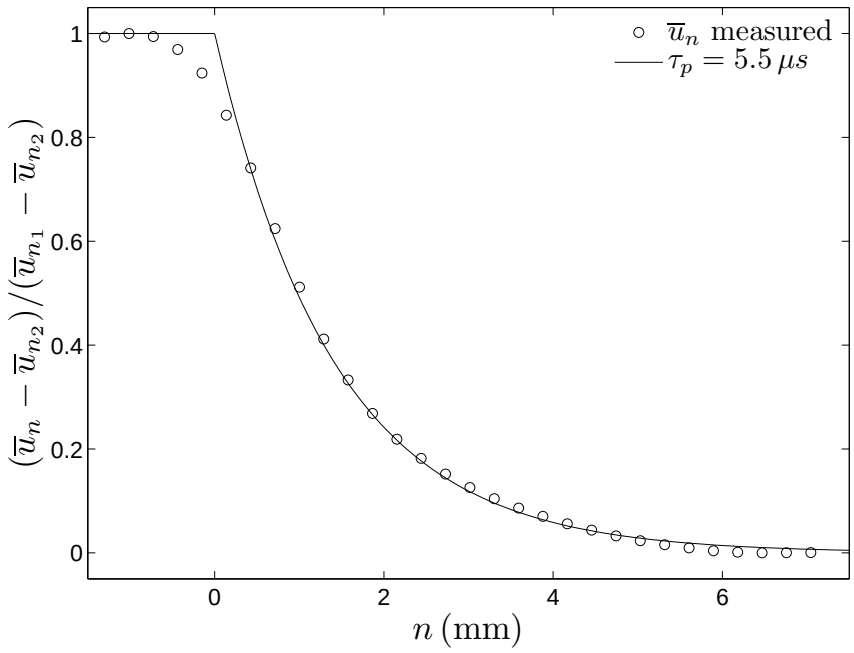

Figure 3.1: Measured particle response through an oblique shock. The velocity component normal to the shock, $\overline{u}_n$, is normalized by the pre-shock ($\overline{u}_{n_1}$) and post-shock ($\overline{u}_{n_2}$) velocities and shown as a function of the shock-normal direction, n. An exponential fit to the data reveals the particle relaxation time, $\tau_p = 5.5\,\mu$s.

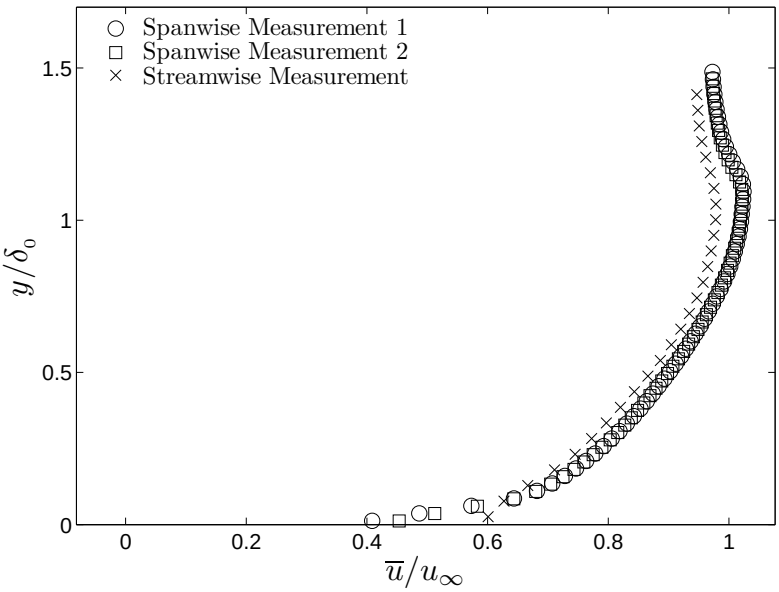

Figure 3.2: Repeatability of the present SPIV measurements of SBLI, demonstrated by three independent measurements of the mean streamwise velocity profile $\overline{u}(y)$ across the boundary layer. Two measurements are from spanwise planes while the third is from a streamwise plane, all located at the same downstream distance.

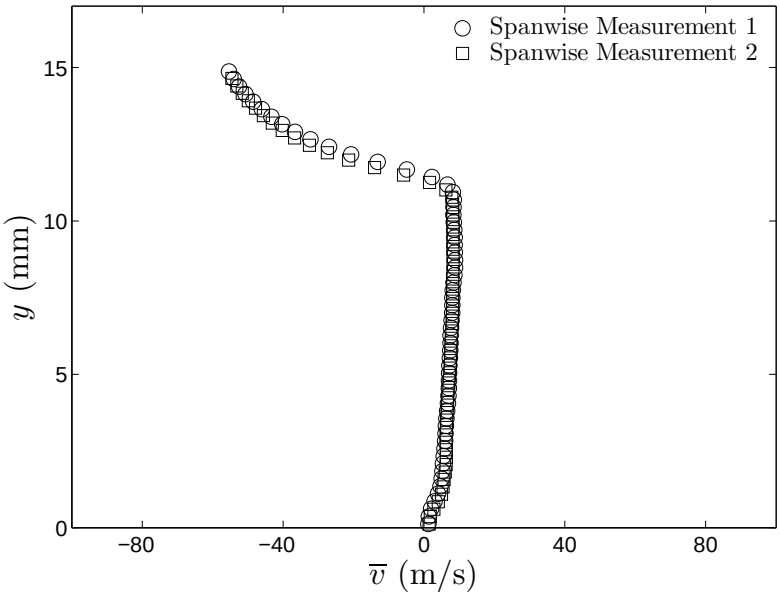

Figure 3.3: Repeatability of the present SPIV measurements of SBLI, demonstrated by two independent measurements of the mean wall-normal velocity profile $\overline{v}(y)$ across the boundary layer. Data are from spanwise planes located at the same downstream distance.

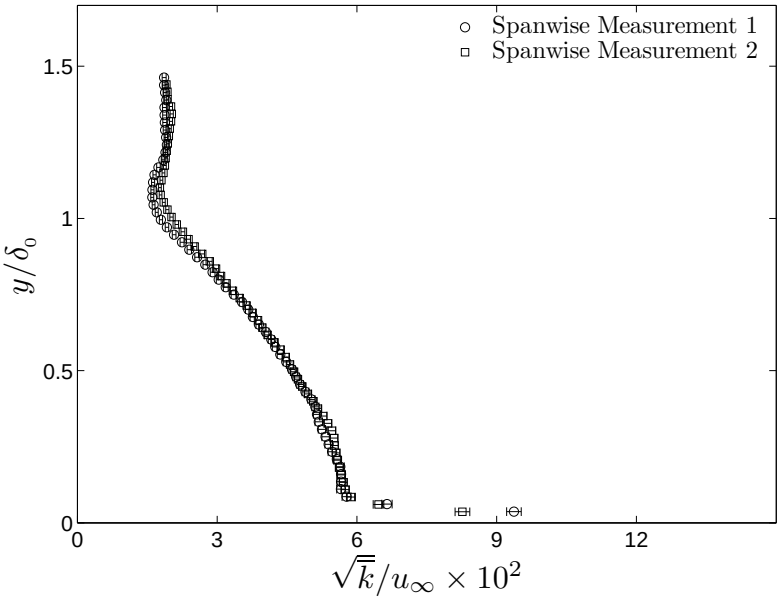

Figure 3.4: Repeatability of the present SPIV measurements of SBLI, demonstrated by two independent measurements of the mean turbulence kinetic energy profile $\overline{k}(y)$ across the boundary layer. Data are from spanwise planes located at the same downstream distance; error bars give 95% confidence intervals showing the level of statistical convergence.

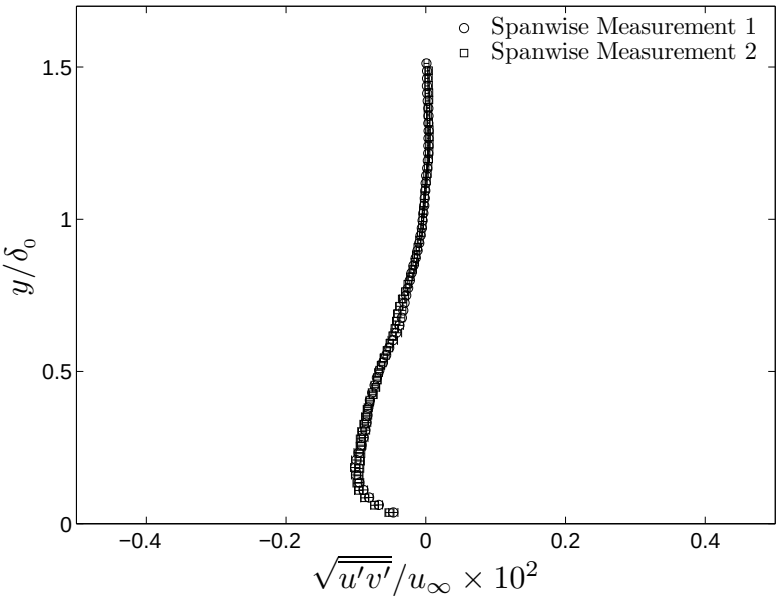

Figure 3.5: Repeatability of the present SPIV measurements of SBLI, demonstrated by two independent measurements of the mean Reynolds shear stress profile $\overline{u'v'}(y)$ across the boundary layer. Data are from spanwise planes located at the same downstream distance; error bars give 95% confidence intervals showing the level of statistical convergence.

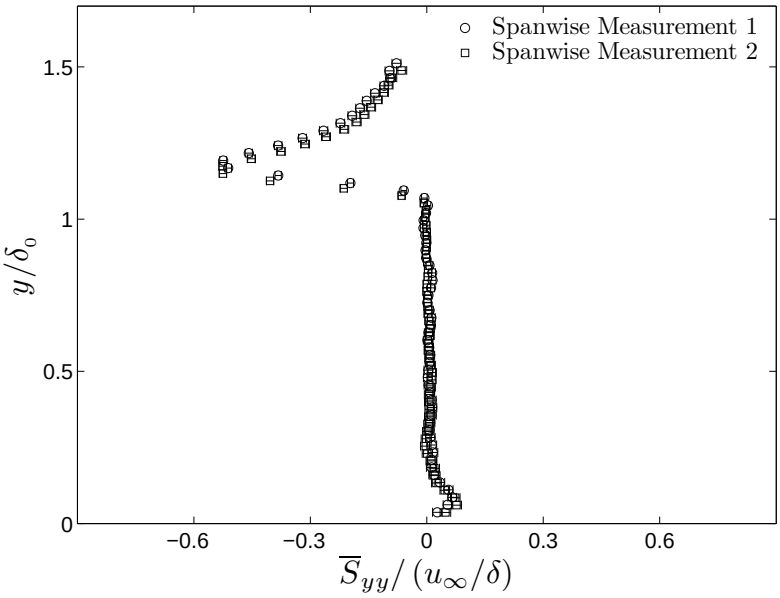

Figure 3.6: Repeatability of the present SPIV measurements of SBLI, demonstrated by two independent measurements of the mean normal strain rate profile $\overline{S}_{yy}(y)$ across the boundary layer. Data are from spanwise planes located at the same downstream distance; error bars give 95% confidence intervals showing the level of statistical convergence.

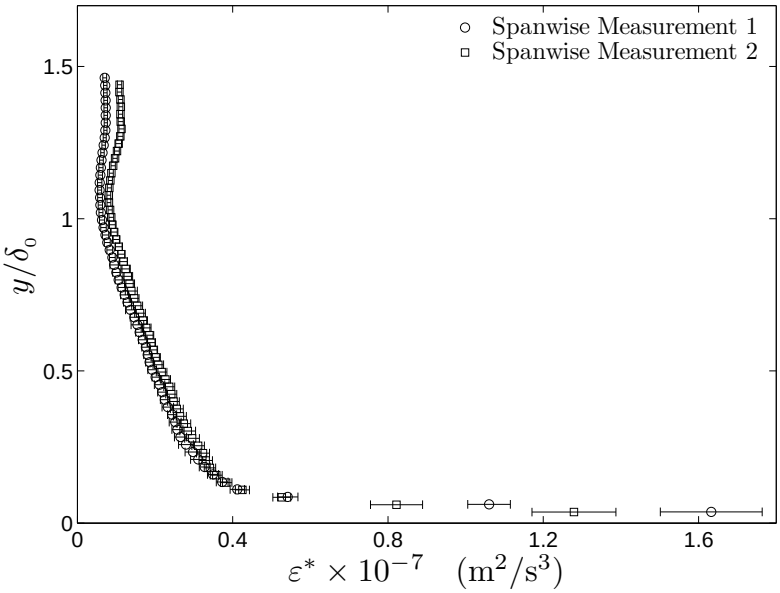

Figure 3.7: Repeatability of the present SPIV measurements of SBLI, demonstrated by two independent measurements of an approximation to the mean dissipation rate profile ε^* across the boundary layer. Data are from spanwise planes located at the same downstream distance; error bars give 95% confidence intervals showing the level of statistical convergence.

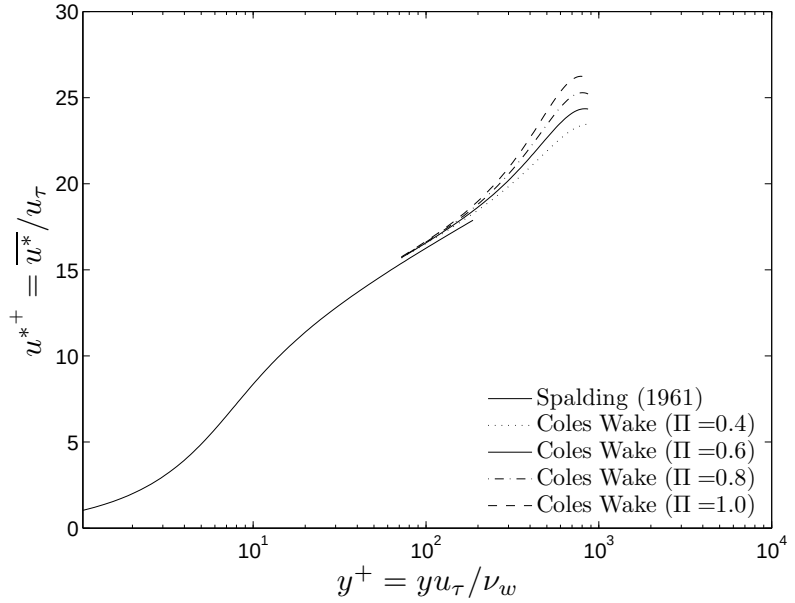

Figure 3.8: Effect of the Coles wake parameter Π on the boundary layer structure, plotted using inner variables u^+ and y^+. $\Pi < 0.6$ is representative of boundary layers with favorable pressure gradients, while $\Pi > 0.6$ represents boundary layers with adverse pressure gradients.

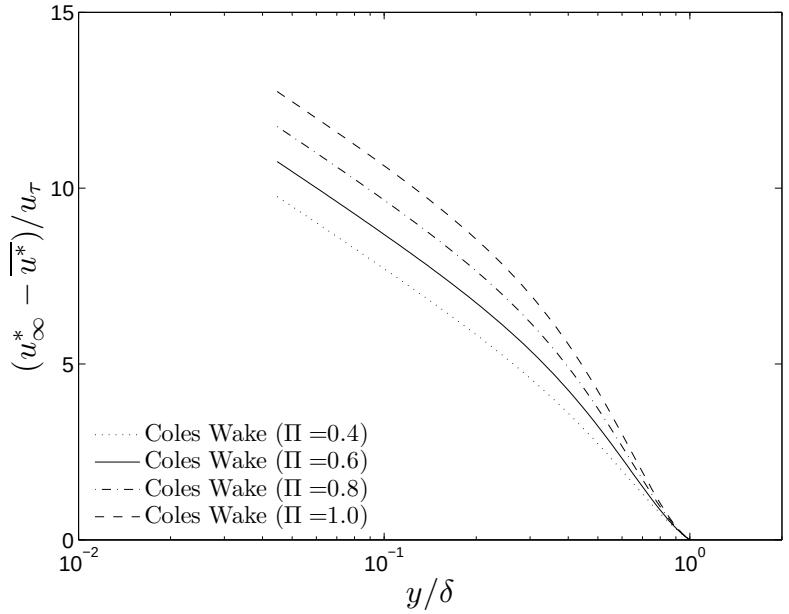

Figure 3.9: Effect of the Coles wake parameter Π on the boundary layer structure, plotted using outer variables. $\Pi < 0.6$ is representative of boundary layers with favorable pressure gradients, while $\Pi > 0.6$ represents boundary layers with adverse pressure gradients.

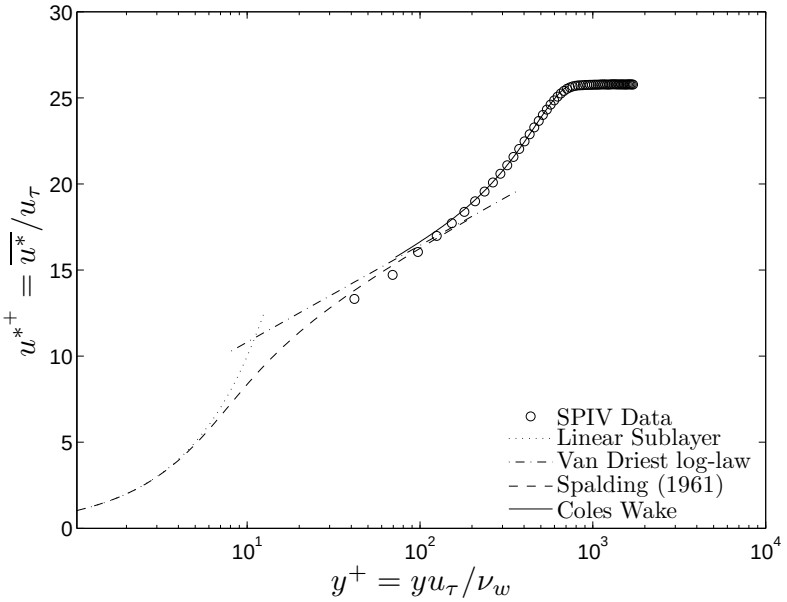

Figure 3.10: Comparison of the mean streamwise velocity $\overline{u}$ at the tunnel inlet location, $x/\delta_0 = -18.2$, to the classic theoretical boundary layer structure, using inner variables u^+ and y^+. The plot shows that the entire outer wake-like region is resolved, with the data point nearest the wall extending into the buffer region.

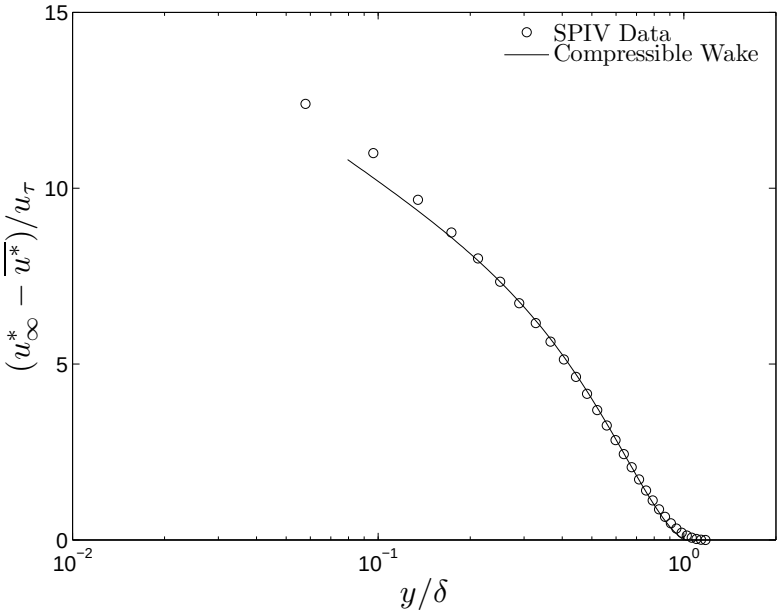

Figure 3.11: Comparison of the mean streamwise velocity $\overline{u}$ at the tunnel inlet location, $x/\delta_0 = -18.2$, to the Coles law of the wake, using outer variables.

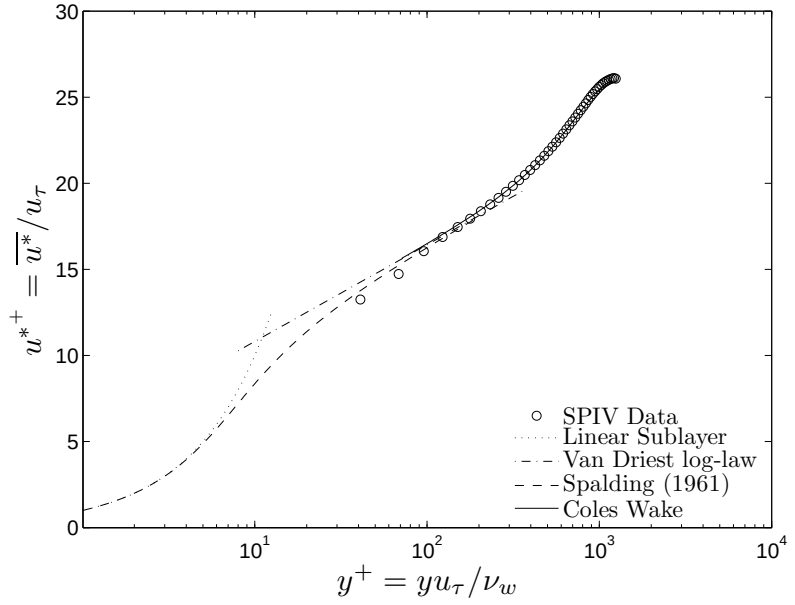

Figure 3.12: Comparison of the mean streamwise velocity $\overline{u}$ immediately upstream of the SBLI region, at $x/\delta_0 = -2.5$, to the classic theoretical boundary layer structure, using inner variables u^+ and y^+. The plot shows that the entire outer wake-like region is resolved, with the data point nearest the wall extending into the buffer region.

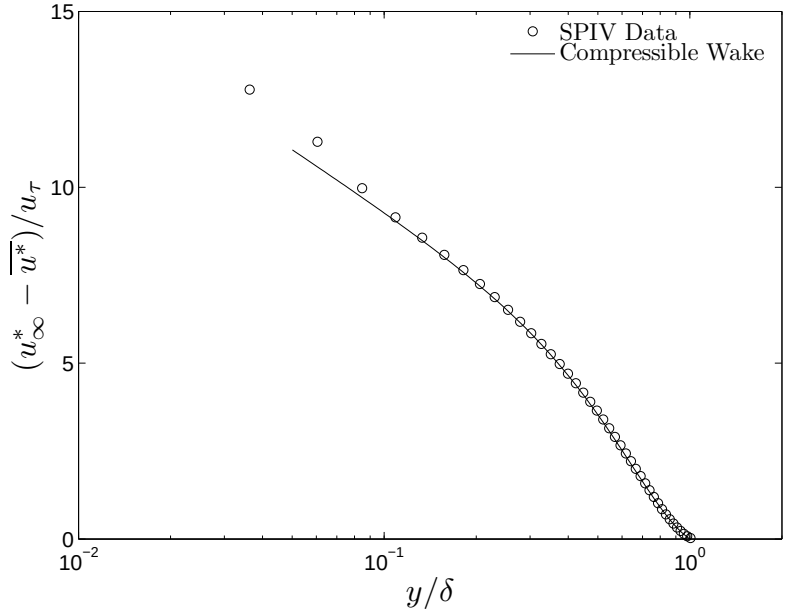

Figure 3.13: Comparison of the mean streamwise velocity $\overline{u}$ immediately upstream of the SBLI region, at $x/\delta_0 = -2.5$, to the Coles law of the wake, using outer variables.

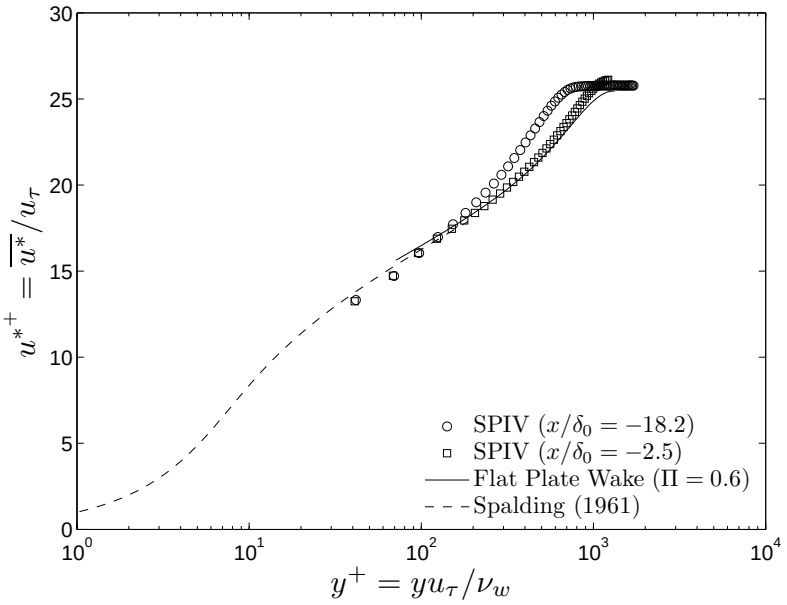

Figure 3.14: Comparison of data from both locations upstream of the SBLI, scaled by inner variables, to the theoretical profile for a fully developed flat plate boundary layer with zero pressure gradient. The boundary layer relaxation from the tunnel inlet location to the SBLI region is clearly evident.

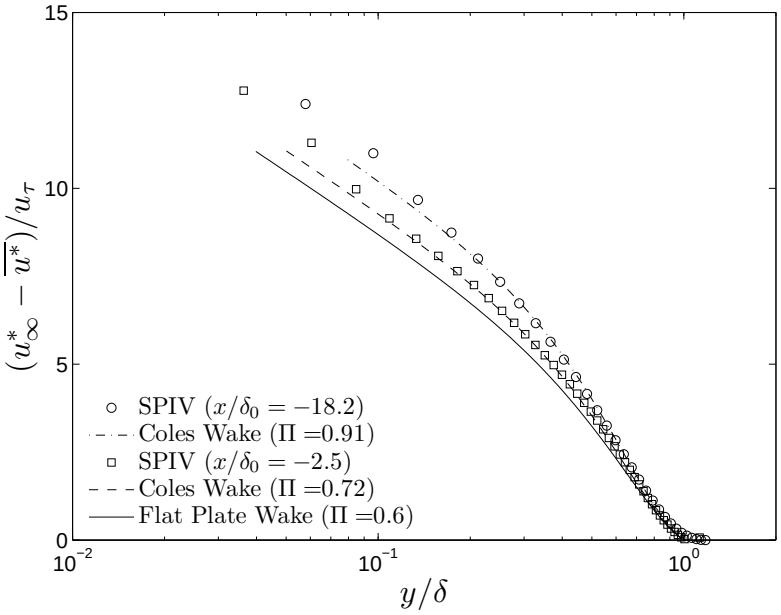

Figure 3.15: Comparison of data from both locations upstream of the SBLI, scaled by outer variables, to the theoretical wake profile for a fully developed flat plate boundary layer with zero pressure gradient. The boundary layer relaxation from the tunnel inlet location to the SBLI region is clearly evident.

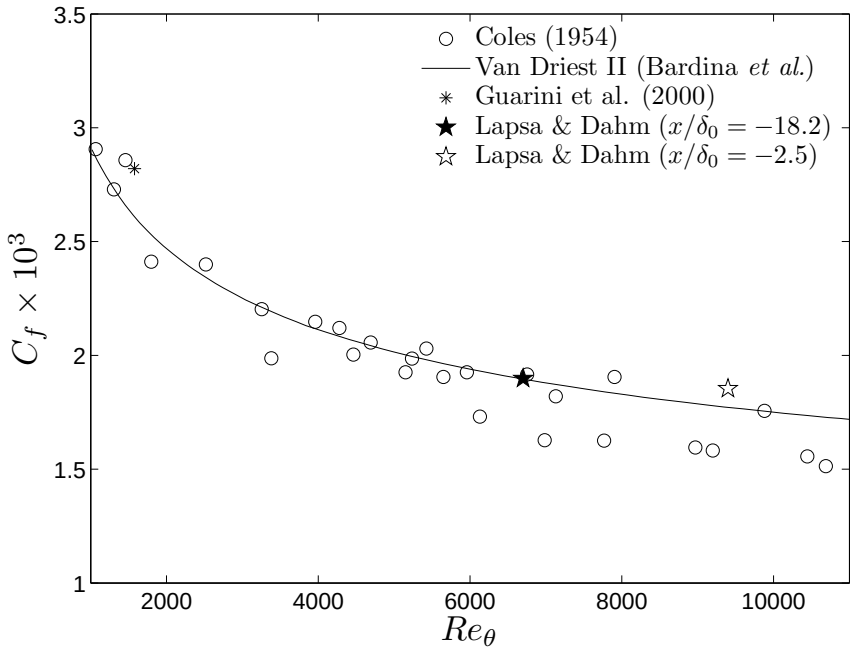

Figure 3.16: Indirect measurement of the friction coefficient at two downstream locations, compared to prior theoretical, numerical, and experimental results for compressible flat plate boundary layers.

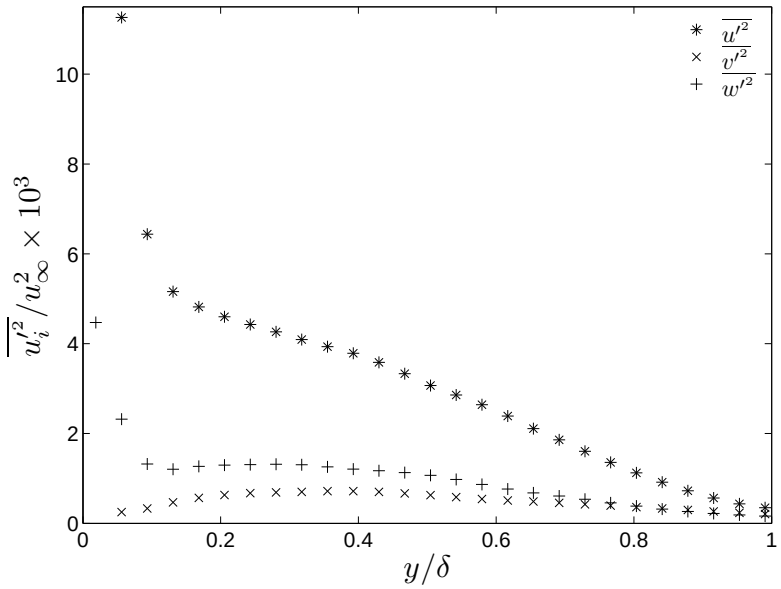

Figure 3.17: Normal Reynolds stresses $\overline{u_i'^2}$ for the compressible boundary layer located at the tunnel inlet location, where $x/\delta_0 = -18.2$, using outer variables.

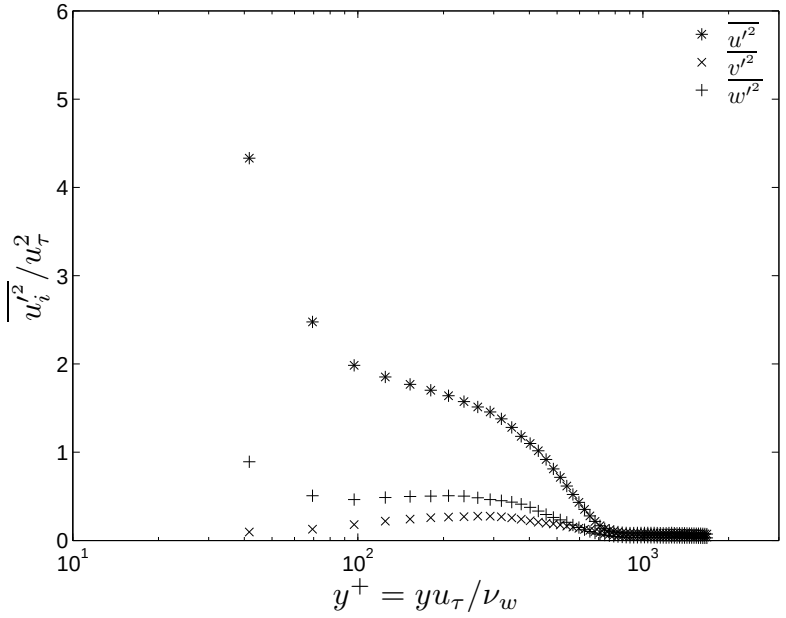

Figure 3.18: Normal Reynolds stresses $\overline{u_i'^2}$ for the compressible boundary layer located at the tunnel inlet location, where $x/\delta_0 = -18.2$, using inner variables.

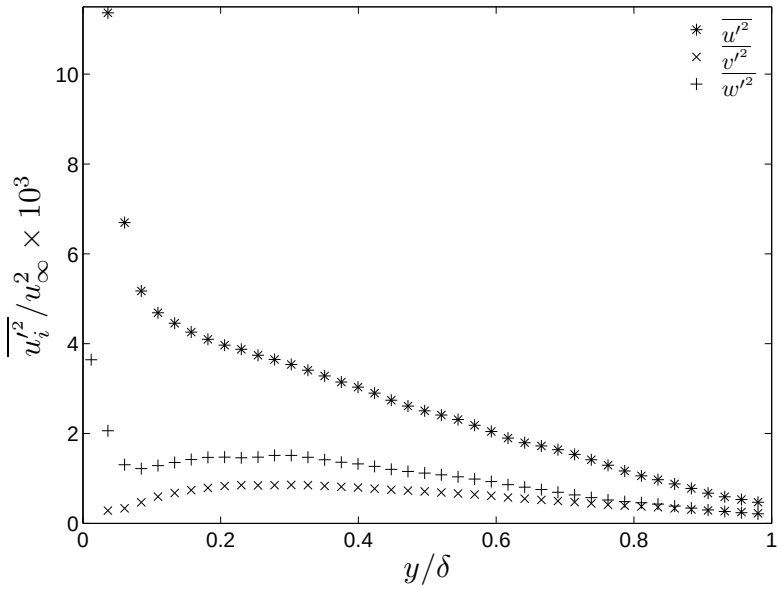

Figure 3.19: Normal Reynolds stresses $\overline{u_i'^2}$ for the compressible boundary layer located immediately upstream of the SBLI region at $x/\delta_0 = -2.5$, using outer variables.

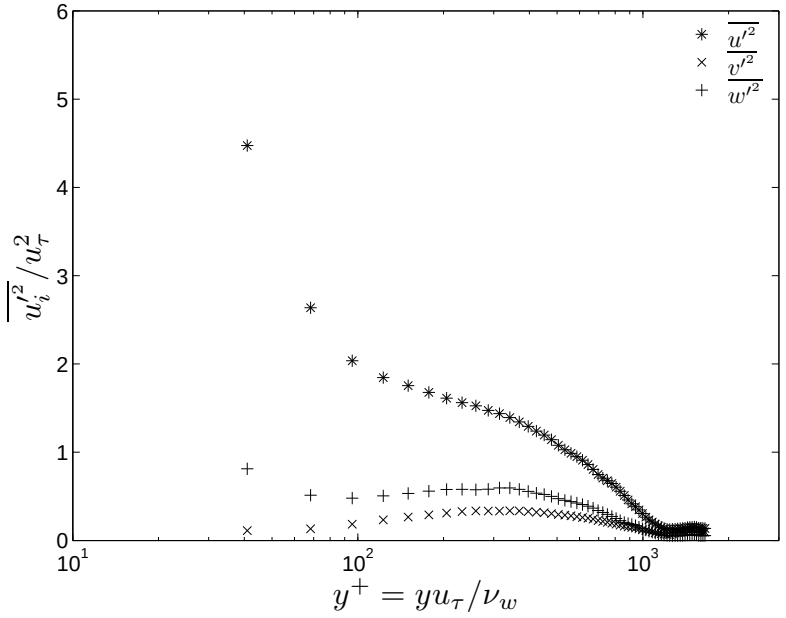

Figure 3.20: Normal Reynolds stresses $\overline{u_i'^2}$ for the compressible boundary layer located immediately upstream of the SBLI region at $x/\delta_0 = -2.5$, using inner variables.

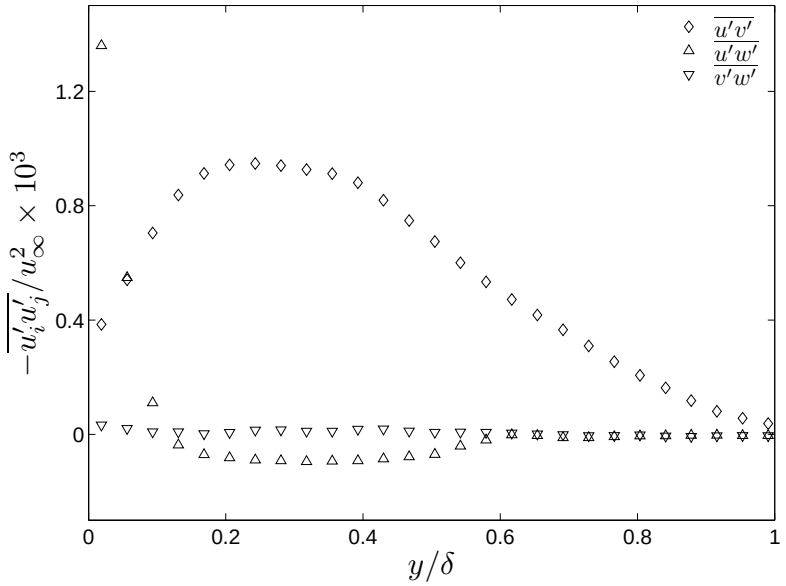

Figure 3.21: Reynolds shear stresses $\overline{u_i'u_j'}$ for the compressible boundary layer located at the tunnel inlet location, where $x/\delta_0 = -18.2$, using outer variables.

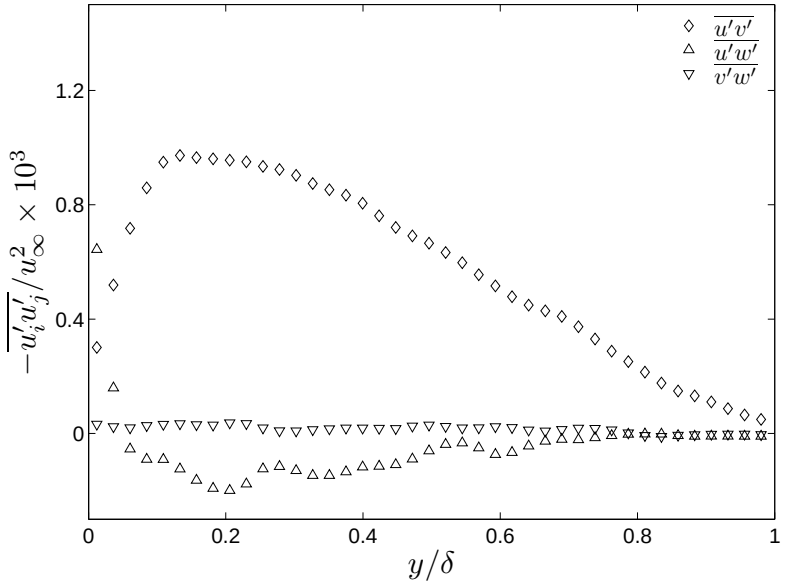

Figure 3.22: Reynolds shear stresses $\overline{u_i'u_j'}$ for the compressible boundary layer located immediately upstream of the SBLI region at $x/\delta_0 = -2.5$, using outer variables.

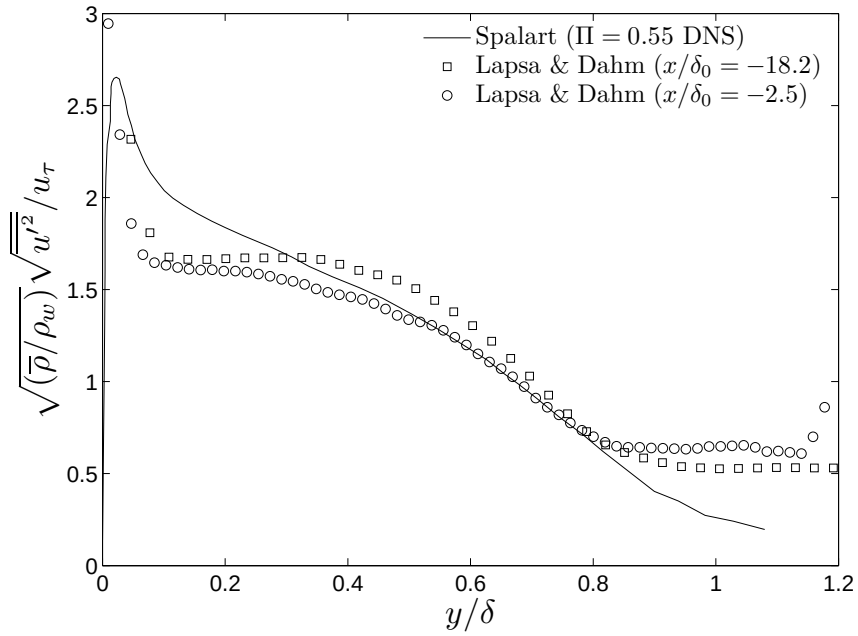

Figure 3.23: The density scaled normal Reynolds stress $\overline{u'^2}$ is approximated using a linear stagnation temperature profile and the isentropic assumption. Although the assumptions are imperfect, the evolution of the boundary layer is clearly evident. The incompressible DNS data of Spalart (1988) is shown for reference.

CHAPTER IV

Shock–boundary layer interactions without passive control

The previous chapter demonstrated the capabilities of the present technique, and in doing so provided highly resolved non-intrusive velocity measurements of an evolving compressible boundary layer. In this chapter the same technique is applied to the interaction between an oblique shock wave and a compressible boundary layer, providing high fidelity stereo particle image velocimetry measurements of incident oblique shock–boundary layer interactions (SBLI). As with any boundary layer flow involving a strong adverse pressure gradient, in the SBLI region the classic boundary layer structure discussed in Chapter III becomes obsolete since, among other reasons, as $u_\tau \to 0$, $u^+ \to \infty$. The present work validates previous descriptions of the interaction structure, quantifies several parameters related to this structure, makes direct conclusions regarding the evolution of the turbulence state, and provides evidence regarding the mechanisms of the large-scale oscillations observed in the SBLI region. Three oblique shock strengths are produced in an otherwise identical flow, providing direct evaluation of the effect of the incident shock strength. The well-resolved mean turbulent and gradient statistics furthermore provide rigorous means for evaluation of computational models. Finally, the chapter provides a baseline against which the

effects of the passive control devices in Chapters V and VI are compared.

Three shock strengths are investigated: $p_3/p_1 = 2.73$, 3.51, and 4.34, which are produced by flow deflection angles of $\theta = 7.75$-deg, 10.0-deg, and 12.0-deg, respectively. The data are arranged in a combination of streamwise and spanwise planes. Averaged quantities in the streamwise planes are comprised of an ensemble of approximately 500 instantaneous visualizations, while averaged quantities in the spanwise planes are comprised of an ensemble of approximately 1500 instantaneous visualizations. For the interactions presented in this chapter, the flow near the tunnel centerline can be correctly approximated as two dimensional. In these cases, profiles of statistical quantities are generated by averaging the data from the central third of the spanwise planes to form a single profile, thus providing approximately 16,000 samples from which each data point is computed. These profiles therefore represent a spanwise average of the central 2.9 mm of the tunnel. Averages taken over both twice and half this distance each produce negligibly different results, demonstrating the validity of the local two-dimensional assumption. The spanwise sampling planes are at seven locations placed progressively throughout the SBLI region. Those positions, normalized by the undisturbed boundary layer height δ_0, are given in Table 4.1. Recall that the $x = 0$ location is defined as the inviscid shock-impingement point.

In any individual plane, the SPIV technique enables measurement of all three velocity components and six of the nine gradient quantities, enabling calculation of all components of the Reynolds stress tensor, three of the six unique components of the strain rate tensor, six of the nine components of the kinetic energy dissipation rate, and one of the three components of the vorticity vector. These averaged quantities together with the instantaneous visualizations are used to draw insight into the

structure and nature of oblique shock boundary layer interactions.

4.1 Instantaneous visualizations

Sample instantaneous visualizations of the streamwise velocity fields $u(x, y)$ produced by the three shock strengths are shown in Fig. 4.1 in planes oriented in the streamwise direction. The bulk flow is traveling from left to right, and recall that the $x = 0$ location is defined as the inviscid shock impingement point. The effects of the incident shock wave clearly thicken the boundary layer upstream of the $x = 0$ location, and the elevated turbulence levels cause localized variations in the structure. Furthermore, cumulative study of many such images demonstrates large overall fluctuations in the size of the interaction. This nature is discussed in more detail in § 4.4.1. Figure 4.2 shows the corresponding wall-normal velocity fields $v(x, y)$, with relatively large fluctuations again being evident. Visualizations of the instantaneous $u(y, z)$ and $v(y, z)$ fields in planes oriented in the spanwise direction are shown in Figs. 4.3 and 4.4, respectively, and these also include the in-plane velocity components (v, w) overlayed. Note the considerable variations in the spanwise direction. In particular, looking at the left spanwise plane produced by the 10.0-deg deflection, the boundary layer thickness apparent in a simultaneously captured streamwise image would vary dramatically were such a plane sampled at $z/\delta_0 = 0$ or at $z/\delta_0 = +0.3$. These observations result from the large scale unsteadiness associated with the SBLI region.

In the sections that follow, this considerable instantaneous variability will be investigated individually and statistically, ultimately providing insight to the insta-

bility of the interaction region.

4.2 Mean velocity measurements

This section presents measurements of the mean streamwise and wall-normal velocity fields, and discusses them in the context of the SBLI structure described in § 1.1.1 and illustrated in Fig. 1.4. The section concludes with a qualitative discussion of the large-scale three-dimensional nature of the flow.

4.2.1 Mean streamwise velocity fields

Figure 4.5 gives visualizations of the mean streamwise velocity component fields $\overline{u}(x, y)$ in streamwise planes located along the tunnel centerline, with each visualization showing one of the three shock strengths. The sharp adverse pressure gradient generated by the shock produces the expected result; the boundary layer thickens considerably in the interaction region, with the amount of thickening being greater for increasingly strong impinging shocks.

Also noteworthy is the protuberance which appears in Fig. 4.5 at the point of maximum thickening. Especially in the case of stronger shocks, its contributions to the overall boundary layer height are not insignificant, but have gone largely unmentioned in previous studies. Recalling the interaction structure from Fig. 1.4, this protuberance results from the finite spacing between the highly unsteady incident C_3 shock and the expansion fan that results from the reflection of C_3. This feature is discussed further in § 4.3.

Figures 4.6–4.8 show the same three interactions, now with the spanwise data planes being included in the central color plot. Velocity profiles are extracted from the center of the spanwise planes and shown in sequential order around the perimeter of the color plot. The progression of the incident shock through the interaction can be deduced by the near-discontinuous velocity reductions at the appropriate location in each profile. As the shock wave impinges on the boundary layer the adverse pressure gradient acts to slow the fluid in the subsonic layer, which subsequently thickens the entire interaction region. It is notable, however, that although the near-wall velocity measurements at the center of the interaction decrease progressively with increasing shock strength, a mean recirculation zone is not observed for any of the interactions. Instantaneous pockets of reverse flow, however, appear frequently. This is consistent with the findings of Smits and Dussauge (2006), Pirozzoli and Grasso (2006), and Humble et al. (2007) who cumulatively provide both experimental and computational views of incident oblique SBLI. Through assimilation of the prior work it appears clear that the extent of the instantaneous reverse flow regions, and by extension the mean reverse flow regions, depends heavily on the upstream conditions. In particular, the local Reynolds number and free stream turbulence level play preeminent roles (Delery and Marvin, 1986).

The velocity profiles downstream of the interaction are also noteworthy. In Position 7 in Fig. 4.6 and Position 6 in Figs. 4.7 and 4.8, the mean streamwise velocity reaches a maximum at $y/\delta_0 \approx 1$, with the maximum becoming more pronounced with increasing shock strength. This is a direct result of the interaction structure illustrated in Fig. 1.4. At $y/\delta_0 \approx 1$ the local streamline traverses the entire expansion fan that results from the reflected incident shock wave C_3, but for $y/\delta_0 > 1$ the streamwise velocity is still accelerating through the expansion. This acceleration is

evident in the progression from Position 6 to Position 7 in Figs. 4.7 and 4.8. Note, therefore, that the velocity in these positions is greater than the inviscid solution for the post-shock velocity, and that it will remain as such until its full interaction with the downstream compression waves is complete.

4.2.2 Mean wall-normal velocity fields

Dramatic views of the interaction are produced using the wall-normal velocity component $\overline{v}$, shown in the streamwise planes in Fig. 4.9. Again, the incident shock location can be easily deduced by the sharp change in $\overline{v}$ at appropriate points in both the color and profile plots. The preeminent feature is the region of positive wall-normal velocity at the shock foot, the size of which grows progressively with the shock strength. Again referring to Fig. 1.4, this large vertical velocity is produced by the upstream reflected shock, C_2, which, consistent with previous authors, moves progressively farther upstream with increasing shock strength. Figures 4.10–4.12 incorporate the quantitative profiles obtained from the spanwise planes. Here it can be seen that the wall-normal velocity induced by the C_2 shock wave is approximately equal and opposite to that produced by the incident C_1 shock, noting in particular Positions 3, 2, and 3 of Figs. 4.10, 4.11, and 4.12, respectively. The expansion fan formed from the reflection of the incident C_3 shock is also clearly evident; underneath the reflected shock C_4 the wall-normal velocity component becomes negative. As with the streamwise velocity component, the inviscid post-shock velocity will not be realized until each pathline has completed its interaction with the downstream system of compression waves.

4.2.3 Comments regarding three-dimensionality

Several previous authors have identified large scale three-dimensional structures at the shock foot. Owing to the use of periodic boundary conditions or two-dimensional constraints in computational simulations, most of these observations to date are through experimental works (e.g. Bookey et al., 2005a; Dussauge et al., 2006). The recent DNS study of Robinet (2007) and the RANS simulation of Galbraith et al. (2009) are notable exceptions.

Through his linearized global stability analysis, Robinet (2007) showed that flows of this type are globally unstable for strong enough incident shock waves, and that a complex large-scale three-dimensional structure results from this. Numerous experiments have shown that these three-dimensional structures can appear as one of two types, or as a combination of both. The first is due to a mean recirculation zone formed at the shock impingement location, in which two counter-rotating vortices form on the flat plate boundary. Such structures were noted by Bookey et al. (2005a) through a surface flow visualization, a sketch of which is reproduced here in Fig. 4.13. In the present study, a separation region at the shock foot does not occur in the mean and therefore structures of this type are not observed. The second type, also resulting in a mean recirculation zone, is a result of the interaction between the flat plate boundary layer, the impinging oblique shock, and the boundary layers that form along the sidewalls of any wind tunnel or inlet. A schematic of the surface visualization of such structures, based on observations from the present study, is shown in Fig. 4.14.

Large structures of the types shown in Figs. 4.13 and 4.14 are not yet fully understood, but they are not the primary topic of this work. A further discussion, though still introductory, is provided by Smits and Dussauge (2006). In the present

work the imaging locations are located near the centerline of the tunnel, as indicated in Fig. 4.14, where the effects of this three dimensionality are minimal. Still, a measurable "pinching" effect does occur and although it is inconsequential to the analyses in the present chapter, it will play an important role in Chapters V and VI.

4.3 Measurements of gradient quantities

This section presents selected components of the mean strain rate tensor, $\overline{S}_{ij}$, and mean vorticity, $\overline{\omega}$, each of which are computed from the gradient quantities. The definitions of these quantities, along with their discretizations to the SPIV sampling grid, are provided in § 4.3.1, with SPIV measurements following in § 4.3.2–4.3.3.

4.3.1 Definitions of gradient quantities

Throughout this work, all gradient quantities are computed using central difference methods; that is,

$$\left(\frac{df}{dx}\right)_i \approx \frac{f_{i+1} - f_{i-1}}{2\Delta x}, \tag{4.1}$$

where in this case i indicates the position along the discretized measurement grid. Each measurement plane provides gradients in two directions and therefore only three of the six unique quantities in the symmetric strain rate tensor, which is defined in the traditional way as

$$\overline{S}_{ij} \equiv \frac{1}{2}\overline{\left(\frac{\partial u_i}{\partial x_j} + \frac{\partial u_j}{\partial x_i}\right)}. \tag{4.2}$$

The vorticity ω is also defined through the gradient quantities as

$$\omega \equiv \nabla \times \mathbf{u}. \tag{4.3}$$

In the present work, one of the three components of the vorticity vector can be measured in each sampling plane. The vorticity is measured by means of the circulation Γ, which is related by Stokes theorem as

$$\Gamma = \int \omega \cdot d\mathbf{S} = \oint \mathbf{u} \cdot d\mathbf{l}, \tag{4.4}$$

where $\mathbf{l}$ is the path of integration around the surface $\mathbf{S}$. All vorticity measurements in the present study are computed via the circulation approach described by Raffel et al. (1998), who discretize Equations 4.3 and 4.4 to give

$$(\overline{\omega}_z)_{i,j} = \frac{1}{A}\Gamma_{i,j} = \frac{1}{A}\oint_{\mathbf{l}(x,y)} (u,v) \cdot d\mathbf{l}, \tag{4.5}$$

where in this case i and j represent the indices of the discretized grid, and u and v are the velocity values at the corresponding grid point. The circulation provided by the integral is divided by the area of the loop of integration, thus providing an average vorticity within the area of integration. For Equation 4.5 only, then, the overline indicates the average within the path of integration and *not* the ensemble average. From Equation 4.5, the estimation of vorticity at a point (i,j), based on the circulation defined by the eight nearest surrounding points, becomes

$$\begin{aligned}
(\omega_z)_{i,j} &= \frac{\Gamma_{i,j}}{4\Delta x \Delta y}, \qquad \text{with} \\
\Gamma_{i,j} &= \frac{1}{2}\Delta x \left(u_{i-1,j-1} + 2u_{i,j-1} + u_{i+1,j-1}\right) \\
&+ \frac{1}{2}\Delta y \left(v_{i+1,j-1} + 2v_{i+1,j} + v_{i+1,j+1}\right) \\
&- \frac{1}{2}\Delta x \left(u_{i+1,j+1} + 2u_{i,j+1} + u_{i-1,j+1}\right) \\
&- \frac{1}{2}\Delta y \left(v_{i-1,j+1} + 2v_{i-1,j} + v_{i-1,j-1}\right).
\end{aligned} \tag{4.6}$$

4.3.2 Mean strain rates

As before, recall the SBLI structure from Fig. 1.4. The mean normal streamwise strain rate $\overline{S}_{xx}$, given in Fig. 4.15, clearly marks the streamwise acceleration of the flow. For clarity, Fig. 4.16 reproduces the streamwise normal strain rate $\overline{S}_{xx}$ for the $\theta = 12.0$-deg interaction, now with the structure schematic from Fig. 1.4 overlayed. The incident C_1 and reflected C_4 shock waves each produce localized decelerations. The apparently finite thickness of each of these shock waves is due to a combination of shock "jitter" and particle lag. Note, for example, that in all cases the incident shock wave C_1, which has a steady anchor point, appears discernably thinner than the reflected shock wave C_4, which is anchored by the unsteady SBLI region.

The effects of the large-scale unsteadiness can also be deduced by consideration of the reflected shock C_2 and incident shock C_3, which reside below the intersection point I. As with the C_1 and C_4 waves, C_2 and C_3 also locally decelerate the flow, however the large oscillations of this inner portion of the interaction region cause the effect to become delocalized in the mean field. Due to the instability, in the mean visualization the area between C_2 and C_3 appears as a continuous region of deceleration instead of as two distinct localized events.

Figure 4.16 also shows two contours of constant velocity. The sonic line is approximated using the $u_\infty/2.75$ velocity contour from the mean velocity field, and an additional constant velocity contour is also shown to illustrate the location of the protuberance mentioned in § 4.2.1. The streamwise bounds of the protuberance mark almost exactly the region of the highest magnitudes of $\overline{S}_{xx}$, which can be inferred roughly as the spatial amplitude of the incident shock C_3 oscillation. When C_3 reflects from the sonic line it produces an expansion fan, which then rapidly accelerates the flow in the second half of the interaction. The protuberance in streamwise veloc-

ity forms in the confined region between the incident C_3 shock and its expansion fan reflection. The feature also leaves its signature as an "island" of high shear strain rate $\overline{S}_{xy}$, fields of which are shown in Fig. 4.17.

The coalescence of the compression waves that form the reflected shock, C_2, can be seen well in the S_{yy} fields of Fig. 4.18, which shows weak structures in the near-wall regions that grow in strength as the intersection points I are approached. The spanwise imaging planes, shown for all three shock strengths in Figs. 4.19–4.21, make this information quantitative. The incident shock wave, C_1, and the reflected wave, C_4, are marked unambiguously by the local maxima in the strain rate magnitude. The inner portion of the reflected shock, C_2, is less obvious due to its large fluctuations and gradual formation, however it is evident in Position 2 of Figs. 4.19 and 4.20 with its peak strain rate at $y/\delta_0 \approx 0.4$. While the C_2 shock wave itself is only weakly evident, its effect in the near wall region is clear; the impulsively generated wall-normal velocity together with the continuity requirement produce the large positive wall-normal strain rate in the near wall regions of the upstream portion of the interaction.

In the nominally two-dimensional mean flow near the centerline of the tunnel, where all imaging in the present study takes place, the velocities and gradients in the spanwise direction are expectedly small throughout the entirety of the boundary layer. This is shown in Fig. 4.22, which shows $\overline{S}_{yz}$ for the 10-deg deflection angle and is representative of all the strain rates involving spanwise derivatives.

4.3.3 Mean vorticity

Of both fundamental and practical interest is a quantification of the boundary layer thickness through the interaction region. Traditional definitions for the boundary layer thickness, including the momentum and displacement thicknesses, become ill-defined in the absence of a steady free stream. In its purest form, however, a boundary layer is not the description of a velocity profile, but rather an elucidation of the transport of the vorticity generated near the wall. While the present measurements cannot simultaneously measure all three components of the vorticity, in a boundary layer the mean vorticity vector is aligned predominantly in the velocity-normal and wall-parallel direction, in this case the spanwise z-direction. This vorticity component can be measured via the streamwise sampling planes.

The mean vorticity field $\overline{\omega}_z(x, y)$ is visualized in the streamwise planes for all three shock strengths in Fig. 4.23. Contours of the vorticity are natural markers of the thickness of any boundary layer, and in the absence of a uniform free stream are the most suitable for defining the evolution of the present boundary layer thickness. Choosing a contour with small vorticity provides quantification of the overall size of the boundary layer, δ^{ω}, and this is done in Fig. 4.24 using the vorticity contour $\overline{\omega}_z/(u_\infty/\delta_0) = -0.25$. Not unexpectedly, the boundary layer thickens progressively more with increasing shock strength, with the maximum degree of thickening being about 20% for the weakest shock and about 50% for the strongest shock.

Unlike a classical boundary layer, however, the inner structure of the oblique SBLI region is highly nonuniform. As a result, the degree of boundary layer thickening is heavily dependent on the choice of vorticity contour. This point is made clear in Fig. 4.25, which shows the boundary layer evolution for the same interactions using the higher contour level $\overline{\omega}_z/(u_\infty/\delta_0) = -0.70$. Again the layer grows progressively

thicker for increasing shock strength, however this time the layer thickens by up to 250% as compared to its pre-interaction size. The structure of the boundary layer growth is also markedly different in Fig. 4.25 as compared to Fig. 4.24. The contours marking the outer portion of the boundary layers, shown in Fig. 4.24, pass essentially through the intersection point I. The inner contours in Fig. 4.25, however, intersect the incident C_3 shock wave as well as the reflected expansion fan. The C_3 shock and the expansion fan both rapidly turn the flow toward the wall, producing a local rise in spanwise vorticity $\overline{\omega}$. This rise constitutes a significant fraction of the overall boundary layer thickening, and is the same protuberance observed in the $\overline{u}$ and $\overline{S}_{xy}$ fields. The peak thickening ratios $(\delta^{\omega}/\delta_0^{\omega})_{max}$ for each shock strength and both contour levels are tabulated in Table 4.2.

4.4 Fluctuation quantities

The SPIV technique enables measurement of all components of the Reynolds stress tensor $\overline{u_i' u_j'}$, where all fluctuations herein are defined by the Reynolds decomposition $f = \overline{f} + f'$. Figure 4.26 shows spanwise visualizations of the mean turbulence kinetic energy, defined by the normal Reynolds stress components as $\overline{k} \equiv \frac{1}{2}\overline{u_i' u_i'}$. The peak turbulence levels are concentrated in the region between the reflected shock wave, C_2, and the incident shock wave, C_3, shown previously in Figs. 1.4 and 4.16.

The magnitudes of the turbulence levels are shown quantitatively in Figs. 4.27–4.29. In the free stream at the tunnel inlet location, the square root of the turbulence kinetic energy is 1.4% of the bulk streamwise velocity. As discussed in § 3.4–3.5 and consistent with classical results, the turbulence kinetic energy at this location

grows smoothly for decreasing wall-normal distance until $y_0^+ \approx 70$, at which point the kinetic energy increases sharply. Moving downstream and into the interaction region, the large $\overline{k}$ value initially observed for $y_0^+ \lesssim 70$ decreases considerably while the kinetic energy in the region $y_0^+ \gtrsim 70$ increases until eventually it surpasses the level in the near-wall region. Beyond the interaction, the kinetic energy values in the region $y_0^+ \gtrsim 70$ decrease and approach their undisturbed states, while the kinetic energy in $y_0^+ \lesssim 70$ also reassumes its initially high levels. These consistent trends are shown in Figs. 4.30 and 4.31. In Figs. 4.27–4.29 it is additionally noteworthy that the peak magnitude of the kinetic energy in the $y_0^+ \gtrsim 70$ region is essentially constant for all three incident shock strengths and that only the wall-normal height of the affected area changes.

4.4.1 Comments regarding large-scale unsteadiness

It is now well established within the literature that large scale oscillations of the SBLI region occur at frequencies much lower than those associated with the characteristic boundary layer turbulence. As discussed in § 1.1.2, the cause remains the subject of debate. Consider the nature of the interaction, however. The incoming high speed boundary layer flow is turned by the reflected shock, C_2, so that it is directed around a region of slow moving fluid, which exists at the shock foot as a result of the upstream propagation of the pressure gradient. Thus in any instantaneous snapshot the high velocity incoming stream is in close proximity to the low velocity fluid, producing thin layers of extremely high shear.

Two representative instantaneous visualizations of such layers, together with the mean visualization, are provided in Fig. 4.32 by means of the velocity gradient $\partial\overline{u}/\partial y$. Free shear layers of this kind are known to be highly unsteady due to the Kelvin-

Helmholtz instability, and this must be true in the present flow in order for the two representative instantaneous visualizations to produce the corresponding ensemble mean field. Furthermore, the flapping shear layer provides a direct explanation for the turbulence kinetic energy $\overline{k}$ fields shown in Fig. 4.26 and reproduced in Fig. 4.33 with the structure schematic overlayed. Essentially all of the kinetic energy is not only concentrated between C_2 and C_3 but it is also located almost exclusively below the sonic line, which must be the case if the flapping shear layer is to be the source. These visualizations add to the evidence provided by Pirozzoli and Grasso (2006) and Dupont et al. (2008), which suggest that the mechanism for the large scale oscillations of the interaction result from an unstable shear layer developing at the reflected C_3 shock impingement point.

4.4.2 Evolution of the turbulence state

Correct prediction of the relative magnitudes of each component of the Reynolds stress tensor $\overline{u_i' u_j'}$ is of fundamental interest to computational efforts. The anisotropy tensor b_{ij} provides a concise means by which to quantify these. While the relation between the normal stresses and shear stresses depends on the choice of coordinate system, the nature of the turbulence can be deduced by decomposing it into its isotropic and anisotropic components. In isotropic turbulence the Reynolds stress is readily shown to be $\frac{2}{3}\overline{k}\delta_{ij}$, where δ_{ij} is defined as the Kronecker delta tensor. The anisotropic component, a_{ij}, is defined as the deviation from the isotropic state, so that

$$\overline{a}_{ij} \equiv \overline{u_i' u_j'} - \frac{2}{3}\overline{k}\delta_{ij}. \tag{4.7}$$

The normalized anisotropy tensor, $\overline{b}_{ij} = \overline{a}_{ij}/2\overline{k}$, is then simply

$$\overline{b}_{ij} = \frac{\overline{u_i' u_j'}}{2\overline{k}} - \frac{1}{3}\delta_{ij}. \tag{4.8}$$

As with any $\mathbb{R}^2$ tensor, the anisotropy tensor has three invariants, the first of which is simply the trace of the tensor, given by

$$I = \mathrm{tr}(b_{ij}) = b_{11} + b_{22} + b_{33}, \tag{4.9}$$

and this is necessarily zero by the definition of b_{ij}. Thus for any turbulent state the degree of anisotropy can be fully characterized by the second and third invariants only. For symmetric 3×3 tensors, the second and third invariants are given by

$$II = \frac{1}{2}\left(\mathrm{tr}\left(b_{ij}\right)^2 - \mathrm{tr}\left(b_{ij}b_{ij}\right)\right) = \lambda_1\lambda_2 + \lambda_2\lambda_3 + \lambda_1\lambda_3 \tag{4.10}$$

and

$$III = \det\left(b_{ij}\right) = \lambda_1\lambda_2\lambda_3, \tag{4.11}$$

where λ_1, λ_2, and λ_3 are the eigenvalues of b_{ij}. As is the case for any phenomenon described by a traceless tensor, not only can any turbulent state be described by the second and third invariants, but that arbitrary state can occupy only a small portion of the $II - III$ space. In regards to turbulence, this "realizable" space is termed the Lumley triangle.

Figure 4.34 shows the Reynolds stresses in this context from the incompressible DNS channel flow data of Kim et al. (1987). The solid lines represent the bounds of the Lumley triangle, and each has specific meaning. Perfectly isotropic turbulence is located at the origin. The upper boundary represents two-dimensional turbulence, while the two lower bounds represent the two modes of axisymmetric turbulence; the left branch being the "rod-like" limit of axisymmetric turbulence where, in principle axes, the two equal fluctuation components are large, and the right branch being

the "ring-like" limit for axisymmetric turbulence where one fluctuation component dominates and the two equal fluctuation components are small. Finally, the intersection between the lower right bound and the two-dimensional boundary indicates the one-dimensional turbulence limit.

Note the implications of the DNS data in Fig. 4.34, which is typical of wall-bounded shear flows. In the free stream the turbulence state is near-isotropic and thus located near the origin of the $II-III$ space. Moving into the boundary layer and toward the wall, the turbulence state hugs the lower right axisymmetric boundary since there is one large fluctuation component, namely the streamwise component $\overline{u'^2}$, and two small fluctuation components, namely $\overline{v'^2}$ and $\overline{w'^2}$. In the logarithmic region of the boundary layer the wall-normal component tends to zero quickly and as a result the turbulence state becomes removed from the lower boundary and moves in the direction of the two-dimensional limit. Moving progressively closer to the wall, the two minor fluctuation components $\overline{v'^2}$ and $\overline{w'^2}$ approach zero while the major component increases sharply, and as a result the turbulence state approaches the one-dimensional limit. Still closer to the wall, at $y^+ \approx 20$, the wall-normal fluctuation component is essentially zero and the major fluctuation component also declines, making the turbulence state approximately two-dimensional.

Figures 4.35–4.37 show the anisotropy from the present experimental study from a few select spanwise planes. Figures 4.35*a*–4.37*a* each show data from planes located upstream of the interaction region, with Fig. 4.35*a* showing the $\theta = 7.75$-deg case, Fig. 4.36*a* showing the $\theta = 10.0$-deg case, and Fig. 4.37*a* showing the $\theta = 12.0$-deg case. With the exception of the presence of the shock, which is located immediately above the boundary layer in each of Figs. 4.35*a*–4.37*a* and produces the "bubble" in the near-isotropic region, the results bear direct resemblance to the incompressible

DNS data in Fig. 4.34, and the associated previous discussion applies.

Figures 4.35*b*–4.37*b* show the turbulence states in planes located immediately downstream of the SBLI. Here, the turbulence states are consistently shifted toward the "rod-like" axisymmetric limit as compared to the upstream turbulence states. The evolution from the upstream turbulence states in Figs. 4.35*a*–4.37*a* to the downstream states in Figs. 4.35*b*–4.37*b* is a progressive one, with no particular location in the SBLI region contributing discernably more change to the turbulence state than any other. Note also that in each of the downstream cases, the turbulence states still migrate toward the two-dimensional limit as the wall is approached, indicating the necessary decay in the wall-normal fluctuation component.

4.5 Dissipation rate

The turbulence kinetic energy dissipation rate is a quantity of fundamental importance to computational simulations, and particularly to RANS codes, but one that is rarely reported in high speed flows due to the high fidelity and large ensembles required to achieve statistical convergence. The dissipation rate is defined as

$$\Phi \equiv 2\nu S_{ij} S_{ij}, \tag{4.12}$$

where S_{ij} is the strain rate tensor

$$S_{ij} \equiv \frac{1}{2}\left(\frac{\partial u_i}{\partial x_j} + \frac{\partial u_j}{\partial x_i}\right). \tag{4.13}$$

Separating the strain rate tensor into its mean and fluctuating components, the total mean dissipation rate can be written as:

$$\overline{\Phi} = 2\nu\overline{\left(\overline{S}_{ij} + S'_{ij}\right)\left(\overline{S}_{ij} + S'_{ij}\right)}. \tag{4.14}$$

The dissipation rate then can be similarly decomposed after noting that $\overline{S'_{ij}} = 0$, giving

$$\overline{\Phi} = 2\nu\overline{S_{ij}S_{ij}} + 2\nu\overline{S'_{ij}S'_{ij}}. \tag{4.15}$$

Thus the total average dissipation is the sum of the dissipation resulting from the mean flow field and the dissipation resulting from the turbulent fluctuations. The relative magnitude of these terms can be deduced by

$$\frac{\overline{S'_{ij}S'_{ij}}}{\overline{S}_{ij}\overline{S}_{ij}} \sim \frac{\left(\nu/\lambda_\nu^2\right)^2}{\left(u/\delta\right)^2} \sim \left(\frac{\nu}{u\delta}\right)^2 \left(\frac{\delta}{\lambda_\nu}\right)^4 \sim \left(Re_\delta^{-1}\right)^2 \left(Re_\delta^{3/4}\right)^4 = Re_\delta. \tag{4.16}$$

Thus, for large Reynolds number flows such as the one in the present study, for which $Re_\delta > 5 \times 10^4$, essentially all of the dissipation results from the turbulent fluctuations. The dissipation then can be approximated as

$$\overline{\Phi} \approx \varepsilon \equiv 2\nu\overline{S'_{ij}S'_{ij}} = \nu\left(\overline{\frac{\partial u'_i}{\partial x_j}\frac{\partial u'_i}{\partial x_j}} + \overline{\frac{\partial u'_i}{\partial x_j}\frac{\partial u'_j}{\partial x_i}}\right), \tag{4.17}$$

where ε is the dissipation rate due to turbulent fluctuations. The term on the right-hand side can be written as

$$\begin{aligned}\left(\overline{\frac{\partial u'_i}{\partial x_j}\frac{\partial u'_j}{\partial x_i}}\right) &= \overline{\frac{\partial}{\partial x_j}\left(u'_i\frac{\partial u'_j}{\partial x_i}\right)} - \overline{u'_i\frac{\partial}{\partial x_j}\frac{\partial u'_j}{\partial x_i}} \\ &= \overline{\frac{\partial}{\partial x_j}\left(\frac{\partial}{\partial x_i}u'_iu'_j - u'_j\frac{\partial u'_i}{\partial x_i}\right)} - \overline{u'_i\frac{\partial}{\partial x_i}\frac{\partial u'_j}{\partial x_j}}.\end{aligned} \tag{4.18}$$

In the weak compressibility regime, namely for $M \lesssim 5$, continuity requires that $\partial u'_i/\partial x_i \approx 0$, and therefore

$$\left(\overline{\frac{\partial u'_i}{\partial x_j}\frac{\partial u'_j}{\partial x_i}}\right) \approx \overline{\frac{\partial}{\partial x_i}\frac{\partial}{\partial x_j}u'_iu'_j} = \frac{\partial^2}{\partial x_i\partial x_j}\overline{u'_iu'_j}. \tag{4.19}$$

In homogeneous turbulence this quantity is zero, and in turbulent shear flows the scaling goes as

$$\left(\overline{\frac{\partial u'_i}{\partial x_j}\frac{\partial u'_j}{\partial x_i}}\right) \approx \frac{\partial^2}{\partial x_i\partial x_j}\overline{u'_iu'_j} \sim \left(u/\delta\right)^2. \tag{4.20}$$

Therefore, in turbulent shear flows, the scaling of the two terms on the right-hand side of Equation 4.17 goes as

$$\frac{\left(\overline{\frac{\partial u_i'}{\partial x_j}\frac{\partial u_i'}{\partial x_j}}\right)}{\left(\overline{\frac{\partial u_i'}{\partial x_j}\frac{\partial u_j'}{\partial x_i}}\right)} \sim \frac{\left(\nu/\lambda_\nu^2\right)^2}{\left(u/\delta\right)^2} \sim \left(\frac{\nu}{u\delta}\right)^2 \left(\frac{\delta}{\lambda_\nu}\right)^4 \sim Re_\delta, \tag{4.21}$$

and thus for $Re \gg 1$ the second term in Equation 4.17 is negligible. The kinetic energy dissipation rate can thus finally be given as

$$\overline{\Phi} \approx \varepsilon \approx \nu \left(\overline{\frac{\partial u_i'}{\partial x_j}\frac{\partial u_i'}{\partial x_j}}\right). \tag{4.22}$$

The right hand side of Equation 4.22 can be written in cartesian coordinates, showing three streamwise and six spanwise gradients:

$$\begin{aligned}\overline{\frac{\partial u_i'}{\partial x_j}\frac{\partial u_i'}{\partial x_j}} = &\overline{\left(\frac{\partial u'}{\partial x}\right)^2} + \overline{\left(\frac{\partial v'}{\partial x}\right)^2} + \overline{\left(\frac{\partial w'}{\partial x}\right)^2} \\ &+ \overline{\left(\frac{\partial u'}{\partial y}\right)^2} + \overline{\left(\frac{\partial v'}{\partial y}\right)^2} + \overline{\left(\frac{\partial w'}{\partial y}\right)^2} \\ &+ \overline{\left(\frac{\partial u'}{\partial z}\right)^2} + \overline{\left(\frac{\partial v'}{\partial z}\right)^2} + \overline{\left(\frac{\partial w'}{\partial z}\right)^2}.\end{aligned} \tag{4.23}$$

4.5.1 Estimations for the dissipation rate

In the spanwise planes presented in the present study the gradients in y and z are measured experimentally, however single-plane SPIV leaves the gradients in x unresolved. Thus $\overline{(\partial u'/\partial x)^2}$, $\overline{(\partial v'/\partial x)^2}$, and $\overline{(\partial w'/\partial x)^2}$ must be approximated. Of these, $\overline{(\partial u'/\partial x)^2}$ is a streamwise fluctuation derivative while $\overline{(\partial v'/\partial x)^2}$ and $\overline{(\partial w'/\partial x)^2}$ are both spanwise fluctuation derivatives. These are considered separately to produce two estimations for the dissipation rate.

The streamwise derivative $\overline{(\partial u'/\partial x)^2}$ is approximated twice by using first the continuity assumption and then an isotropy assumption. The incompressible continuity

equation gives

$$\frac{\partial u'}{\partial x} + \frac{\partial v'}{\partial y} + \frac{\partial w'}{\partial z} = 0, \tag{4.24}$$

and thus

$$\frac{\partial u'}{\partial x} = -\left(\frac{\partial v'}{\partial y} + \frac{\partial w'}{\partial z}\right). \tag{4.25}$$

Equation 4.25 gives an incompressible estimate for $\overline{(\partial u'/\partial x)^2}$. In the present study the mean flow is undoubtedly compressible, however note that the turbulence Mach number $M_t = (1/a)\sqrt{\frac{2}{3}k} \ll 1$. Thus most of the pressure variations are due to the mean flow, making the incompressible assumption for the fluctuations plausible.

The isotropic assumption can also be used to estimate the streamwise derivative. In this case

$$\overline{\left(\frac{\partial u'}{\partial x}\right)^2} = \overline{\left(\frac{\partial v'}{\partial y}\right)^2} = \overline{\left(\frac{\partial w'}{\partial z}\right)^2}. \tag{4.26}$$

Under this assumption, the best estimate for $\overline{(\partial u'/\partial x)^2}$ is then

$$\overline{\left(\frac{\partial u'}{\partial x}\right)^2} = \frac{1}{2}\left[\overline{\left(\frac{\partial v'}{\partial y}\right)^2} + \overline{\left(\frac{\partial w'}{\partial z}\right)^2}\right]. \tag{4.27}$$

Isotropy can again be assumed to estimate the two transverse gradients. Namely,

$$\begin{aligned}\overline{\left(\frac{\partial v'}{\partial x}\right)^2} &= \overline{\left(\frac{\partial w'}{\partial x}\right)^2} \\ &= \frac{1}{4}\left[\overline{\left(\frac{\partial v'}{\partial z}\right)^2} + \overline{\left(\frac{\partial w'}{\partial y}\right)^2} + \overline{\left(\frac{\partial u'}{\partial y}\right)^2} + \overline{\left(\frac{\partial u'}{\partial z}\right)^2}\right].\end{aligned} \tag{4.28}$$

Equations 4.25, 4.27, and 4.28 thus provide two estimates for the streamwise derivatives and one estimate for the spanwise derivatives. These provide two estimations for the dissipation rate:

$$\begin{aligned}\varepsilon^* = \frac{3\nu_w}{2}\Bigg[&\overline{\left(\frac{\partial u'}{\partial y}\right)^2} + \overline{\left(\frac{\partial v'}{\partial y}\right)^2} + \overline{\left(\frac{\partial w'}{\partial y}\right)^2} \\ &+ \overline{\left(\frac{\partial u'}{\partial z}\right)^2} + \overline{\left(\frac{\partial v'}{\partial z}\right)^2} + \overline{\left(\frac{\partial w'}{\partial z}\right)^2}\Bigg]\end{aligned} \tag{4.29}$$

$$\varepsilon^{\dagger} = \frac{3\nu_w}{2}\left[\overline{\left(\frac{\partial u'}{\partial y}\right)^2} + \overline{\left(\frac{\partial v'}{\partial y}\right)^2} + \overline{\left(\frac{\partial w'}{\partial y}\right)^2} + \overline{\left(\frac{\partial u'}{\partial z}\right)^2} + \overline{\left(\frac{\partial v'}{\partial z}\right)^2} + \overline{\left(\frac{\partial w'}{\partial z}\right)^2}\right] + \frac{\nu_w}{2}\left[\overline{\left(\frac{\partial v'}{\partial y}\right)^2} + \overline{\left(\frac{\partial w'}{\partial z}\right)^2} + 4\left(\overline{\frac{\partial v'}{\partial y}\frac{\partial w'}{\partial z}}\right)\right], \tag{4.30}$$

where ε^* assumes full isotropy and $\varepsilon^{\dagger}$ uses the incompressible assumption for $\overline{(\partial u'/\partial x)^2}$ and the isotropic assumption for $\overline{(\partial v'/\partial x)^2}$ and $\overline{(\partial w'/\partial x)^2}$. These estimations are shown from two downstream locations in Figures 4.38–4.39, with the discrepancy between two estimations being below the statistical error. In the results that follow, the fully isotropic estimation for the dissipation rate ε^* is used.

Note that the true dissipation rate is a function of the local kinematic viscosity. Due to the strong variations in the static temperature and density fields both upstream and through the interaction, the kinematic viscosity will vary considerably in both the streamwise x and wall-normal y directions. For simplicity, and due to the lack of rigorous methods to accurately approximate the viscosity fields, Equations 4.29 and 4.30 are defined using a constant value for the kinematic viscosity, namely the value at the wall of the incoming boundary layer, ν_w.

The isotropic approximation for the dissipation rate is shown in Figs. 4.40–4.42 for all three shock strengths. Similar to the turbulence kinetic energy, the peak dissipation rates in the $y_0^+ \lesssim 70$ and $y_0^+ \gtrsim 70$ regions of the boundary layer have distinct and opposite evolutions.

4.6 Summary of findings

Cumulative study of the measured velocity fields reveals detailed quantifications of the shock–boundary layer interactions. The boundary layer thickness through the

interaction is quantified via the spanwise vorticity component $\overline{\omega}_z$ in Figs. 4.24 and 4.25. Contours of the vorticity also reveal aspects of the inner structure, including a rapid increase in the boundary layer size that occurs between the fluctuating incident shock C_3 and its expansion fan reflection. The same protuberance is observed through inspection of the $\overline{u}(x, y)$ and $\overline{S}_{xy}(x, y)$ fields in Figs. 4.5 and 4.17, respectively. Its contribution to the overall boundary layer height is not insignificant, particularly for stronger incident shock strengths.

The strain rate fields illuminate the interaction structure particularly well, as shown by Fig. 4.16, for example. Measurements of the intersection point I and the upstream penetration distance L_0, measured as the inviscid extension of the reflected C_2 shock, are made for all three shock strengths through averaged information from the strain rate fields $\overline{S}_{xx}$, $\overline{S}_{yy}$, and $\overline{S}_{xy}$. Those results are given in Table 4.3, and show an approximately linear increase in the upstream penetration distance, as well as in both coordinates of the interaction point (x, y), as a function of the incident shock strength.

The reflected shock C_2 induces a wall normal velocity component in the near-wall region upstream of the intersection point I. Profiles of the wall-normal velocity, given in Figs. 4.10–4.12, quantify the strength of this inner portion of the reflected shock, as well as the expansion fan that forms as the reflection of the incident shock C_3.

The reflected shock C_2 enables the pathlines of high velocity fluid originating upstream of the interaction to be directed around the region of low velocity fluid at the shock foot. A highly unsteady free shear layer, visualized in Fig. 4.32, is formed beginning at the anchor point of the reflected shock C_2. The highly unsteady nature of the shear layer is evidenced by simultaneous inspection of the instantaneous and

mean $\partial\overline{u}(x,y)/\partial y$ fields from Fig. 4.32 and the mean $\overline{k}(x,y)$ fields in Fig. 4.26. These visualizations add to the evidence offered by Pirozzoli and Grasso (2006) and Dupont et al. (2008) that the oscillations of this shear layer are fundamental to the cause of the low-frequency high-amplitude oscillations of the overall interaction region.

The SPIV technique enables measurements of the full anisotropy tensor. Figs. 4.35–4.37 show that the effect of the shock–boundary layer interaction dramatically changes the turbulence state within the boundary layer, bringing it from a largely two-dimensional state upstream of the interaction to a relatively near-isotropic state immediately downstream of the interaction. The fidelity of the present measurements also enables an account of the kinetic energy dissipation rate ε, an approximation for which is shown in Figs. 4.40–4.42. These quantities are particularly important for computational modeling, as they are at the root of the models used in RANS simulations.

Deflection angle θ (deg)	x_1/δ_0	x_2/δ_0	x_3/δ_0	x_4/δ_0	x_5/δ_0	x_6/δ_0	x_7/δ_0
7.75	-2.5	-1.9	-1.5	-1.1	-0.7	-0.4	+0.8
10.0	-2.5	-1.9	-1.5	-1.1	-0.7	-0.2	+0.3
12.0	-3.6	-2.9	-2.3	-1.7	-1.1	-0.5	-0.05

Table 4.1: Downstream distances x/δ_0 of the spanwise sampling planes for each shock strength investigated.

θ (deg)	p_3/p_1	$(\delta^\omega/\delta_0^\omega)_{max}$ $\omega_{z_t} = -0.25$	$(\delta^\omega/\delta_0^\omega)_{max}$ $\omega_{z_t} = -0.70$
7.75	2.73	1.20	2.55
10.0	3.51	1.29	2.86
12.0	4.34	1.47	3.40

Table 4.2: The peak amount of boundary layer thickening through the interaction region is given for all three shock strengths using a choice of two vorticity contours to define the boundary layer height. Quantities correspond to Figs. 4.23–4.25.

θ (deg)	p_3/p_1	L_0	I	
			x_I/δ_0	y_I/δ_0
7.75	2.73	-2.39	-1.42	0.62
10.0	3.51	-3.22	-1.84	0.80
12.0	4.34	-4.12	-2.12	1.07

Table 4.3: Quantifications of the size of the oblique SBLI region as a function of the impinging shock strength, listing the upstream propagation distance L_0 and the intersection point I.

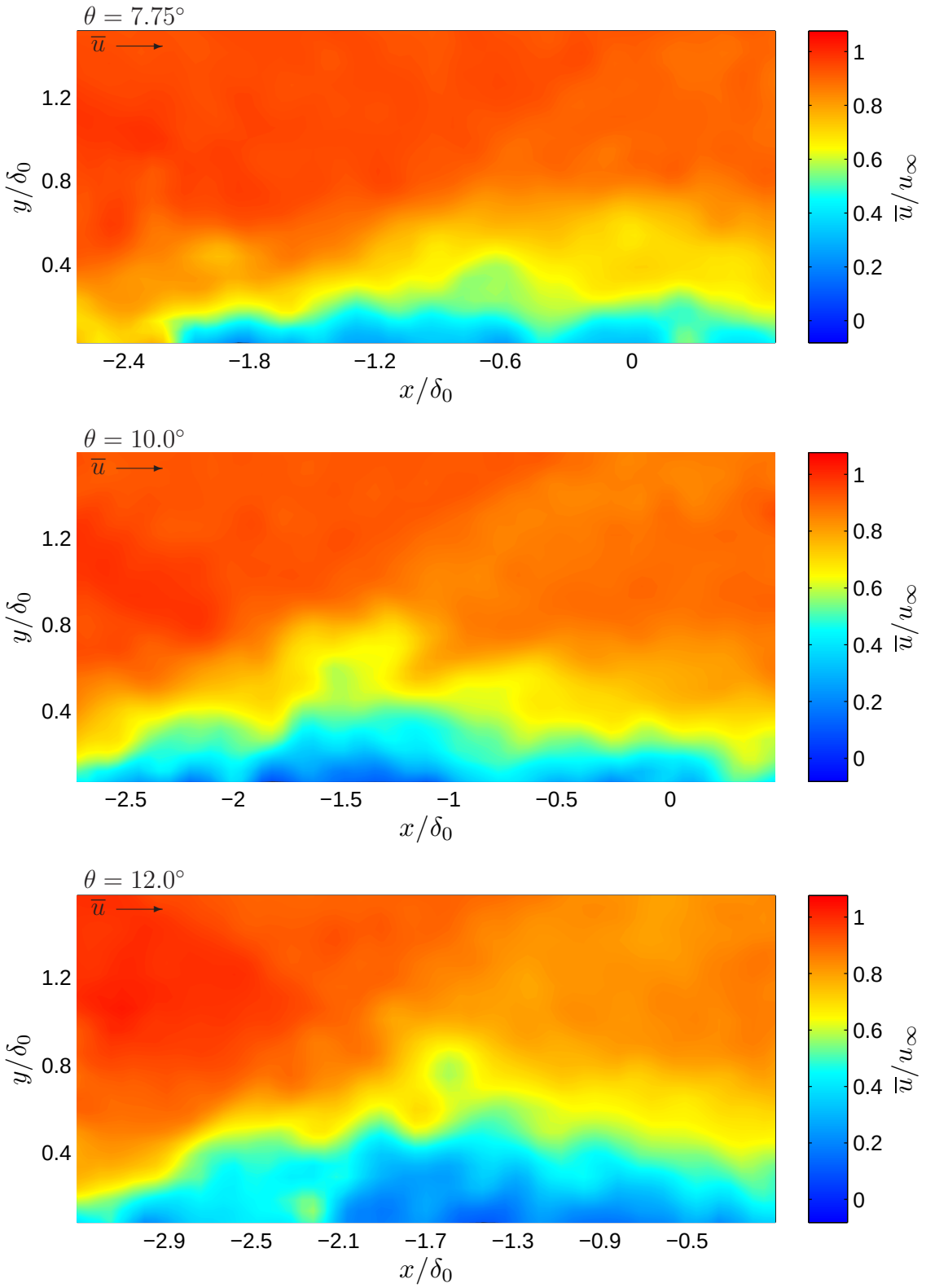

Figure 4.1: Representative instantaneous visualizations of the streamwise velocity component u for each of the three flow deflection angles in planes oriented in the streamwise direction along the tunnel centerline.

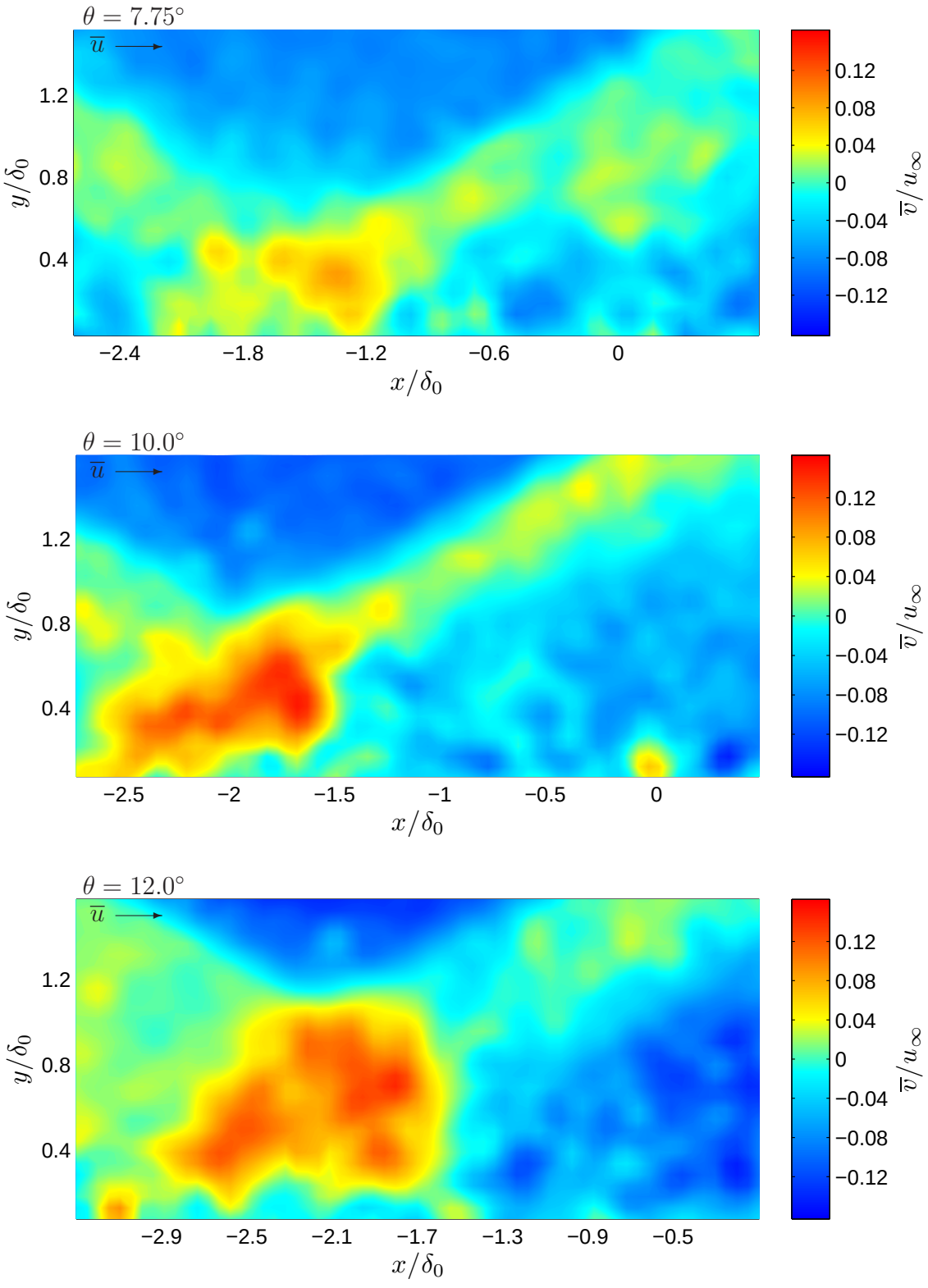

Figure 4.2: Representative instantaneous visualizations of the wall-normal velocity component v for each of the three flow deflection angles in planes oriented in the streamwise direction along the tunnel centerline.

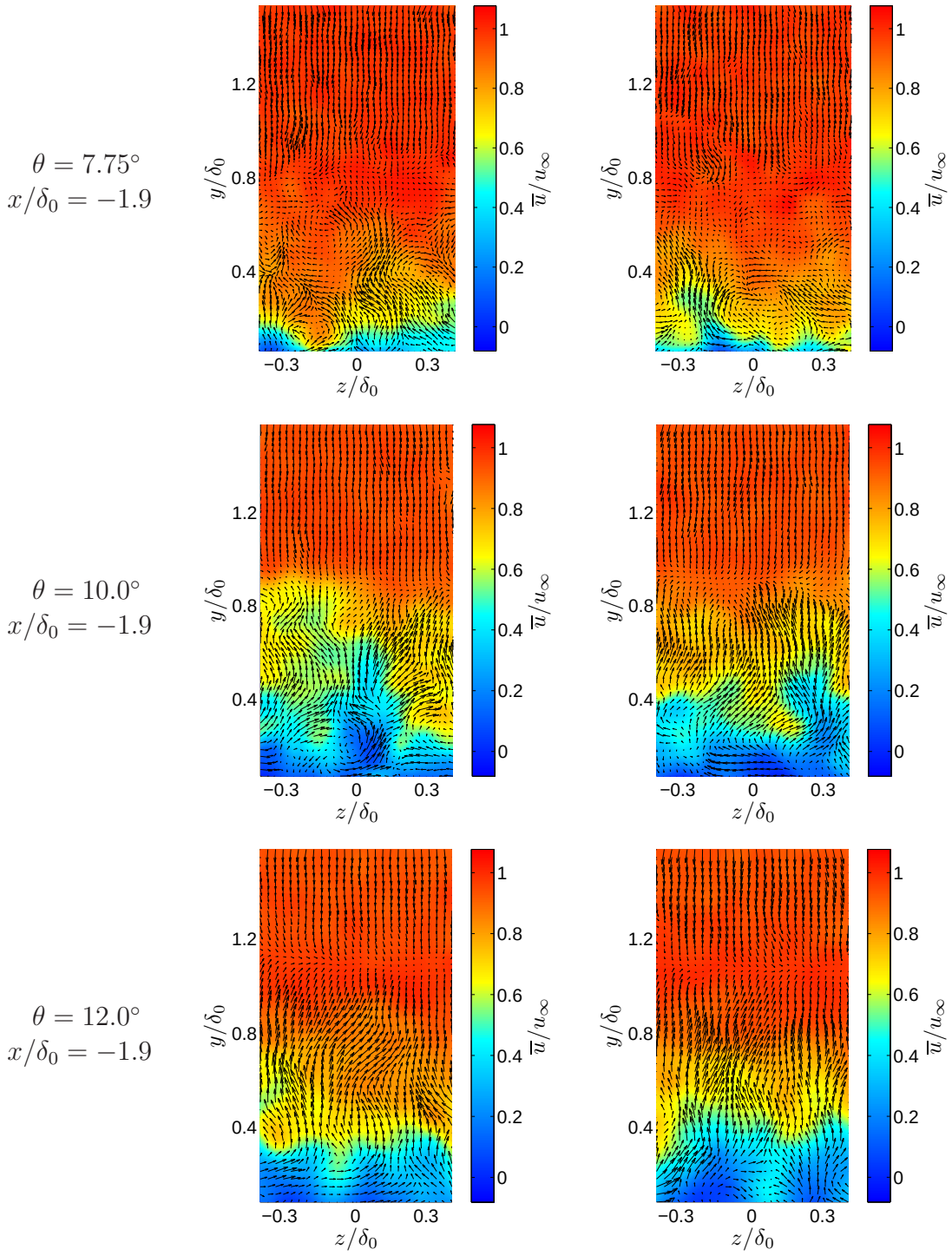

Figure 4.3: Representative instantaneous visualizations of the streamwise velocity component u for each of the three flow deflection angles in planes oriented in the spanwise direction and downstream positions near the center of the shock foot. Overlayed on the color maps are vectors showing the in-plane v and w velocity components.

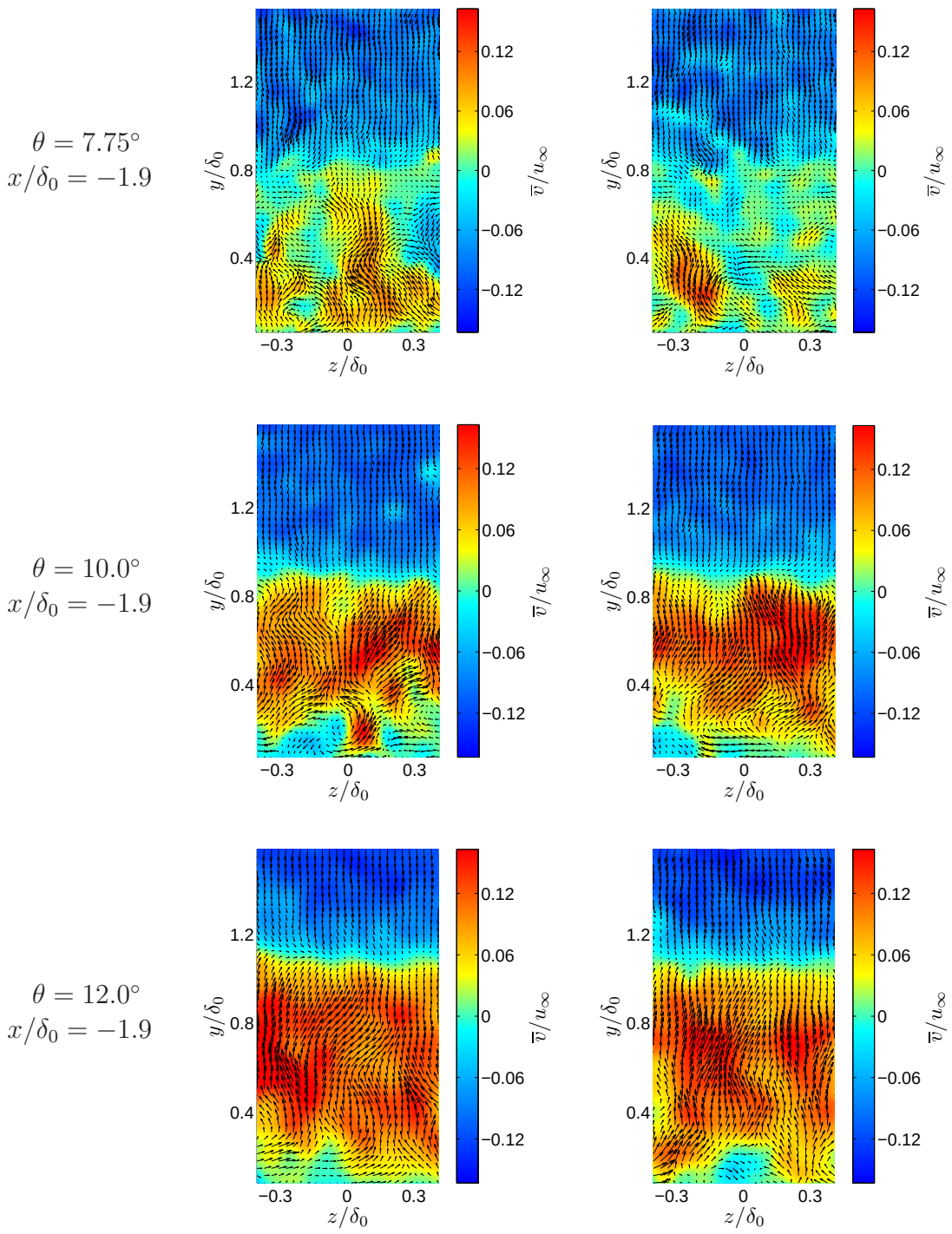

Figure 4.4: Representative instantaneous visualizations of the wall-normal velocity component v for each of the three flow deflection angles in planes oriented in the spanwise direction and downstream positions near the center of the shock foot. Overlayed on the color maps are vectors showing the in-plane v and w velocity components.

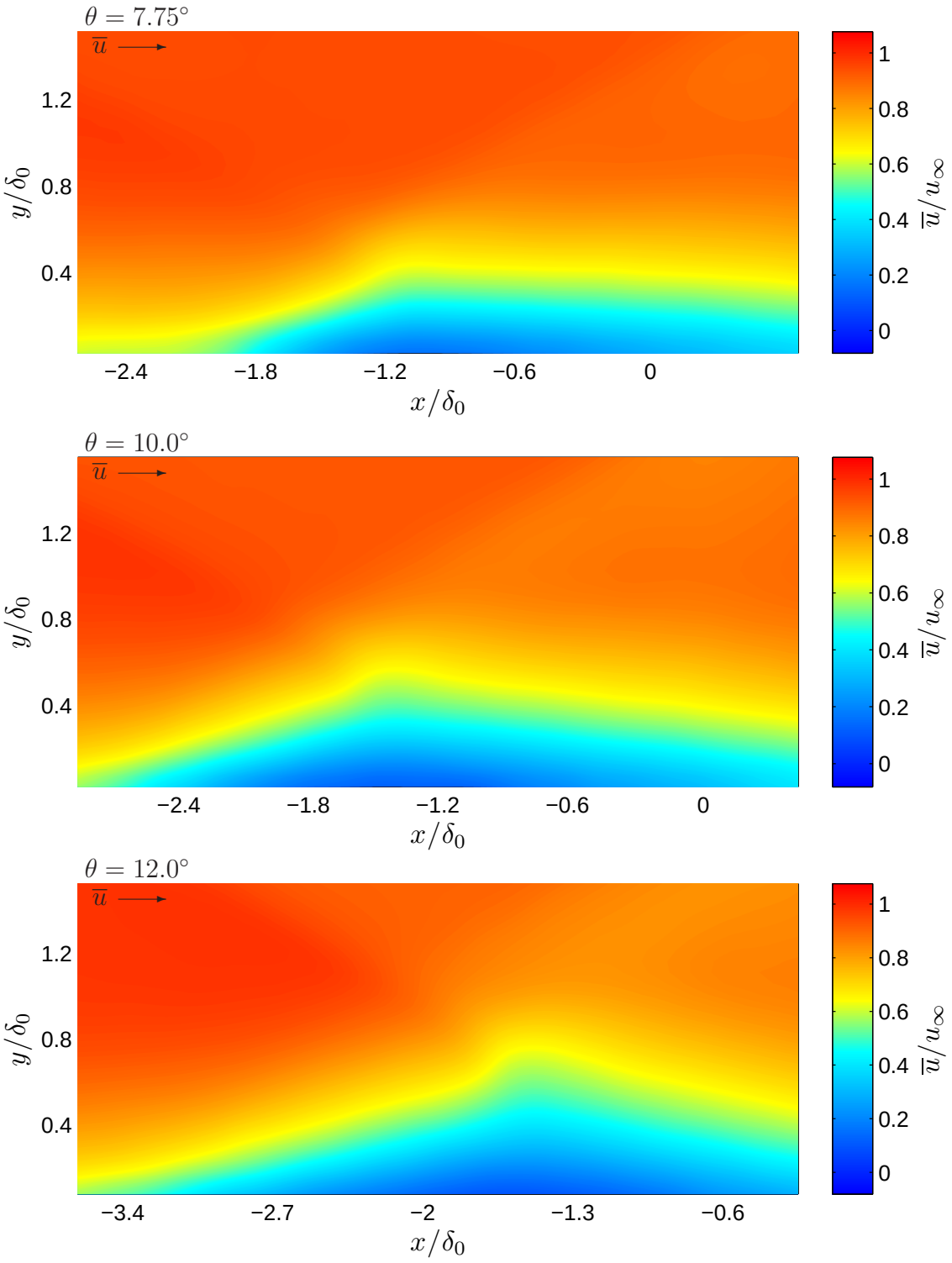

Figure 4.5: Mean streamwise velocity $\overline{u}$ fields in planes oriented in the streamwise direction for each of the three shock strengths. The thickening of the boundary layer through the interaction is obvious, with the level of thickening clearly increasing with increasing shock strength.

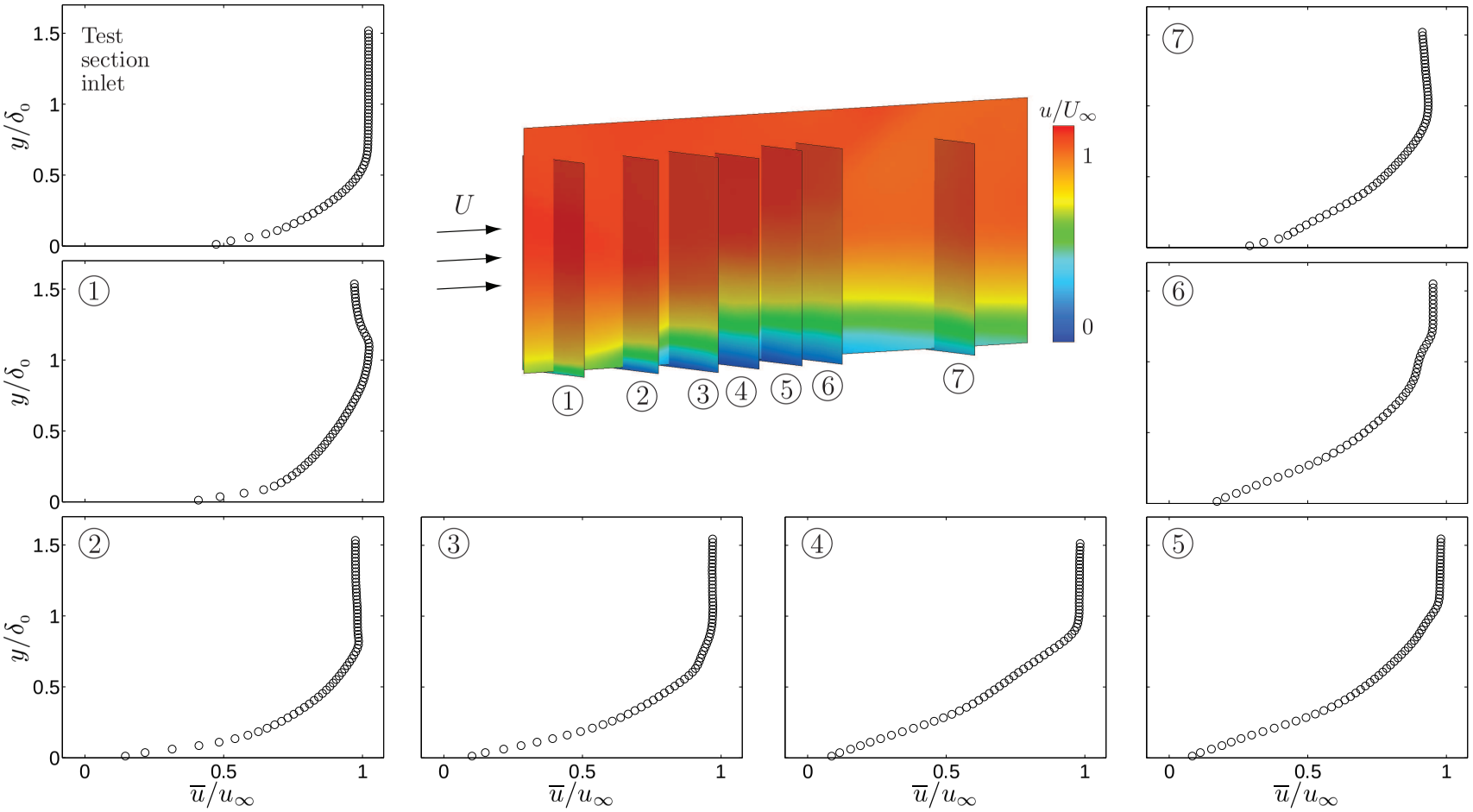

Figure 4.6: Evolution of $\overline{u}$ through the SBLI region for a flow deflection angle of $\theta = 7.75$–deg. The seven sampling locations correspond to 1: $x/\delta_0 = -2.5$, 2: $x/\delta_0 = -1.9$, 3: $x/\delta_0 = -1.5$, 4: $x/\delta_0 = -1.1$, 5: $x/\delta_0 = -0.7$, 6: $x/\delta_0 = -0.4$, and 7: $x/\delta_0 = +0.8$. At top, colors show the $\overline{u}$ field throughout each sampling plane, and also indicate their relative locations.

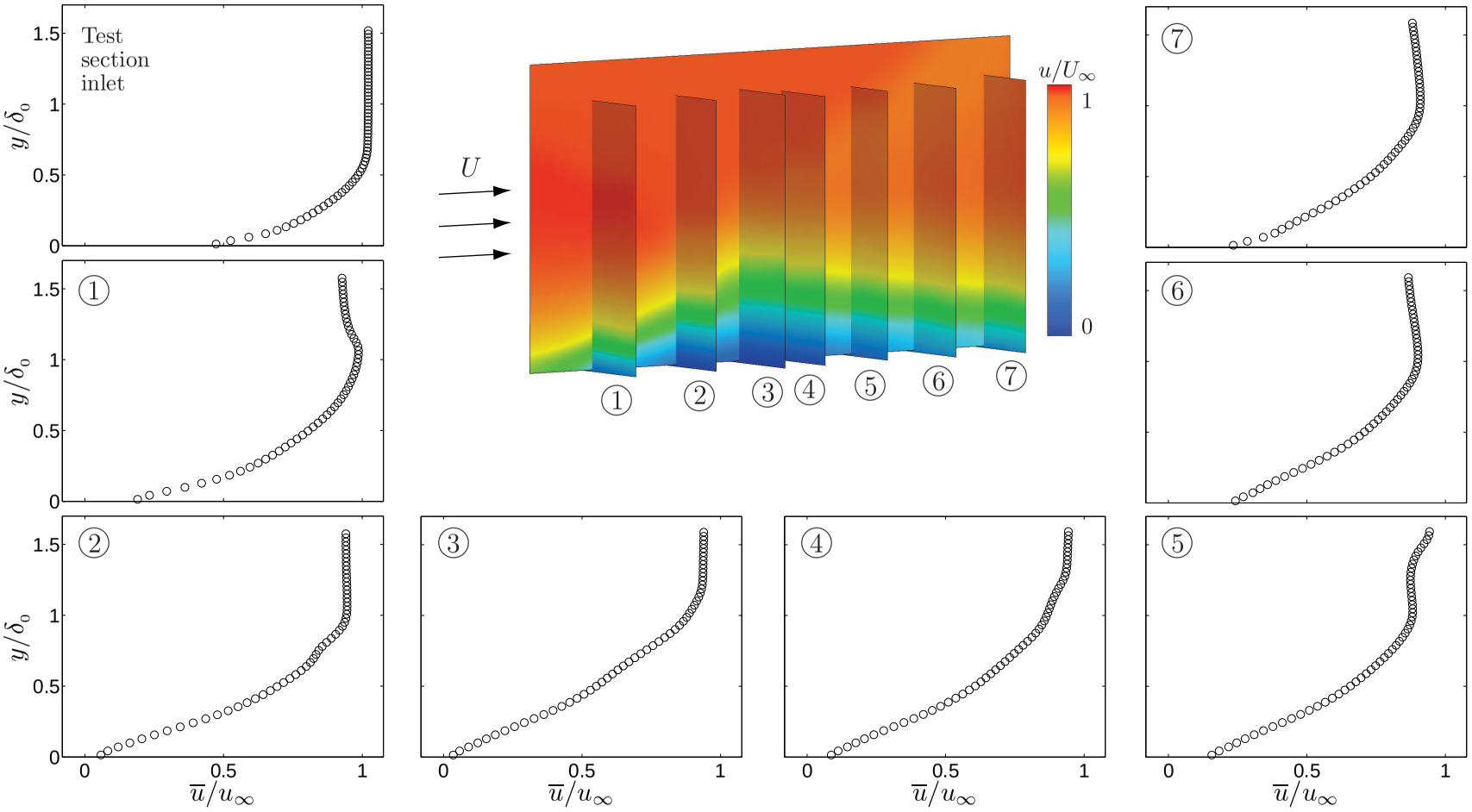

Figure 4.7: Evolution of $\overline{u}$ through the SBLI region for a flow deflection angle of $\theta = 10.0$–deg. The seven sampling locations correspond to 1: $x/\delta_0 = -2.5$, 2: $x/\delta_0 = -1.9$, 3: $x/\delta_0 = -1.5$, 4: $x/\delta_0 = -1.1$, 5: $x/\delta_0 = -0.7$, 6: $x/\delta_0 = -0.2$, and 7: $x/\delta_0 = +0.3$. At top, colors show the $\overline{u}$ field throughout each sampling plane, and also indicate their relative locations.

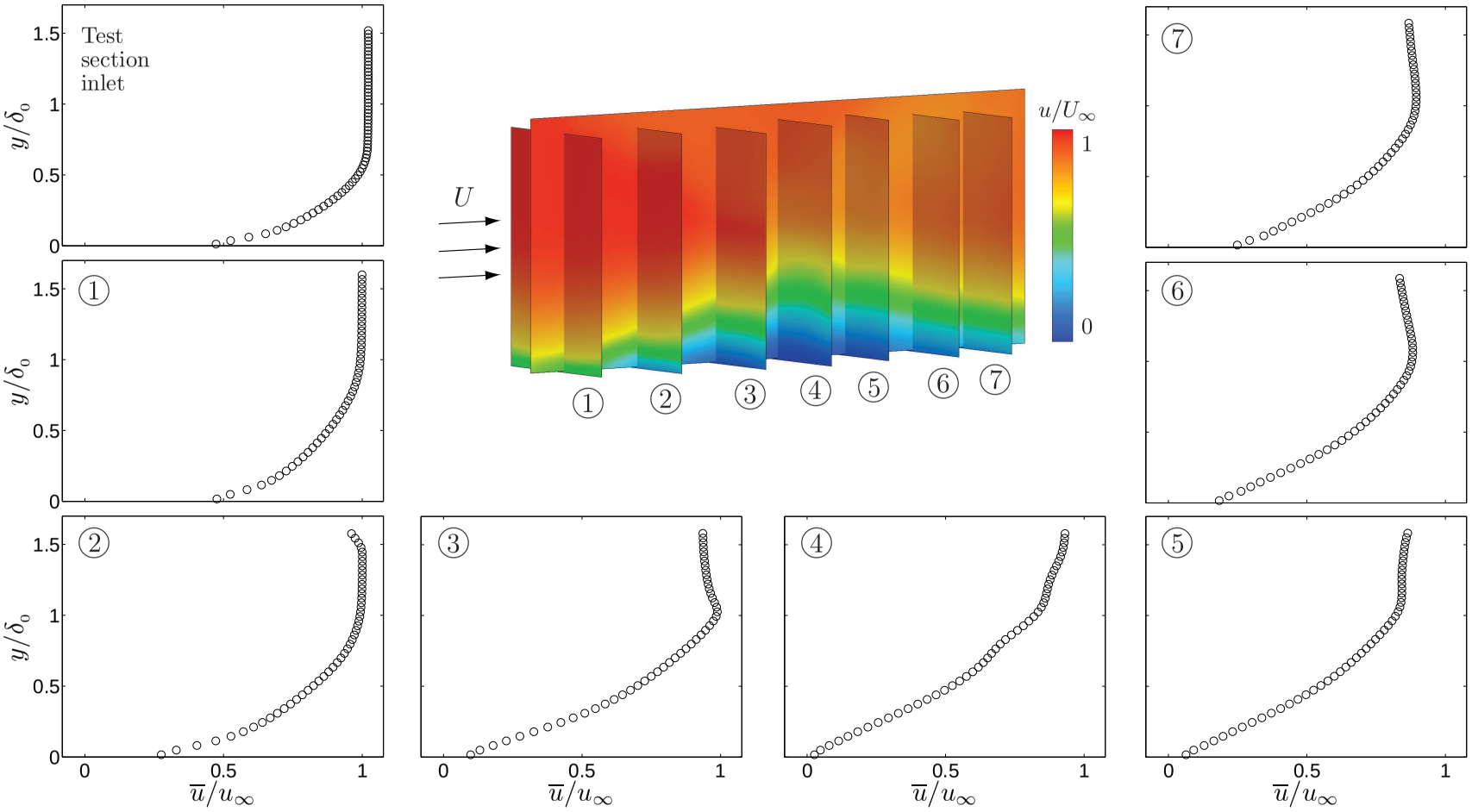

Figure 4.8: Evolution of $\overline{u}$ through the SBLI region for a flow deflection angle of $\theta = 12.0$–deg. The seven sampling locations correspond to 1: $x/\delta_0 = -3.6$, 2: $x/\delta_0 = -2.9$, 3: $x/\delta_0 = -2.3$, 4: $x/\delta_0 = -1.7$, 5: $x/\delta_0 = -1.1$, 6: $x/\delta_0 = -0.5$, and 7: $x/\delta_0 = -0.05$. At top, colors show the $\overline{u}$ field throughout each sampling plane, and also indicate their relative locations.

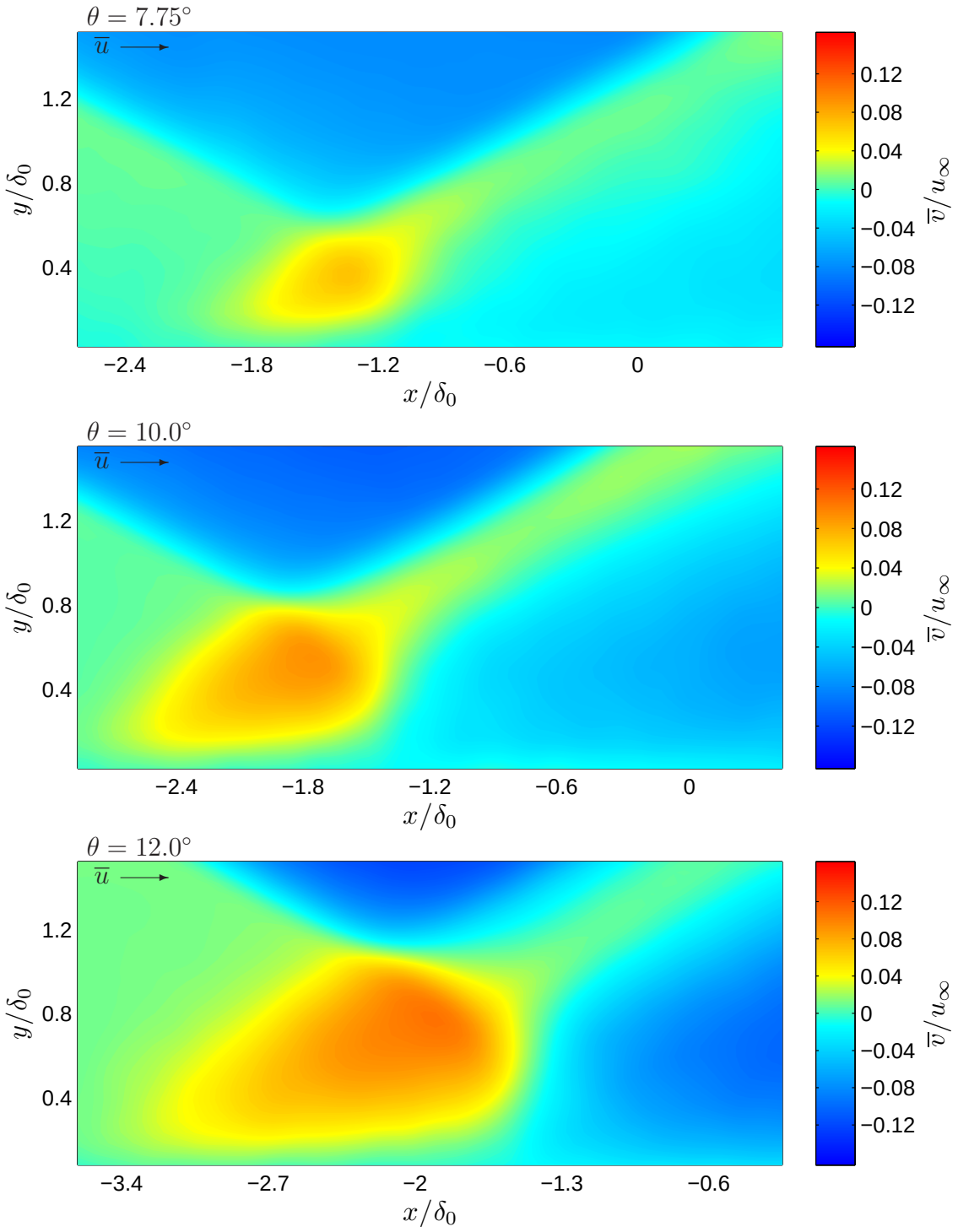

Figure 4.9: Mean wall-normal velocity $\overline{v}$ fields in planes oriented in the streamwise direction for each of the three shock strengths. An "upwash" region located at the shock foot grows clearly in size and intensity, and penetrates increasingly far upstream, as the shock strength increases.

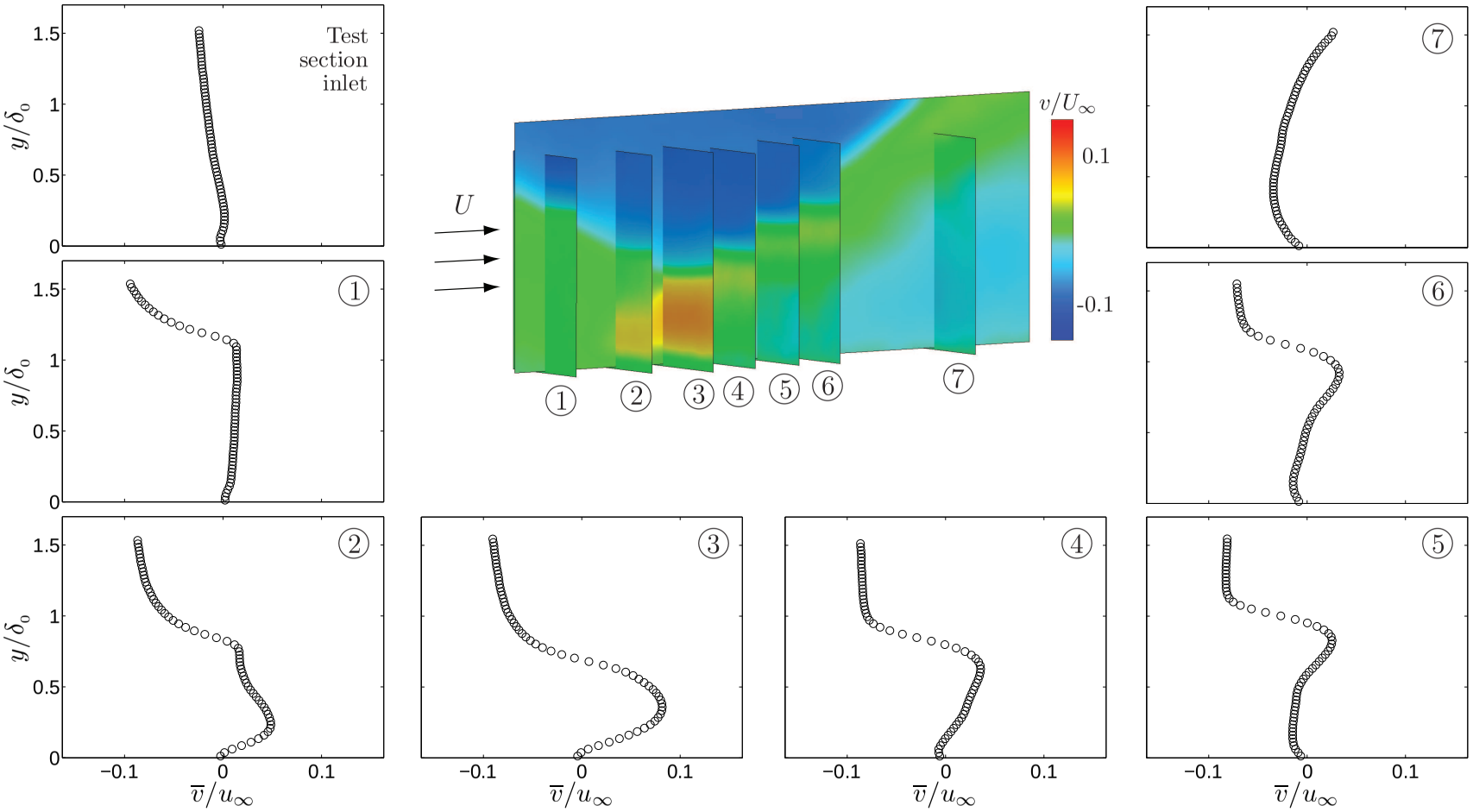

Figure 4.10: Evolution of $\overline{v}$ through the SBLI region for a flow deflection angle of $\theta = 7.75$–deg. The seven sampling locations correspond to 1: $x/\delta_0 = -2.5$, 2: $x/\delta_0 = -1.9$, 3: $x/\delta_0 = -1.5$, 4: $x/\delta_0 = -1.1$, 5: $x/\delta_0 = -0.7$, 6: $x/\delta_0 = -0.4$, and 7: $x/\delta_0 = +0.8$. At top, colors show the $\overline{v}$ field throughout each sampling plane, and also indicate their relative locations.

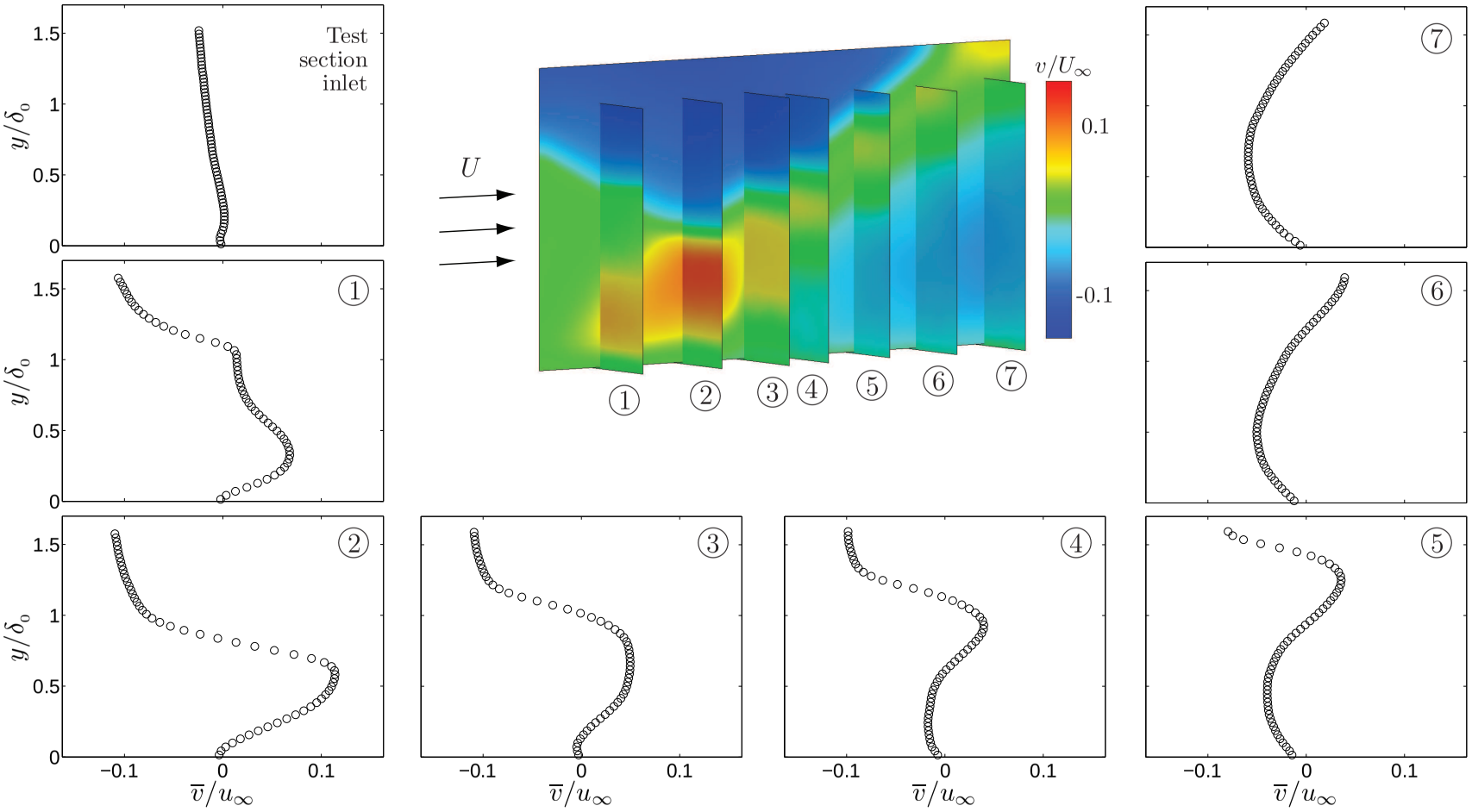

Figure 4.11: Evolution of $\overline{v}$ through the SBLI region for a flow deflection angle of $\theta = 10.0$–deg. The seven sampling locations correspond to 1: $x/\delta_0 = -2.5$, 2: $x/\delta_0 = -1.9$, 3: $x/\delta_0 = -1.5$, 4: $x/\delta_0 = -1.1$, 5: $x/\delta_0 = -0.7$, 6: $x/\delta_0 = -0.2$, and 7: $x/\delta_0 = +0.3$. At top, colors show the $\overline{v}$ field throughout each sampling plane, and also indicate their relative locations.

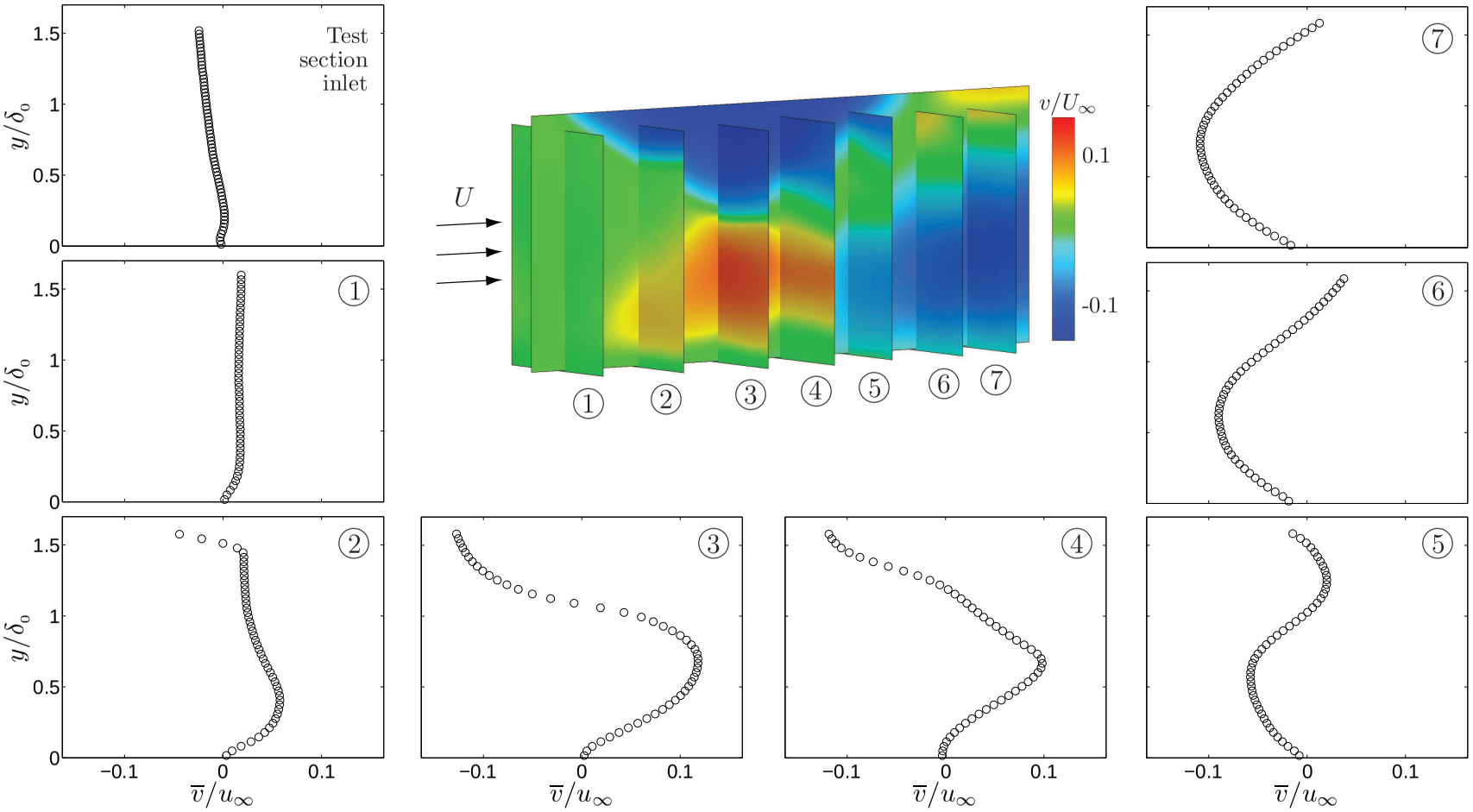

Figure 4.12: Evolution of $\overline{v}$ through the SBLI region for a flow deflection angle of $\theta = 12.0$–deg. The seven sampling locations correspond to 1: $x/\delta_0 = -3.6$, 2: $x/\delta_0 = -2.9$, 3: $x/\delta_0 = -2.3$, 4: $x/\delta_0 = -1.7$, 5: $x/\delta_0 = -1.1$, 6: $x/\delta_0 = -0.5$, and 7: $x/\delta_0 = -0.05$. At top, colors show the $\overline{v}$ field throughout each sampling plane, and also indicate their relative locations.

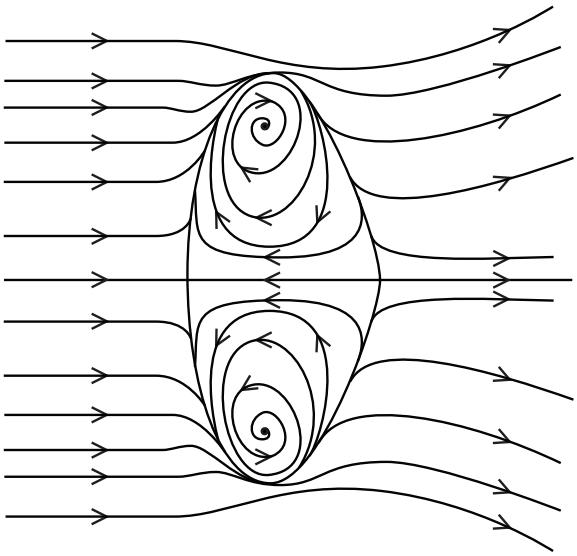

Figure 4.13: Schematic of surface flow visualizations reproduced from Bookey et al. (2005a), showing the separation region located at the shock foot. In their study, two large scale vortical structures were formed in the recirculation zone.

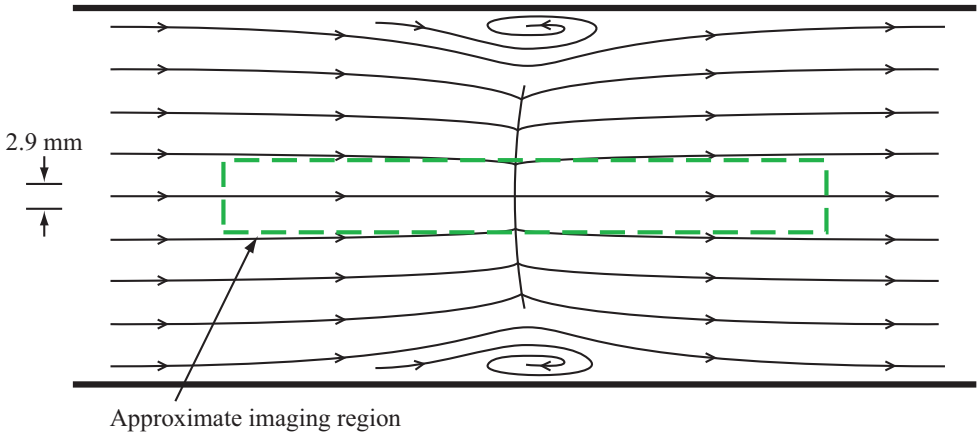

Figure 4.14: Schematic of surface flow at the shock foot in the present study. No mean recirculation zone is observed for any of the shock strengths, however two recirculation zones form along the tunnel sidewalls, far removed from the measurement locations.

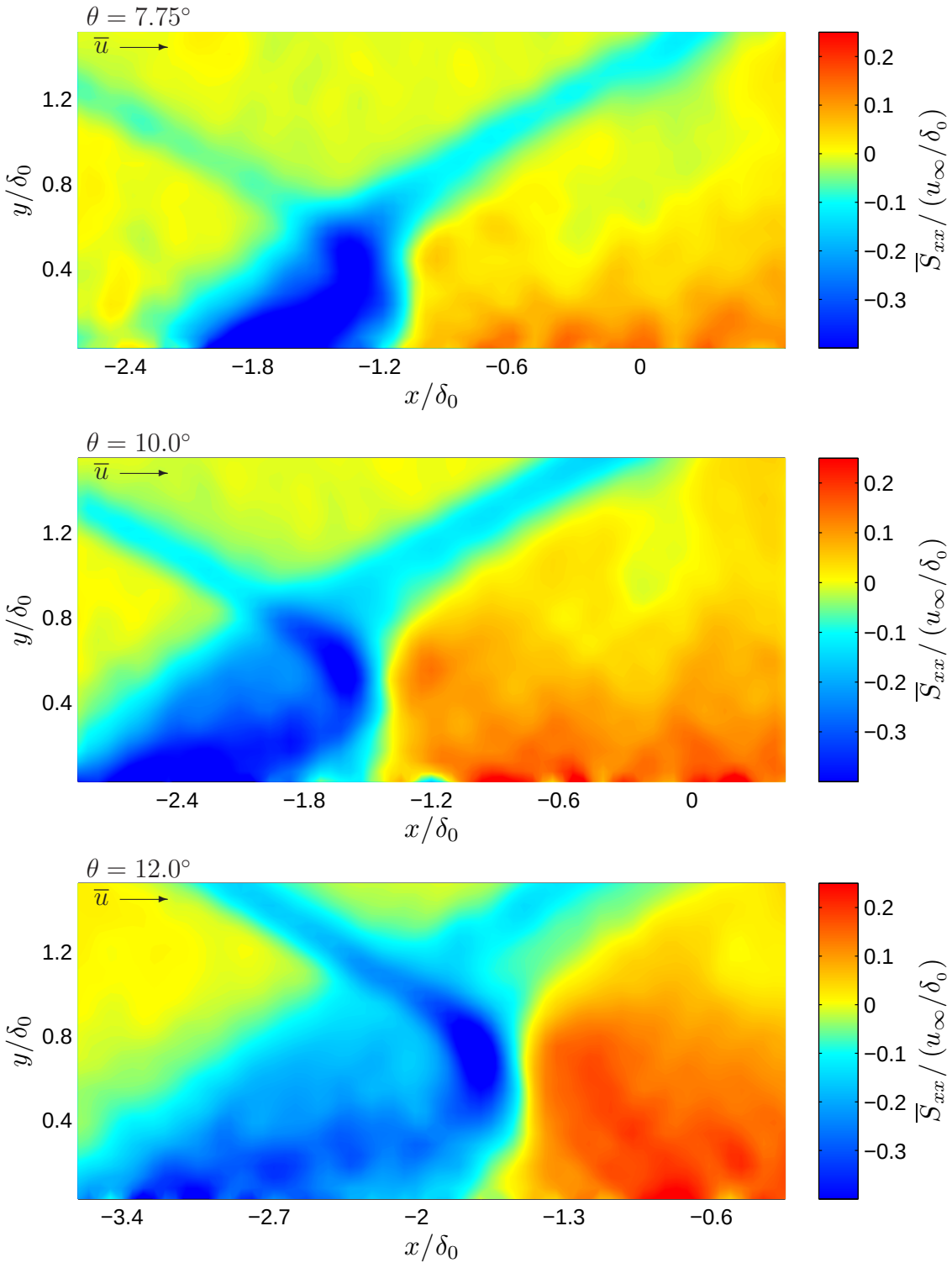

Figure 4.15: Normal strain rate component in the streamwise direction $\overline{S}_{xx}$ in planes oriented in the streamwise direction for each of the three shock strengths.

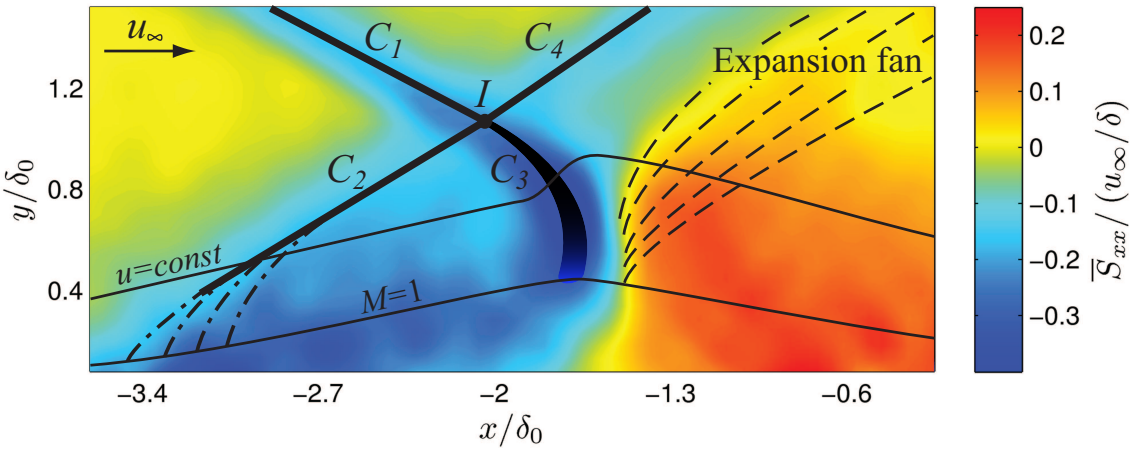

Figure 4.16: Oblique shock boundary layer interaction structure, showing also the inviscid impingement point of the C_2 shock x_{C2i} and the inviscid impingement point of the C_1 impinging shock $x_{C1i} \equiv x_0$.

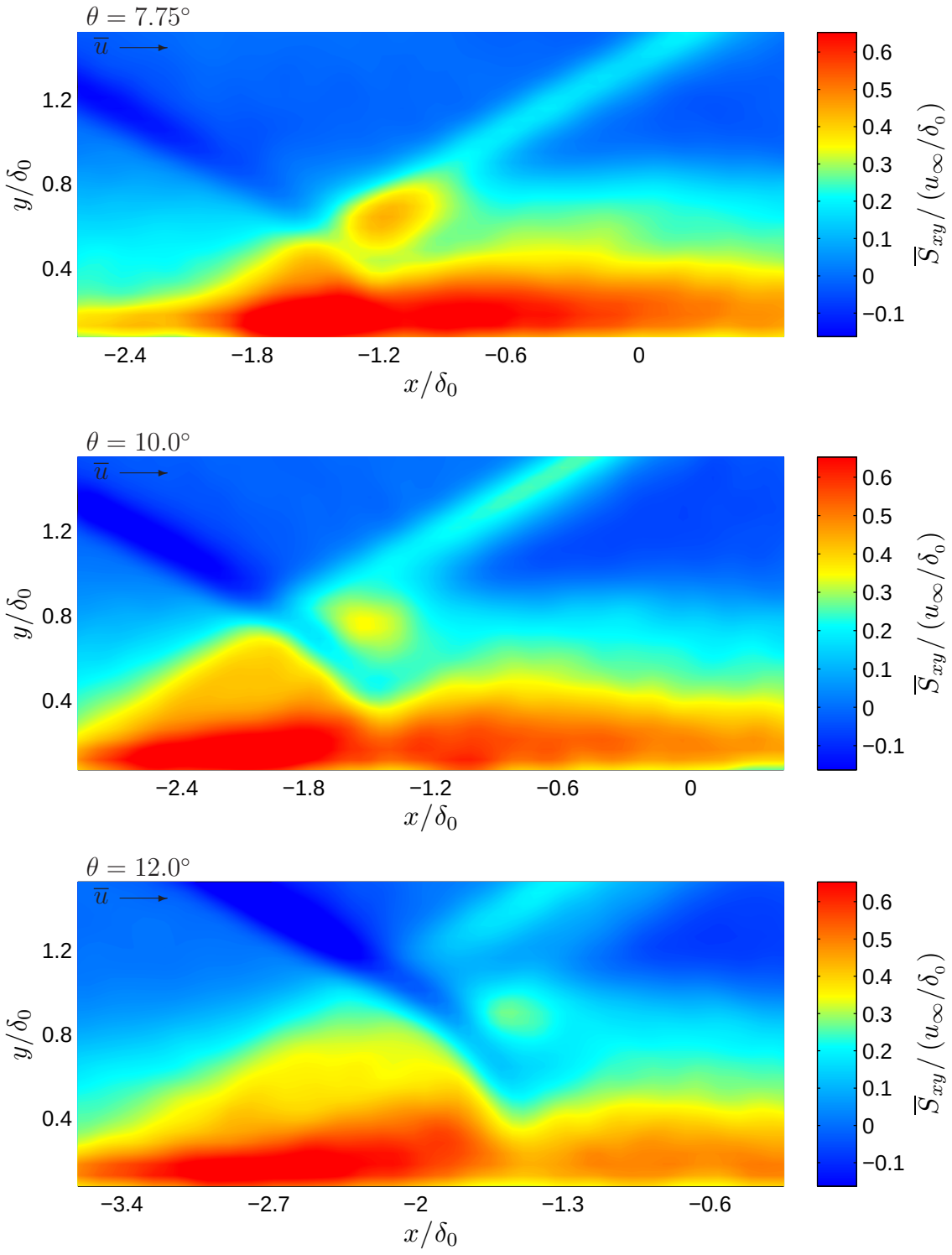

Figure 4.17: Shear strain rate component $\overline{S}_{xy}$ in planes oriented in the streamwise direction for each of the three shock strengths.

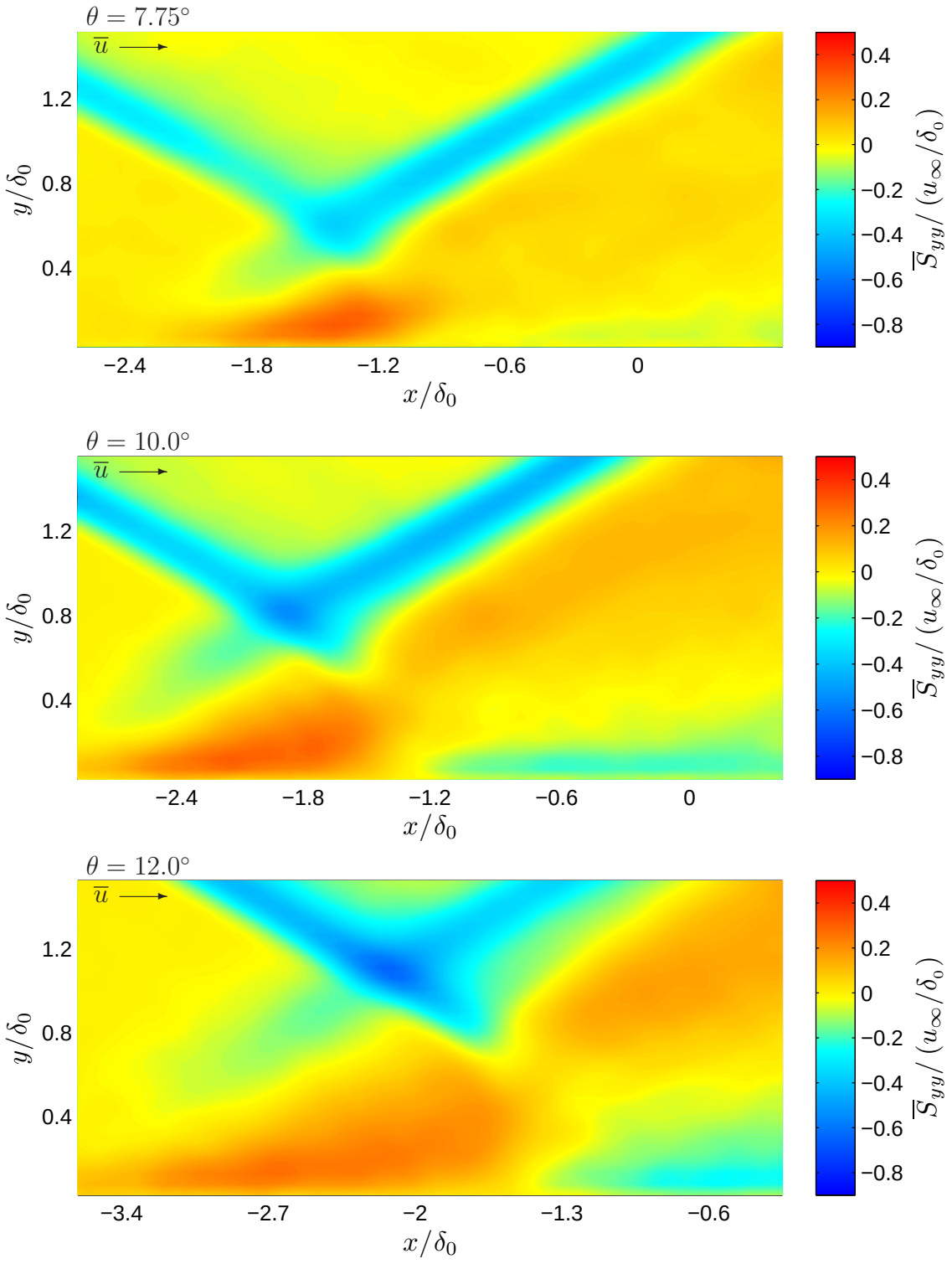

Figure 4.18: Normal strain rate component in the wall-normal direction $\overline{S}_{yy}$ in planes oriented in the streamwise direction for each of the three shock strengths.

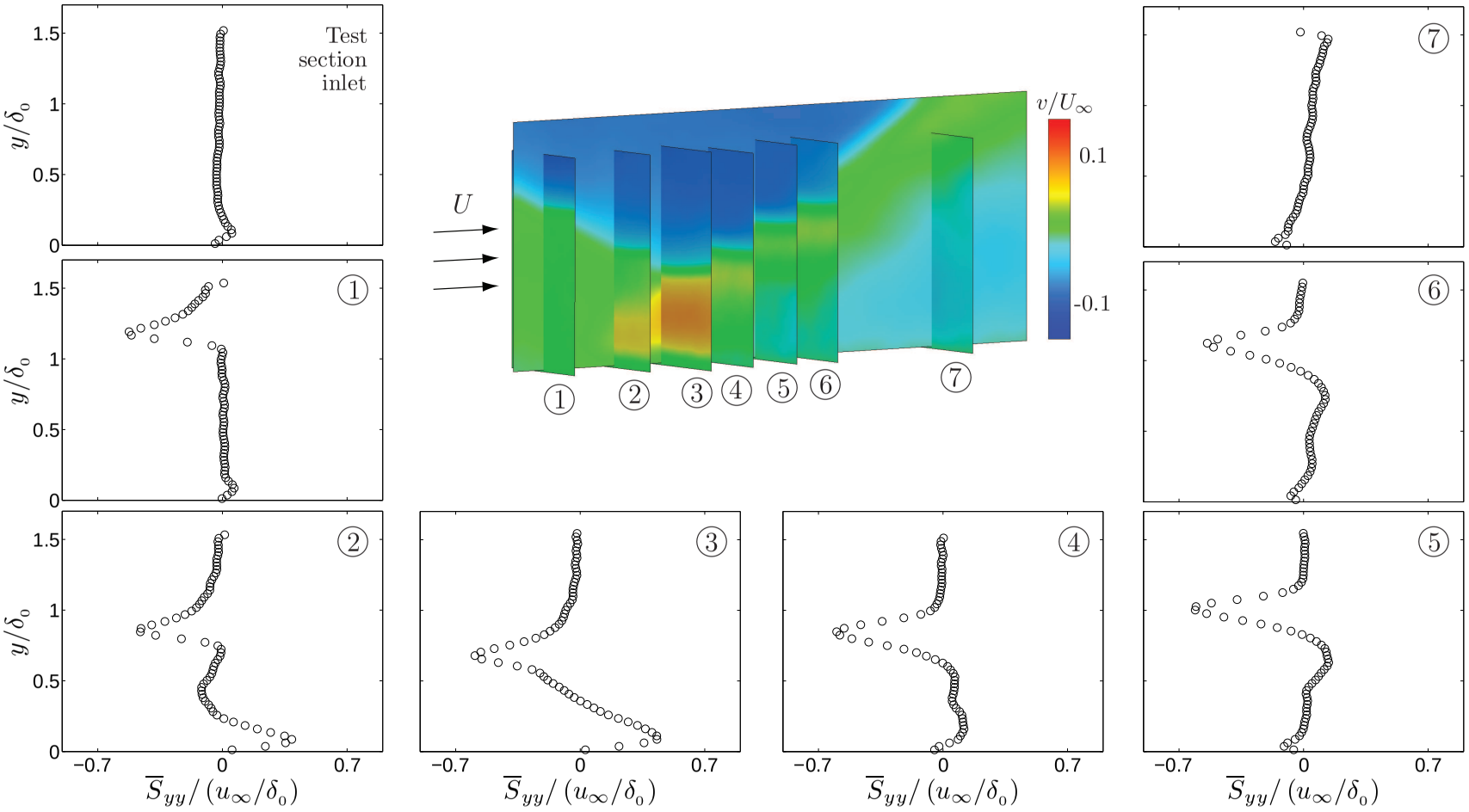

Figure 4.19: Evolution of $\overline{S}_{yy}$ through the SBLI region for a flow deflection angle of $\theta = 7.75$–deg. The seven sampling locations correspond to 1: $x/\delta_0 = -2.5$, 2: $x/\delta_0 = -1.9$, 3: $x/\delta_0 = -1.5$, 4: $x/\delta_0 = -1.1$, 5: $x/\delta_0 = -0.7$, 6: $x/\delta_0 = -0.4$, and 7: $x/\delta_0 = +0.8$. At top, colors show the $\overline{v}$ field throughout each sampling plane, and also indicate their relative locations.

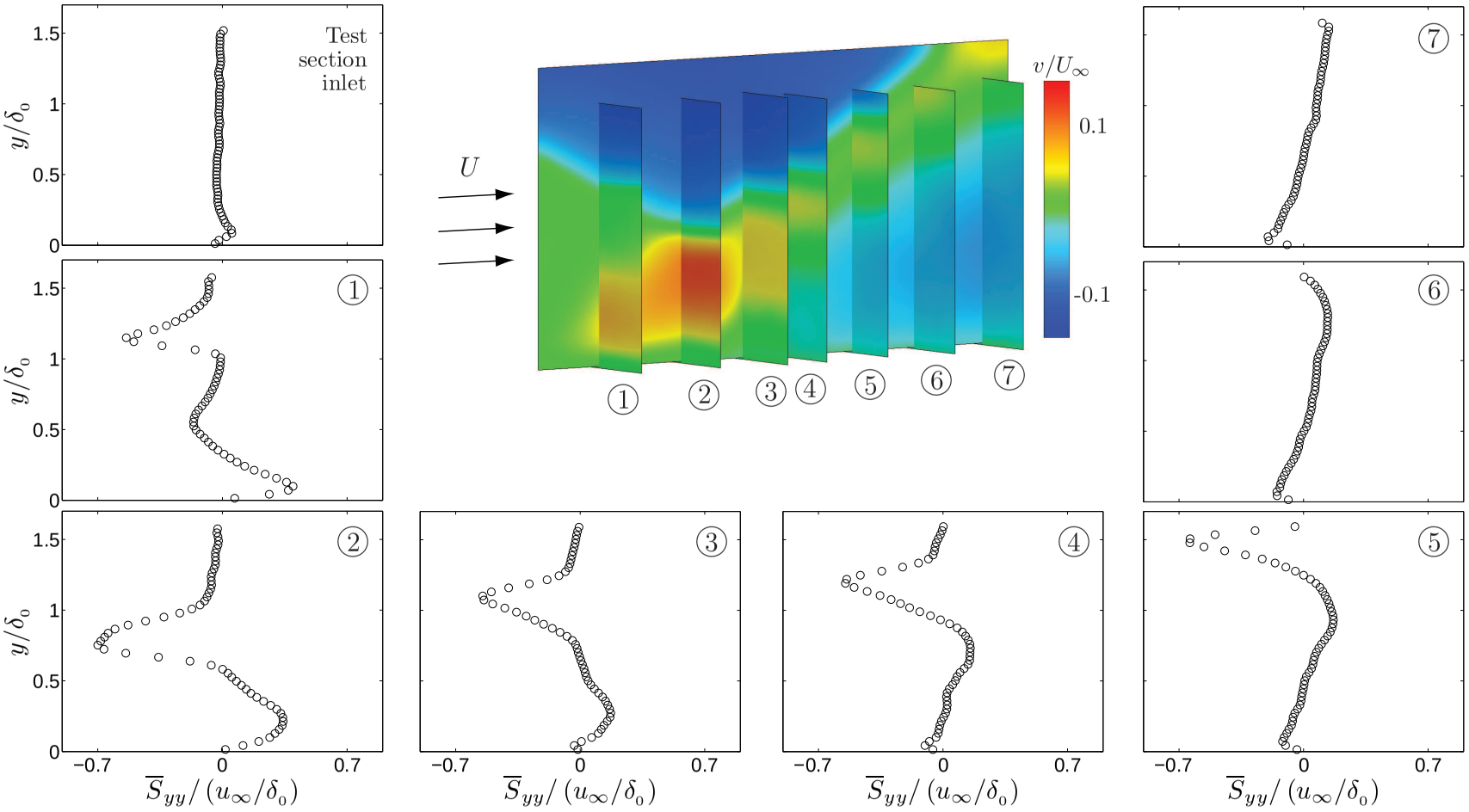

Figure 4.20: Evolution of $\overline{S}_{yy}$ through the SBLI region for a flow deflection angle of $\theta = 10.0$–deg. The seven sampling locations correspond to 1: $x/\delta_0 = -2.5$, 2: $x/\delta_0 = -1.9$, 3: $x/\delta_0 = -1.5$, 4: $x/\delta_0 = -1.1$, 5: $x/\delta_0 = -0.7$, 6: $x/\delta_0 = -0.2$, and 7: $x/\delta_0 = +0.3$. At top, colors show the $\overline{v}$ field throughout each sampling plane, and also indicate their relative locations.

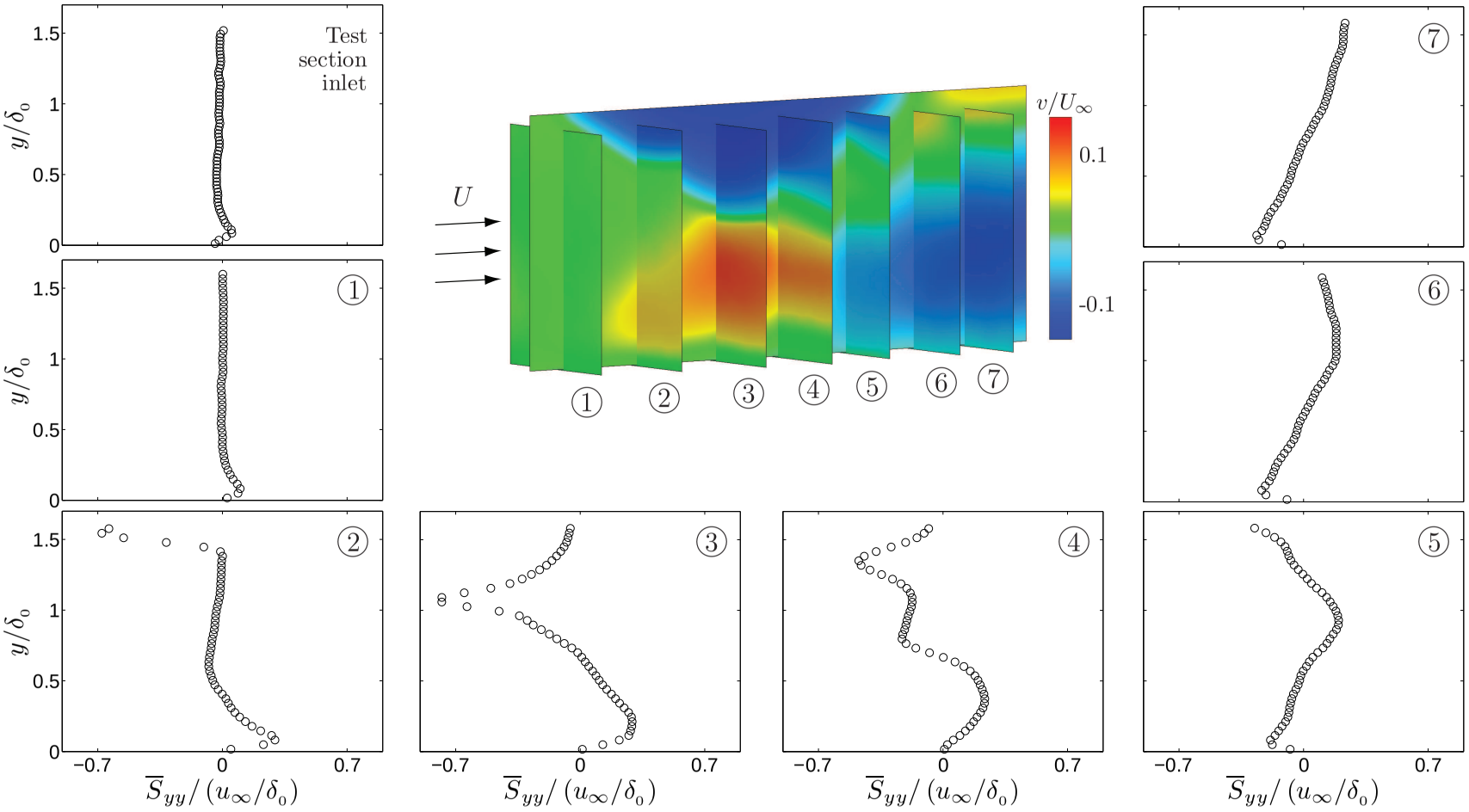

Figure 4.21: Evolution of $\overline{S}_{yy}$ through the SBLI region for a flow deflection angle of $\theta = 12.0$–deg. The seven sampling locations correspond to 1: $x/\delta_0 = -3.6$, 2: $x/\delta_0 = -2.9$, 3: $x/\delta_0 = -2.3$, 4: $x/\delta_0 = -1.7$, 5: $x/\delta_0 = -1.1$, 6: $x/\delta_0 = -0.5$, and 7: $x/\delta_0 = -0.05$. At top, colors show the $\overline{v}$ field throughout each sampling plane, and also indicate their relative locations.

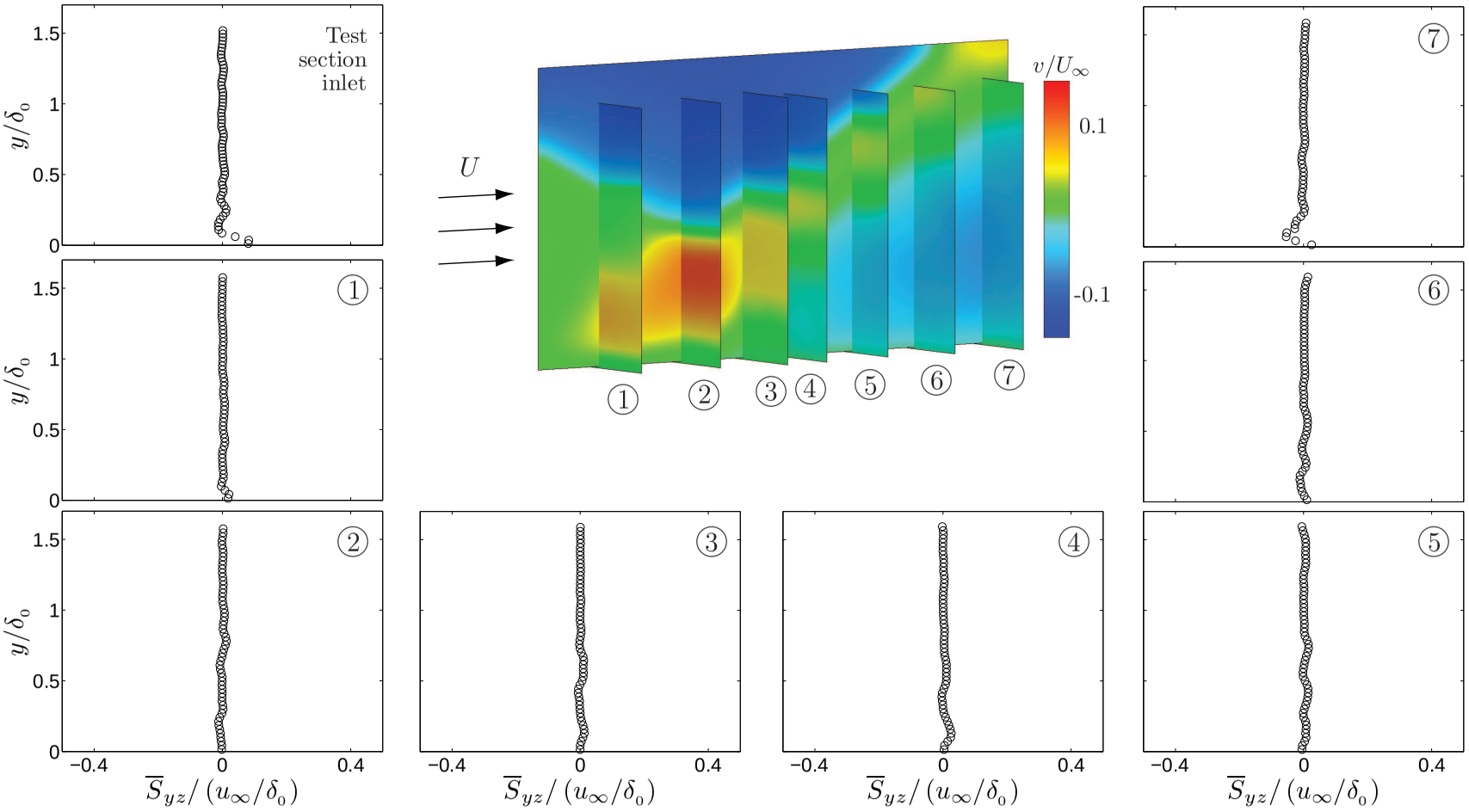

Figure 4.22: Evolution of $\overline{S}_{yz}$ through the SBLI region for a flow deflection angle of $\theta = 10.0$–deg. The seven sampling locations correspond to 1: $x/\delta_0 = -2.5$, 2: $x/\delta_0 = -1.9$, 3: $x/\delta_0 = -1.5$, 4: $x/\delta_0 = -1.1$, 5: $x/\delta_0 = -0.7$, 6: $x/\delta_0 = -0.2$, and 7: $x/\delta_0 = +0.3$. At top, colors show the $\overline{v}$ field throughout each sampling plane, and also indicate their relative locations.

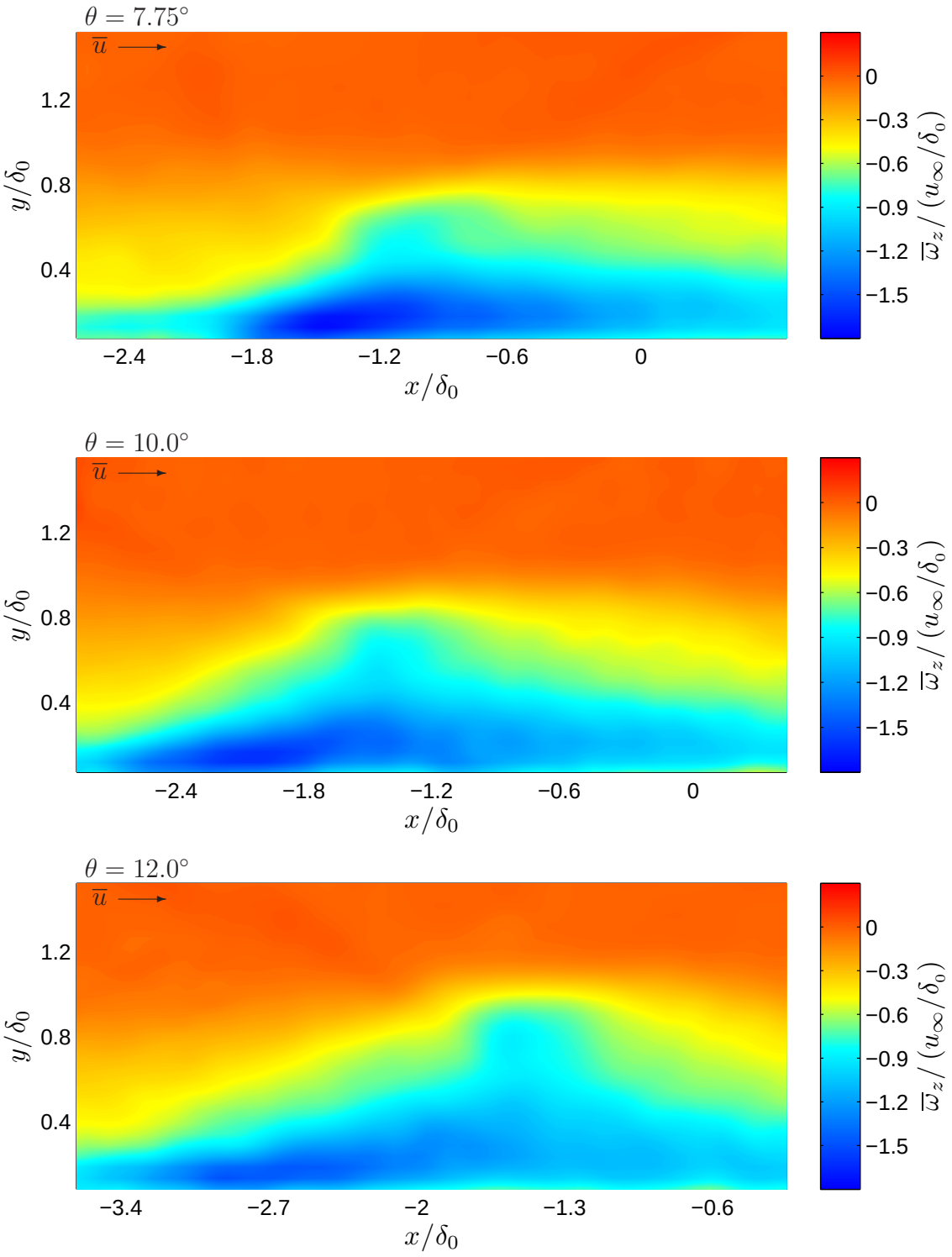

Figure 4.23: Vorticity component $\overline{\omega}_z$ in planes oriented in the streamwise direction for each of the three shock strengths. Contours of the vorticity illuminate the thickening of the boundary layer through the interaction region.

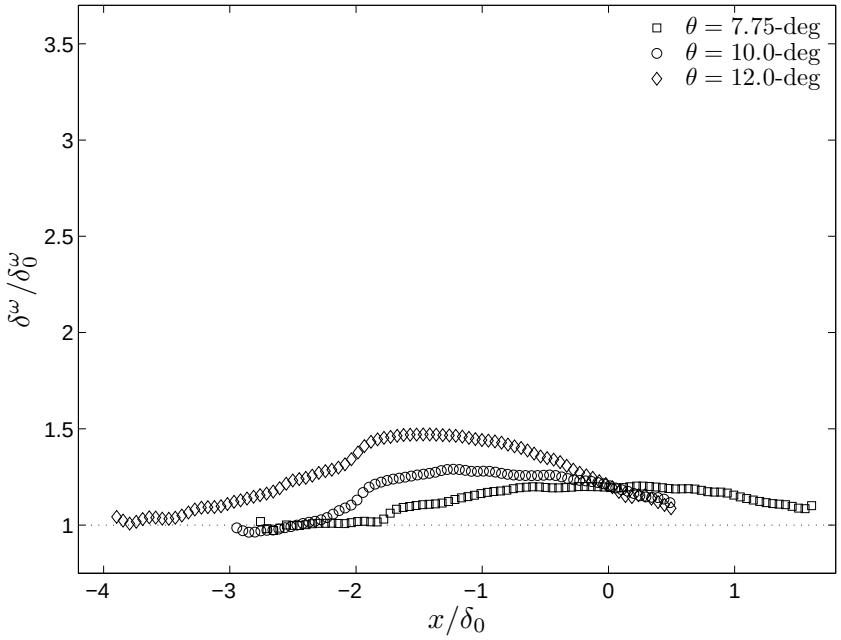

Figure 4.24: Degree of boundary layer thickening based on contours of vorticity δ^{ω} for each of the three shock strengths. Here, the near-free stream vorticity level of $\overline{\omega_z}/\left(u_{\infty}/\delta\right) = -0.25$ is used as the threshold to define the boundary layer height.

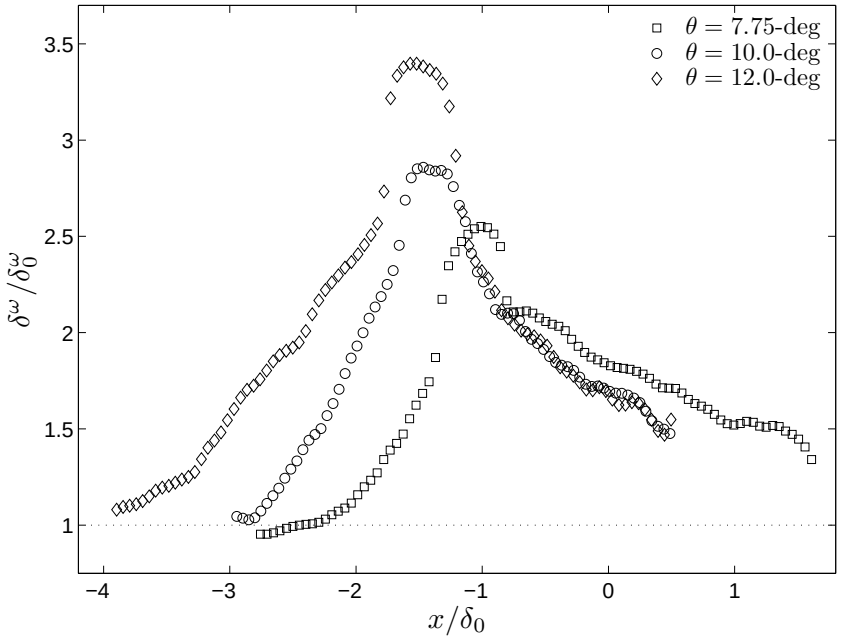

Figure 4.25: Degree of boundary layer thickening based on contours of vorticity δ^{ω} for each of the three shock strengths. Here, the relatively high vorticity value of $\overline{\omega_z}/\left(u_{\infty}/\delta\right) = -0.70$ is used as the threshold to define the boundary layer height.

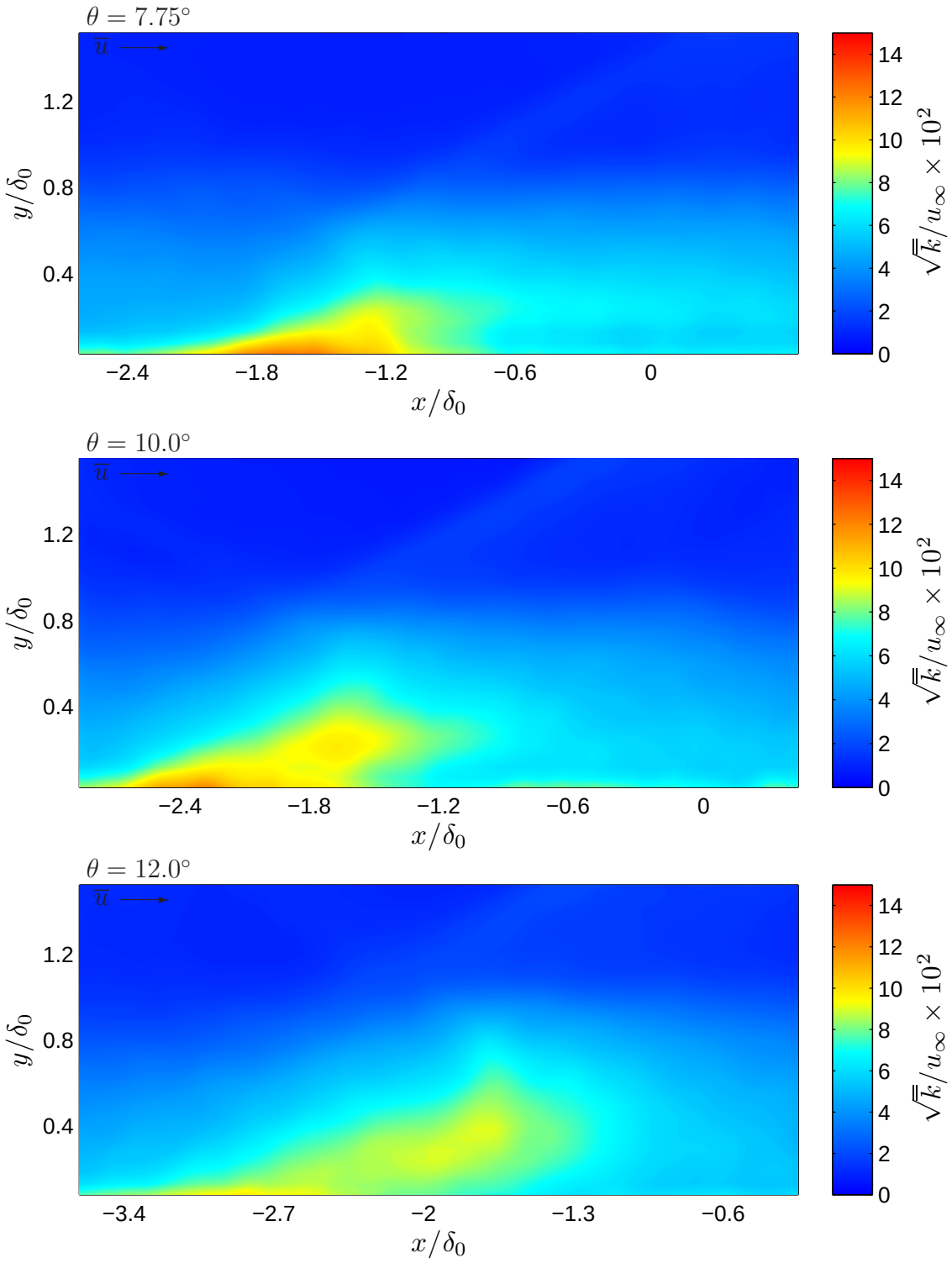

Figure 4.26: Mean turbulence kinetic energy $\overline{k}$ fields in planes oriented in the streamwise direction for each of the three shock strengths.

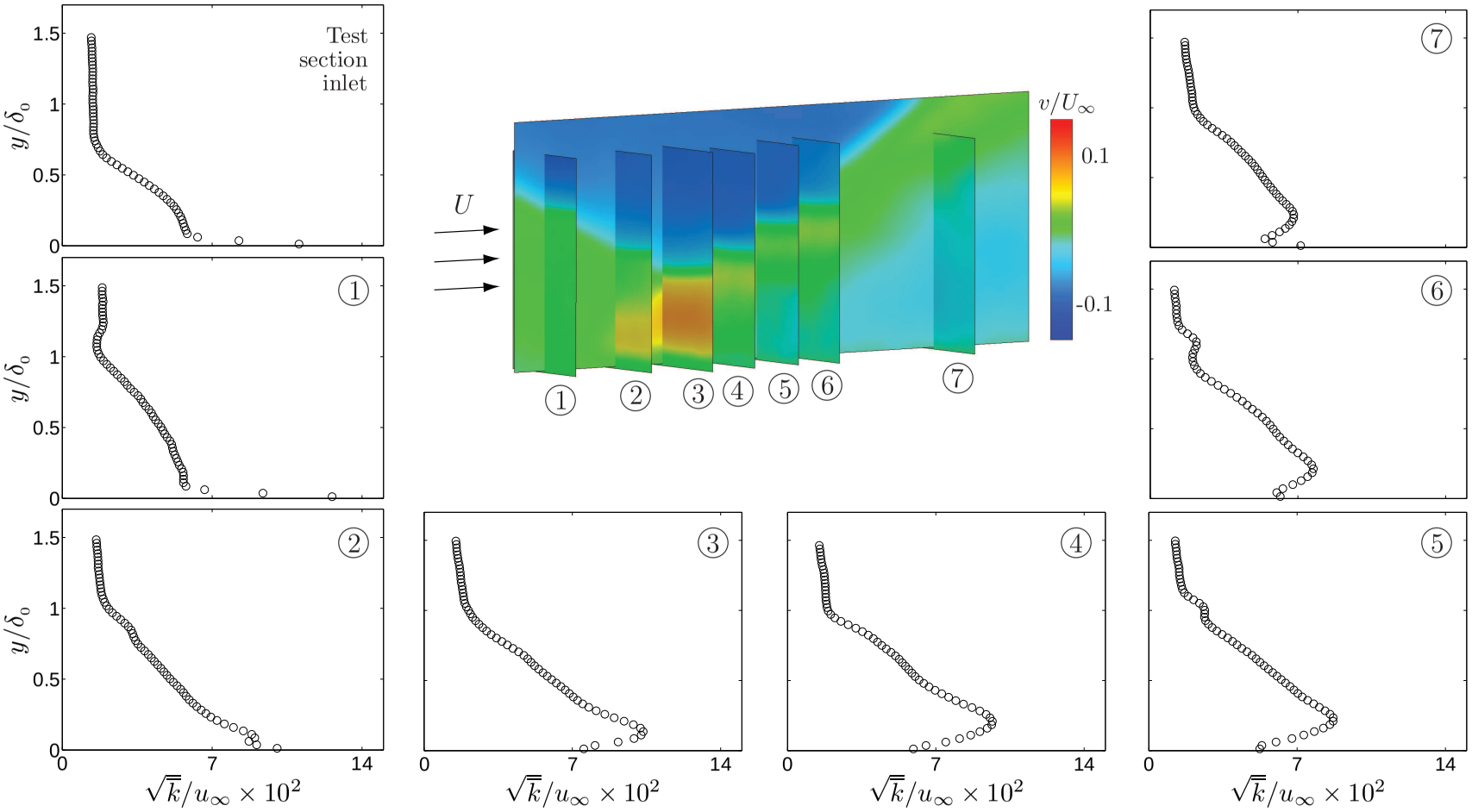

Figure 4.27: Evolution of $\overline{k}$ through the SBLI region for a flow deflection angle of $\theta = 7.75$–deg. The seven sampling locations correspond to 1: $x/\delta_0 = -2.5$, 2: $x/\delta_0 = -1.9$, 3: $x/\delta_0 = -1.5$, 4: $x/\delta_0 = -1.1$, 5: $x/\delta_0 = -0.7$, 6: $x/\delta_0 = -0.4$, and 7: $x/\delta_0 = +0.8$. At top, colors show the $\overline{v}$ field throughout each sampling plane, and also indicate their relative locations.

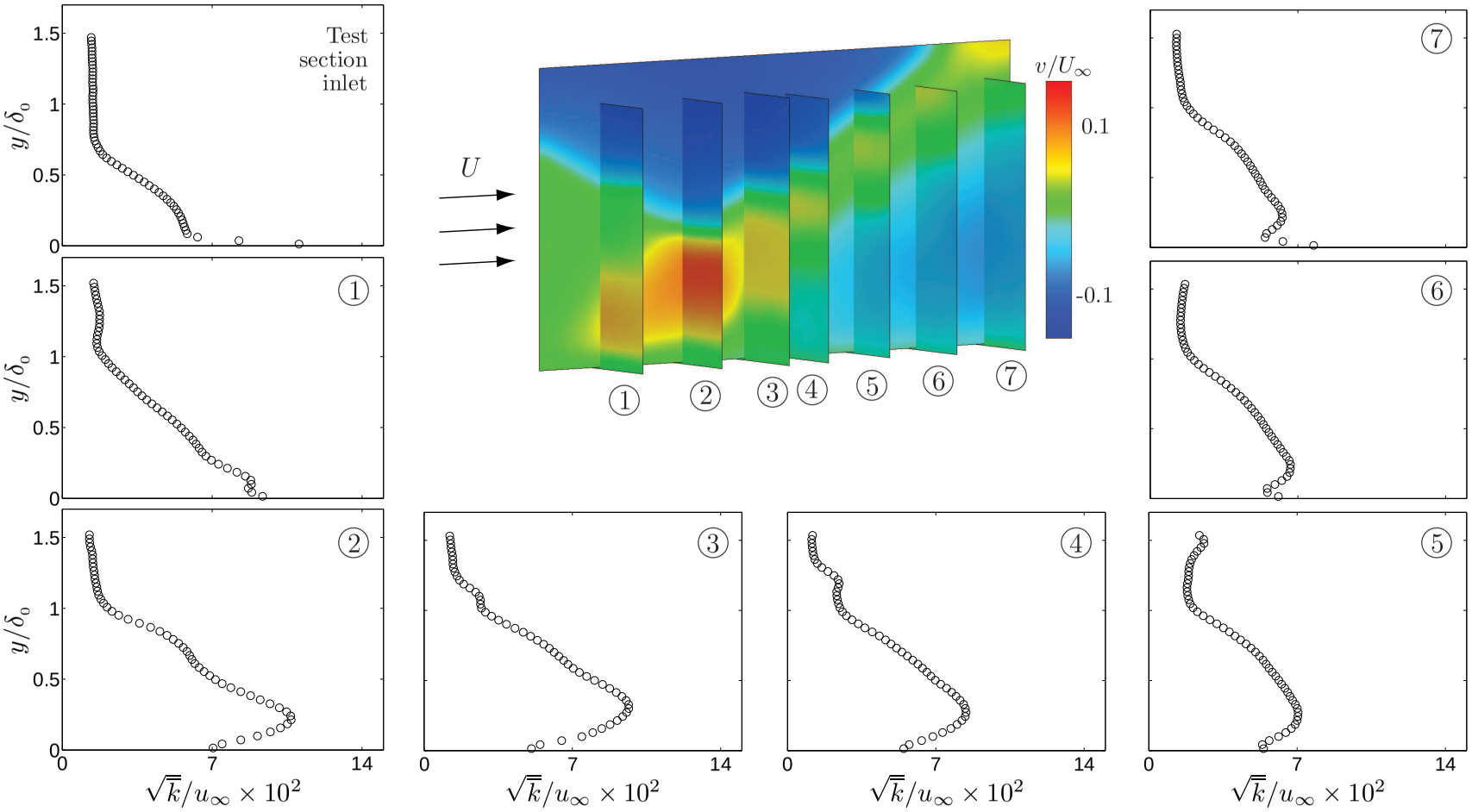

Figure 4.28: Evolution of $\overline{k}$ through the SBLI region for a flow deflection angle of $\theta = 10.0$–deg. The seven sampling locations correspond to 1: $x/\delta_0 = -2.5$, 2: $x/\delta_0 = -1.9$, 3: $x/\delta_0 = -1.5$, 4: $x/\delta_0 = -1.1$, 5: $x/\delta_0 = -0.7$, 6: $x/\delta_0 = -0.2$, and 7: $x/\delta_0 = +0.3$. At top, colors show the $\overline{v}$ field throughout each sampling plane, and also indicate their relative locations.

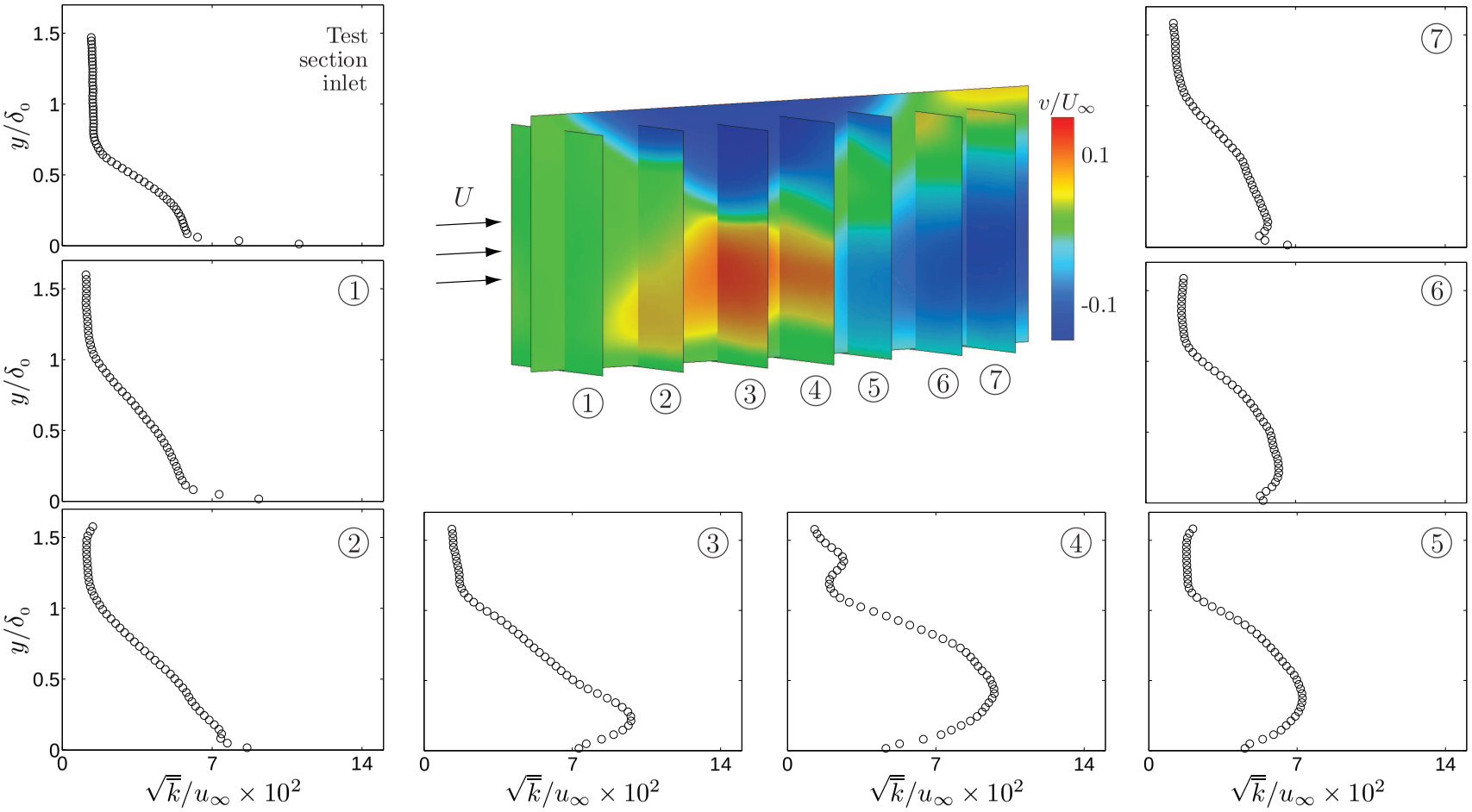

Figure 4.29: Evolution of $\overline{k}$ through the SBLI region for a flow deflection angle of $\theta = 12.0$–deg. The seven sampling locations correspond to 1: $x/\delta_0 = -3.6$, 2: $x/\delta_0 = -2.9$, 3: $x/\delta_0 = -2.3$, 4: $x/\delta_0 = -1.7$, 5: $x/\delta_0 = -1.1$, 6: $x/\delta_0 = -0.5$, and 7: $x/\delta_0 = -0.05$. At top, colors show the $\overline{v}$ field throughout each sampling plane, and also indicate their relative locations.

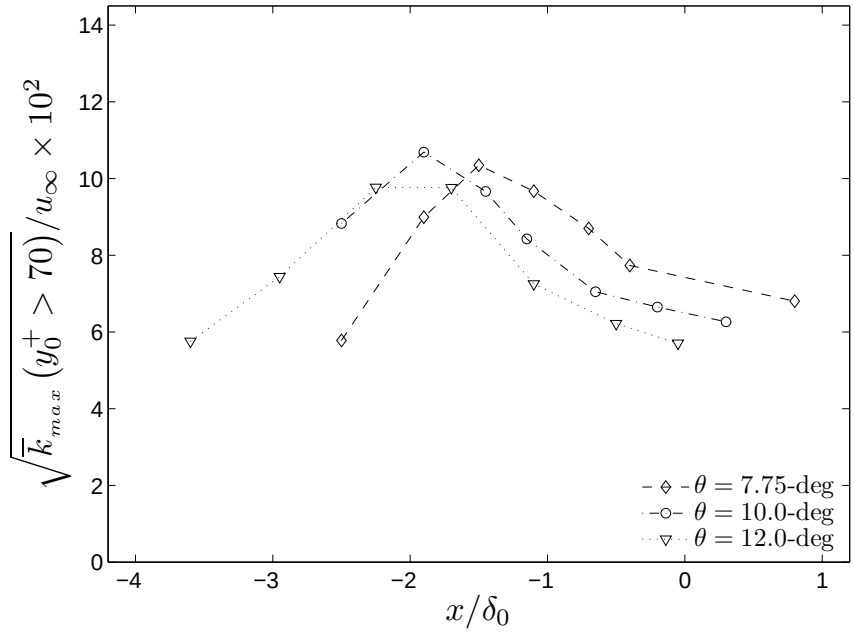

Figure 4.30: Maximum turbulence kinetic energy in the $y_0^+ \gtrsim 70$ region as a function of the streamwise position x/δ_0 for each of the flow deflection angles.

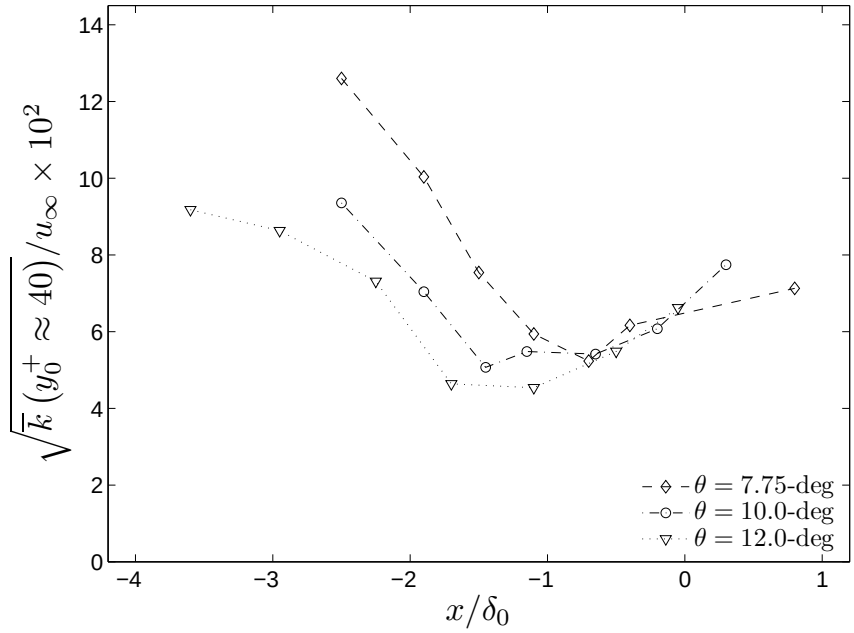

Figure 4.31: Turbulence kinetic energy measured nearest to the wall, corresponding to $y_0^+ \approx 40$, as a function of the streamwise position x/δ_0 for all three shock strengths.

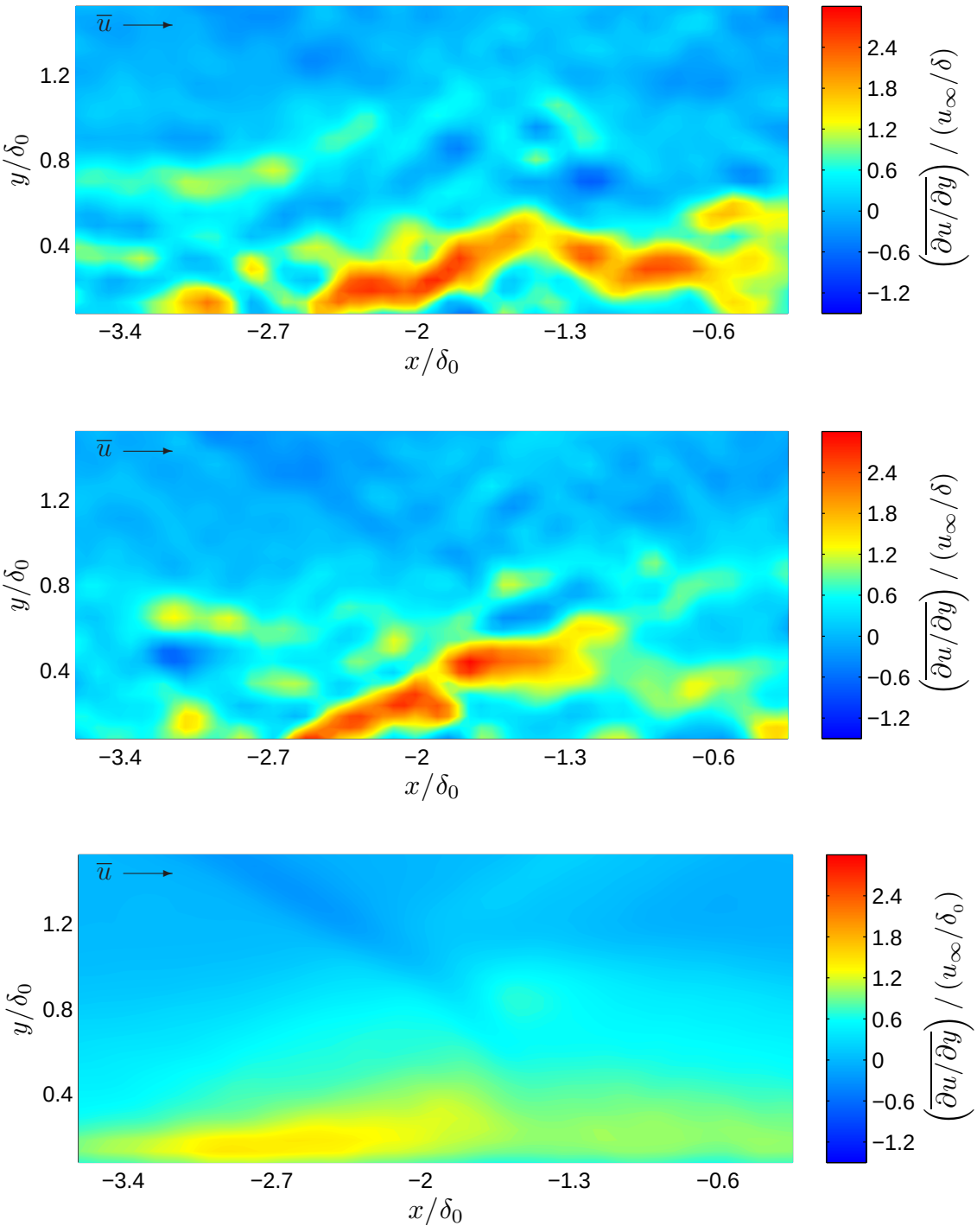

Figure 4.32: Two instantaneous and one mean fields of the gradient $\partial\overline{u}/\partial y$ in planes oriented in the streamwise direction for the $\theta = 12.0$-deg flow deflection angle. The instantaneous fields show the unsteady but extremely high levels of shear that exist between the "exterior" and "interior" regions of the boundary layer through the interaction region.

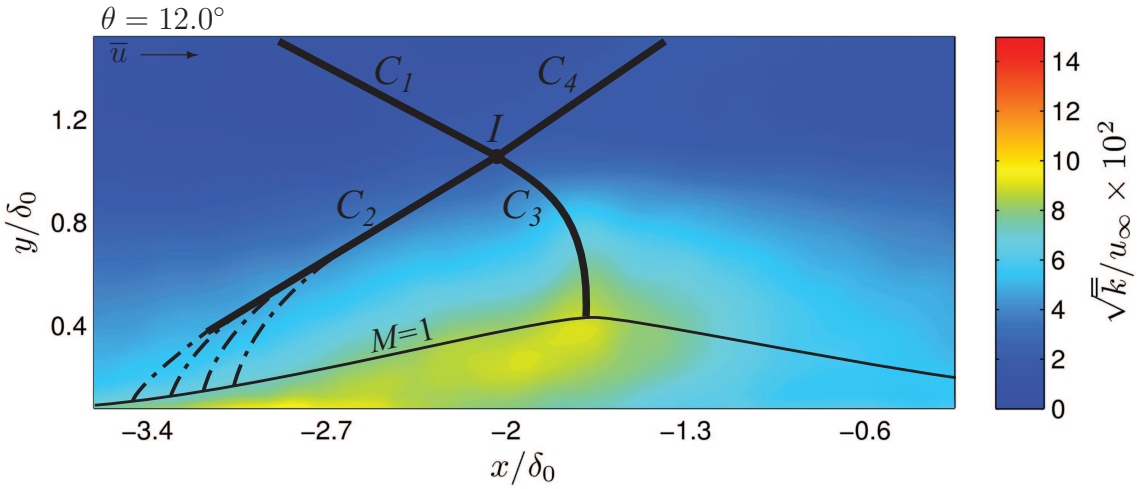

Figure 4.33: Mean turbulence kinetic energy $\overline{k}$ from the $\theta = 12.0$-deg interaction, showing the mean SBLI structure overlayed. The turbulence kinetic energy concentrates below the approximate sonic line and between the C_2 and C_3 shock waves.

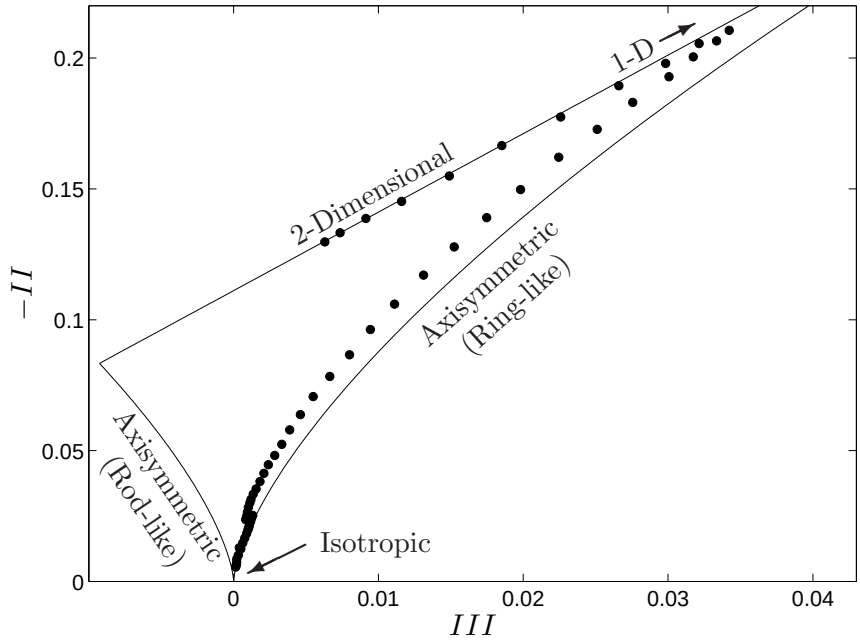

Figure 4.34: Anisotropy of the turbulence in a wall-bounded shear flow from the DNS Kim et al. (1987), shown in invariant space. The bounds of the Lumley triangle are indicated by the solid lines.

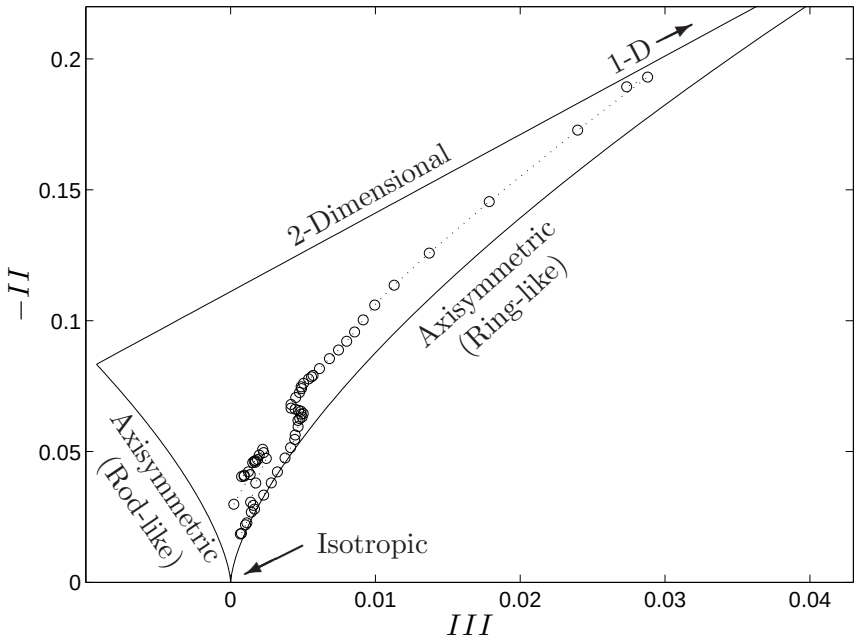

(a)

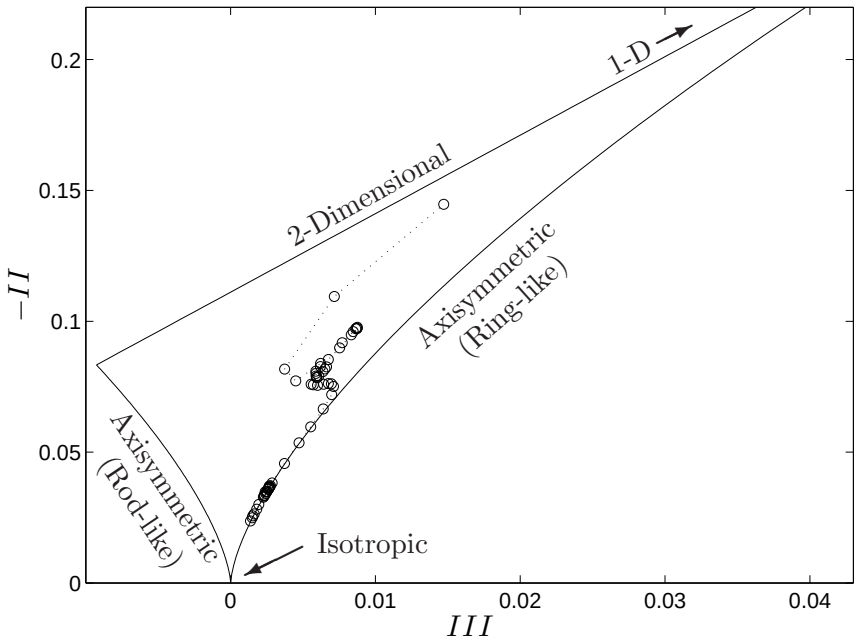

(b)

Figure 4.35: The anisotropy of the turbulence along the wall-normal direction is shown on invariant space *(a)* before the SBLI at $x/\delta_0 = -2.5$ and *(b)* after the SBLI at $x/\delta_0 = +0.8$ for the $\theta = 7.75$–deg flow deflection angle. While the turbulence is near-isotropic throughout the interaction far from the wall, the turbulence state is altered significantly by the interaction closer to the wall.

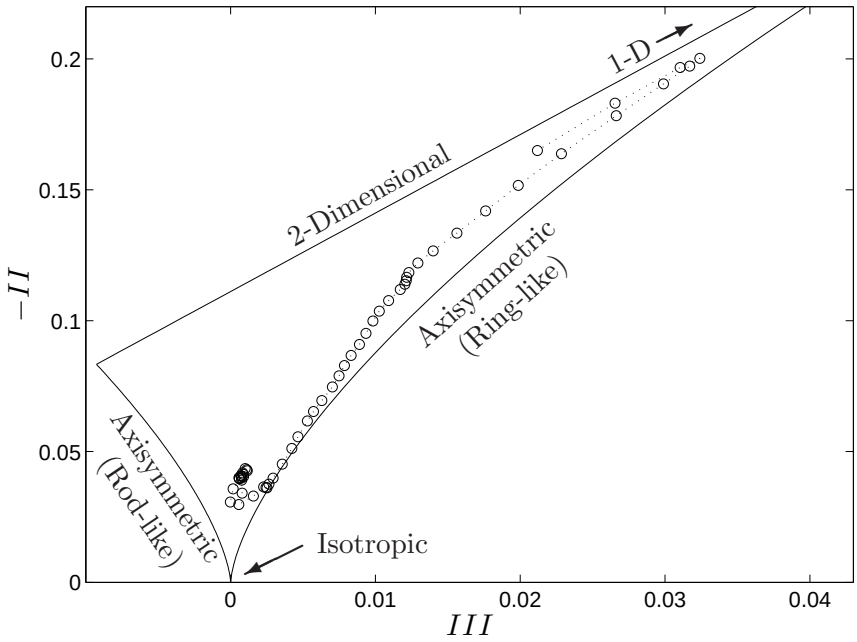

(a)

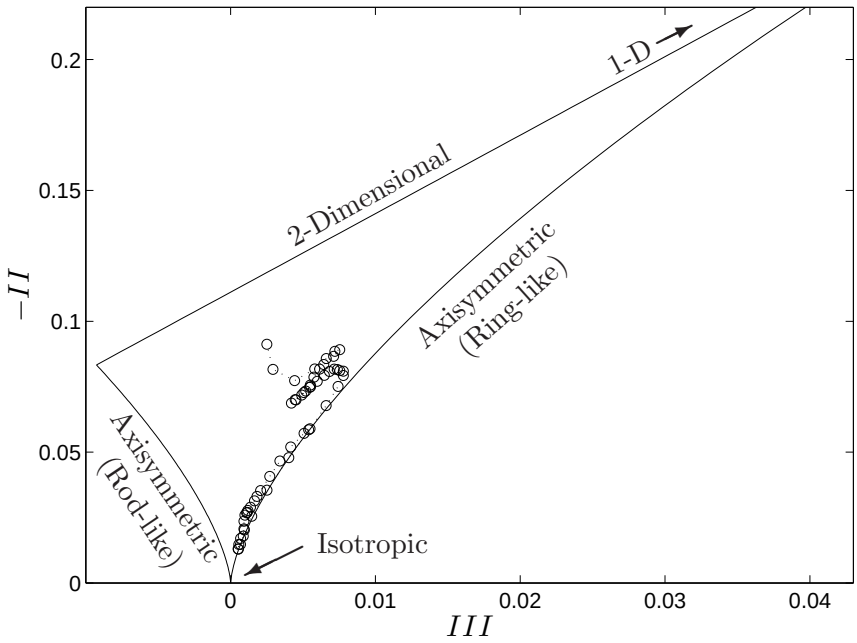

(b)

Figure 4.36: The anisotropy of the turbulence along the wall-normal direction is shown on invariant space *(a)* before the SBLI at $x/\delta_0 = -2.5$ and *(b)* after the SBLI at $x/\delta_0 = -0.2$ for the $\theta = 10.0$–deg flow deflection angle. While the turbulence is near-isotropic throughout the interaction far from the wall, the turbulence state is altered significantly by the interaction closer to the wall.

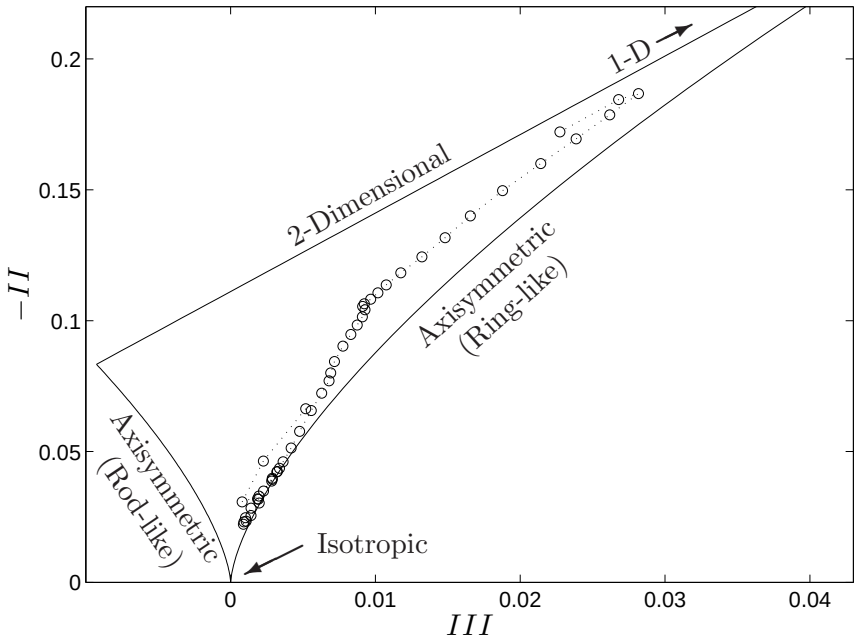

(a)

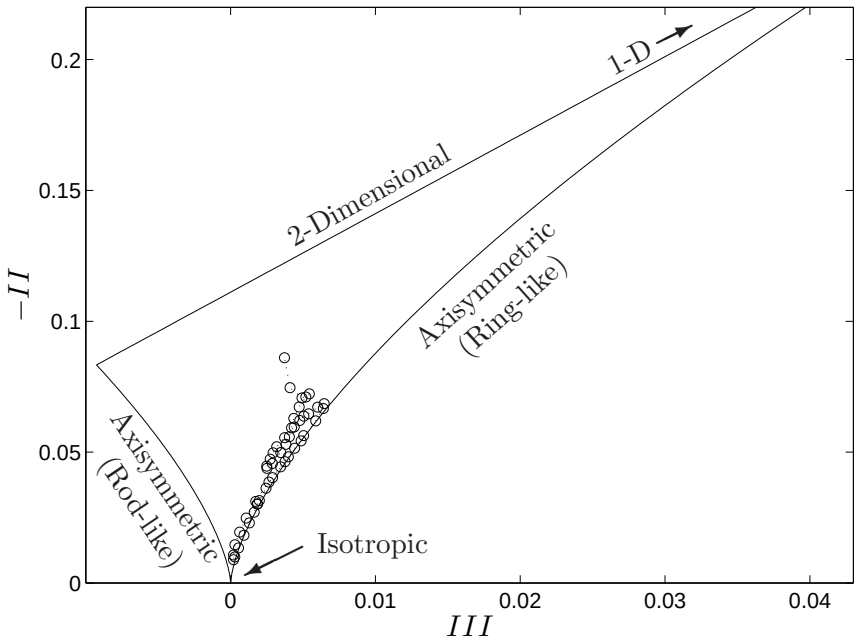

(b)

Figure 4.37: The anisotropy of the turbulence along the wall-normal direction is shown on invariant space *(a)* before the SBLI at $x/\delta_0 = -2.9$ and *(b)* after the SBLI at $x/\delta_0 = -0.5$ for the $\theta = 12.0$–deg flow deflection angle. While the turbulence is near-isotropic throughout the interaction far from the wall, the turbulence state is altered significantly by the interaction closer to the wall.

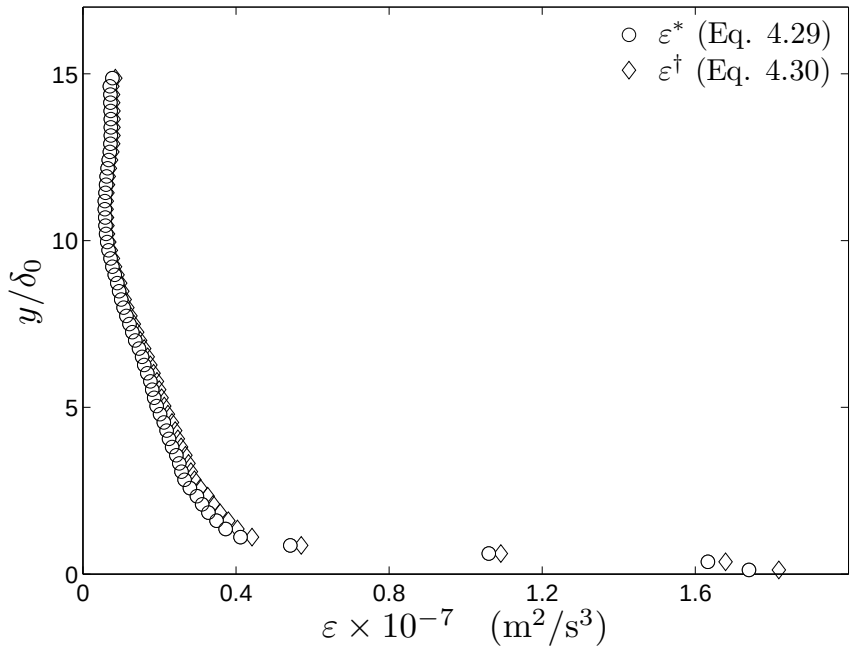

Figure 4.38: Comparison of two estimations for the turbulence kinetic energy dissipation rate, ε^* from Equation 4.29 and $\varepsilon^\dagger$ from Equation 4.30. Results are shown from the $\theta = 7.75$-deg interaction at $x/\delta_0 = -2.5$.

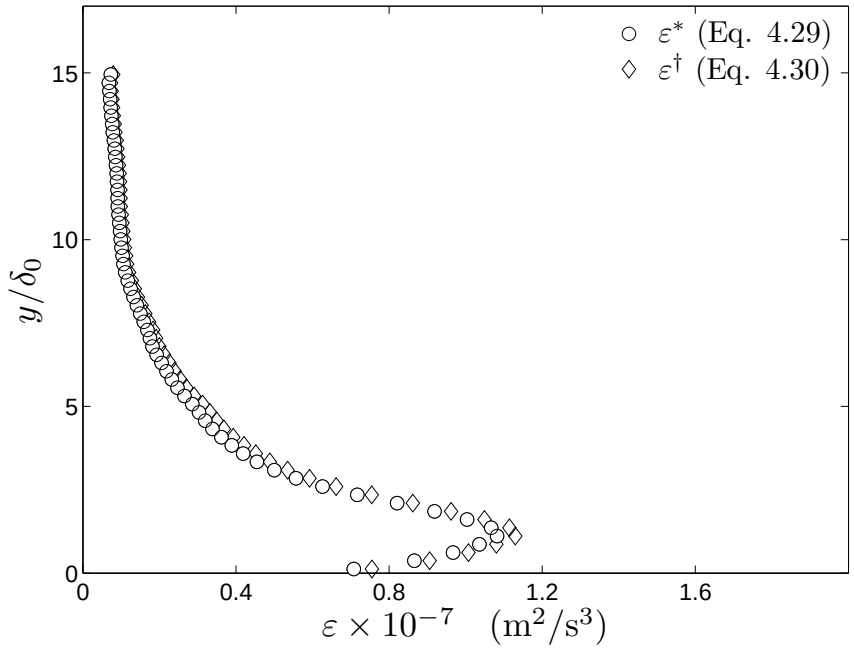

Figure 4.39: Comparison of two estimations for the turbulence kinetic energy dissipation rate, ε^* from Equation 4.29 and $\varepsilon^\dagger$ from Equation 4.30. Results are shown from the $\theta = 7.75$-deg interaction at $x/\delta_0 = -1.5$.

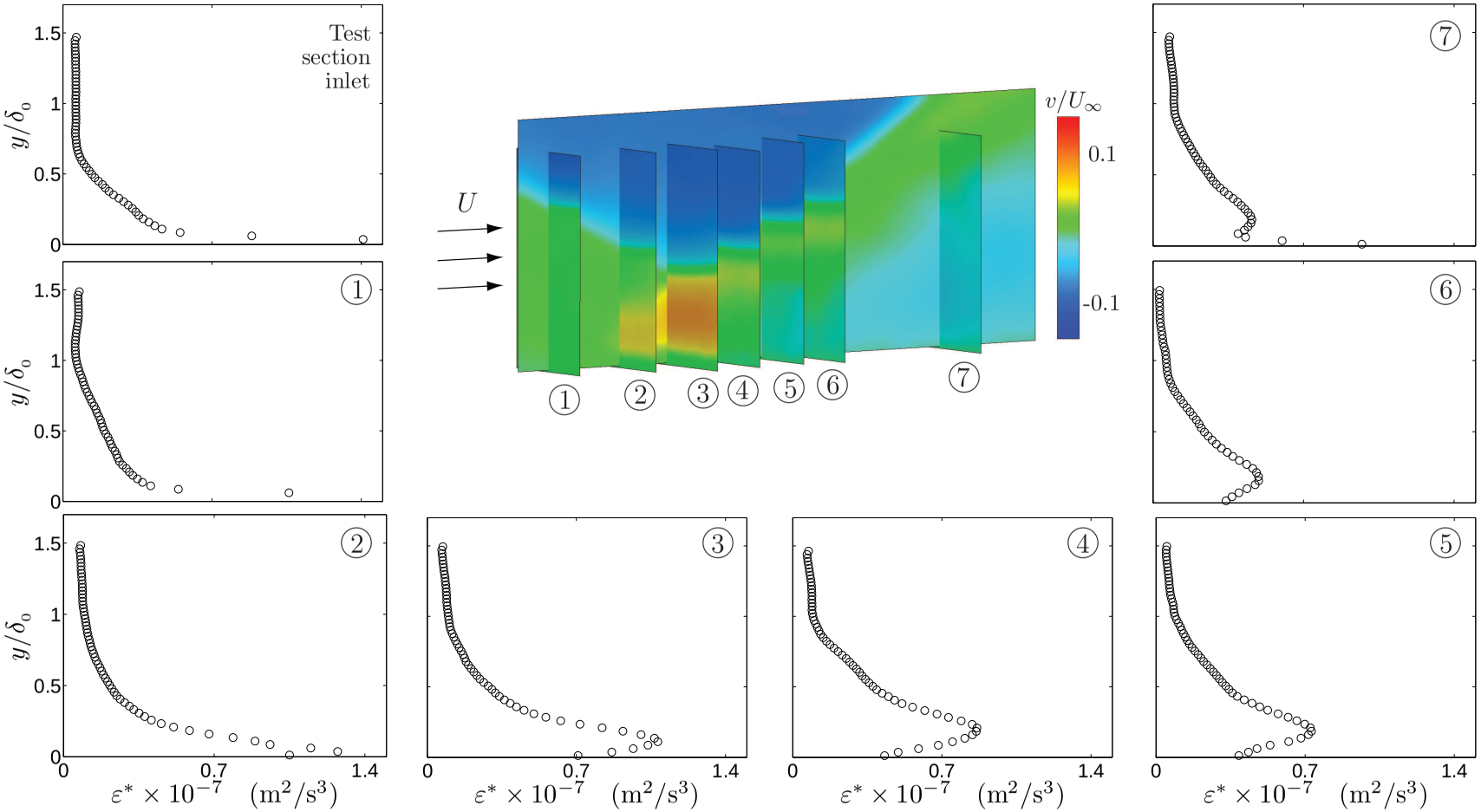

Figure 4.40: Evolution of an approximation to the dissipation rate, ε^* defined by Equation 4.29, through the SBLI region for a flow deflection angle of $\theta = 7.75$–deg. The seven sampling locations correspond to 1: $x/\delta_0 = -2.5$, 2: $x/\delta_0 = -1.9$, 3: $x/\delta_0 = -1.5$, 4: $x/\delta_0 = -1.1$, 5: $x/\delta_0 = -0.7$, 6: $x/\delta_0 = -0.4$, and 7: $x/\delta_0 = +0.8$. At top, colors show the $\overline{v}$ field throughout each sampling plane, and also indicate their relative locations.

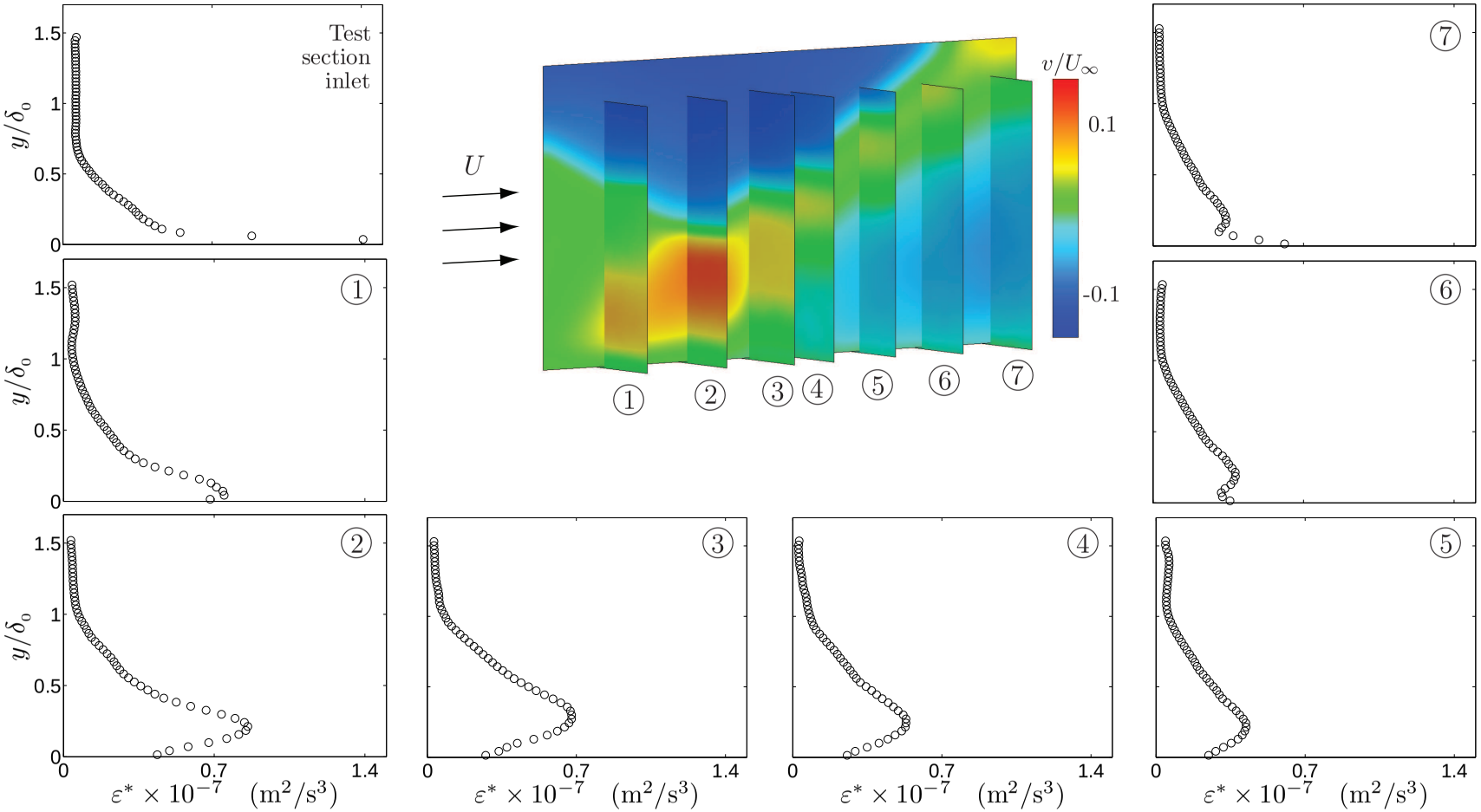

Figure 4.41: Evolution of an approximation to the dissipation rate, ε^* defined by Equation 4.29, through the SBLI region for a flow deflection angle of $\theta = 10.0$–deg. The seven sampling locations correspond to 1: $x/\delta_0 = -2.5$, 2: $x/\delta_0 = -1.9$, 3: $x/\delta_0 = -1.5$, 4: $x/\delta_0 = -1.1$, 5: $x/\delta_0 = -0.7$, 6: $x/\delta_0 = -0.2$, and 7: $x/\delta_0 = +0.3$. At top, colors show the $\overline{v}$ field throughout each sampling plane, and also indicate their relative locations.

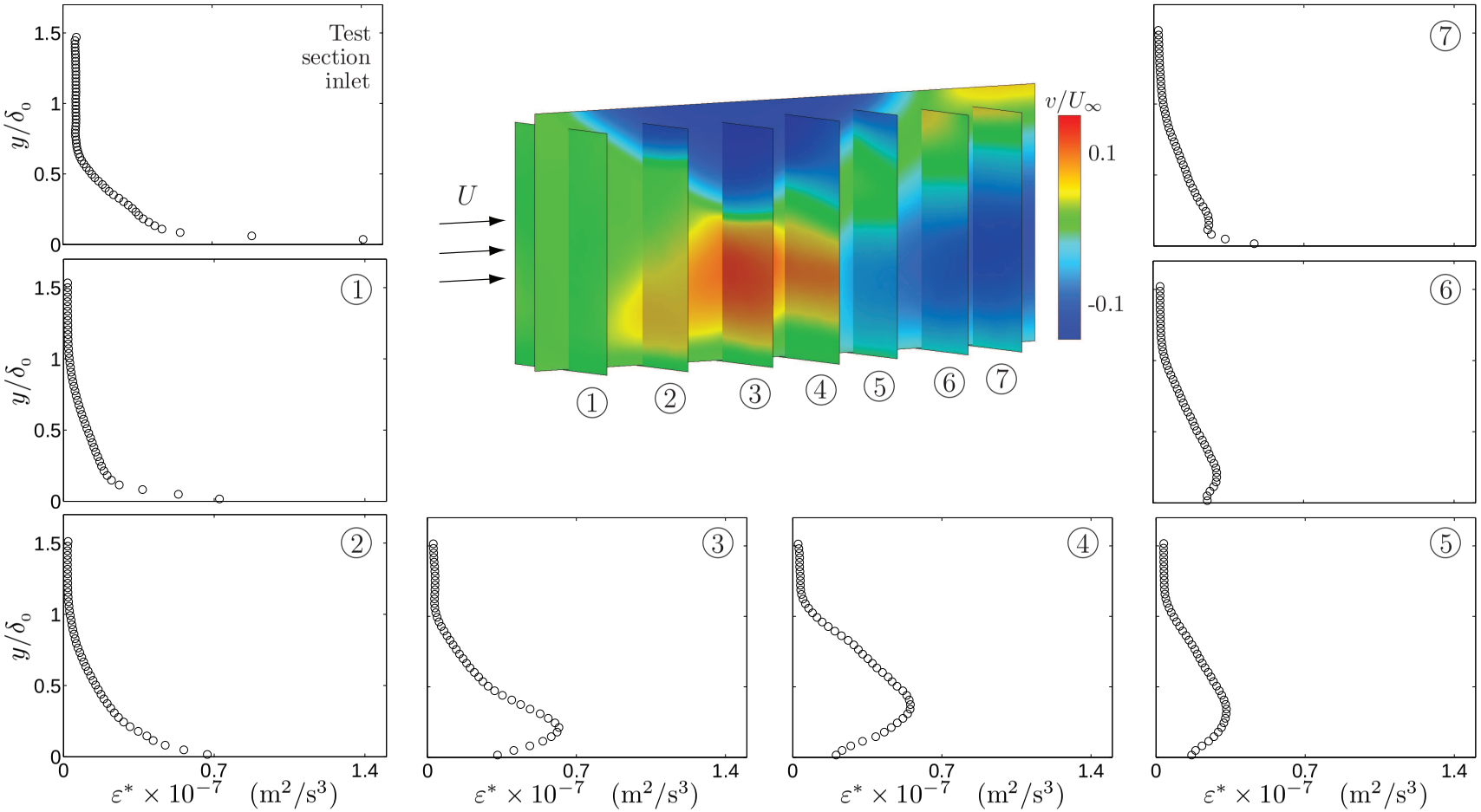

Figure 4.42: Evolution of an approximation to the dissipation rate, ε^* defined by Equation 4.29, through the SBLI region for a flow deflection angle of $\theta = 12.0$–deg. The seven sampling locations correspond to 1: $x/\delta_0 = -3.6$, 2: $x/\delta_0 = -2.9$, 3: $x/\delta_0 = -2.3$, 4: $x/\delta_0 = -1.7$, 5: $x/\delta_0 = -1.1$, 6: $x/\delta_0 = -0.5$, and 7: $x/\delta_0 = -0.05$. At top, colors show the $\overline{v}$ field throughout each sampling plane, and also indicate their relative locations.

CHAPTER V

Passive Boundary Layer Control Using a "Standard" Micro-Ramp

In most applications the thickened boundary layer that results from shock wave–boundary layer interactions (SBLI) has adverse or prohibitive effects. On transonic airfoils the normal shock formed above the wing can lead to boundary layer separation, and in supersonic inlets, the effective inlet area is substantially reduced by the thickened boundary layers. For the case of inlets the boundary layer often undergoes several oblique shock wave interactions, and in the absence of boundary layer control it thickens with each. Commonly employed techniques involve bleeding the boundary layer at or near the interaction region, which results in a direct and substantial efficiency loss. Passive control techniques aim to reduce or eliminate boundary layer thickening without suction techniques, thus enabling bleedless or reduced-bleed inlets with ultimately improved inlet efficiency.

Techniques for passive control of boundary layers began in the 1950's with a focus on transonic airfoils. Much of the early attention was therefore paid to the interaction between boundary layers and normal shock waves. With increasing demand for more efficient supersonic inlets, attention is now being increasingly directed toward interactions with oblique shock waves. Several recent experimental and computa-

tional efforts, including those of Anderson et al. (2006), Ford and Babinsky (2007), and Lee et al. (2007) have investigated passive control of oblique SBLI using "standard" micro-ramp arrays, a term introduced by Anderson et al. (2006) and used throughout the present work. The prior experimental works, however, have been limited to one dimensional probe measurements and surface visualizations, leaving full velocity field measurements unexplored. The standard ramp arrays are similar in concept to those originally proposed by Wheeler (1984), and are designed to produce pairs of counter-rotating vorticies whose axes are oriented in the streamwise direction. The vortex pair preferentially entrains high-velocity air from the free stream and convectively transports it deep into the boundary layer. In theory, the resulting pre-conditioned boundary layer is less susceptible to the adverse pressure gradient located at the shock foot, ultimately reducing thickening or separation.

This chapter provides a detailed quantification of the effects of the standard micro-ramp array on the interactions produced by the $\theta = 7.75$-deg, 10.0-deg, and 12.0-deg flow deflection angles. The standard micro-ramp design is first discussed. Experimental results of SPIV velocity data are then presented from streamwise and spanwise planes similar to those in Chapter IV. The vorticity produced by the standard ramps is quantified, as well as the other pertinent mean and turbulence statistics. Ultimately, the net benefit of the standard micro-ramp array is quantified by means of modified integral boundary layer relations.

5.1 Design for "Standard" Micro-Ramp

The standard micro-ramp design is shown schematically in Fig. 5.1*a*, and consists of a triangular ramp whose downstream faces form angled dumps. The ramp-like design is considerably more structurally robust than otherwise similar micro-vanes, which have also been investigated for similar applications. The flow is initially deflected upward by the ramp before it passes over the angled dumps, producing a counter-rotating vortex pair whose size and strength depends on the specific dimensions of the ramps. Figure 5.1*b* shows these counter-rotating vorticies as viewed from a downstream location, looking in the upstream direction at the rearward faces of the micro-ramp. The vortex pair produces an upwash region directly behind the ramp, along with two downwash regions on either side. The micro-ramps are installed in the test section after being formed on the interchangeable dovetail inserts described in Chapter II and shown in Fig. 2.8*a*.

The defining dimensions of the standard micro-ramp geometry are shown in Fig. 5.2, and include the feature height, h, the side length, c, the half-angle of the triangle, A_p, and the spacing between each micro-ramp in the array, s. The ramp array is located at a distance x_R upstream of the inviscid shock impingement location. The magnitude of the streamwise vorticity $|\omega_x|$ produced by the ramps depends heavily on the height, h, and half angle, A_p, with the net effect on the interaction region becoming greater with increasing vorticity magnitude. The array of ramps also produces drag through the resulting velocity deficit wake and through any Mach waves or shock waves generated by the flow deflection. The associated losses therefore scale with the total frontal area of the array and with the incident angle of the ramp. Anderson et al. (2006) performed a parametric study using RANS simulations in

order to gain insight into this complex design space. According to the recommendations made therein, the standard micro-ramps are defined such that $c/h = 7.2$, $s/h = 7.5$, $A_p = 24$-deg, and $h/\delta_0 = 0.20$. The location of the ramp array in relation to the inviscid shock impingement points, x_R/δ_0, in addition to the locations of the spanwise sampling planes, are given in Table 5.1 for all three shock strengths. The present study uses an array of three standard micro-ramps, shown Fig. 2.8*a*. In the results that follow, all imaging is centered around the tunnel centerline and therefore directly in the wake of the central micro-ramp.

5.2 Generation and evolution of vorticity

The primary objective of the standard micro-ramp design is to produce intense streamwise vortices deep in the boundary layer for effective convective transport of high velocity gas into the lower region of the boundary layer without causing significant effects in the free stream. The streamwise vorticity ω_x can be directly computed from the velocity data in the same way as in Eq. 4.6, except now using the data contained in the spanwise planes. Figure 5.3 shows a visualization of the mean vorticity in a spanwise plane located immediately upstream of the interaction region. The vorticity magnitude is indicated by the color map, and the mean in-plane velocity components ($\overline{v}$, $\overline{w}$) are overlayed as vectors. Additionally, a scale representation of the standard micro-ramp that produces the vorticity is superimposed on the image. In this case the micro-ramp is located at a distance of $6.5\delta_0$ upstream of the spanwise plane.

Figures 5.4–5.6 show visualizations of the vorticity in each of six spanwise planes,

which are located throughout the interaction regions produced by the three shock strengths. Overlayed onto the six spanwise visualizations are the mean in-plane velocity field vectors $(\overline{v}, \overline{w})$. The vortex pair is clearly evident in all planes upstream of the interaction, corresponding roughly to Planes 1–4 in Figs. 5.4–5.6. Downstream of the interaction, corresponding roughly to Planes 5–6, the vorticity decreases considerably with respect to the upstream magnitudes. Furthermore, the reduction in vorticity increases as the shock strength increases. This is due, at least in part, to the pinching effect that results from the three dimensionality of the interaction, discussed previously in § 4.2.3. The counter-rotating vortices are forced together by the three dimensional effects of the interaction, and as they are their respective vorticity of opposite sense is mutually negated. This pinching effect becomes stronger with increasing shock strength, and as a consequence the effects of the vortex pair are progressively reduced.

The vorticity produced by the ramp is shown quantitatively in Figs. 5.7–5.9, which show profiles from each spanwise plane for all shock strengths. Each plot contains three profiles: one from the centerline at $z/\delta_0 = 0$, and two located at equal but opposite distances away from the centerline at $z/\delta_0 = \pm 0.20$, chosen to correspond with the incoming vortex centers.

The evolution of the vorticity is additionally quantified in two ways. First, the total circulation Γ contained in each constituent streamwise vortex is computed by spatially integrating the vorticity over each half-plane. The circulation of the two constituent vortices is averaged at each downstream location and shown as a function of x/δ_0 in Fig. 5.10. The measured circulation begins at a consistent value of $\Gamma/(u_{\tau_0} h) \approx 2$ upstream of the shock interaction, where h is the ramp height and u_{τ_0} the pre-interaction friction velocity. This value is maintained in the case of

the weakest shock where the three-dimensional effects are small and the vortex pair remains relatively separated. For increasing shock strength, the three-dimensional pinching effect described in §4.2.3 become substantial even in the near-centerline region. In the $\theta = 10.0$-deg case the total vorticity is almost exactly negated leaving each half-plane with approximately zero net streamwise circulation downstream of the interaction. When the shock strength is increased still further, not only are the ramp-generated vortices negated, but the pinching effect itself creates measurable vorticity in the near-wall region downstream of the shock foot. This is the cause for the negative circulation measurements in the $\theta = 12.0$-deg curve of Fig. 5.10.

Figure 5.11 shows the centroids of the streamwise vortices at downstream distances through the three interactions, including all six spanwise locations through the $\theta = 7.75$-deg interaction, Positions 1–3 (ending at $x/\delta_0 = -1.5$) for the $\theta = 10.0$-deg interaction, and Positions 1–4 (ending at $x/\delta_0 = -1.7$) for the $\theta = 12.0$-deg interaction. The vortices enter the interaction with their centroids at $y/\delta_0 \approx 0.37$, and they are consistently separated by a distance of $\Delta z_{\omega_c} \approx 0.4\delta_0$. These locations will be compared to those produced by the "inverse" micro-ramp design in Chapter VI.

5.3 Effect on mean velocity fields

Figures 5.12–5.14 visualize the streamwise velocity component fields $\overline{u}(y, z)$ with color maps in each of the spanwise sampling planes, again showing the mean in-plane velocity components $(\overline{v}, \overline{w})$ with overlayed vectors. Recall that the upwash produced by the streamwise vortex pair is located along the centerline, and its effect

is obvious. In this location, the boundary layer is considerably thicker than that in the downwash regions of the vortex pair. Figures 5.15–5.17 compare profiles from the downwash regions, corresponding to $z/\delta_0 = \pm 0.3$, to profiles from the upwash region at $z = 0$. As is made obvious, the boundary layer character now has considerable spanwise variation. The effects of this variation are quantified through modified integral relations discussed in §5.3.1.

5.3.1 Mean boundary layer integral relations

To further investigate the considerable spanwise variation produced by the micro-ramps, a quantitative account of the boundary layer thickness measured as a function of the spanwise dimension is desirable. The vorticity-based description of the boundary layer height discussed in Chapter IV is unavailable here since it is derived from the spanwise vorticity component ω_z, and thus is available only in the streamwise imaging plane located along the centerline of the tunnel. Note, however, that although the free stream velocity and density values vary in both the wall-normal and streamwise directions, the nominal mean values for a given shock strength are consistent at fixed streamwise locations regardless of the method of boundary layer control. In this section, therefore, the incompressible definitions of the displacement and momentum thicknesses, and by extension the shape factor, are introduced not as a rigorous quantification of the boundary layer thickness but instead to provide a consistent means for comparison between the controlled boundary layers discussed here and the uncontrolled boundary layer of Chapter IV.

The displacement thickness δ^* is defined in the traditional way as

$$\delta^* \equiv \int_0^\infty \left(1 - \frac{\overline{u}}{u_\infty}\right) dy, \tag{5.1}$$

and the momentum thickness is expressed as

$$\theta \equiv \int_0^\infty \frac{\overline{u}}{u_\infty}\left(1 - \frac{\overline{u}}{u_\infty}\right) dy. \tag{5.2}$$

The shape factor follows simply as $H \equiv \delta^*/\theta$. Recall that for typical boundary layers, where the velocity is everywhere less than the free stream value, the shape factor is always greater than one. For the infinite favorable pressure gradient limit, where the velocity is equal to the free stream value everywhere, the shape factor has a value of one, while the effect of an adverse pressure gradient is to raise the value of the shape factor. Therefore, reduced shape factors are indicative of boundary layers less susceptible to separation.

Because the free stream changes continuously in the present case, the pre-shock free stream velocity, u_∞, is used in these definitions regardless of the sampling location. As such, the integral taken to the true limit of $y = \infty$ does not converge for any location within or downstream of the interaction. In the present work, the integrations for δ^* and θ are computed in a consistent manner to fixed wall-normal heights. The result is a modified shape factor H^*, defined using the fixed pre-shock free stream velocity and fixed integration limits. Again, while these modifications render the numerical value of the quantities essentially meaningless in the post-shock locations, it makes for consistent and relevant comparison at like downstream locations and for like impinging shock strengths.

The modified shape factor H^* is measured in pre- and post-shock spanwise planes, and compared to those at equal or similar downstream locations from the uncontrolled interactions of Chapter IV. Where one-to-one comparisons are not available,

measurements from two surrounding locations in the uncontrolled boundary layer are used for comparison with the controlled boundary layer.

Figure 5.18 shows the modified shape factor H^* as a function of the spanwise dimension in a streamwise location upstream of the $\theta = 7.75$-deg interaction. The shape factor profile for the controlled boundary layer is qualitatively correct; the momentum thickness is greater along the centerline where low momentum fluid is convected toward the free stream, and lower away from the centerline where high momentum fluid is convected deeper into the boundary layer. Comparing the controlled and uncontrolled boundary layers, the standard micro-ramp array clearly acts to reduce the shape factor and delay the influence of the impinging shock. Fig. 5.19 similarly shows H^* in streamwise locations downstream of the $\theta = 7.75$-deg interaction. Although less obvious in this case, one might make favorable conclusions as to the utility of the standard micro-ramp array.

Figures 5.20–5.23 show pre- and post-shock shape factors for the $\theta = 10.0$-deg and $\theta = 12.0$-deg interactions. The standard micro-ramps consistently show decreased shape factors in the upstream boundary layer, which is the desired effect. Downstream of the interaction, however, there is no apparent benefit provided by the standard micro-ramp array for these stronger shock strengths. These observations are supported by considering the net effect of the ramps across the span, which follows in § 5.3.2.

5.3.2 Net effect on displacement thickness

In applications such as supersonic inlets, the thickened boundary layer that results from the SBLI reduces the effective inlet area and in turn affects the flow rate of air

to the engine. The displacement thickness is representative of this effect. To evaluate the net utility of the standard micro-ramps across the entire span, the displacement thickness, modified using finite integration limits and a constant free stream velocity as in § 5.3.1, is averaged across the spanwise field-of-view so that

$$\langle \delta^* \rangle \equiv \frac{1}{\Delta z} \int \delta^* dz = \frac{1}{\Delta z} \int_{\Delta z} \int_{\Delta y} \left(1 - \frac{\overline{u}}{u_\infty} \right) dy dz. \tag{5.3}$$

Figures 5.24–5.26 show the averaged displacement thickness $\langle \delta^* \rangle$ through the three shock interactions as a function of the downstream distance x/δ_0 for both the uncontrolled interactions and those controlled by the standard micro-ramp array. Note that as a result of consistently using the pre-shock free stream velocity u_∞, and because of the rise in density through the shock, the post-shock inviscid theoretical minimum values of this quantity are 1.8, 2.4, and 3.1 for the 7.75-deg, 10.0-deg, and 12.0-deg deflections, respectively. Looking at the farthest upstream and downstream points, the comparisons are consistent with the findings in § 5.3.1. First, the effects of the impinging shock are shifted downstream by the micro-ramps, as can be surmised from investigation of Figs. 5.18 and 5.20, with the effect being progressively diminished with rising shock strength. Additionally, downstream of the interaction the effect of the ramps becomes marginal, if not detrimental, as the downstream flow rate deficit is comparable to or larger than that for the uncontrolled boundary layer.

Of central importance for inlet design, however, is not only the pre- and post-interaction boundary layer thicknesses, but also the maximum amount of thickening that occurs through the interaction region. In this regard the standard micro-ramp array provides utility, as the peak net displacement thickness is reduced by the ramps in all three interactions. This is summarized in Table 5.2, which shows the peak values of $\langle \delta^* \rangle$ through the interaction for each shock strength with and without the

standard micro-ramp control. The percent benefit provided by the standard micro-ramp array is also given, showing substantial gains of up to 22% in the weakest shock case.

5.3.3 Effect on mean wall-normal velocity

Figure 5.27 shows visualizations of the wall-normal velocity component through the $\theta = 10.0$-deg interaction region, which is representative of the other two shock strengths. The three-dimensional structure created by the micro-ramp array again is apparent, particularly in the upstream locations. The effect of the three-dimensionality on the shock wave is notable. The incident wave impinges on the boundary layer as a nominally two dimensional structure but reflects with three-dimensional curvature.

Profiles of the wall normal velocity component are given in Figs. 5.28–5.30. As in Figs. 5.15–5.17, three profiles are given; one along the centerline in the direct wake of the micro-ramp, and two in off-centerline locations at $z/\delta_0 = \pm 0.3$. Thus the centerline profile captures the direct upwash region of the streamwise vortex pair, and the off-centerline locations capture the direct downwash regions. As from the profiles of the in-plane vorticity ω_x, the difference between on- and off-centerline locations provide a quantification of the vortex-pair strength. In Chapter VI, this and other characteristics will be compared to a vortex pair produced by the "inverse" micro-ramp design.

Recall from §4.2 and Fig. 1.4 the positive wall-normal velocity component induced by the reflected shock, C_2, upstream of the shock foot. Comparing the profiles from Figs. 5.28–5.30 to those from Figs. 4.10–4.12, the wall-normal velocity magnitudes in these regions are considerably reduced by the presence of the micro-ramps, with

the reduction being more pronounced for weaker shock strengths. This implies a reduction in the reflected C_2 shock strength, which is tied directly to the previous observation that the maximum boundary layer thickness through the interaction is reduced by the ramps. Additionally, it is an indication of potentially reduced wave drag associated with the interaction since the entropy production through a shock wave decreases with decreasing shock strength.

5.4 Fluctuation and gradient quantifications

The turbulence kinetic energy field in the streamwise plane located along the tunnel centerline $\overline{k}(x, y)$ is shown in Fig. 5.31 for the $\theta = 10.0$-deg interaction, with Fig. 5.31a showing the uncontrolled interaction and Fig. 5.31b showing the interaction controlled by standard micro-ramps. In both cases the largest fluctuations are located in the upstream portion of the interaction. Here, as discussed in §,4.4.1, an intensely unsteady free shear layer exists between the high velocity incoming stream and the low velocity region at the shock foot. The two $\overline{k}$ fields have remarkably similar structure despite the latter field being located directly in the upwash region of the streamwise vortex pair.

Spanwise visualizations, however, reveal a strikingly different three-dimensional nature in the fluctuation intensity fields of the controlled interaction. These are shown in Fig. 5.32 via the normal RMS velocity fluctuations $\sqrt{\overline{u'^2}}$, which overwhelmingly dominate the total turbulence kinetic energy in the boundary layer. Again, the largest fluctuations are seen in the upstream portion of the interaction where the unsteady free shear layer exists. In a statistical sense, the location of this oscillating free shear layer is implied by the turbulence kinetic energy field, with large kinetic

energy representing a higher probability of the shear layer residing in that location. The horseshoe-like pattern observed in Fig. 5.32, seen particularly well in Locations 3 and 4, thus maps the location of the free shear layer across the span of the interaction. With this perspective, it is not surprising that the shear layer is deflected farther from the wall in the vortex-induced upwash region and maintained closer to the wall in the vortex-induced downwash regions.

Profiles of the turbulence kinetic energy are shown in Figs. 5.33–5.35 for all three shock strengths. The displaced unsteady shear layer, together with the fluctuations associated with streamwise vortex pair themselves, produce the second local maximum in the $\overline{k}$ profiles along the tunnel centerline. This feature, which is particularly pronounced in the upstream region of the interaction, is an artifact purely of the ramps as it is not seen in the uncontrolled interactions.

The presence of the micro-ramp array also produces significant contributions from the Reynolds shear stress component $\overline{u'w'}$, shown in Fig. 5.36, which is essentially uniformly zero in the absence of the micro-ramp. The dominant components of the anisotropy tensor, $\overline{u'^2}$, $\overline{u'v'}$ and $\overline{u'w'}$ are shown in Figs. 5.37–5.39, respectively, again showing results from the intermediate $\theta = 10.0$-deg deflection angle. These further illuminate the highly three-dimensional structure of the controlled interaction.

The wall normal strain rate $\overline{S}_{yy}$ is shown in Fig. 5.40, with profiles being given in Figs. 5.41–5.43. As before, the wall-normal strain rate clearly visualizes the shock location. The shock approaches the boundary layer as a thin structure whose finite thickness in the mean field visualizations is due to the combination of particle lag and the relatively small turbulence-generated shock jitter. At its point nearest to the wall, shown approximately in Location 3 of Fig. 5.40, the mean visualization of the shock thickens considerably before reflecting and moving away from the wall.

This dramatic thickening, which occurs at the intersection point I in Fig. 1.4, is a clear indication of the considerable unsteadiness of the entire interaction region. The mean visualizations of the reflected shock in Locations 4–6 are also considerably thicker than those for the incoming shock in Locations 1–2, indicating shock jitter arising from the oscillating anchor point of the reflected shock.

Finally, the isotropic approximation to the turbulence kinetic energy dissipation rate, ε^*, is visualized in Fig. 5.44 for the $\theta = 10.0$-deg deflection, with profile plots for all three shock strengths shown in Figs. 5.45–5.47.

Deflection angle θ (deg)	x_R/δ_0	x_1/δ_0	x_2/δ_0	x_3/δ_0	x_4/δ_0	x_5/δ_0	x_6/δ_0
7.75	-8.50	-2.0	-1.55	-1.2	-0.7	-0.2	+0.3
10.0	-9.42	-2.5	-1.9	-1.5	-1.1	-0.6	0.0
12.0	-9.76	-3.6	-2.9	-2.3	-1.7	-1.1	-0.4

Table 5.1: Locations of the micro-ramps x_R/δ_0 and downstream distances x_i/δ_0 of the spanwise sampling planes with respect to the inviscid shock-impingement location for each shock strength investigated.

	$\theta = 7.75$-deg	$\theta = 10.0$-deg	$\theta = 12.0$-deg
Blank	2.8	3.9	4.3
S. micro-ramp	2.2	3.4	4.1
Net reduction	**22%**	**12%**	**4%**

Table 5.2: The peak average displacement thickness $\langle \delta^* \rangle$ for each shock strength, showing both the uncontrolled boundary layer and the boundary layer controlled by the standard micro-ramp array. The reduction of the maximum displacement thickness provided by the micro-ramps is also shown.

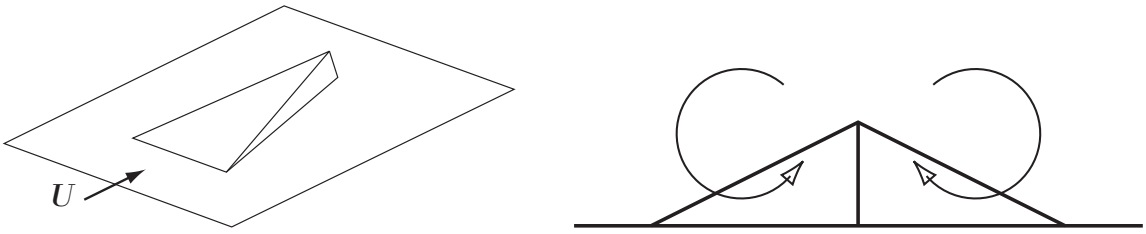

Figure 5.1: Schematics of the standard micro-ramp design are shown from *(a)* a projection view and *(b)* looking upstream at the rearward faces of the ramp. The induced streamwise vortices are also shown.

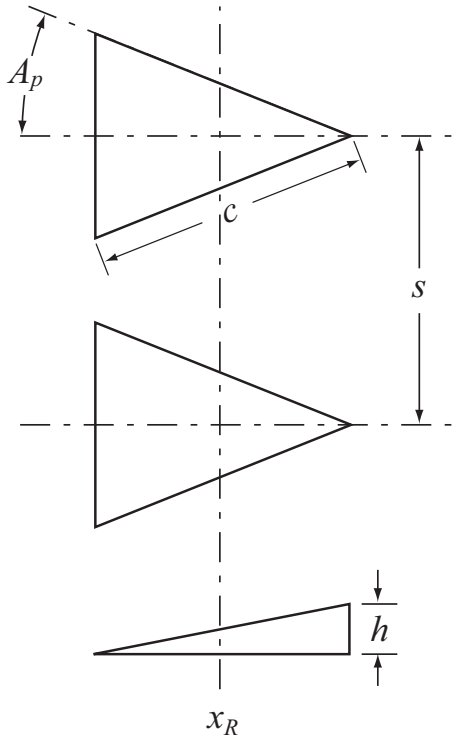

Figure 5.2: The defining dimensions of the standard micro-ramp are shown, including the ramp half-angle A_p, side-length c, height h, and ramp spacing s.

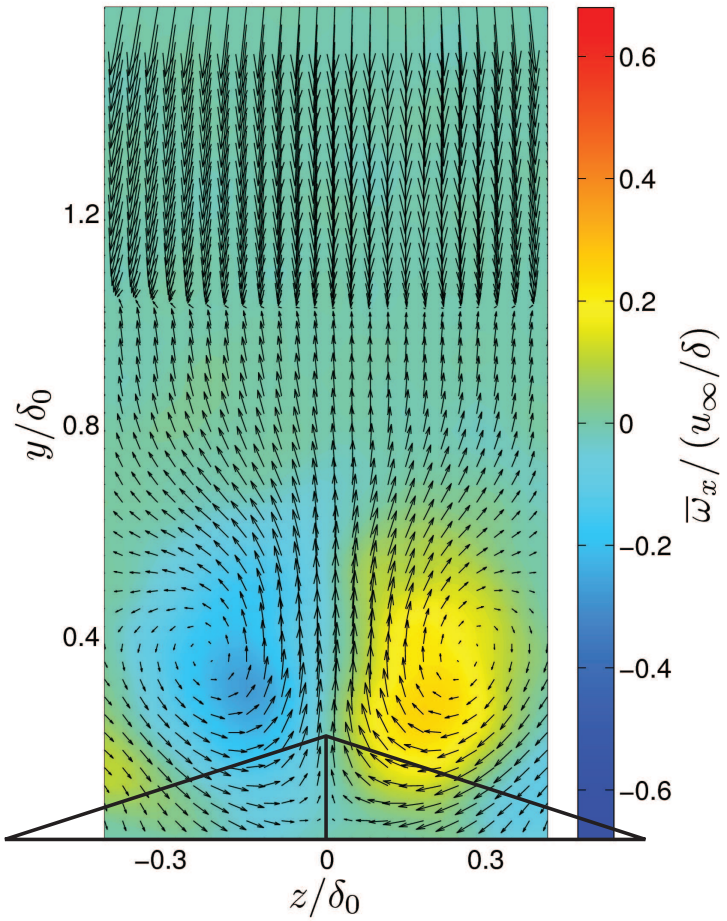

Figure 5.3: Mean vorticity field $\overline{\omega}_x$, in this case located upstream of the interaction at $x/\delta_0 = -2.5$ and with the $\theta = 7.75$-deg flow deflection angle. Figure shows the streamwise vortex pair generated by the micro-ramp. Superimposed on the vector field is a scale representation of the ramp outline.

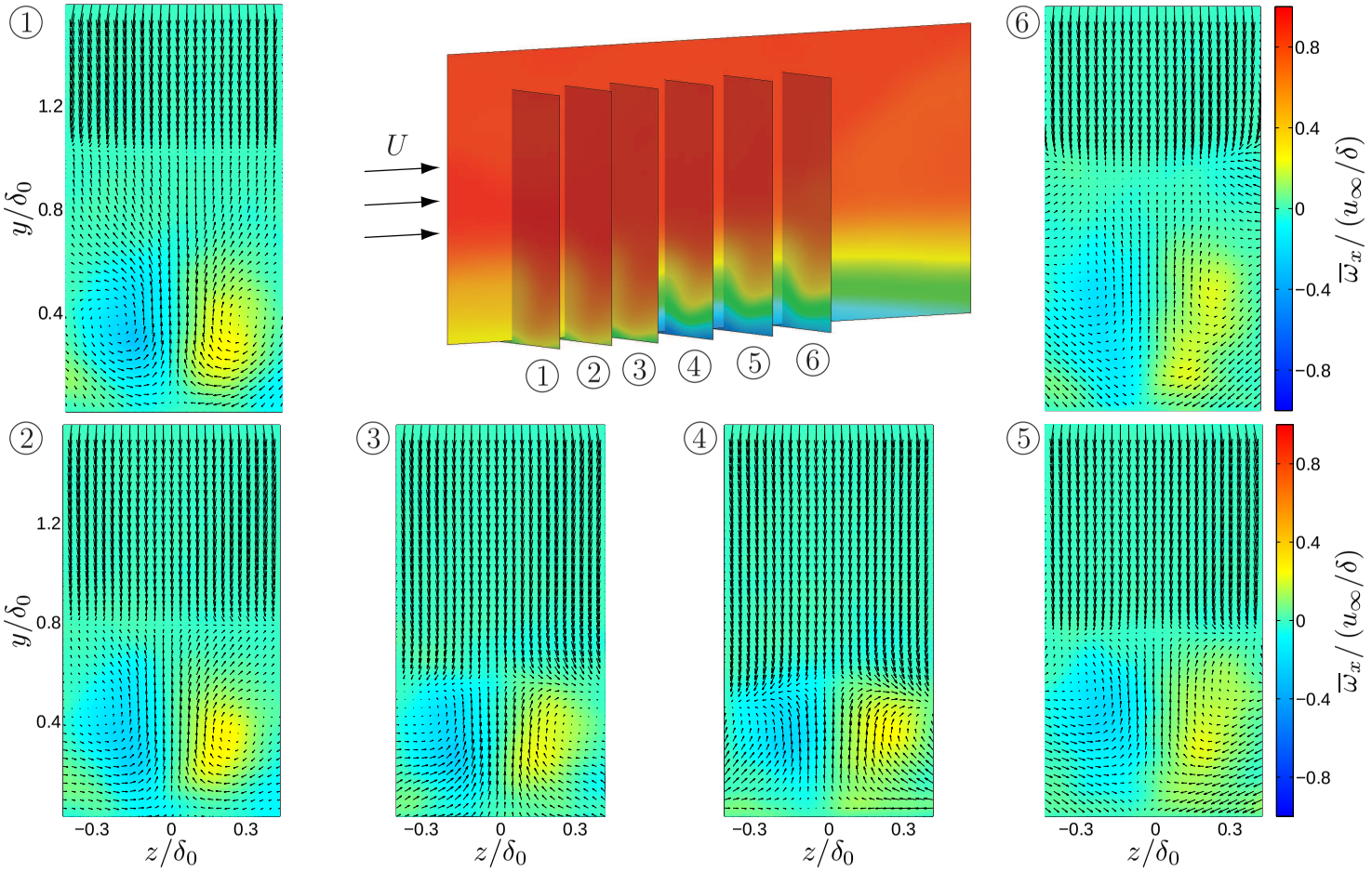

Figure 5.4: Color plots of $\overline{\omega}_x$ show the SBLI region in transverse planes for a flow deflection angle of $\theta = 7.75$-deg and passive control via standard micro-ramps located at $x/\delta_0 = -8.50$. The averaged in-plane velocity fields ($\overline{v}$,$\overline{w}$) are overlayed as vectors. The six sampling locations correspond to 1: $x/\delta_0 = -2.0$, 2: $x/\delta_0 = -1.55$, 3: $x/\delta_0 = -1.2$, 4: $x/\delta_0 = -0.7$, 5: $x/\delta_0 = -0.2$, and 6: $x/\delta_0 = +0.3$. The central perspective plot shows the relative location of each plane.

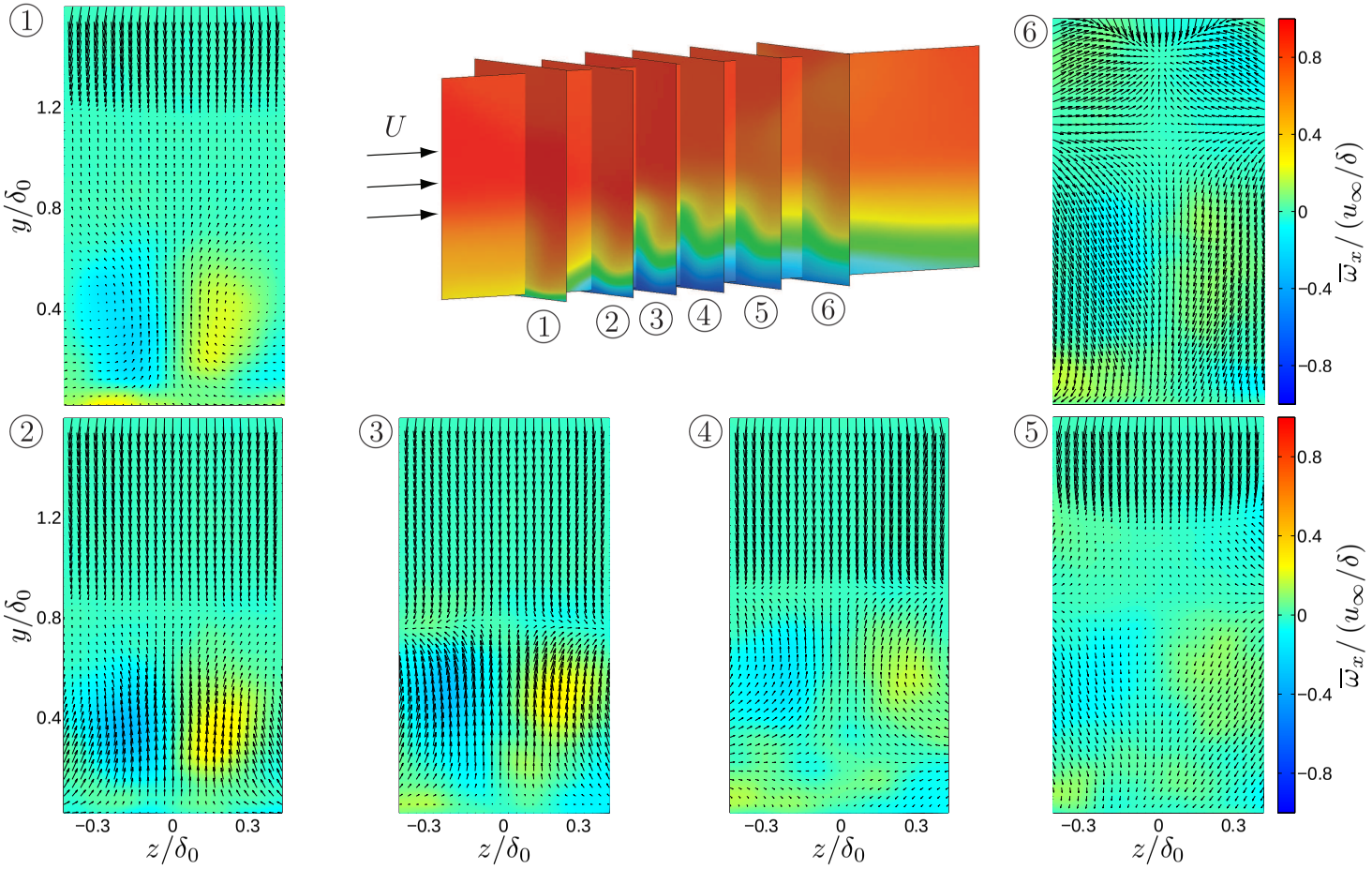

Figure 5.5: Color plots of $\overline{\omega}_x$ show the SBLI region in transverse planes for a flow deflection angle of $\theta = 10.0$-deg and passive control via standard micro-ramps located at $x/\delta_0 = -9.42$. The averaged in-plane velocity fields ($\overline{v}$,$\overline{w}$) are overlayed as vectors. The six sampling locations correspond to 1: $x/\delta_0 = -2.5$, 2: $x/\delta_0 = -1.9$, 3: $x/\delta_0 = -1.5$, 4: $x/\delta_0 = -1.1$, 5: $x/\delta_0 = -0.6$, and 6: $x/\delta_0 = 0.0$. The central perspective plot shows the relative location of each plane.

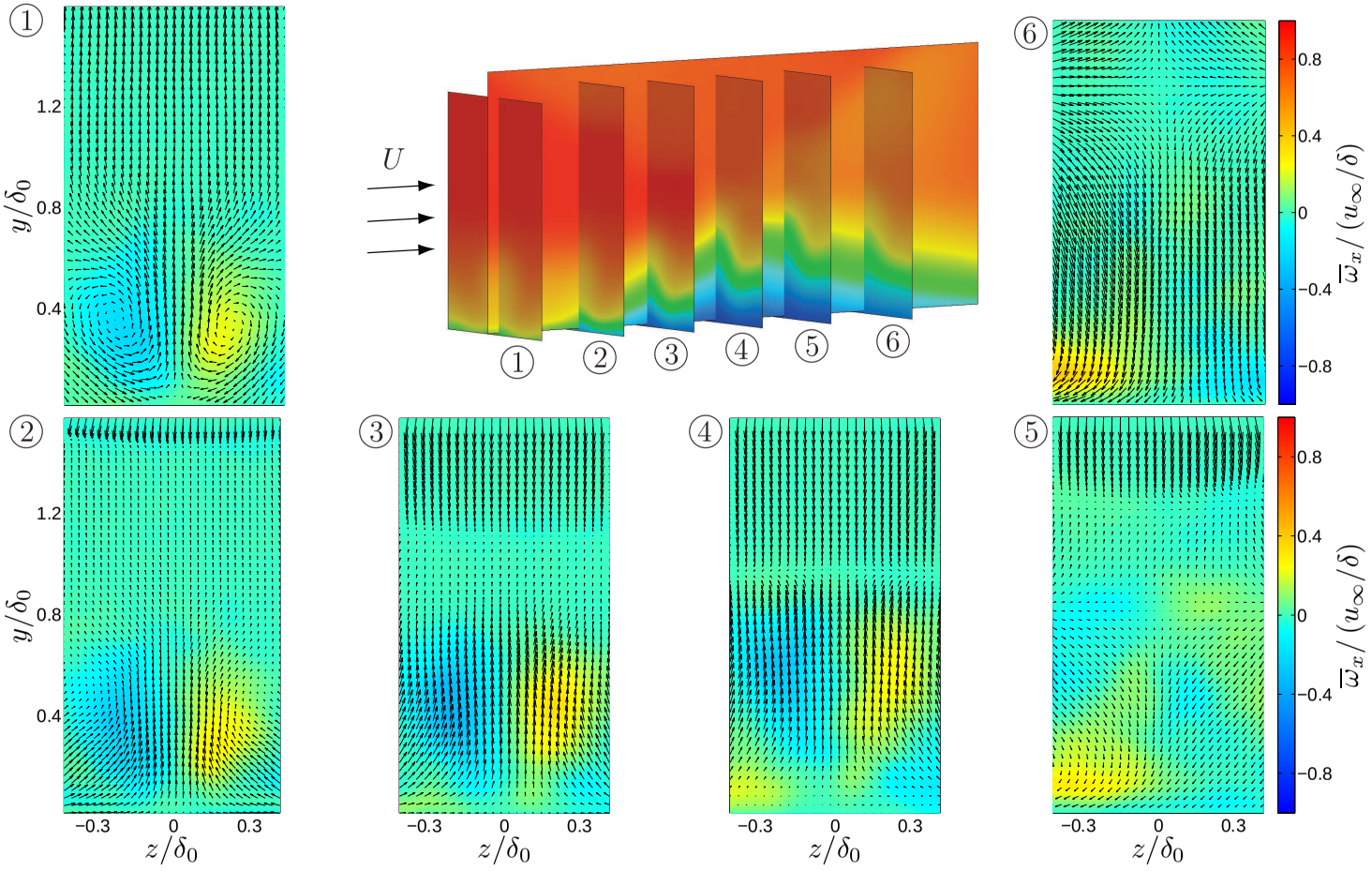

Figure 5.6: Color plots of $\overline{\omega}_x$ show the SBLI region in transverse planes for a flow deflection angle of $\theta = 12.0$-deg and passive control via standard micro-ramps located at $x/\delta_0 = -9.76$. The averaged in-plane velocity fields ($\overline{v}$,$\overline{w}$) are overlayed as vectors. The six sampling locations correspond to 1: $x/\delta_0 = -3.6$, 2: $x/\delta_0 = -2.9$, 3: $x/\delta_0 = -2.3$, 4: $x/\delta_0 = -1.7$, 5: $x/\delta_0 = -1.1$, and 6: $x/\delta_0 = -0.4$. The central perspective plot shows the relative location of each plane.

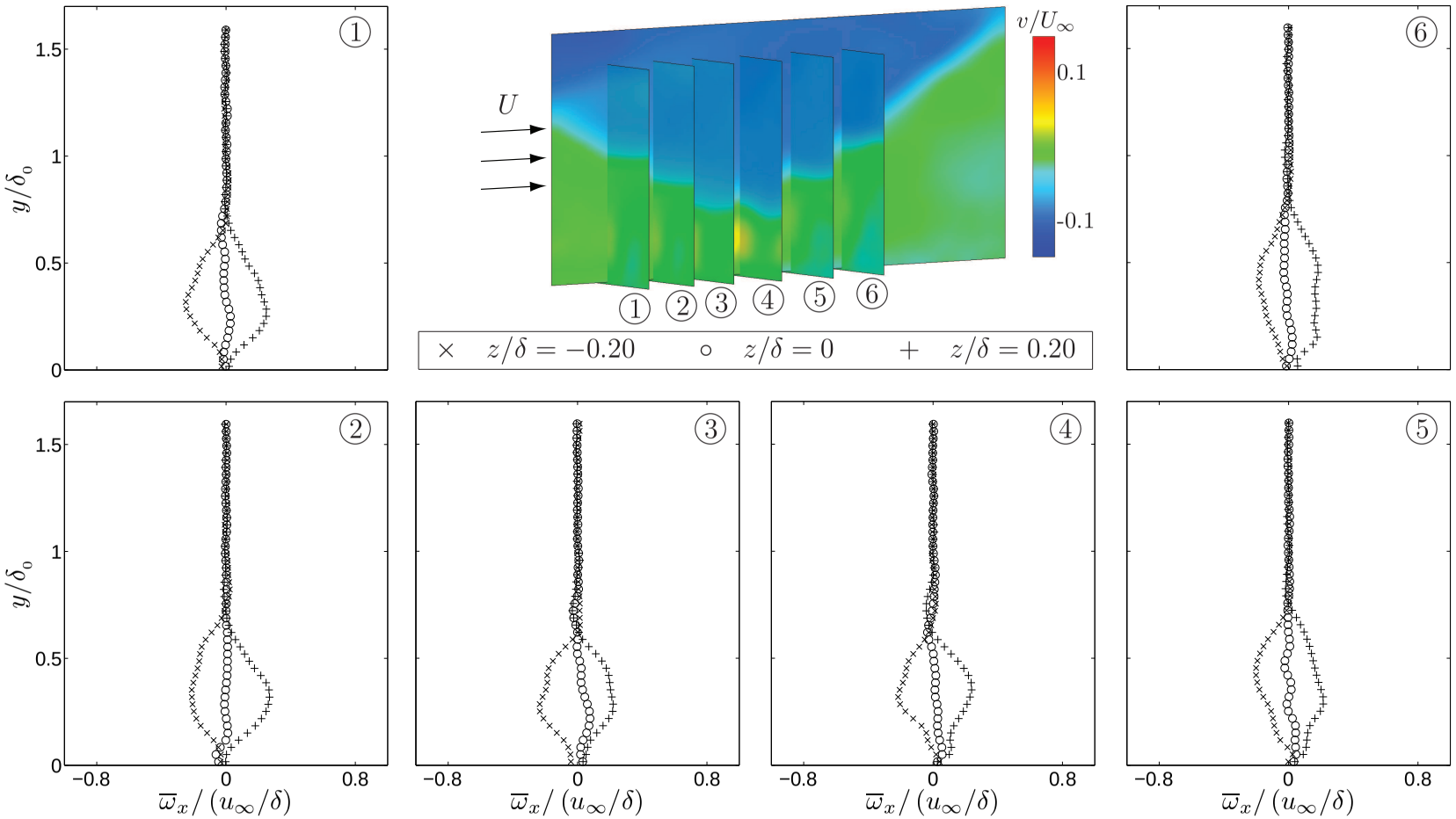

Figure 5.7: The evolution of $\overline{\omega}_x$ through the SBLI region is shown for a flow deflection angle of $\theta = 7.75$-deg and passive control via standard micro-ramps located at $x/\delta_0 = -8.50$. The six sampling locations correspond to 1: $x/\delta_0 = -2.0$, 2: $x/\delta_0 = -1.55$, 3: $x/\delta_0 = -1.2$, 4: $x/\delta_0 = -0.7$, 5: $x/\delta_0 = -0.2$, and 6: $x/\delta_0 = +0.3$. At top, colors show the $\overline{v}$ field throughout each plane and show the relative location of each plane.

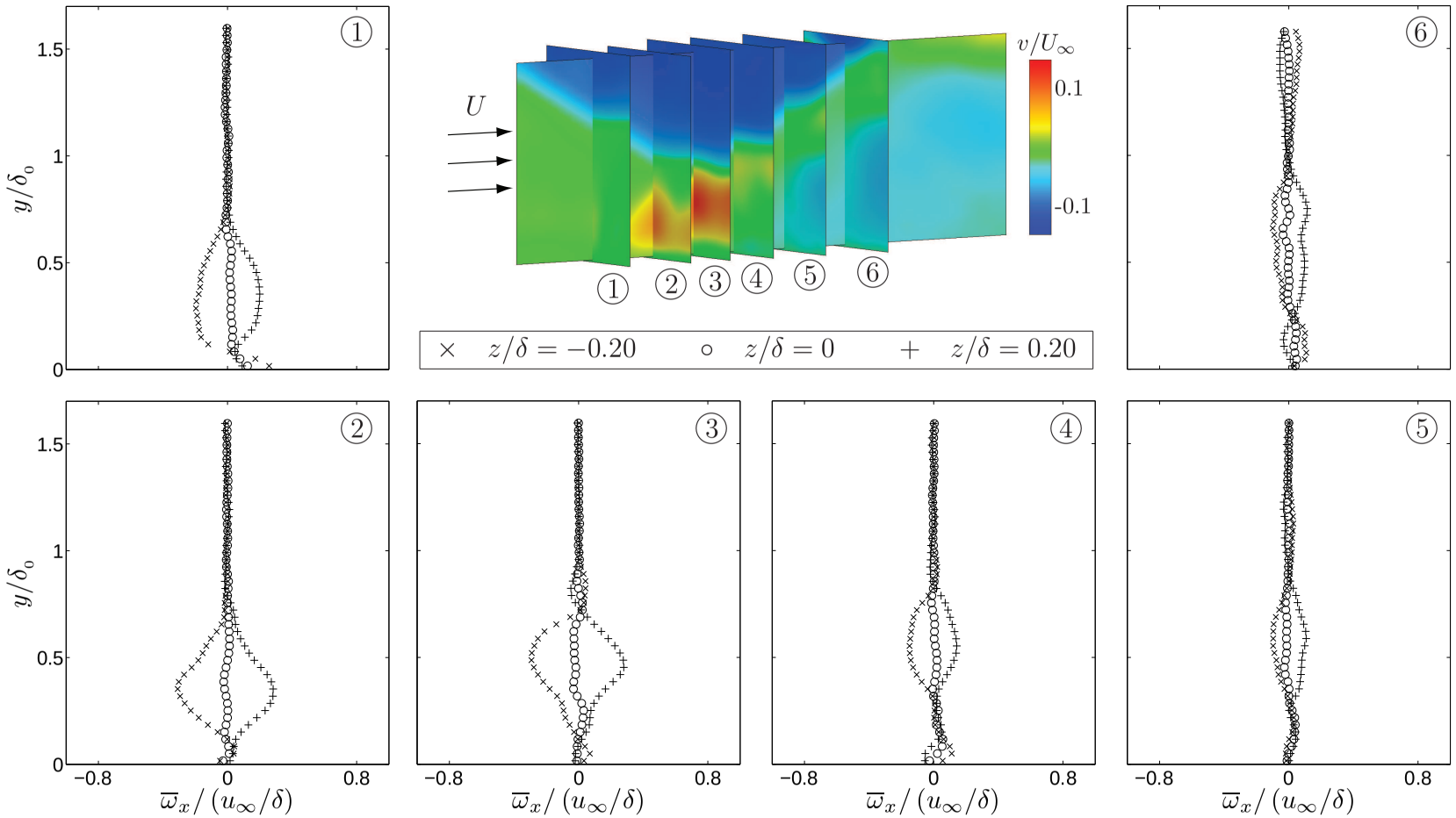

Figure 5.8: The evolution of $\overline{\omega}_x$ through the SBLI region is shown for a flow deflection angle of $\theta = 10.0$-deg and passive control via standard micro-ramps located at $x/\delta_0 = -9.42$. The six sampling locations correspond to 1: $x/\delta_0 = -2.5$, 2: $x/\delta_0 = -1.9$, 3: $x/\delta_0 = -1.5$, 4: $x/\delta_0 = -1.1$, 5: $x/\delta_0 = -0.6$, and 6: $x/\delta_0 = 0.0$. At top, colors show the $\overline{v}$ field throughout each plane and show the relative location of each plane.

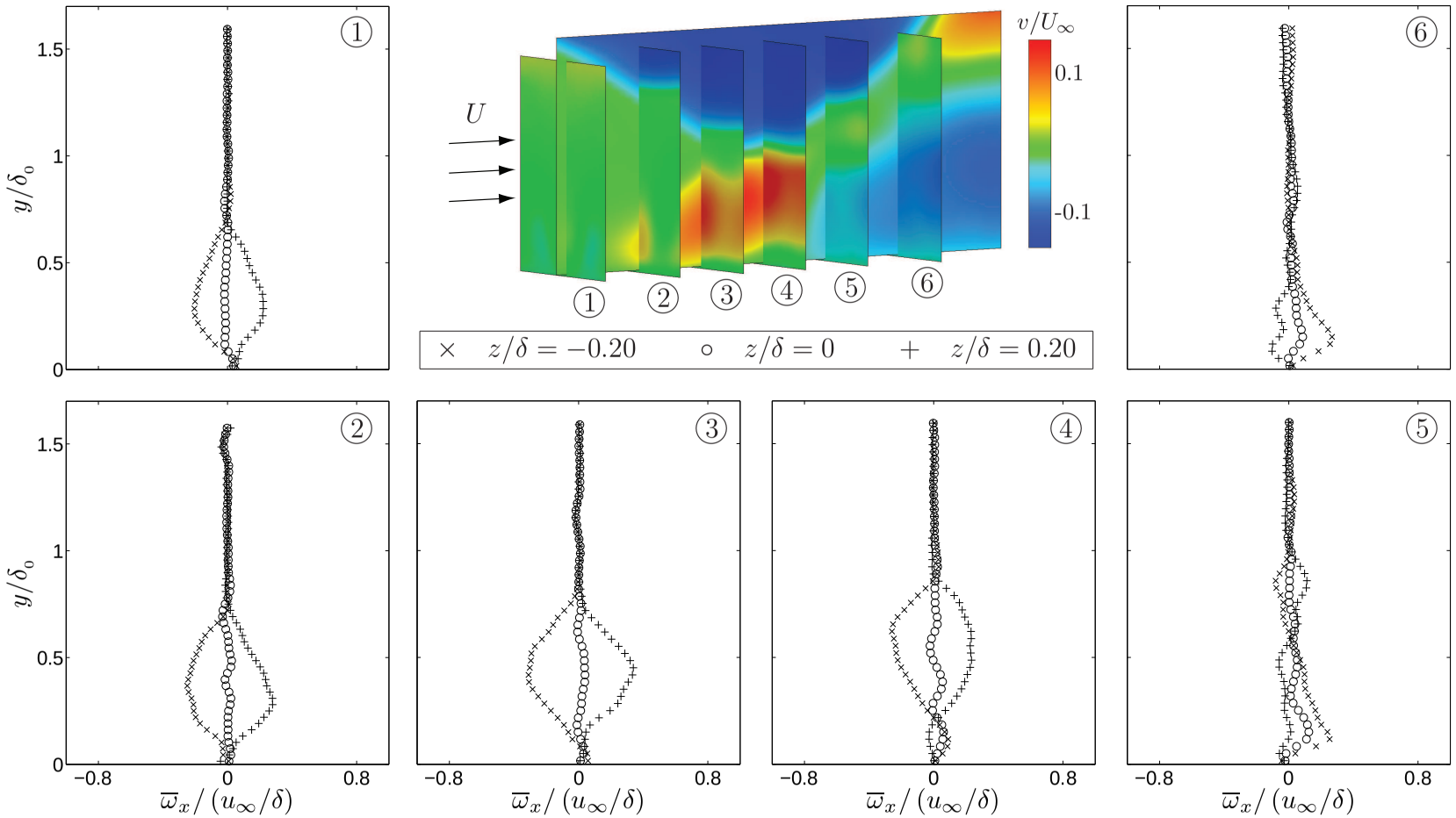

Figure 5.9: The evolution of $\overline{\omega}_x$ through the SBLI region is shown for a flow deflection angle of $\theta = 12.0$-deg and passive control via standard micro-ramps located at $x/\delta_0 = -9.76$. The six sampling locations correspond to 1: $x/\delta_0 = -3.6$, 2: $x/\delta_0 = -2.9$, 3: $x/\delta_0 = -2.3$, 4: $x/\delta_0 = -1.7$, 5: $x/\delta_0 = -1.1$, and 6: $x/\delta_0 = -0.4$. At top, colors show the $\overline{v}$ field throughout each plane and show the relative location of each plane.

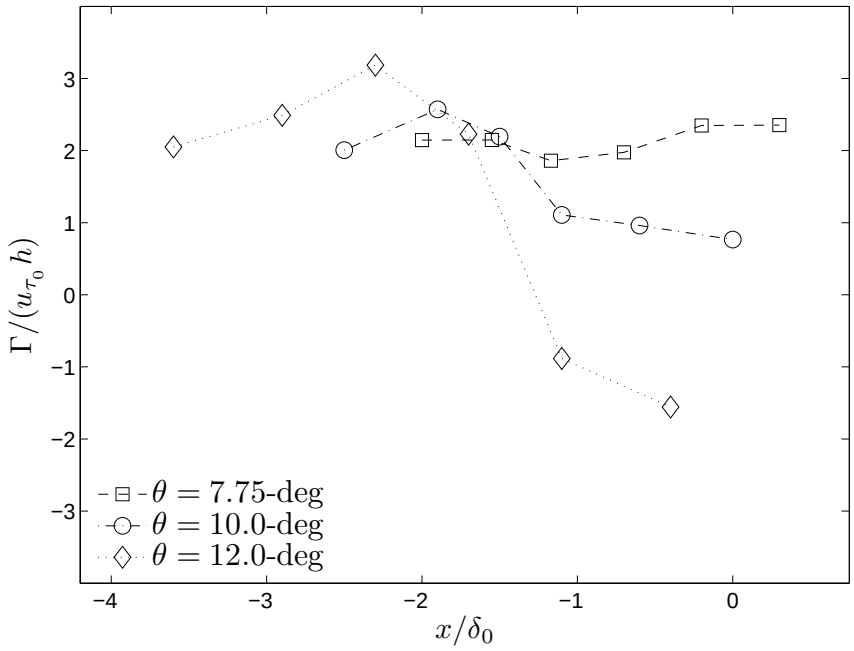

Figure 5.10: Evolution of the circulation Γ generated by the standard micro-ramps, shown as a function of downstream distance x/δ_0 for all three shock strengths.

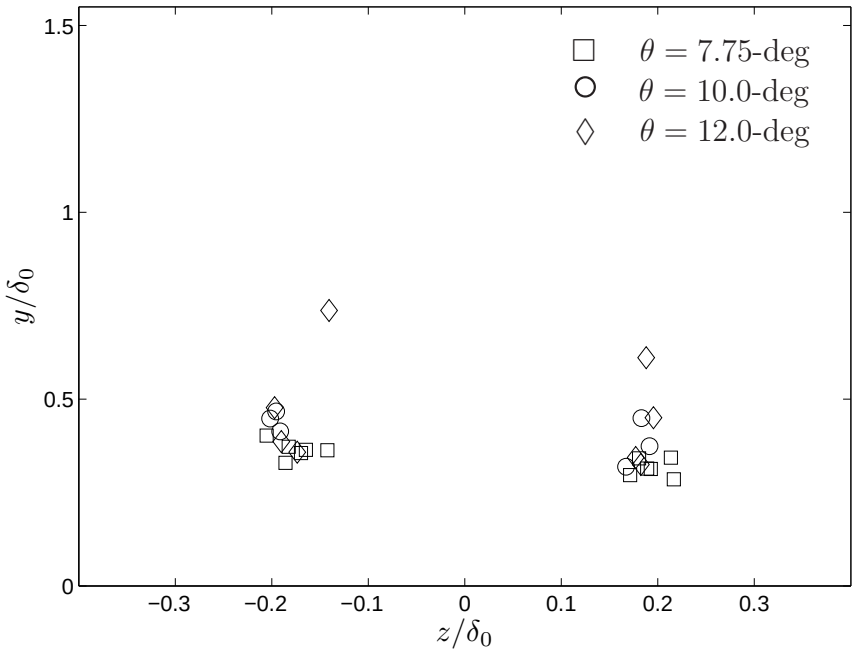

Figure 5.11: Left and right vortex centroids from the standard micro-ramp shown at each x-location and for each shock strength.

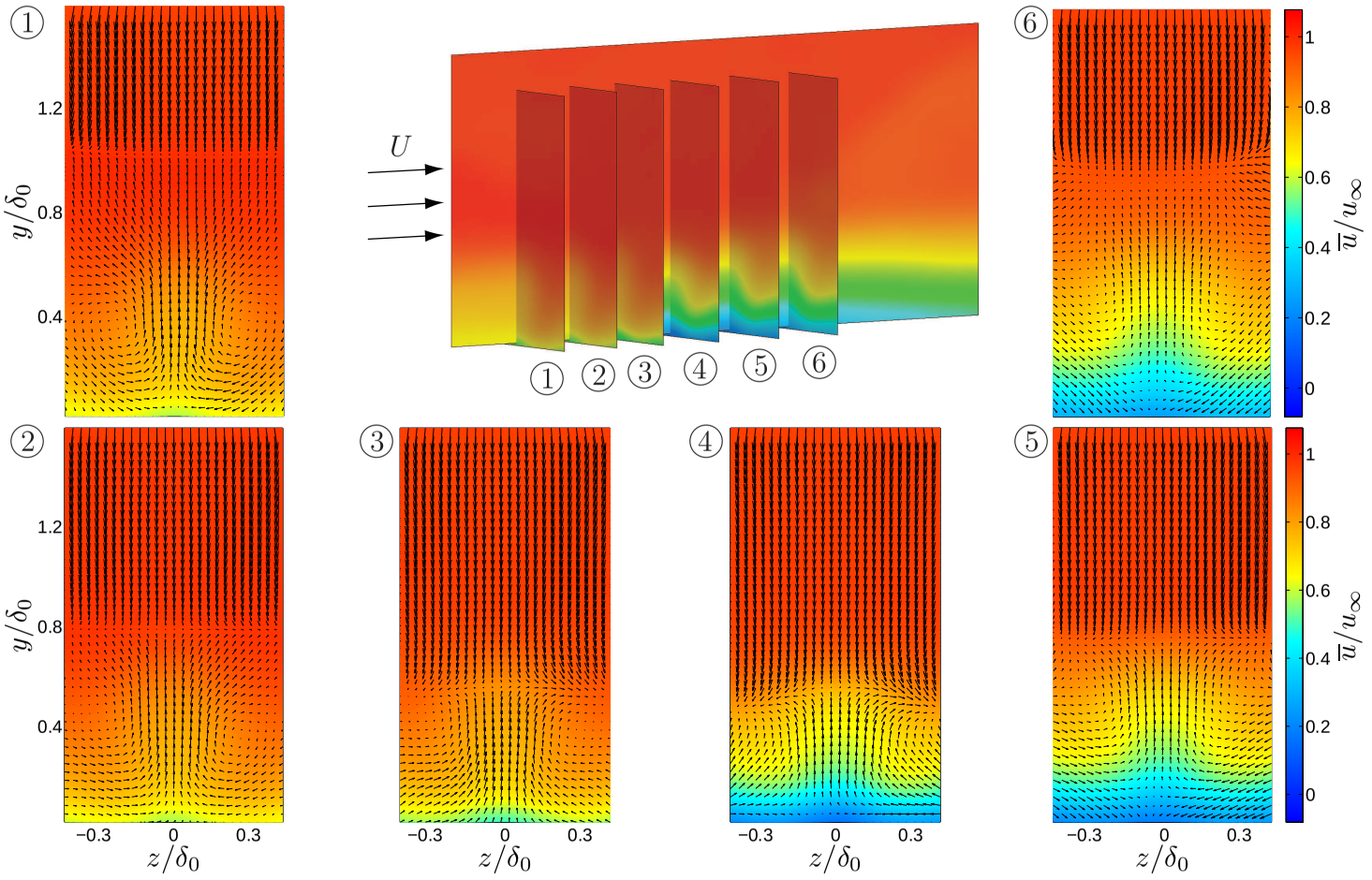

Figure 5.12: Color plots of $\overline{u}$ show the SBLI region in transverse planes for a flow deflection angle of $\theta = 7.75$-deg and passive control via standard micro-ramps located at $x/\delta_0 = -8.50$. The averaged in-plane velocity fields ($\overline{v}$,$\overline{w}$) are overlayed as vectors. The six sampling locations correspond to 1: $x/\delta_0 = -2.0$, 2: $x/\delta_0 = -1.55$, 3: $x/\delta_0 = -1.2$, 4: $x/\delta_0 = -0.7$, 5: $x/\delta_0 = -0.2$, and 6: $x/\delta_0 = +0.3$. The central perspective plot shows the relative location of each plane.

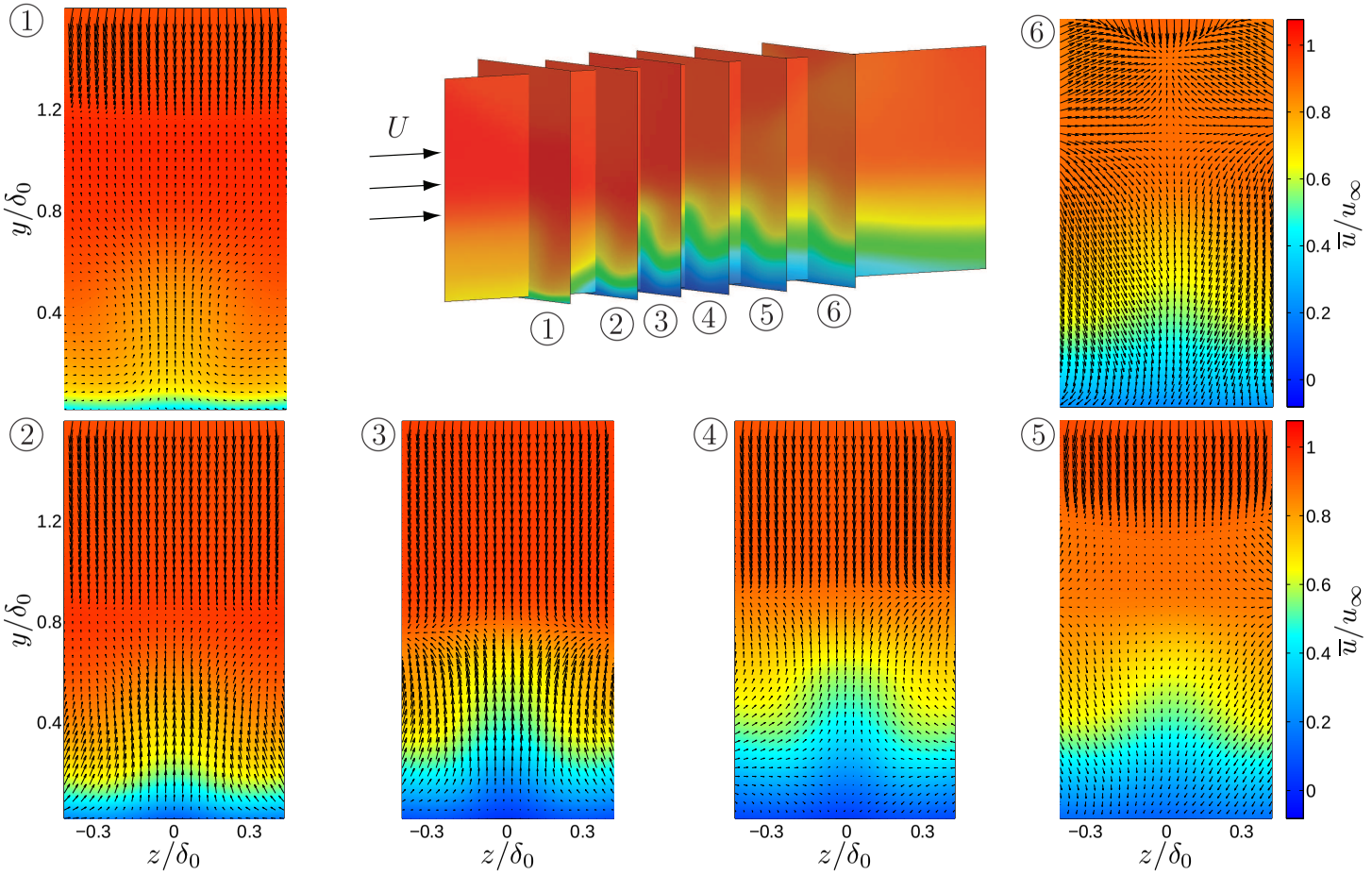

Figure 5.13: Color plots of $\overline{u}$ show the SBLI region in transverse planes for a flow deflection angle of $\theta = 10.0$-deg and passive control via standard micro-ramps located at $x/\delta_0 = -9.42$. The averaged in-plane velocity fields ($\overline{v}$,$\overline{w}$) are overlayed as vectors. The six sampling locations correspond to 1: $x/\delta_0 = -2.5$, 2: $x/\delta_0 = -1.9$, 3: $x/\delta_0 = -1.5$, 4: $x/\delta_0 = -1.1$, 5: $x/\delta_0 = -0.6$, and 6: $x/\delta_0 = 0.0$. The central perspective plot shows the relative location of each plane.

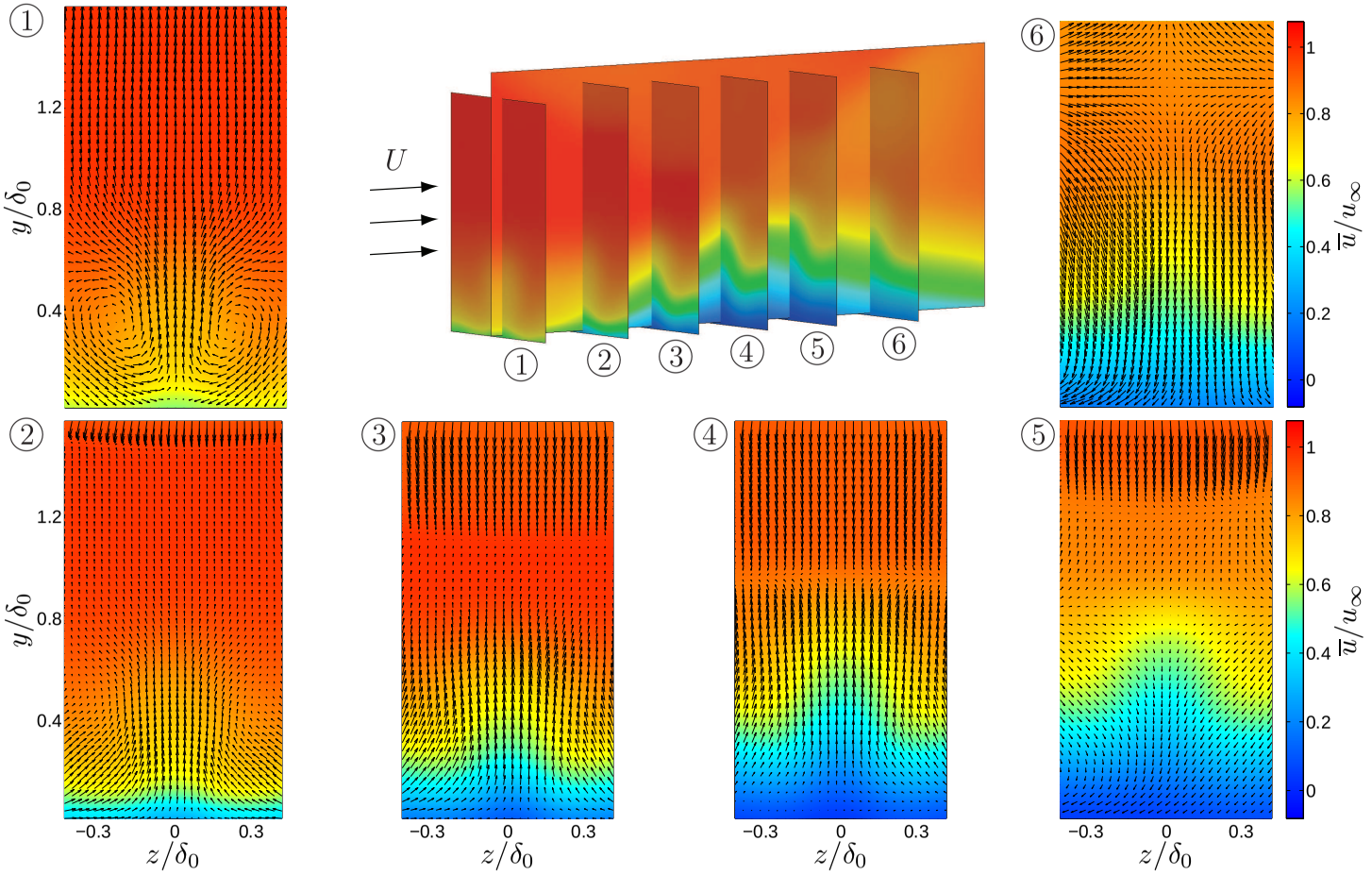

Figure 5.14: Color plots of $\overline{u}$ show the SBLI region in transverse planes for a flow deflection angle of $\theta = 12.0$-deg and passive control via standard micro-ramps located at $x/\delta_0 = -9.76$. The averaged in-plane velocity fields ($\overline{v}$,$\overline{w}$) are overlayed as vectors. The six sampling locations correspond to 1: $x/\delta_0 = -3.6$, 2: $x/\delta_0 = -2.9$, 3: $x/\delta_0 = -2.3$, 4: $x/\delta_0 = -1.7$, 5: $x/\delta_0 = -1.1$, and 6: $x/\delta_0 = -0.4$. The central perspective plot shows the relative location of each plane.

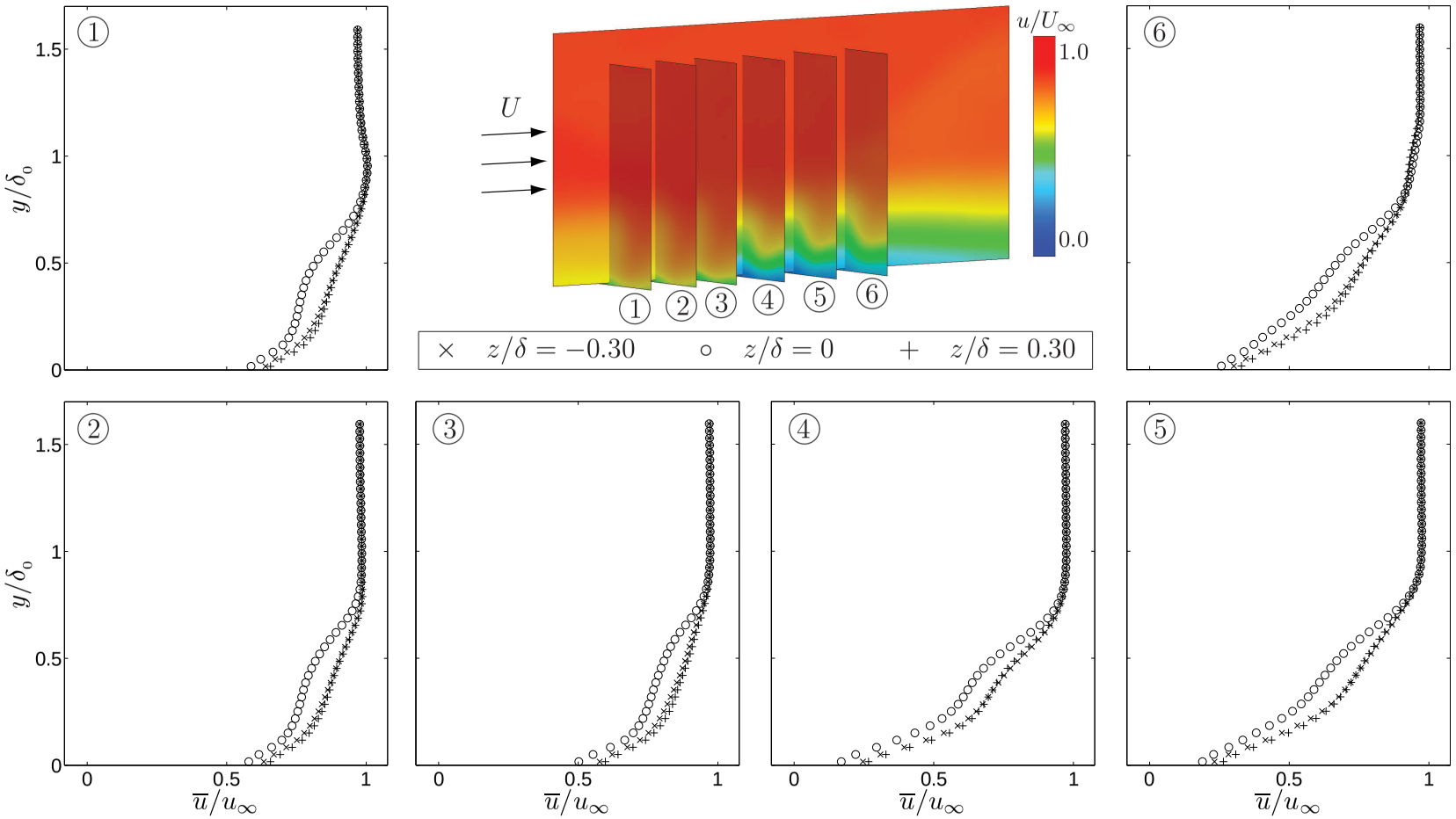

Figure 5.15: The evolution of $\overline{u}$ through the SBLI region is shown for a flow deflection angle of $\theta = 7.75$-deg and passive control via standard micro-ramps located at $x/\delta_0 = -8.50$. The six sampling locations correspond to 1: $x/\delta_0 = -2.0$, 2: $x/\delta_0 = -1.55$, 3: $x/\delta_0 = -1.2$, 4: $x/\delta_0 = -0.7$, 5: $x/\delta_0 = -0.2$, and 6: $x/\delta_0 = +0.3$. At top, colors show the $\overline{u}$ field throughout each plane and show the relative location of each plane.

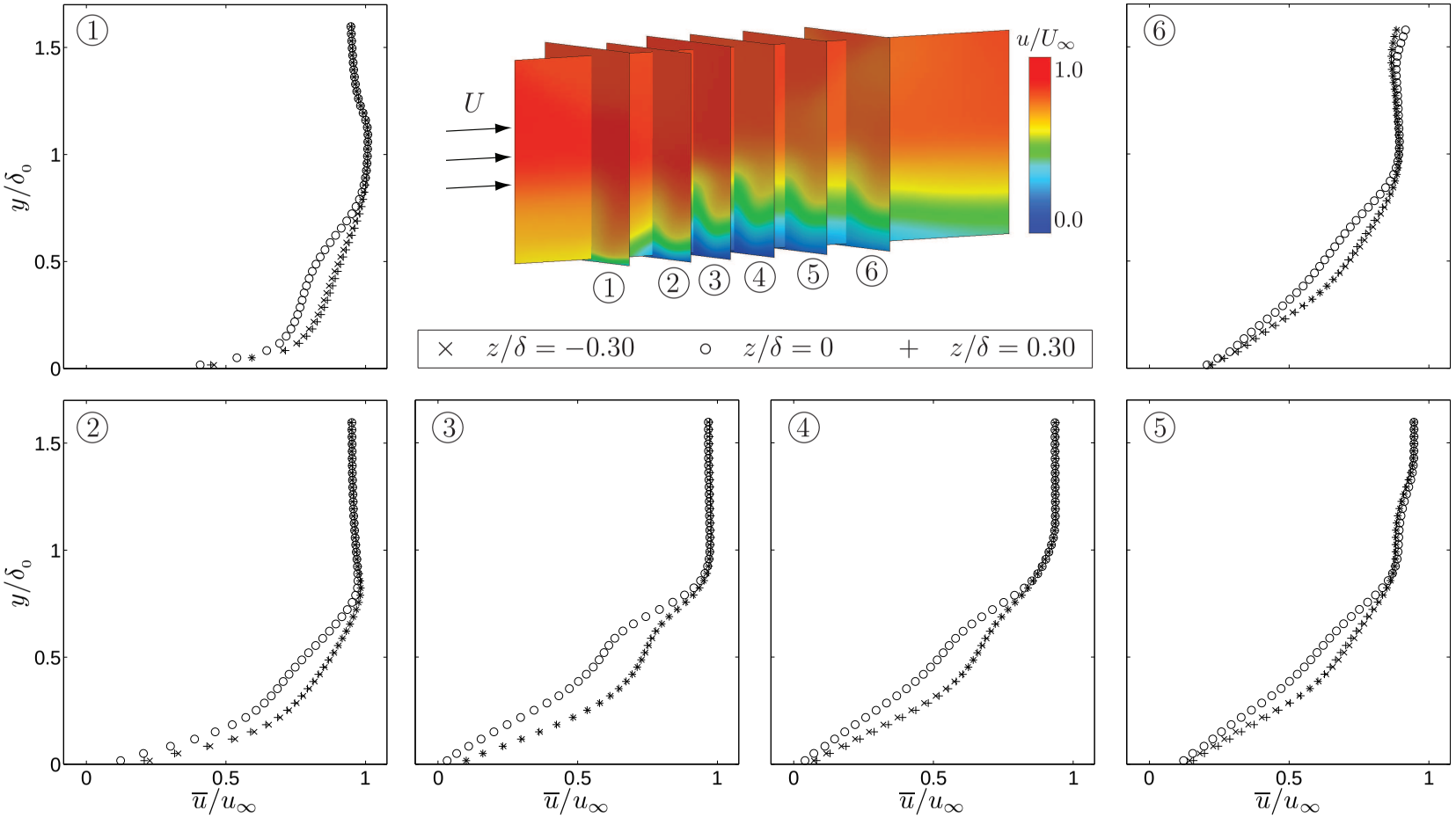

Figure 5.16: The evolution of $\overline{u}$ through the SBLI region is shown for a flow deflection angle of $\theta = 10.0$-deg and passive control via standard micro-ramps located at $x/\delta_0 = -9.42$. The six sampling locations correspond to 1: $x/\delta_0 = -2.5$, 2: $x/\delta_0 = -1.9$, 3: $x/\delta_0 = -1.5$, 4: $x/\delta_0 = -1.1$, 5: $x/\delta_0 = -0.6$, and 6: $x/\delta_0 = 0.0$. At top, colors show the $\overline{u}$ field throughout each plane and show the relative location of each plane.

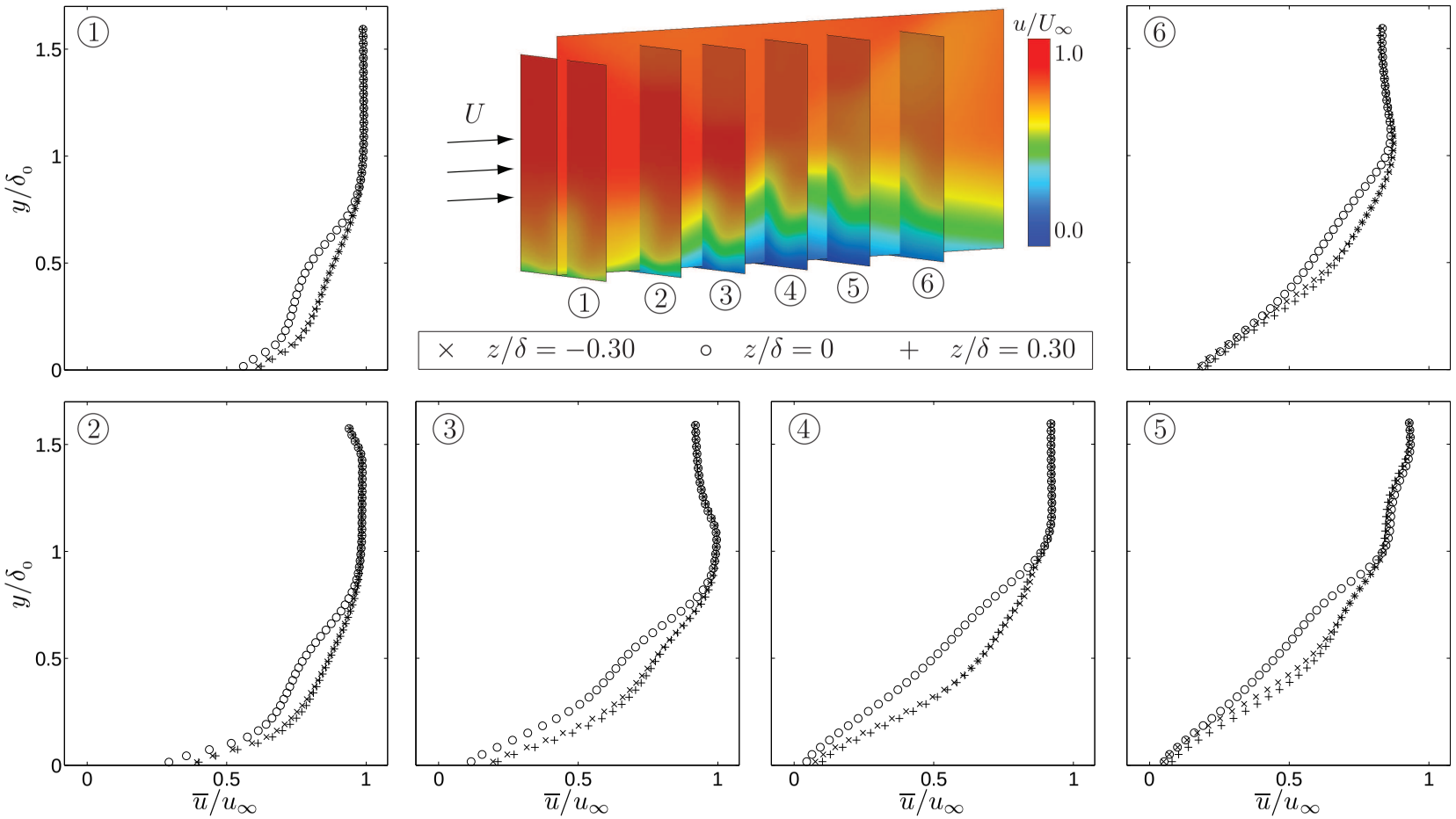

Figure 5.17: The evolution of $\overline{u}$ through the SBLI region is shown for a flow deflection angle of $\theta = 12.0$-deg and passive control via standard micro-ramps located at $x/\delta_0 = -9.76$. The six sampling locations correspond to 1: $x/\delta_0 = -3.6$, 2: $x/\delta_0 = -2.9$, 3: $x/\delta_0 = -2.3$, 4: $x/\delta_0 = -1.7$, 5: $x/\delta_0 = -1.1$, and 6: $x/\delta_0 = -0.4$. At top, colors show the $\overline{u}$ field throughout each plane and show the relative location of each plane.

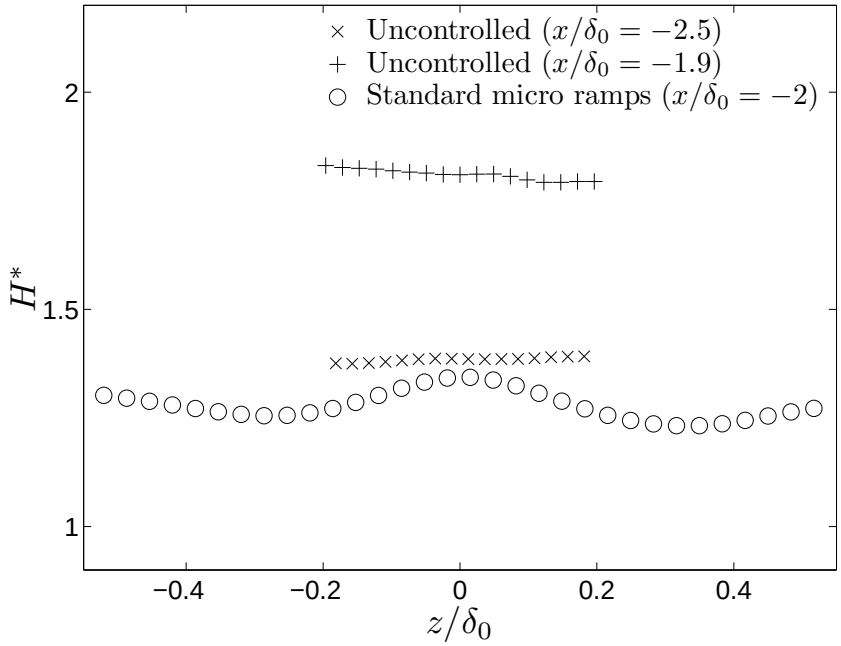

Figure 5.18: Modified shape factor H^* shown upstream of the $\theta = 7.75$-deg interaction as a function of the spanwise coordinate, comparing the uncontrolled boundary layer with that controlled by standard micro-ramps.

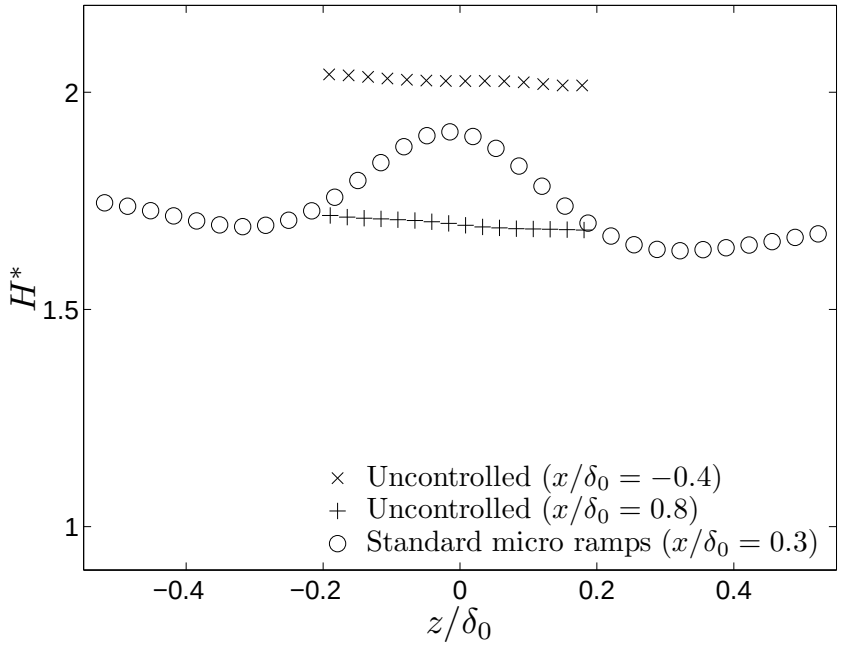

Figure 5.19: Modified shape factor H^* shown downstream of the $\theta = 7.75$-deg interaction as a function of the spanwise coordinate, comparing the uncontrolled boundary layer with that controlled by standard micro-ramps.

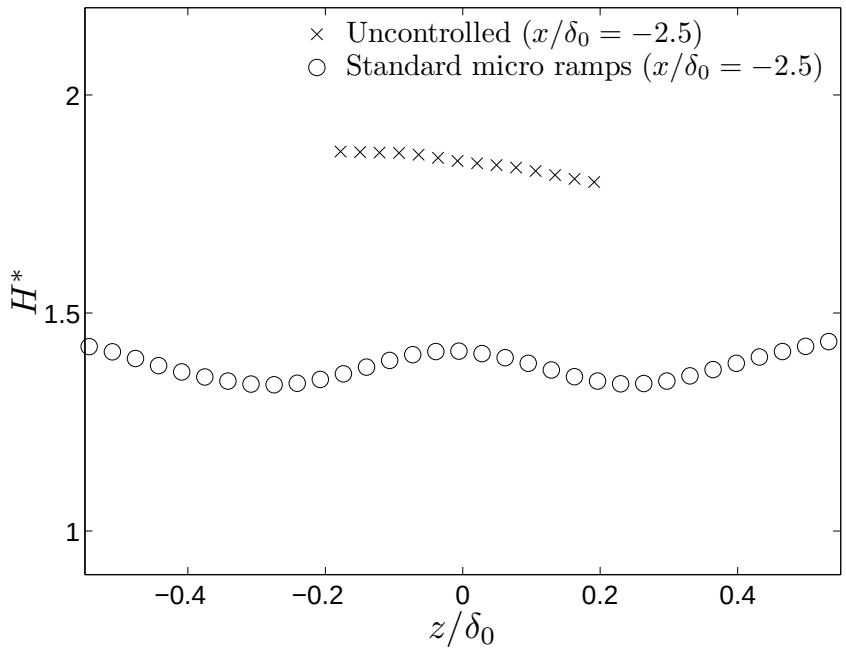

Figure 5.20: Modified shape factor H^* shown upstream of the $\theta = 10.0$-deg interaction as a function of the spanwise coordinate, comparing the uncontrolled boundary layer with that controlled by standard micro-ramps.

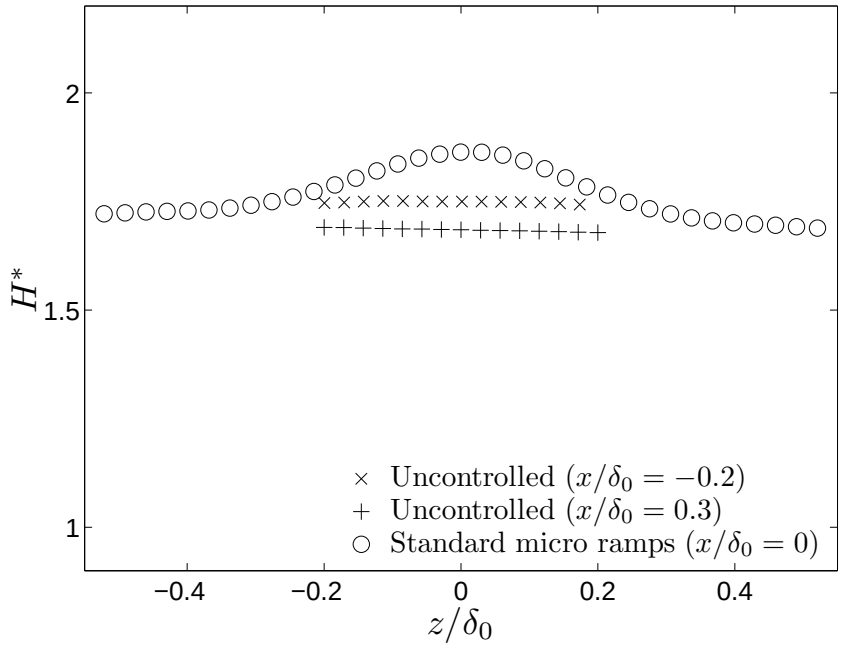

Figure 5.21: Modified shape factor H^* shown downstream of the $\theta = 10.0$-deg interaction as a function of the spanwise coordinate, comparing the uncontrolled boundary layer with that controlled by standard micro-ramps.

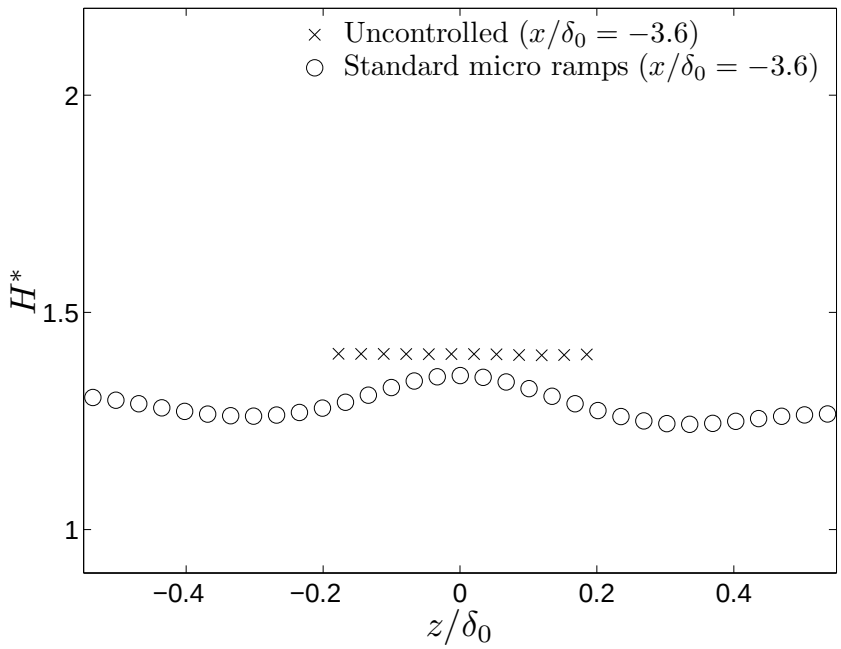

Figure 5.22: Modified shape factor H^* shown upstream of the $\theta = 12.0$-deg interaction as a function of the spanwise coordinate, comparing the uncontrolled boundary layer with that controlled by standard micro-ramps.

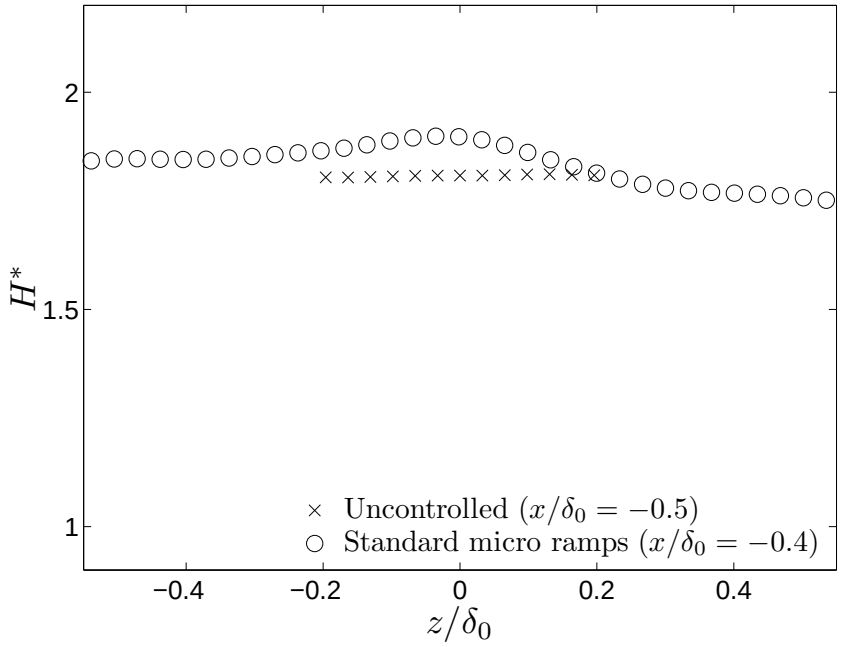

Figure 5.23: Modified shape factor H^* shown downstream of the $\theta = 12.0$-deg interaction as a function of the spanwise coordinate, comparing the uncontrolled boundary layer with that controlled by standard micro-ramps.

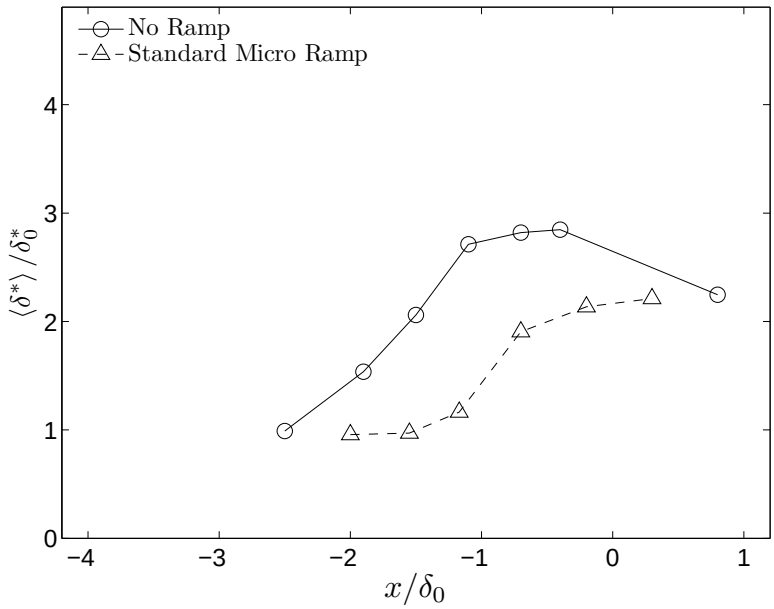

Figure 5.24: The net displacement thickness $\langle\delta^*\rangle$ as a function of the downstream distance x for the $\theta = 7.75$-deg flow deflection angle. The figure compares the interaction controlled by the standard micro-ramp array to that of the uncontrolled interaction, and demonstrates a 22% reduction of the peak value due to the micro-ramps.

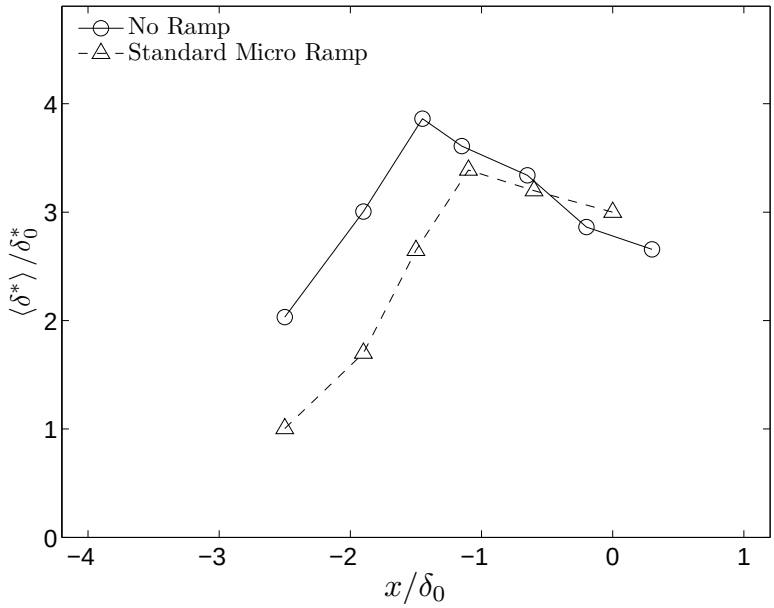

Figure 5.25: The net displacement thickness $\langle\delta^*\rangle$ as a function of the downstream distance x for the $\theta = 10.0$-deg flow deflection angle. The figure compares the interaction controlled by the standard micro-ramp array to that of the uncontrolled interaction, and demonstrates a 13% reduction of the peak value due to the micro-ramps.

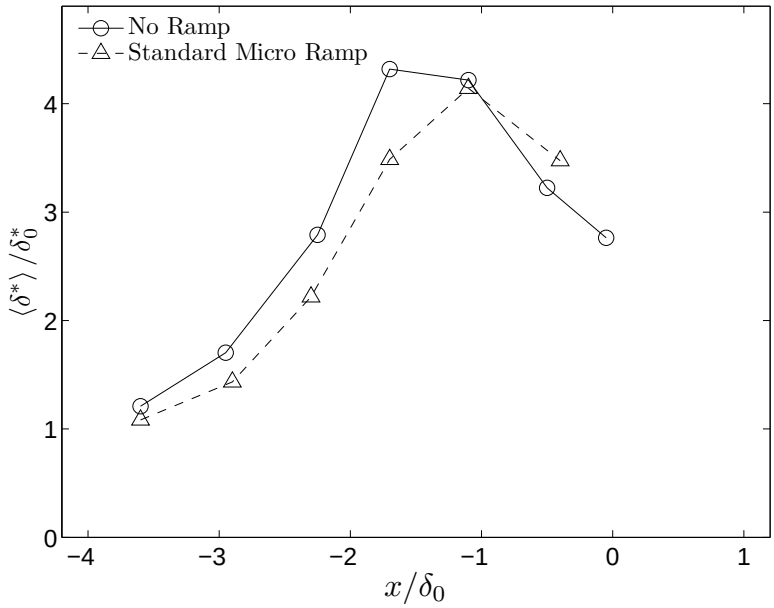

Figure 5.26: The net displacement thickness $\langle \delta^* \rangle$ as a function of the downstream distance x for the $\theta = 12.0$-deg flow deflection angle. The figure compares the interaction controlled by the standard micro-ramp array to that of the uncontrolled interaction, and demonstrates a 4% reduction of the peak value due to the micro-ramps.

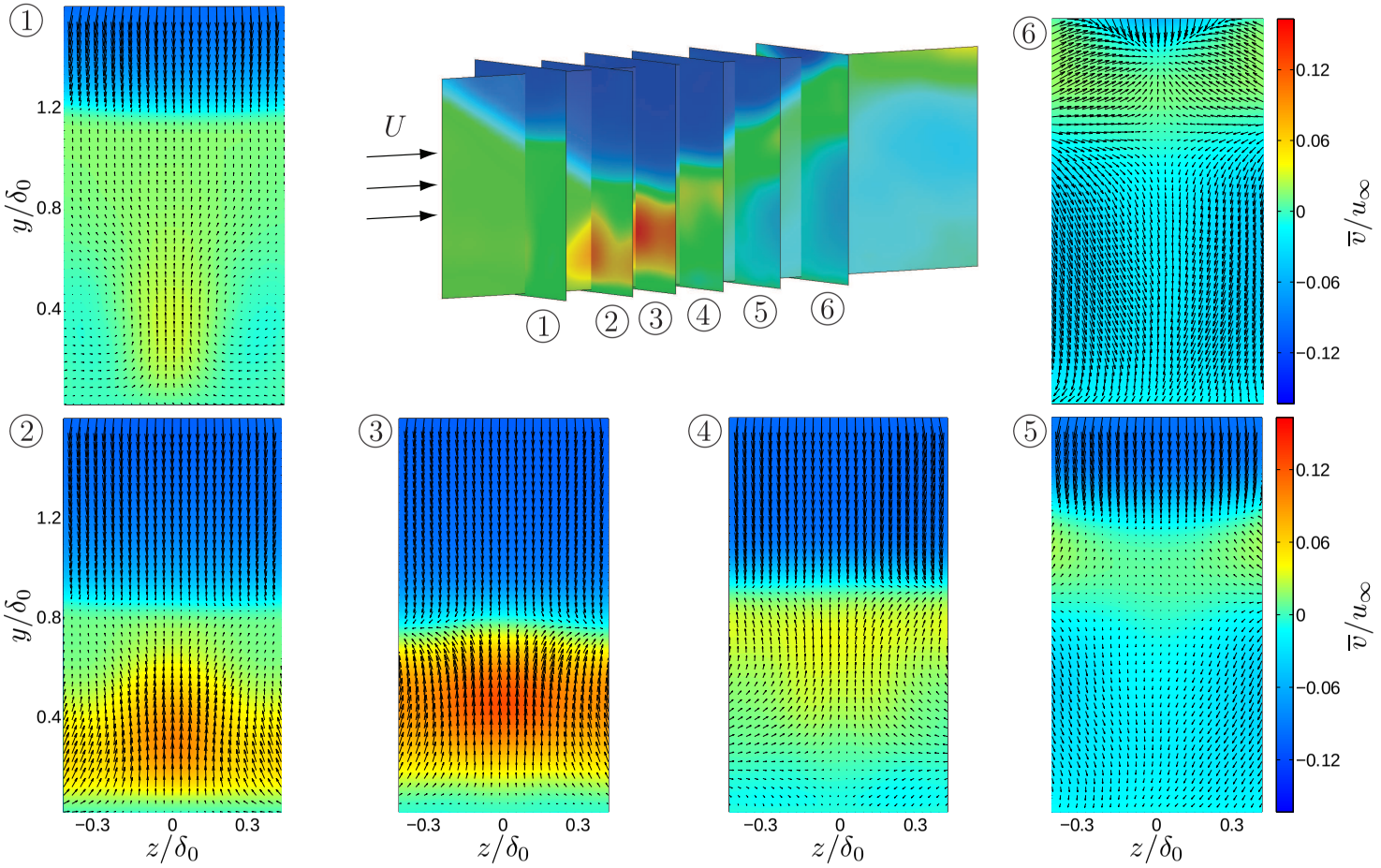

Figure 5.27: Color plots of $\overline{v}$ show the SBLI region in transverse planes for a flow deflection angle of $\theta = 10.0$-deg and passive control via standard micro-ramps located at $x/\delta_0 = -9.42$. The averaged in-plane velocity fields ($\overline{v}$,$\overline{w}$) are overlayed as vectors. The six sampling locations correspond to 1: $x/\delta_0 = -2.5$, 2: $x/\delta_0 = -1.55$, 3: $x/\delta_0 = -1.2$, 4: $x/\delta_0 = -0.7$, 5: $x/\delta_0 = -0.2$, and 6: $x/\delta_0 = +0.3$. The central perspective plot shows the relative location of each plane.

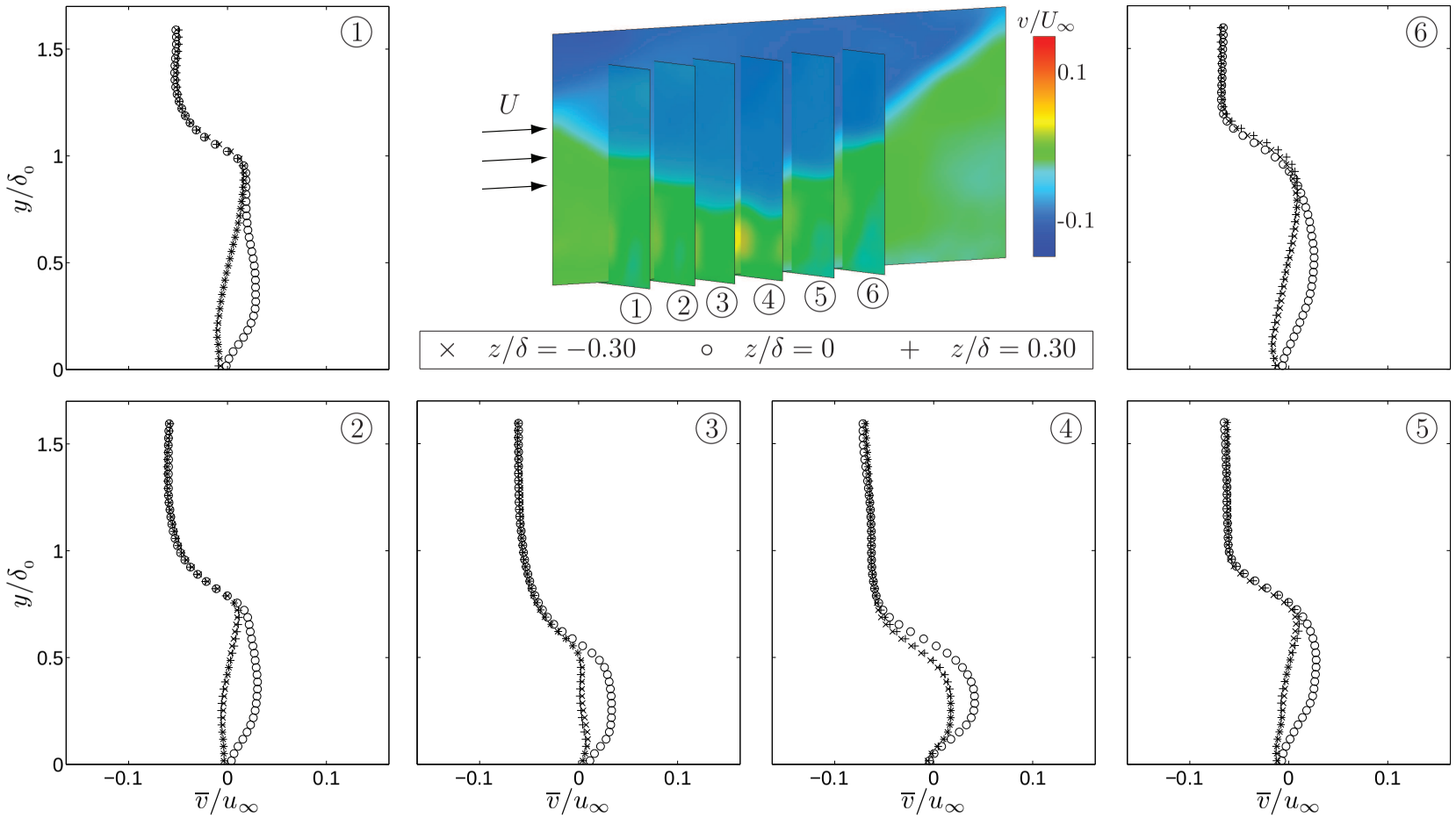

Figure 5.28: The evolution of $\overline{v}$ through the SBLI region is shown for a flow deflection angle of $\theta = 7.75$-deg and passive control via standard micro-ramps located at $x/\delta_0 = -8.50$. The six sampling locations correspond to 1: $x/\delta_0 = -2.0$, 2: $x/\delta_0 = -1.55$, 3: $x/\delta_0 = -1.2$, 4: $x/\delta_0 = -0.7$, 5: $x/\delta_0 = -0.2$, and 6: $x/\delta_0 = +0.3$. At top, colors show the $\overline{v}$ field throughout each plane and show the relative location of each plane.

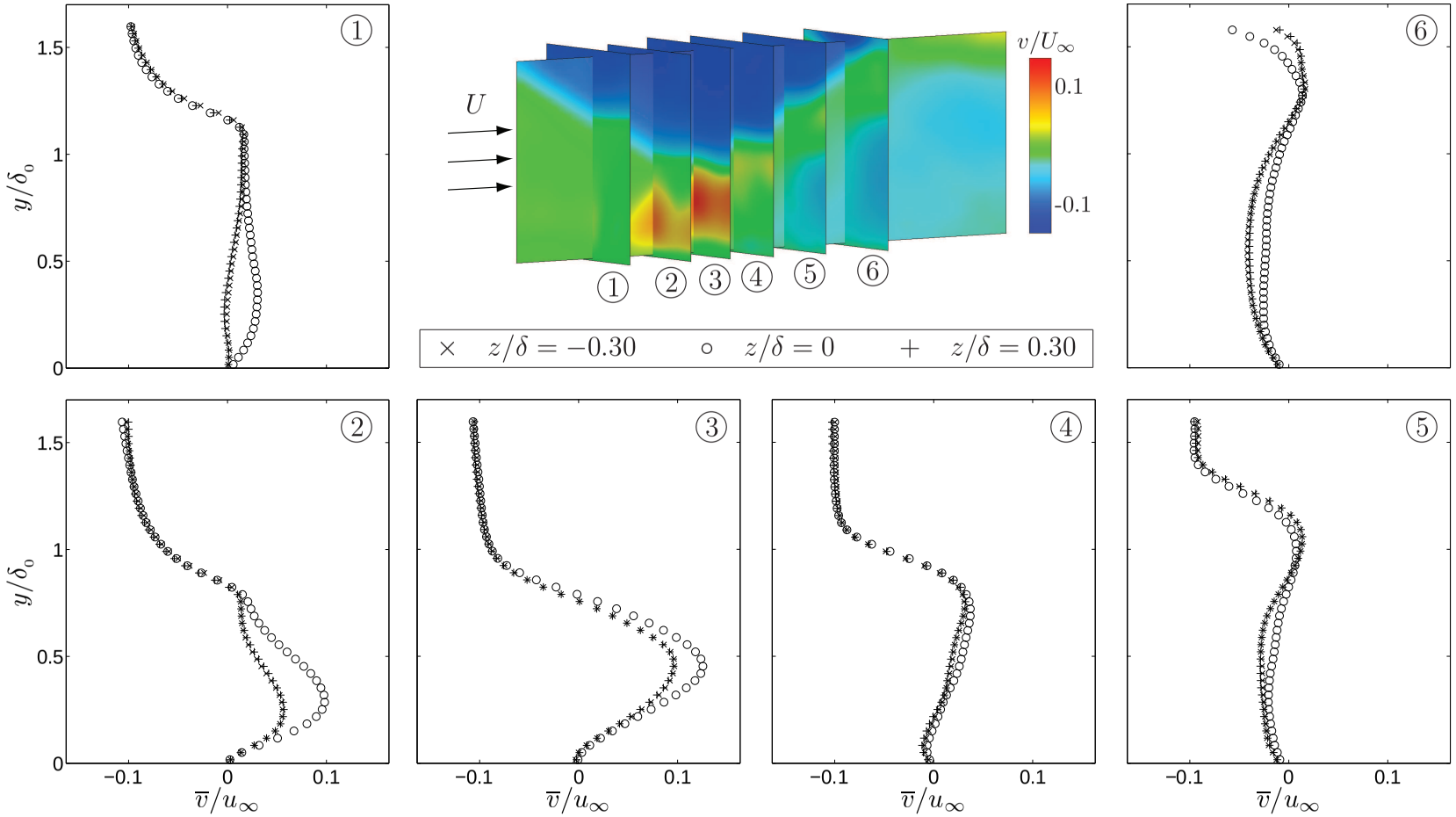

Figure 5.29: The evolution of $\overline{v}$ through the SBLI region is shown for a flow deflection angle of $\theta = 10.0$-deg and passive control via standard micro-ramps located at $x/\delta_0 = -9.42$. The six sampling locations correspond to 1: $x/\delta_0 = -2.5$, 2: $x/\delta_0 = -1.9$, 3: $x/\delta_0 = -1.5$, 4: $x/\delta_0 = -1.1$, 5: $x/\delta_0 = -0.6$, and 6: $x/\delta_0 = 0.0$. At top, colors show the $\overline{v}$ field throughout each plane and show the relative location of each plane.

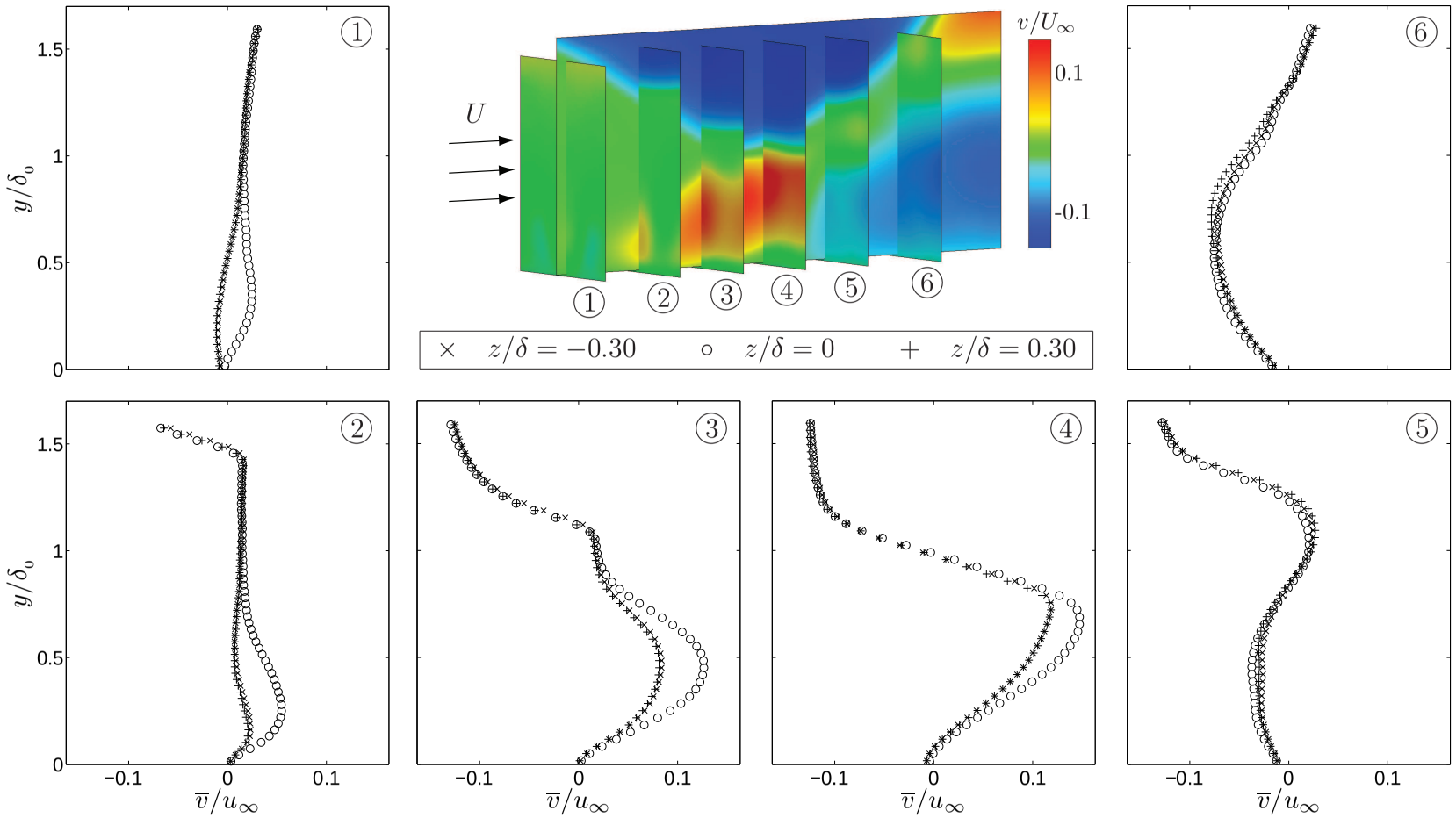

Figure 5.30: The evolution of $\overline{v}$ through the SBLI region is shown for a flow deflection angle of $\theta = 12.0$-deg and passive control via standard micro-ramps located at $x/\delta_0 = -9.76$. The six sampling locations correspond to 1: $x/\delta_0 = -3.6$, 2: $x/\delta_0 = -2.9$, 3: $x/\delta_0 = -2.3$, 4: $x/\delta_0 = -1.7$, 5: $x/\delta_0 = -1.1$, and 6: $x/\delta_0 = -0.4$. At top, colors show the $\overline{v}$ field throughout each plane and show the relative location of each plane.

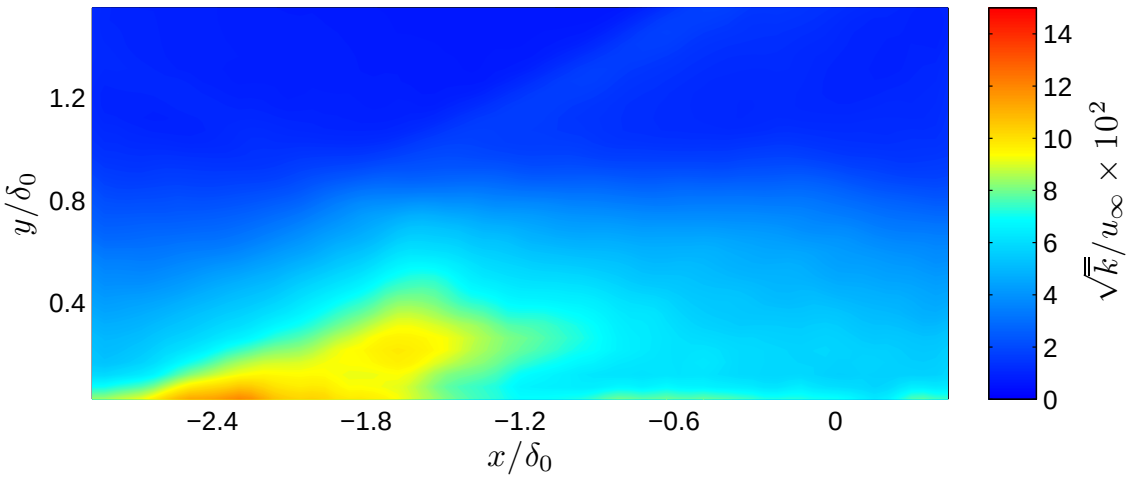

(a)

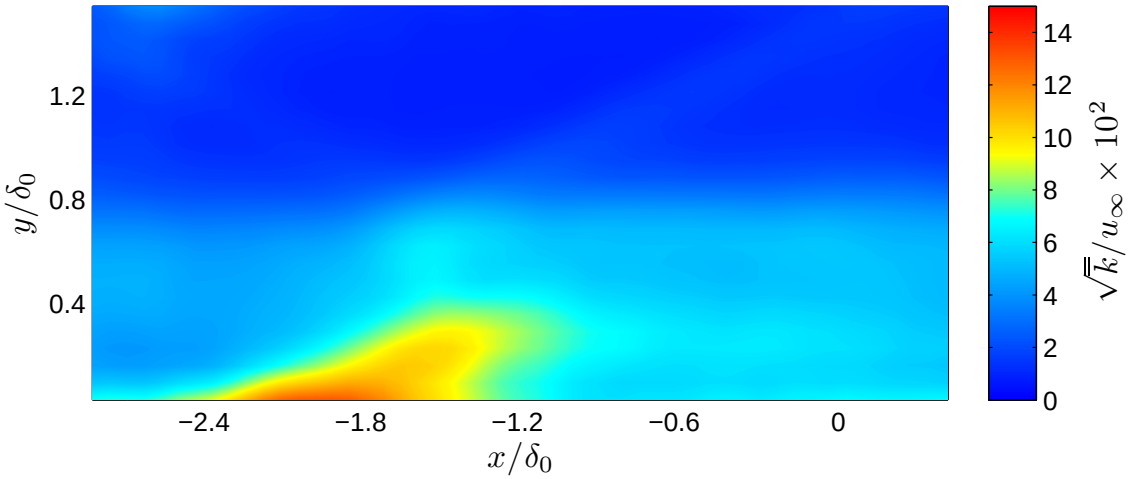

(b)

Figure 5.31: Streamwise image planes along the tunnel centerline showing mean turbulence kinetic energy fields from *(a)* the uncontrolled $\theta = 10.0$-deg interaction and *(b)* the $\theta = 10.0$-deg interaction with standard micro-ramp control.

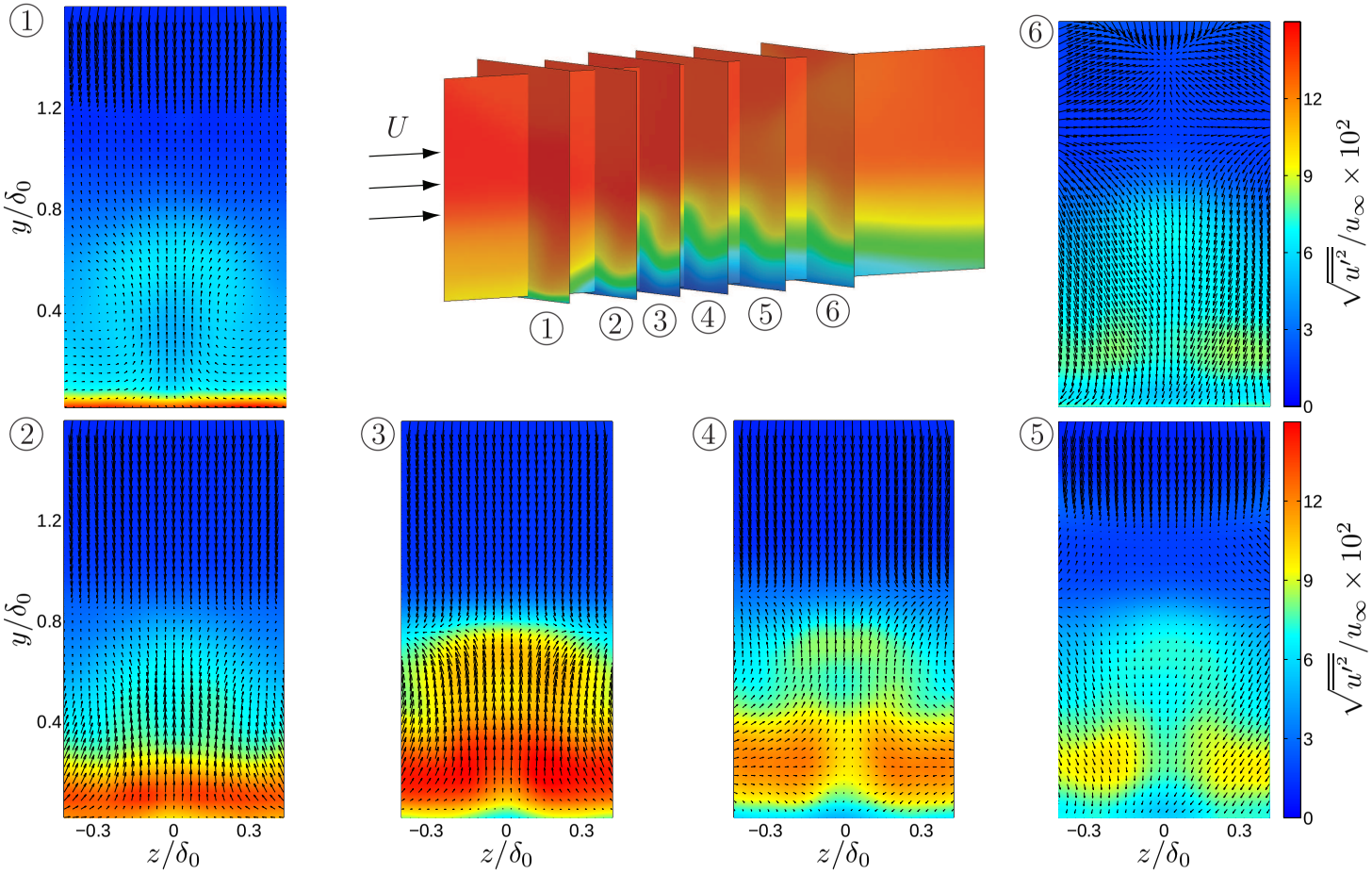

Figure 5.32: Color plots of u'_{RMS} show the SBLI region in transverse planes for a flow deflection angle of $\theta = 10.0$-deg and passive control via standard micro-ramps located at $x/\delta_0 = -9.42$. The averaged in-plane velocity fields ($\overline{v}$,$\overline{w}$) are overlayed as vectors. The six sampling locations correspond to 1: $x/\delta_0 = -2.5$, 2: $x/\delta_0 = -1.9$, 3: $x/\delta_0 = -1.5$, 4: $x/\delta_0 = -1.1$, 5: $x/\delta_0 = -0.6$, and 6: $x/\delta_0 = 0.0$. The central perspective plot shows the relative location of each plane.

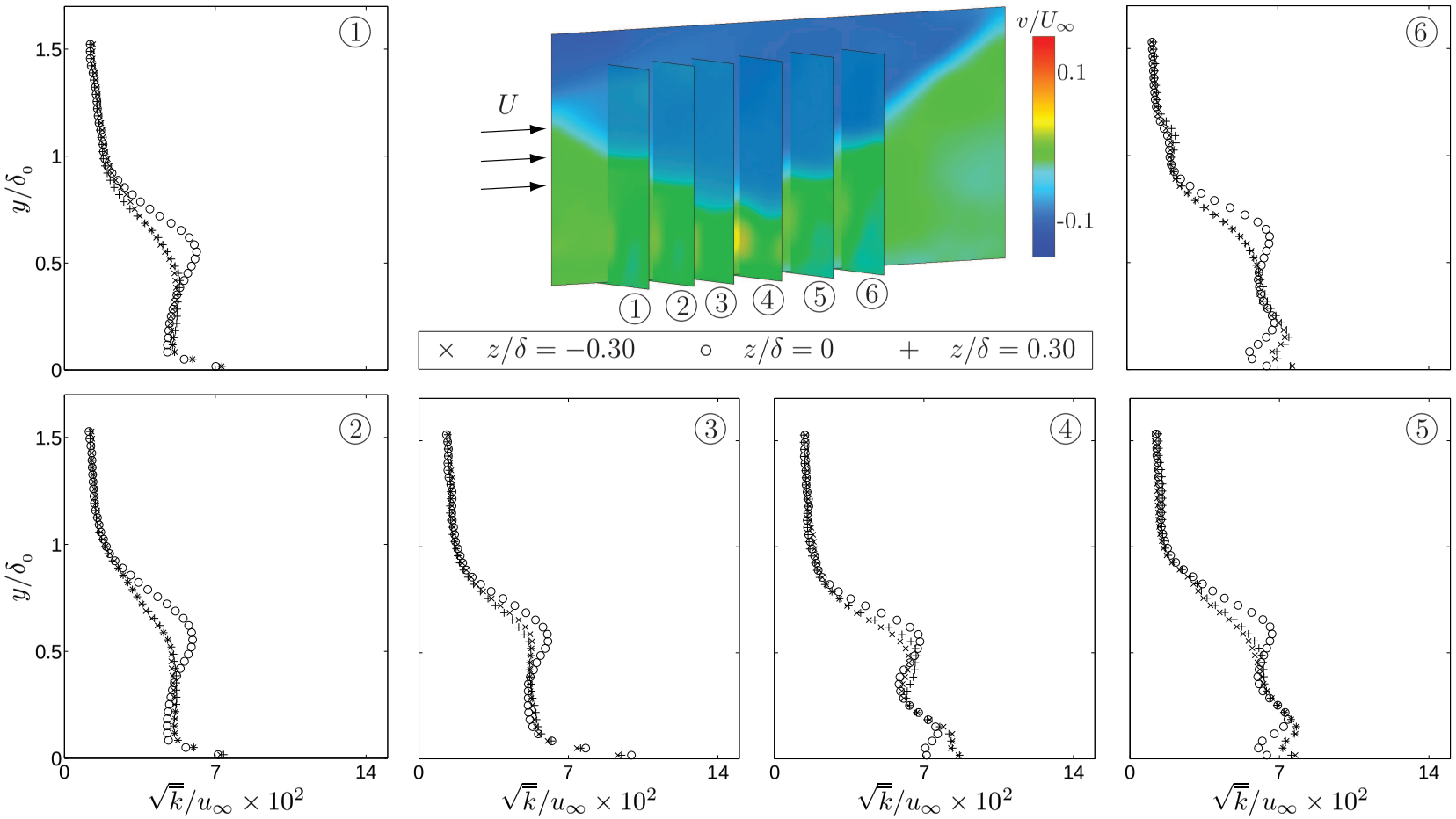

Figure 5.33: The evolution of $\overline{k}$ through the SBLI region is shown for a flow deflection angle of $\theta = 7.75$-deg and passive control via standard micro-ramps located at $x/\delta_0 = -8.50$. The six sampling locations correspond to 1: $x/\delta_0 = -2.0$, 2: $x/\delta_0 = -1.55$, 3: $x/\delta_0 = -1.2$, 4: $x/\delta_0 = -0.7$, 5: $x/\delta_0 = -0.2$, and 6: $x/\delta_0 = +0.3$. At top, colors show the $\overline{v}$ field throughout each plane and show the relative location of each plane.

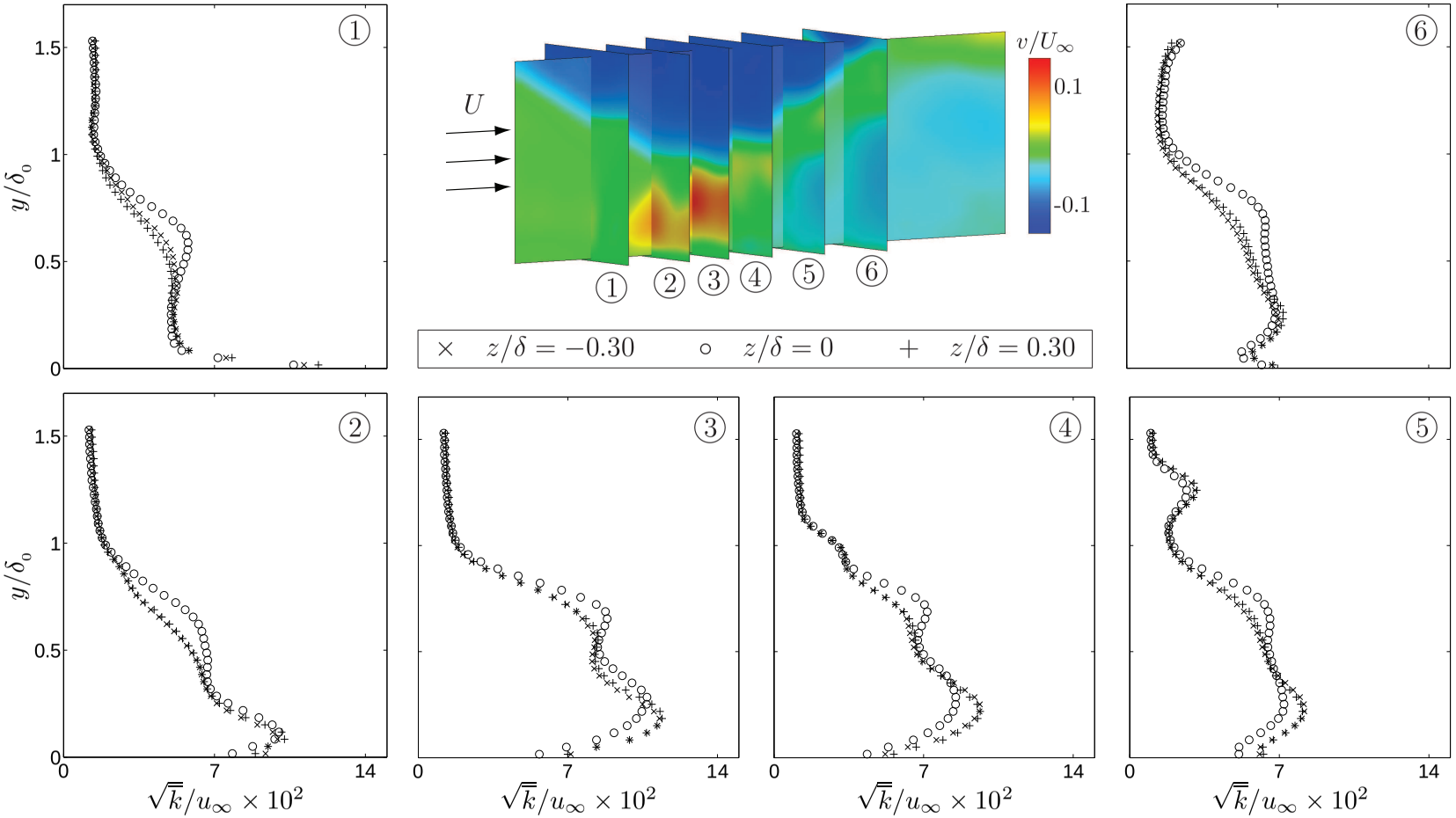

Figure 5.34: The evolution of $\overline{k}$ through the SBLI region is shown for a flow deflection angle of $\theta = 10.0$-deg and passive control via standard micro-ramps located at $x/\delta_0 = -9.42$. The six sampling locations correspond to 1: $x/\delta_0 = -2.5$, 2: $x/\delta_0 = -1.9$, 3: $x/\delta_0 = -1.5$, 4: $x/\delta_0 = -1.1$, 5: $x/\delta_0 = -0.6$, and 6: $x/\delta_0 = 0.0$. At top, colors show the $\overline{v}$ field throughout each plane and show the relative location of each plane.

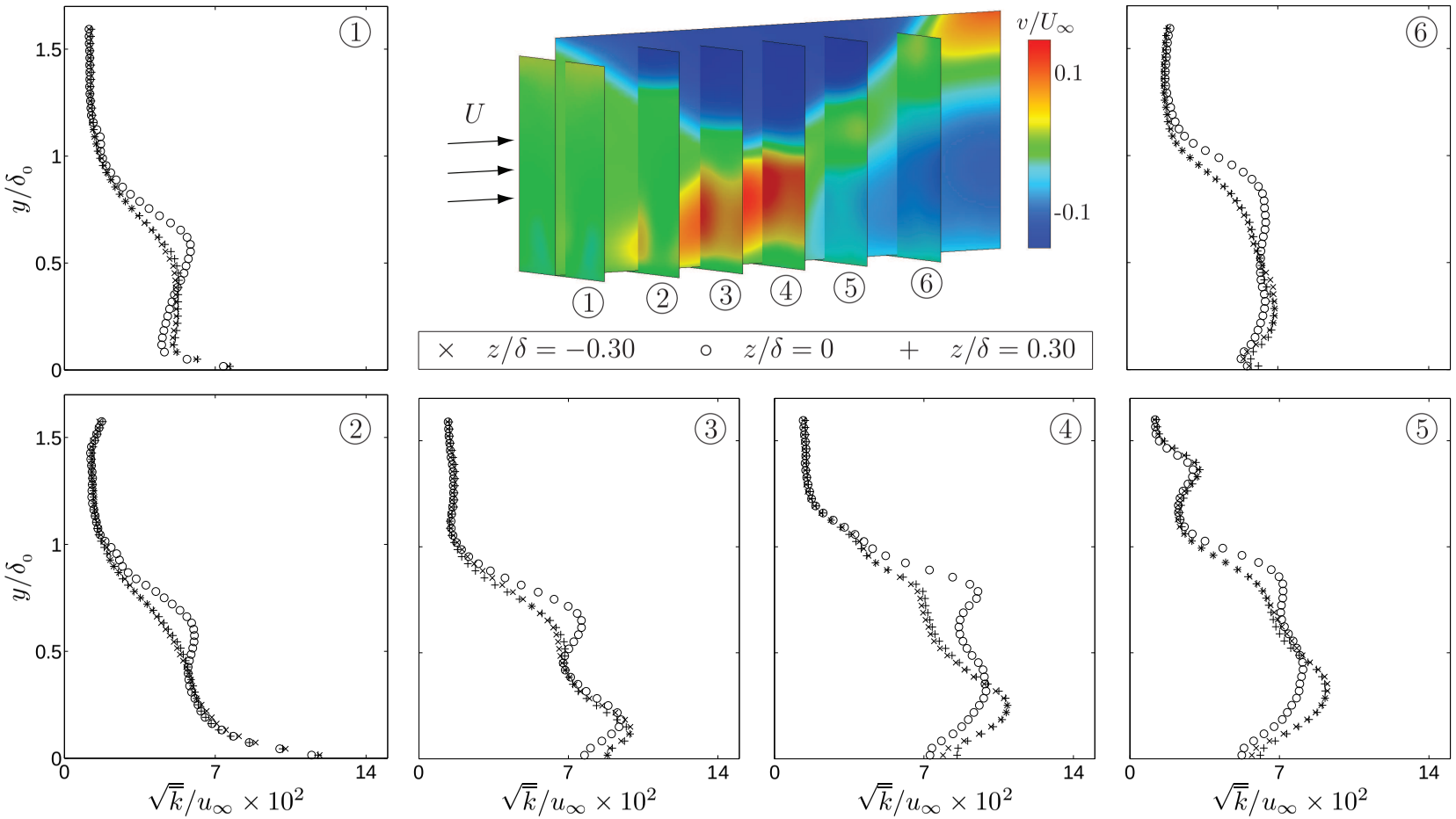

Figure 5.35: The evolution of $\overline{k}$ through the SBLI region is shown for a flow deflection angle of $\theta = 12.0$-deg and passive control via standard micro-ramps located at $x/\delta_0 = -9.76$. The six sampling locations correspond to 1: $x/\delta_0 = -3.6$, 2: $x/\delta_0 = -2.9$, 3: $x/\delta_0 = -2.3$, 4: $x/\delta_0 = -1.7$, 5: $x/\delta_0 = -1.1$, and 6: $x/\delta_0 = -0.4$. At top, colors show the $\overline{v}$ field throughout each plane and show the relative location of each plane.

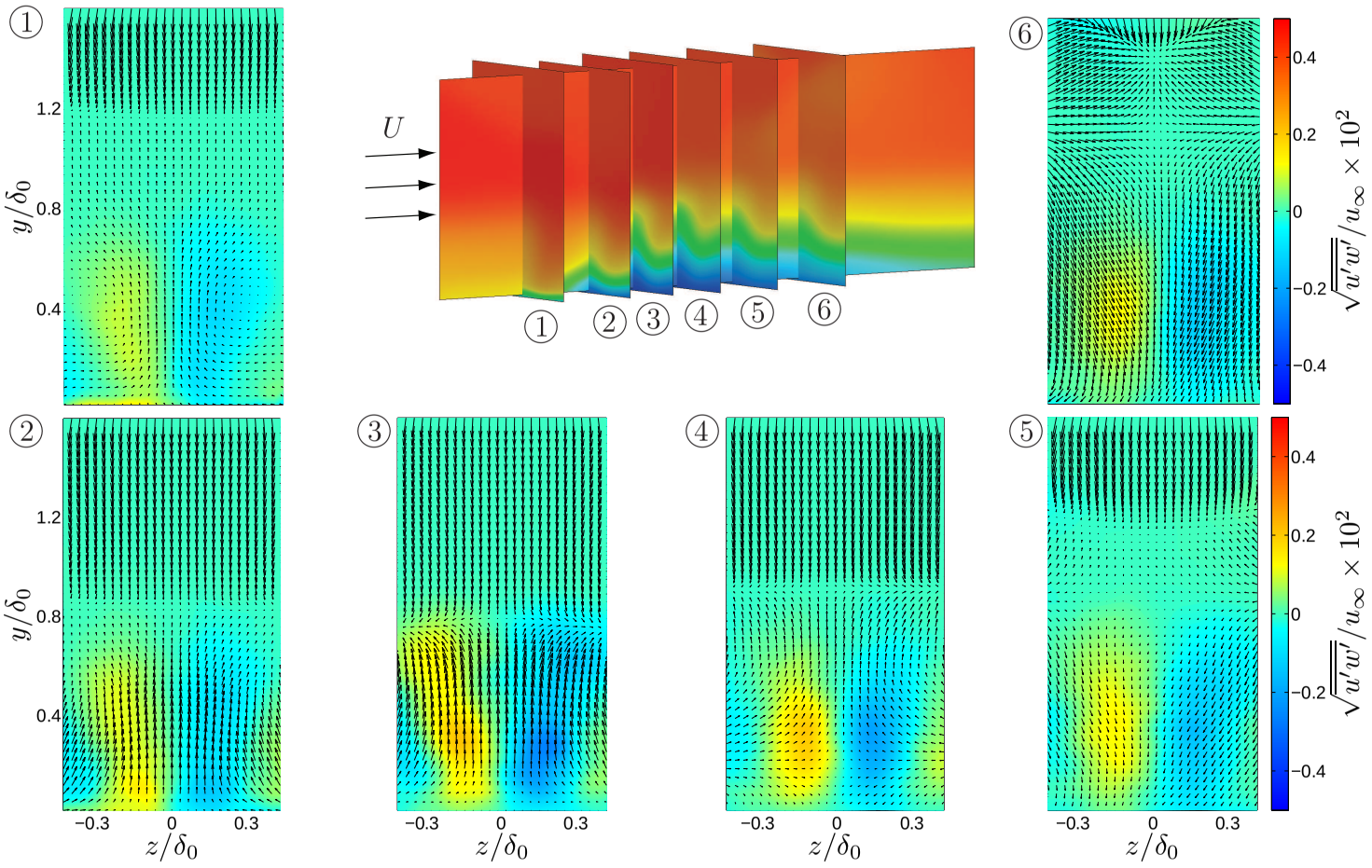

Figure 5.36: Color plots of $\overline{u'w'}$ show the SBLI region in transverse planes for a flow deflection angle of $\theta = 10.0$-deg and passive control via standard micro-ramps located at $x/\delta_0 = -9.42$. The averaged in-plane velocity fields ($\overline{v}$,$\overline{w}$) are overlayed as vectors. The six sampling locations correspond to 1: $x/\delta_0 = -2.5$, 2: $x/\delta_0 = -1.9$, 3: $x/\delta_0 = -1.5$, 4: $x/\delta_0 = -1.1$, 5: $x/\delta_0 = -0.6$, and 6: $x/\delta_0 = 0.0$. The central perspective plot shows the relative location of each plane.

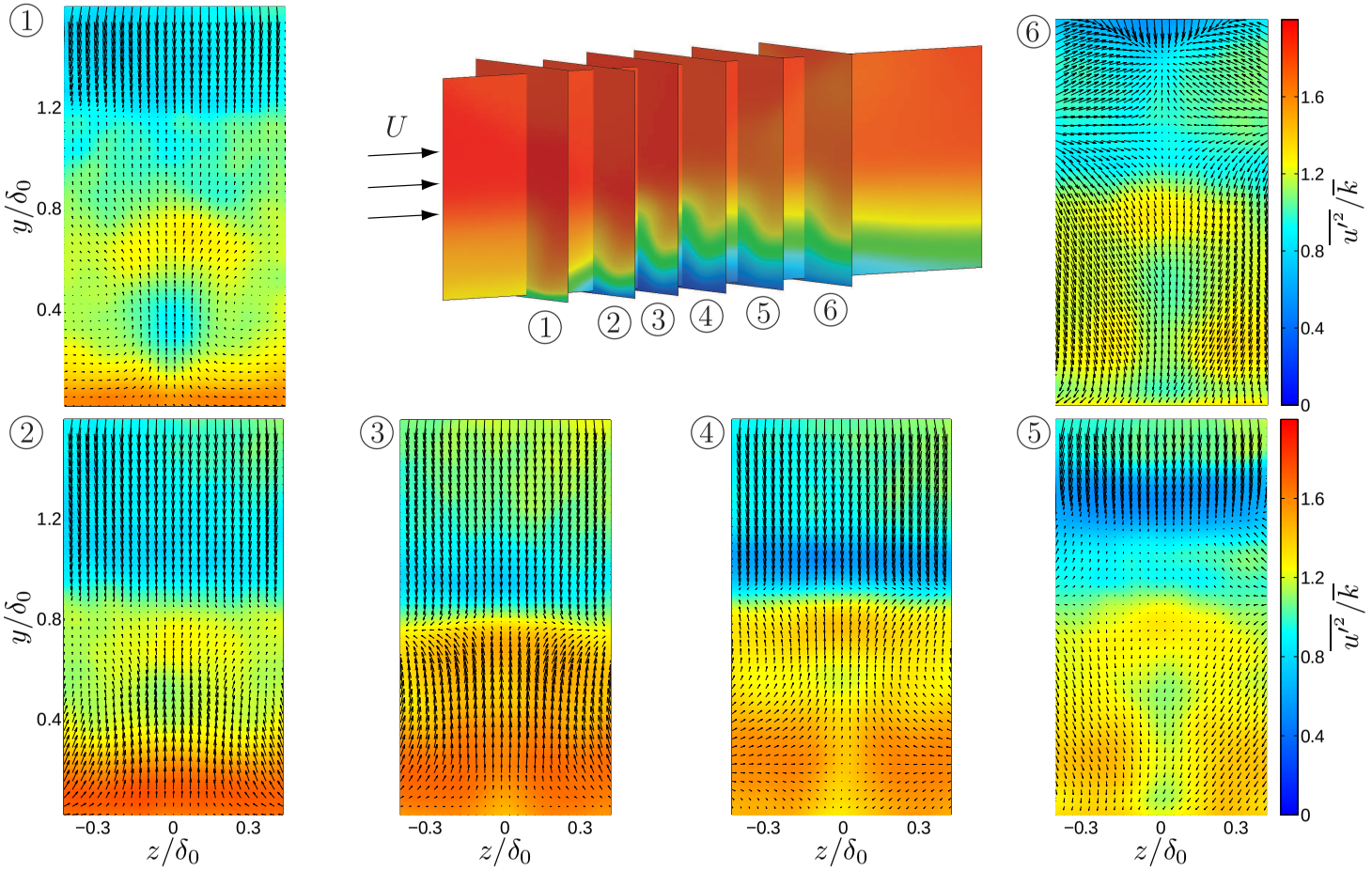

Figure 5.37: Color plots of $\overline{u'^2}/\overline{k}$ show the SBLI region in transverse planes for a flow deflection angle of $\theta = 10.0$-deg and passive control via standard micro-ramps located at $x/\delta_0 = -9.42$. The averaged in-plane velocity fields ($\overline{v}$,$\overline{w}$) are overlayed as vectors. The six sampling locations correspond to 1: $x/\delta_0 = -2.5$, 2: $x/\delta_0 = -1.9$, 3: $x/\delta_0 = -1.5$, 4: $x/\delta_0 = -1.1$, 5: $x/\delta_0 = -0.6$, and 6: $x/\delta_0 = 0.0$. The central perspective plot shows the relative location of each plane.

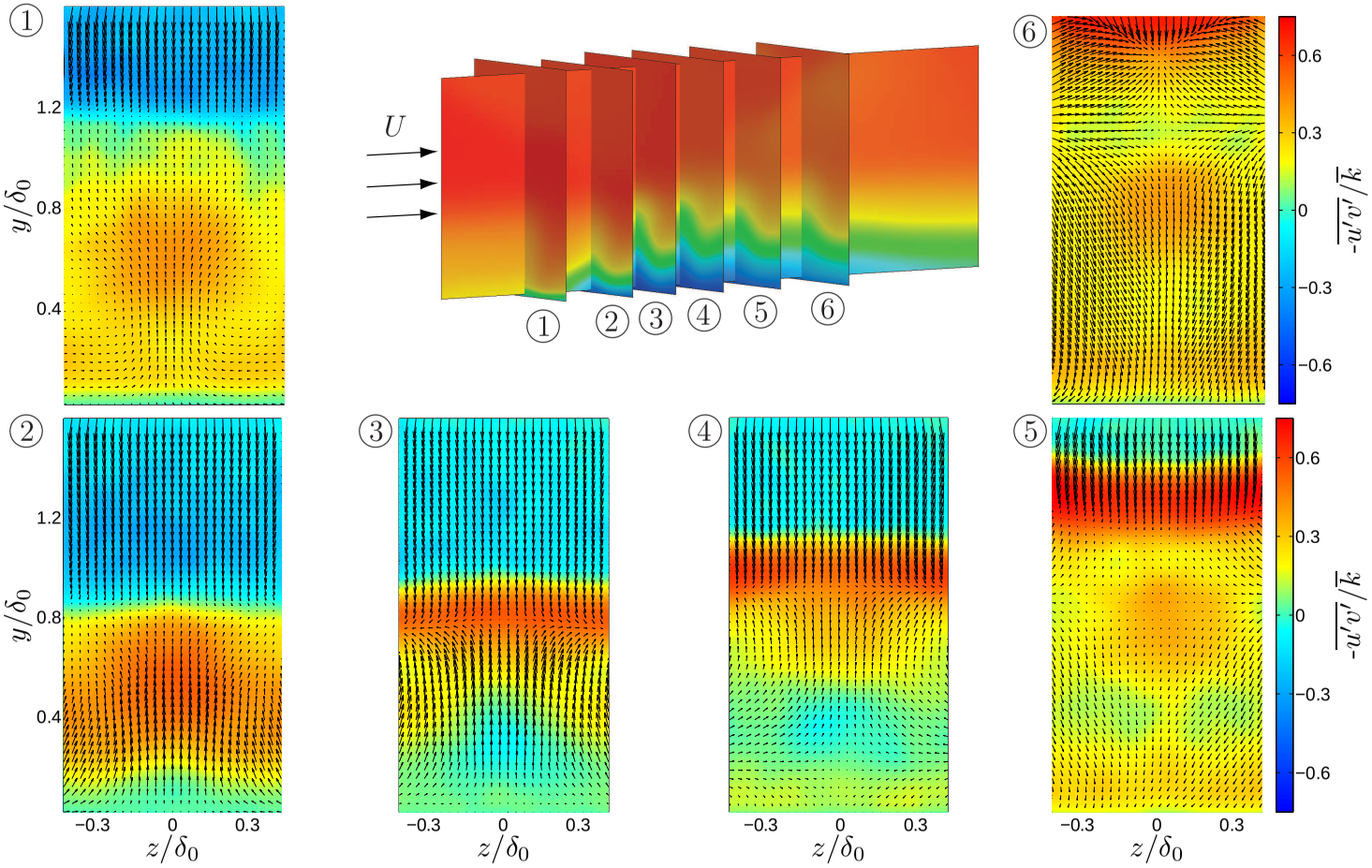

Figure 5.38: Color plots of $\overline{u'v'}/\overline{k}$ show the SBLI region in transverse planes for a flow deflection angle of $\theta = 10.0$-deg and passive control via standard micro-ramps located at $x/\delta_0 = -9.42$. The averaged in-plane velocity fields ($\overline{v}$,$\overline{w}$) are overlayed as vectors. The six sampling locations correspond to 1: $x/\delta_0 = -2.5$, 2: $x/\delta_0 = -1.9$, 3: $x/\delta_0 = -1.5$, 4: $x/\delta_0 = -1.1$, 5: $x/\delta_0 = -0.6$, and 6: $x/\delta_0 = 0.0$. The central perspective plot shows the relative location of each plane.

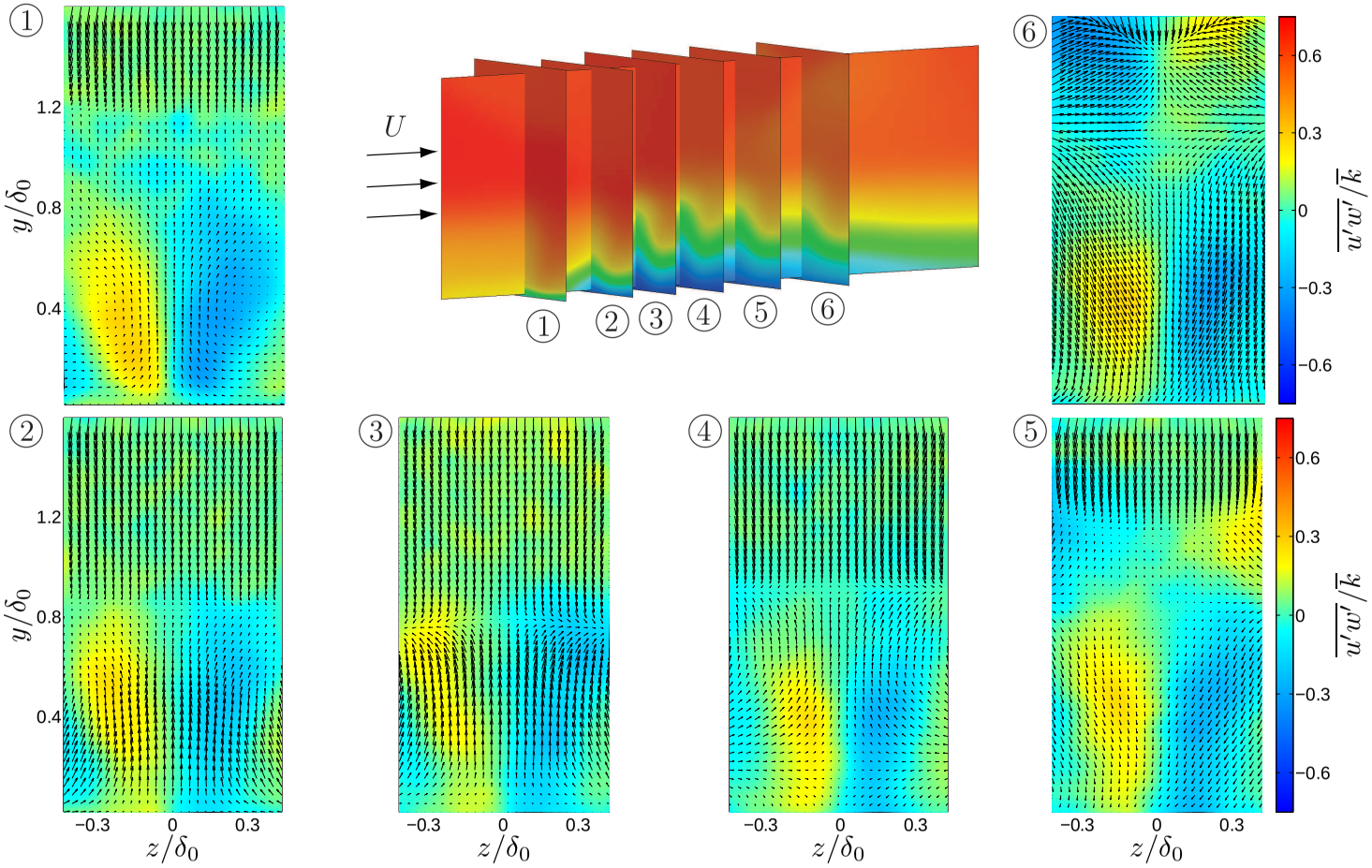

Figure 5.39: Color plots of $\overline{u'w'}/\overline{k}$ show the SBLI region in transverse planes for a flow deflection angle of $\theta = 10.0$-deg and passive control via standard micro-ramps located at $x/\delta_0 = -9.42$. The averaged in-plane velocity fields ($\overline{v}$,$\overline{w}$) are overlayed as vectors. The six sampling locations correspond to 1: $x/\delta_0 = -2.5$, 2: $x/\delta_0 = -1.9$, 3: $x/\delta_0 = -1.5$, 4: $x/\delta_0 = -1.1$, 5: $x/\delta_0 = -0.6$, and 6: $x/\delta_0 = 0.0$. The central perspective plot shows the relative location of each plane.

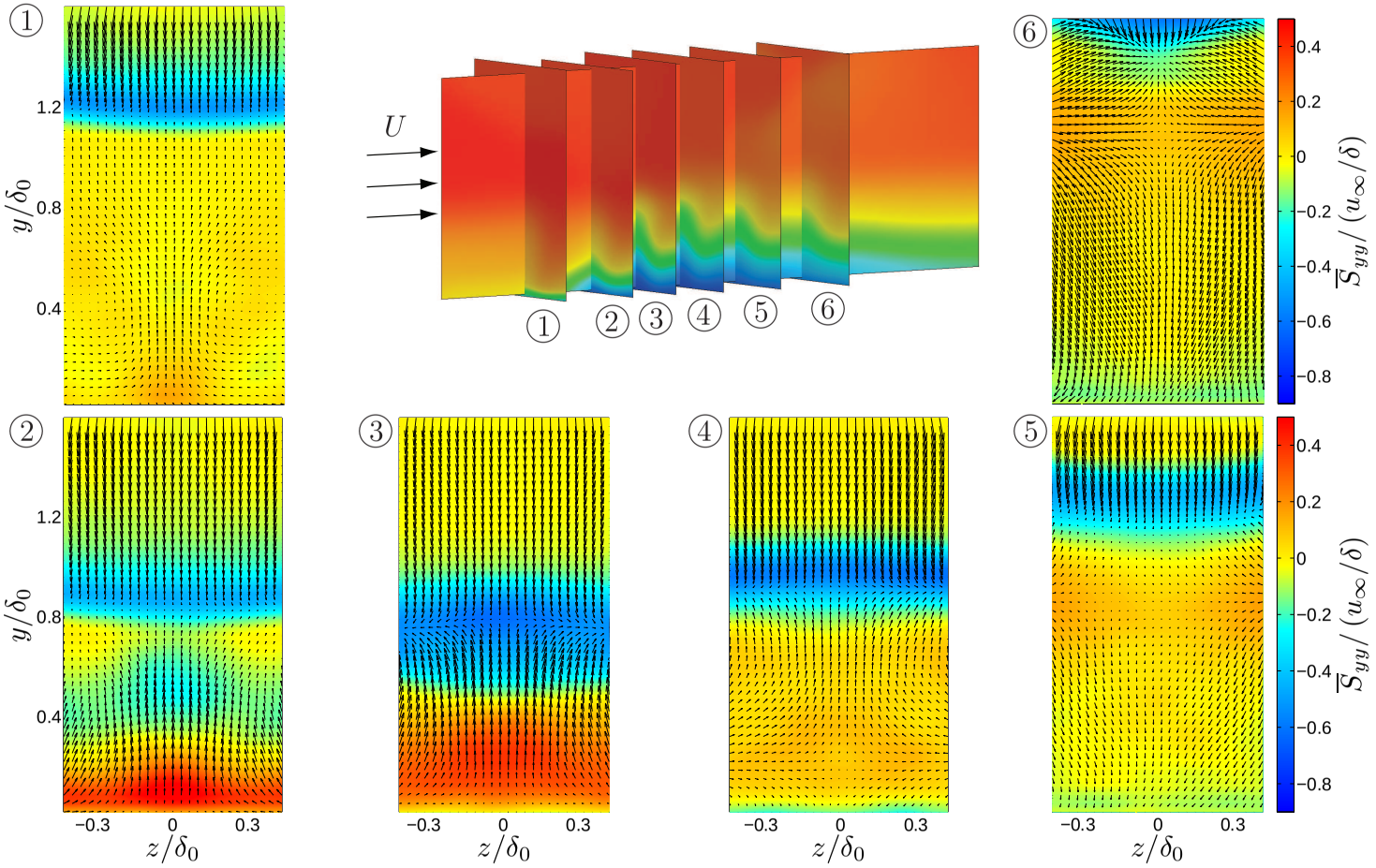

Figure 5.40: Color plots of $\overline{S}_{yy}$ show the SBLI region in transverse planes for a flow deflection angle of $\theta = 10.0$-deg and passive control via standard micro-ramps located at $x/\delta_0 = -9.42$. The averaged in-plane velocity fields ($\overline{v}$,$\overline{w}$) are overlayed as vectors. The six sampling locations correspond to 1: $x/\delta_0 = -2.5$, 2: $x/\delta_0 = -1.9$, 3: $x/\delta_0 = -1.5$, 4: $x/\delta_0 = -1.1$, 5: $x/\delta_0 = -0.6$, and 6: $x/\delta_0 = 0.0$. The central perspective plot shows the relative location of each plane.

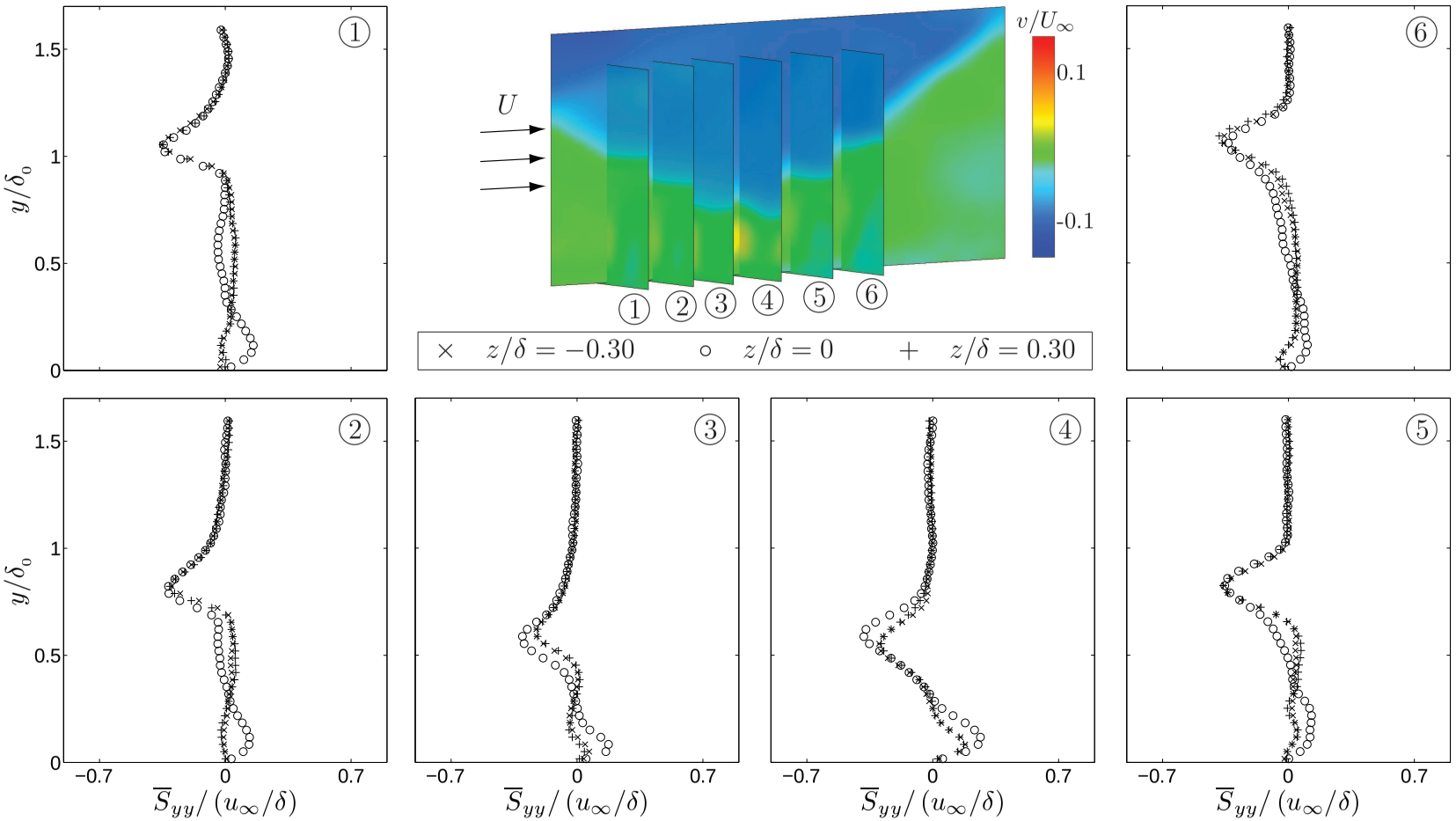

Figure 5.41: The evolution of $\overline{S}_{yy}$ through the SBLI region is shown for a flow deflection angle of $\theta = 7.75$-deg and passive control via standard micro-ramps located at $x/\delta_0 = -8.50$. The six sampling locations correspond to 1: $x/\delta_0 = -2.0$, 2: $x/\delta_0 = -1.55$, 3: $x/\delta_0 = -1.2$, 4: $x/\delta_0 = -0.7$, 5: $x/\delta_0 = -0.2$, and 6: $x/\delta_0 = +0.3$. At top, colors show the $\overline{v}$ field throughout each plane and show the relative location of each plane.

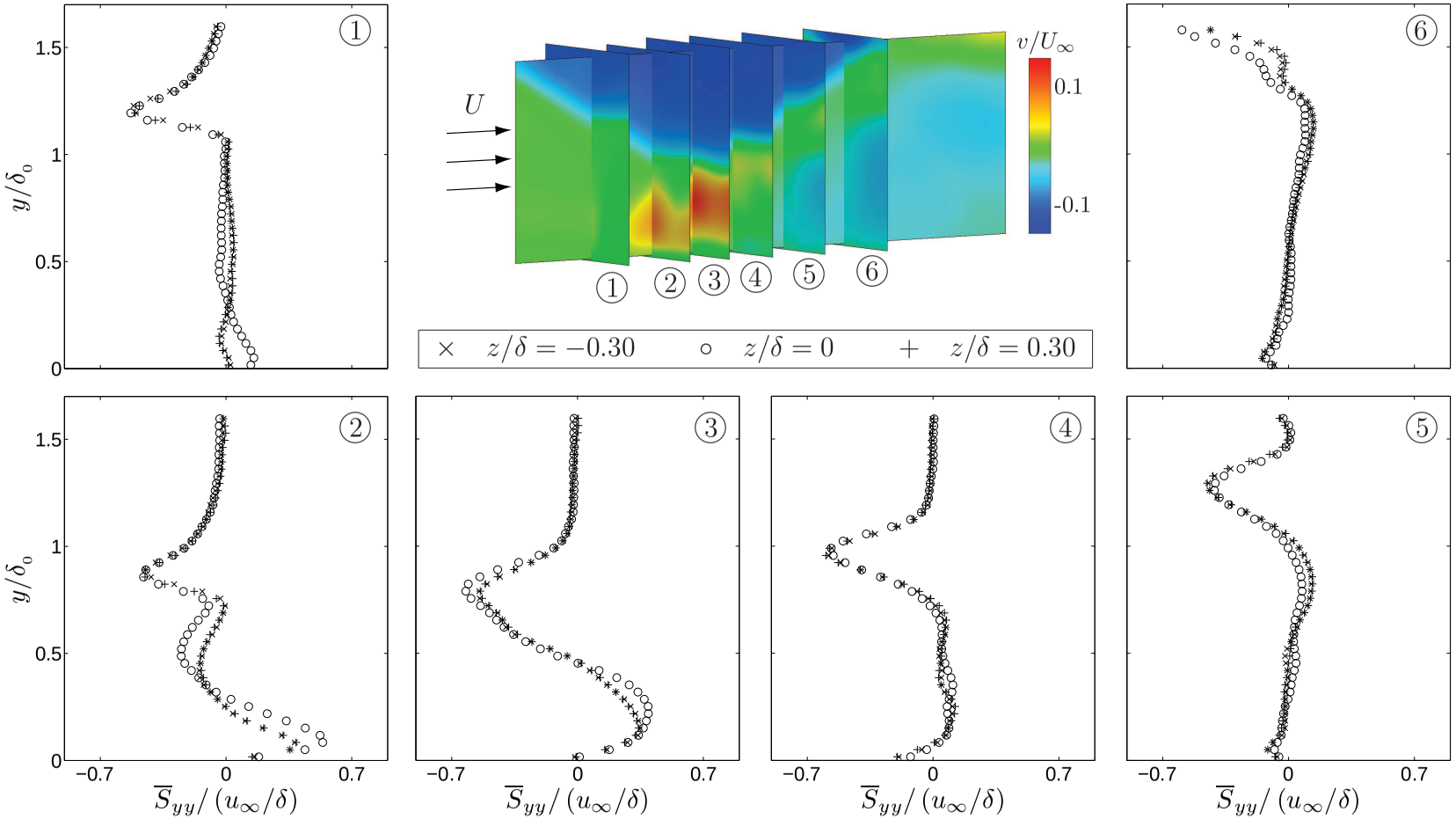

Figure 5.42: The evolution of $\overline{S}_{yy}$ through the SBLI region is shown for a flow deflection angle of $\theta = 10.0$-deg and passive control via standard micro-ramps located at $x/\delta_0 = -9.42$. The six sampling locations correspond to 1: $x/\delta_0 = -2.5$, 2: $x/\delta_0 = -1.9$, 3: $x/\delta_0 = -1.5$, 4: $x/\delta_0 = -1.1$, 5: $x/\delta_0 = -0.6$, and 6: $x/\delta_0 = 0.0$. At top, colors show the $\overline{v}$ field throughout each plane and show the relative location of each plane.

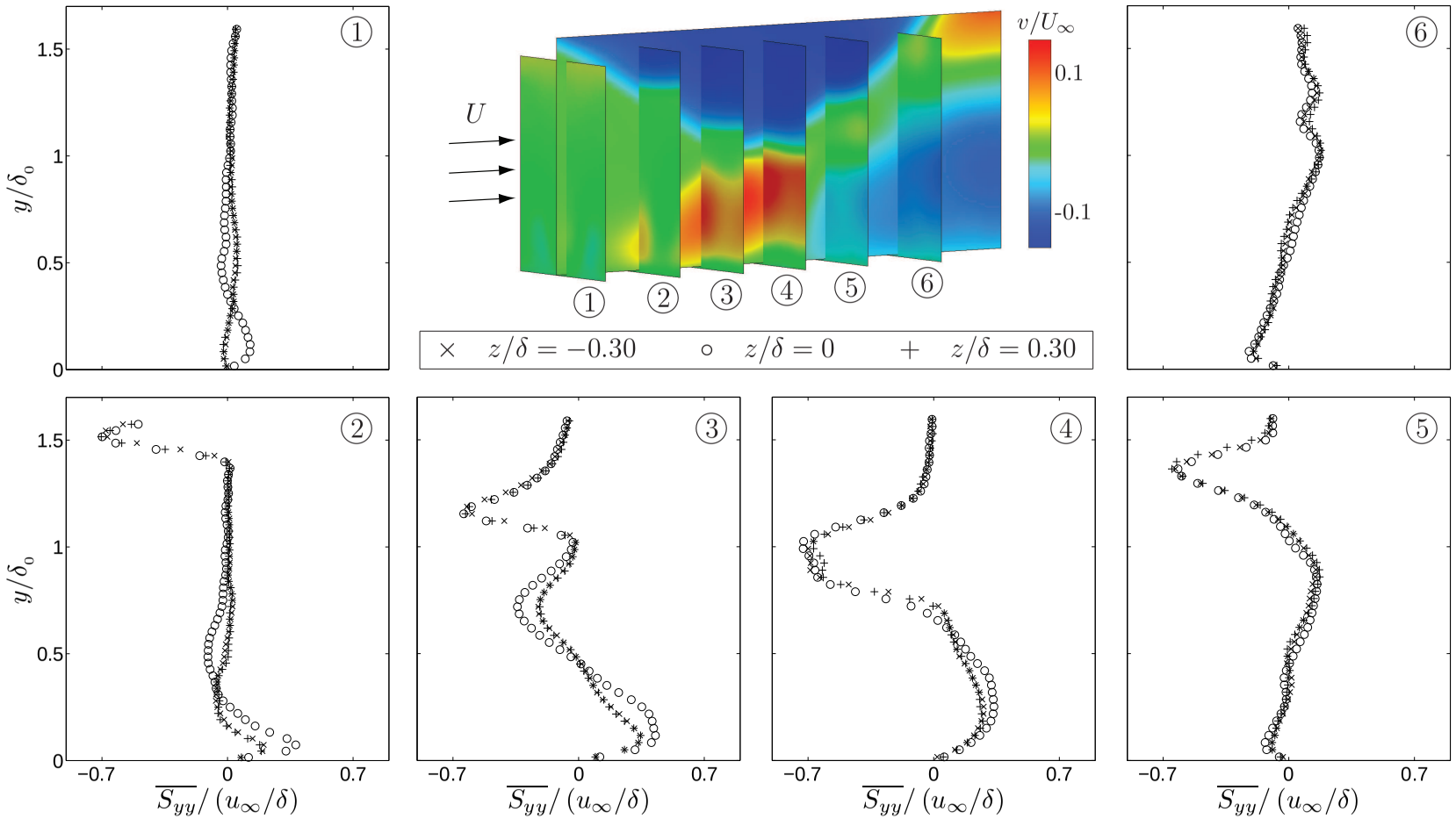

Figure 5.43: The evolution of $\overline{S}_{yy}$ through the SBLI region is shown for a flow deflection angle of $\theta = 12.0$-deg and passive control via standard micro-ramps located at $x/\delta_0 = -9.76$. The six sampling locations correspond to 1: $x/\delta_0 = -3.6$, 2: $x/\delta_0 = -2.9$, 3: $x/\delta_0 = -2.3$, 4: $x/\delta_0 = -1.7$, 5: $x/\delta_0 = -1.1$, and 6: $x/\delta_0 = -0.4$. At top, colors show the $\overline{v}$ field throughout each plane and show the relative location of each plane.

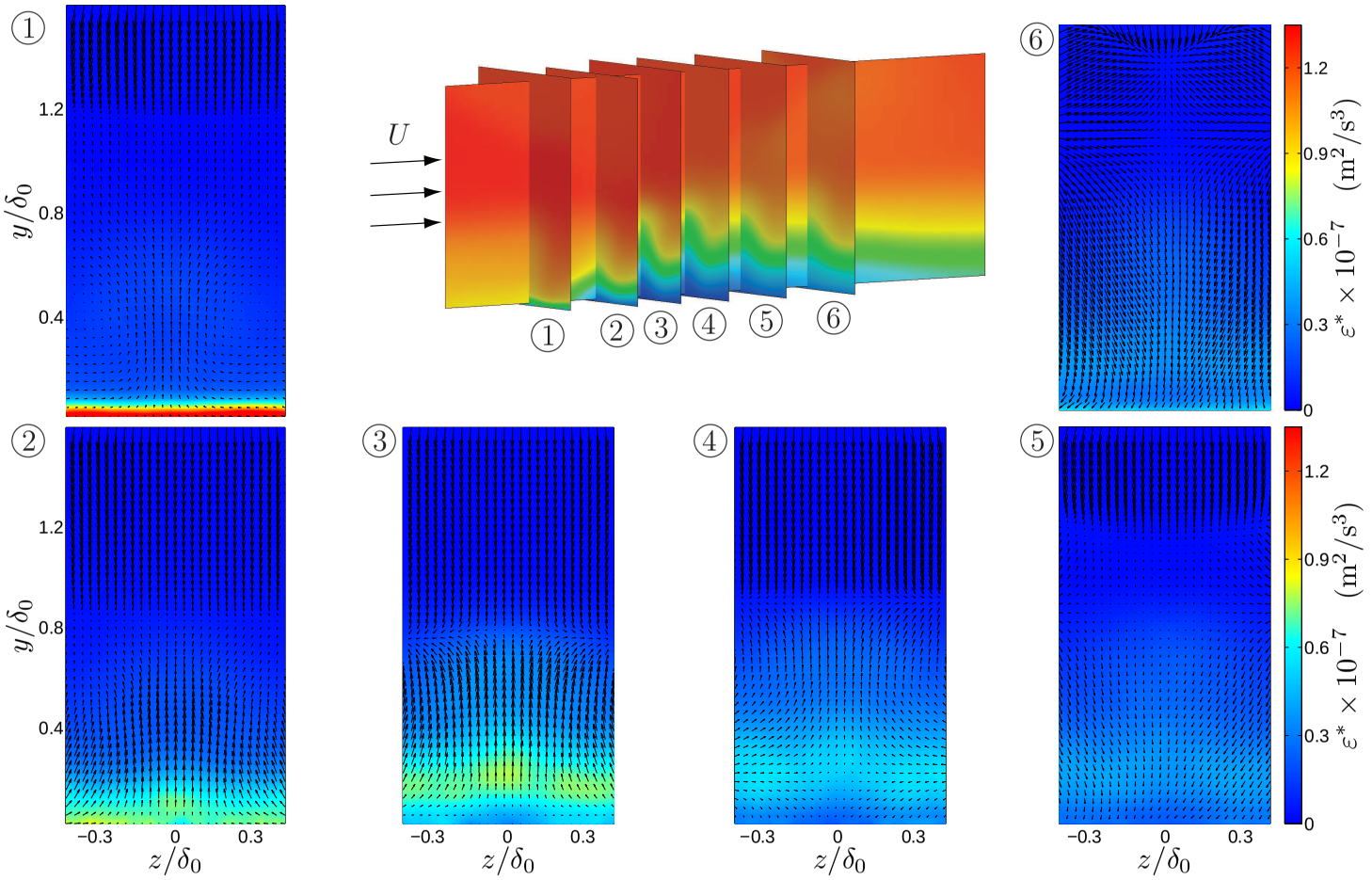

Figure 5.44: Color plots of ε^* show the SBLI region in transverse planes for a flow deflection angle of $\theta = 10.0$-deg and passive control via standard micro-ramps located at $x/\delta_0 = -9.42$. The averaged in-plane velocity fields ($\overline{v}$,$\overline{w}$) are overlayed as vectors. The six sampling locations correspond to 1: $x/\delta_0 = -2.5$, 2: $x/\delta_0 = -1.9$, 3: $x/\delta_0 = -1.5$, 4: $x/\delta_0 = -1.1$, 5: $x/\delta_0 = -0.6$, and 6: $x/\delta_0 = 0.0$. The central perspective plot shows the relative location of each plane.

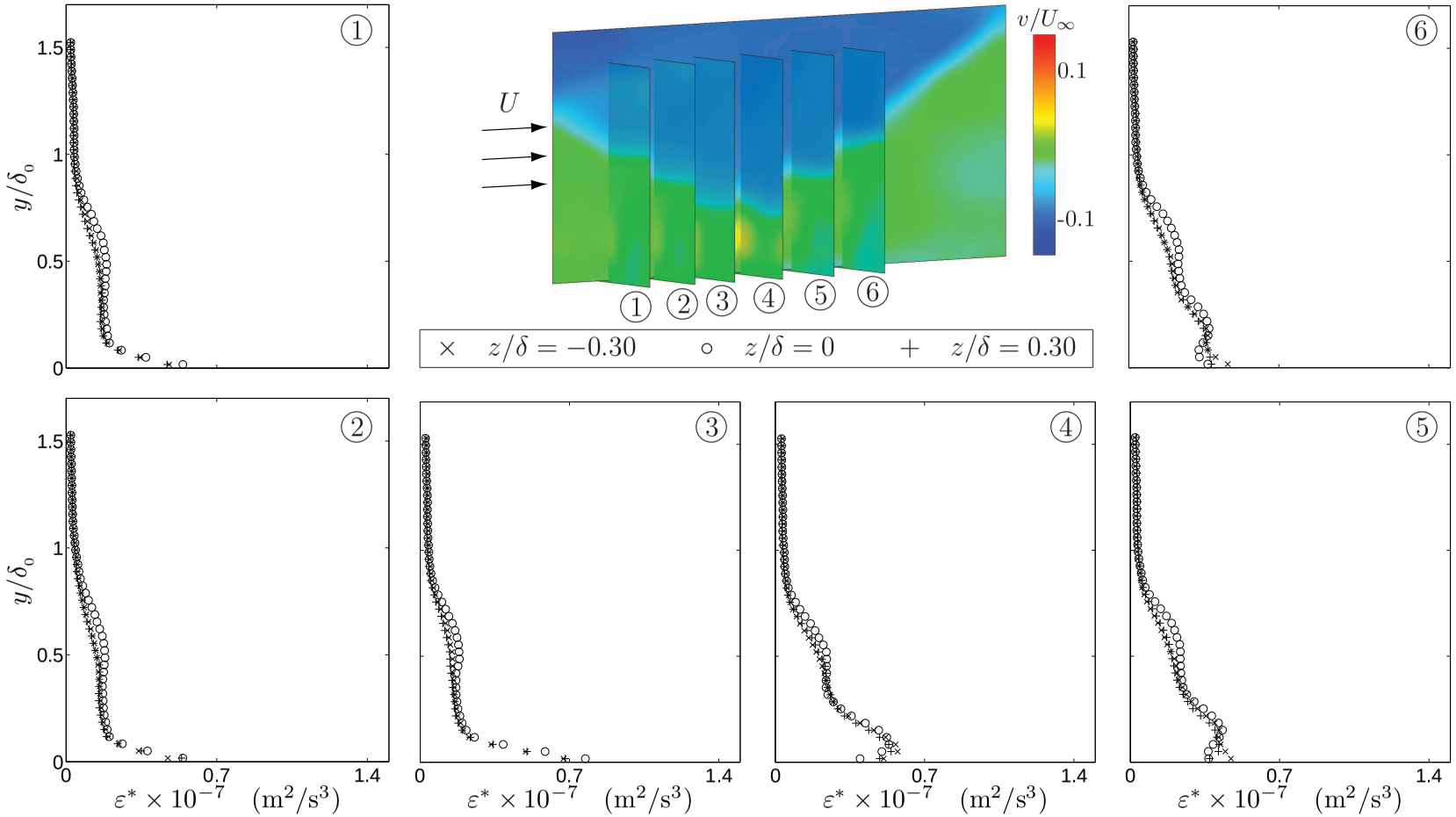

Figure 5.45: The evolution of ε^* through the SBLI region is shown for a flow deflection angle of $\theta = 7.75$-deg and passive control via standard micro-ramps located at $x/\delta_0 = -8.50$. The six sampling locations correspond to 1: $x/\delta_0 = -2.0$, 2: $x/\delta_0 = -1.55$, 3: $x/\delta_0 = -1.2$, 4: $x/\delta_0 = -0.7$, 5: $x/\delta_0 = -0.2$, and 6: $x/\delta_0 = +0.3$. At top, colors show the $\overline{v}$ field throughout each plane and show the relative location of each plane.

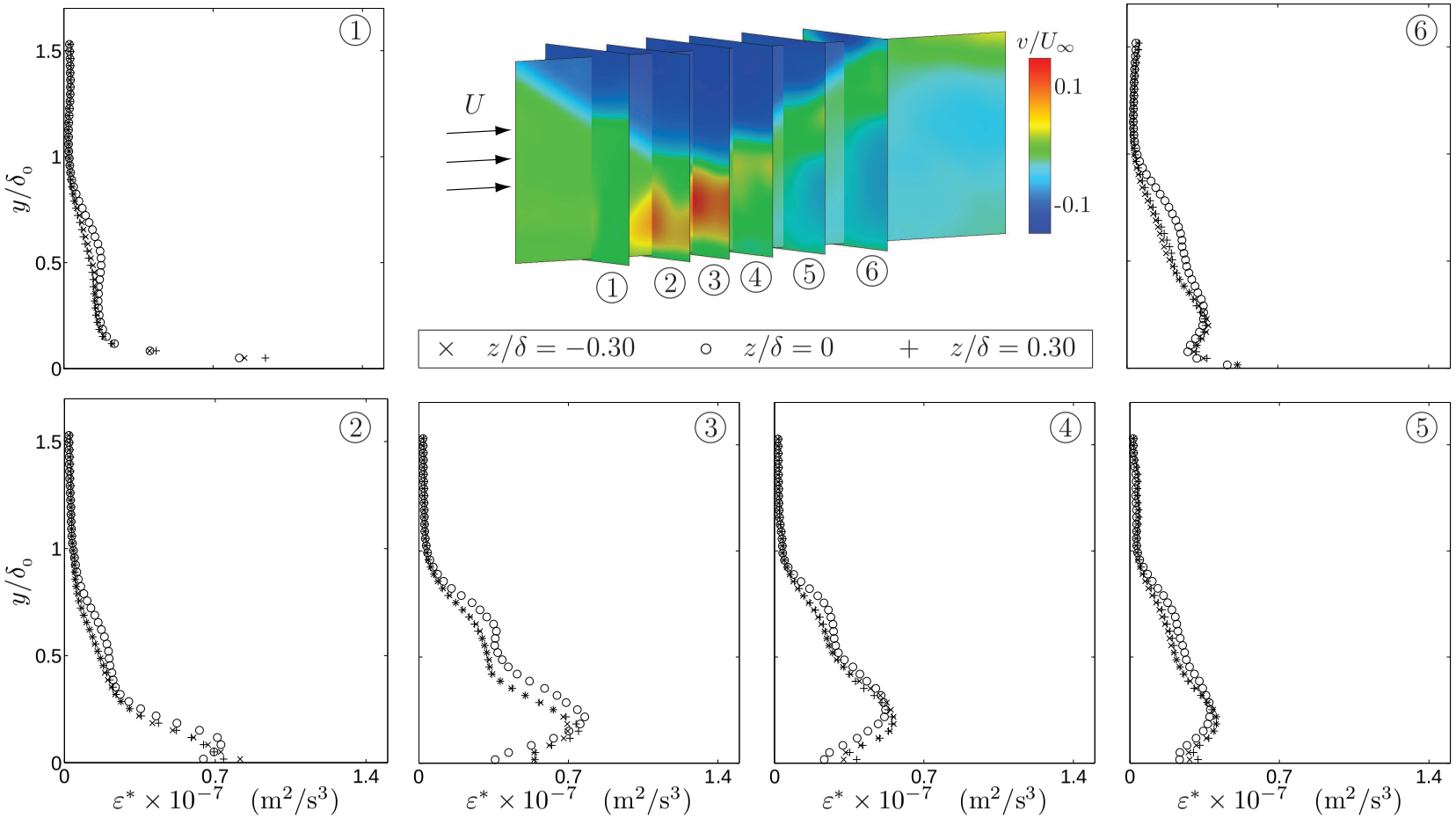

Figure 5.46: The evolution of ε^* through the SBLI region is shown for a flow deflection angle of $\theta = 10.0$-deg and passive control via standard micro-ramps located at $x/\delta_0 = -9.42$. The six sampling locations correspond to 1: $x/\delta_0 = -2.5$, 2: $x/\delta_0 = -1.9$, 3: $x/\delta_0 = -1.5$, 4: $x/\delta_0 = -1.1$, 5: $x/\delta_0 = -0.6$, and 6: $x/\delta_0 = 0.0$. At top, colors show the $\overline{v}$ field throughout each plane and show the relative location of each plane.

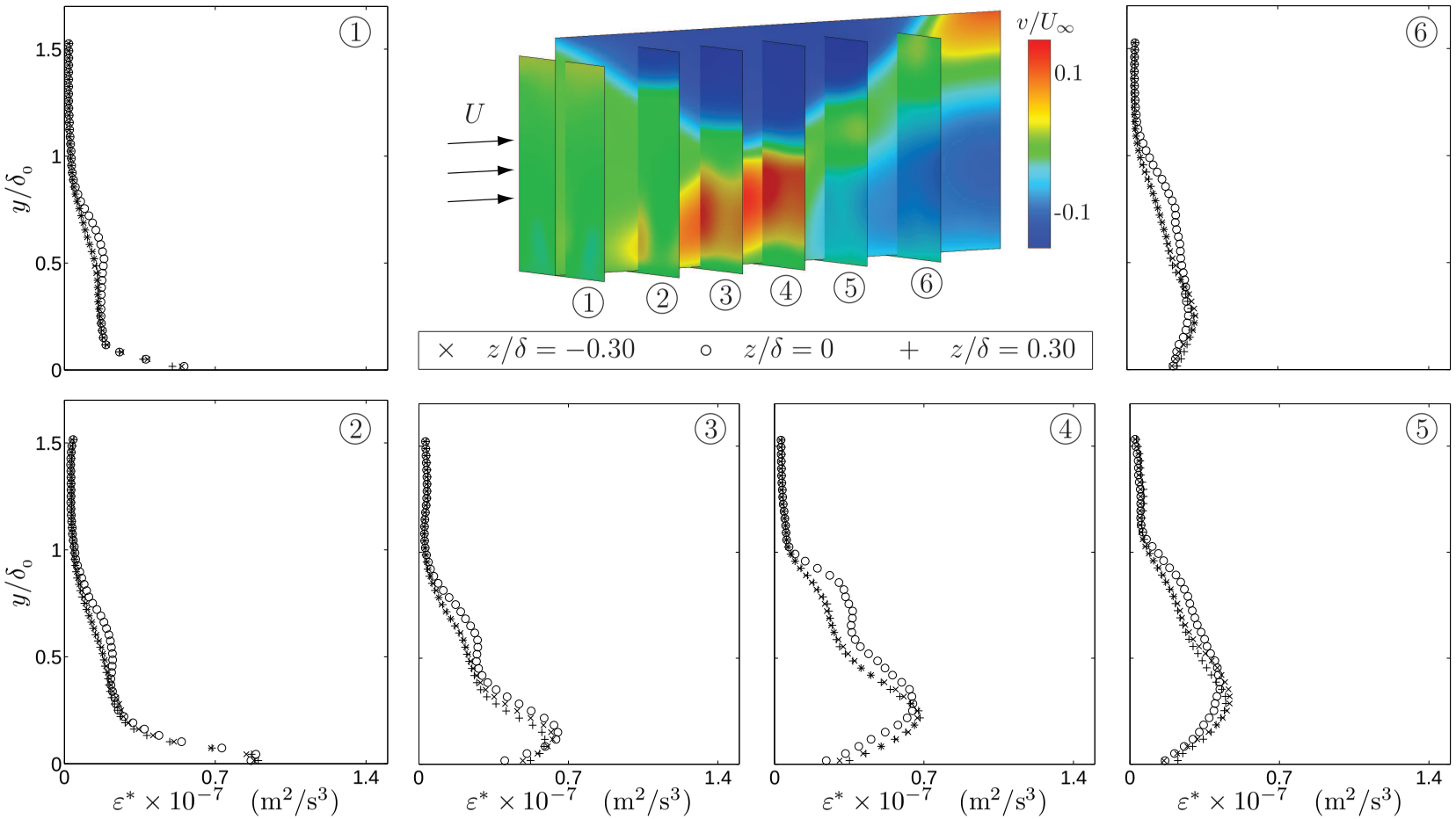

Figure 5.47: The evolution of ε^* through the SBLI region is shown for a flow deflection angle of $\theta = 12.0$-deg and passive control via standard micro-ramps located at $x/\delta_0 = -9.76$. The six sampling locations correspond to 1: $x/\delta_0 = -3.6$, 2: $x/\delta_0 = -2.9$, 3: $x/\delta_0 = -2.3$, 4: $x/\delta_0 = -1.7$, 5: $x/\delta_0 = -1.1$, and 6: $x/\delta_0 = -0.4$. At top, colors show the $\overline{v}$ field throughout each plane and show the relative location of each plane.

CHAPTER VI

Passive Boundary Layer Control Using a Novel "Inverse" Micro-Ramp

The standard micro-ramp design investigated in Chapter V shows promise under certain design conditions, with particular benefit coming from reductions in the peak spanwise-averaged displacement thickness. In addition to their potentially favorable effect on the shock–boundary layer interaction (SBLI), their passive and structurally robust nature are notable advantages over other more fragile or complicated boundary layer control concepts. Still, the effects are not overwhelmingly positive and leave one looking for improvement.

Of fundamental importance to the vortex generator concept is the behavior of the streamwise vortex pair as it propagates downstream, and in particular how the vortex-vortex interactions affect this trajectory. Figure 6.1 shows the standard micro-ramp design from the same downstream vantage as in Fig. 5.1, this time also schematically showing the vortex-vortex interactions. The effect of Vortex 2 on Vortex 1, F_{21}, is to push Vortex 1 in the upward direction, and the same is true for the effect of Vortex 1 on Vortex 2, F_{12}. The effect of the wall on the vortex pair is deduced by considering an image vortex pair, which is a reflection of the real vortices across the boundary. The image vortex pair is shown by the dotted lines in Figure 6.1.

The effect of these image vortices on the actual vortex pair, and by extension the effect of the wall, is to pull the constituent vortices toward each other. Furthermore, since the initially separate constituent vortices are counter-rotating, the strength of Vortex 1 negates the strength of Vortex 2 as the pair is drawn together.

Thus the effect of the vortex-vortex interaction under the the standard micro-ramp design is to pull the vortices together, thereby limiting the spanwise area "controlled" by each individual ramp, while additionally diminishing the strength of the vortex pair. Furthermore, the vortex-vortex interaction drives the pair up out of the boundary layer. Evidence of these effects can be seen in the oil streak and pitot probe measurements of Ford and Babinsky (2007). The oil streak visualizations are reproduced here in Fig. 6.2, and show clearly that the influence of the individual standard ramps is limited to the region directly downstream of the structure. Streamlines from the RANS simulation of Galbraith et al. (2009), which are shown in Fig. 6.3, provide further evidence of this.

Figure 6.2 demonstrates the small inter-ramp spacing s, and thus the large number of individual ramps, required for the standard micro-ramp array to provide constant manipulation of the boundary layer over the spanwise dimension. In fact, the lack of influence in the space between the standard ramps led to Galbraith et al. (2009) arranging the individual ramps in a staggered two-row configuration in order to provide continuous control across the span. Naturally, it would instead be desirable for the constituent vortices produced by the passive control feature to spread away from each other, thus allowing each individual feature to impart control over a larger spanwise area so that ultimately fewer individual features are required. Additionally, it is desirable for the vortex pair to remain deep in the boundary layer so that its designed influence persists farther downstream and leaves the nominally qui-

escent free stream undisturbed. In essence, the vortex-vortex interactions resulting from the standard micro-ramp should be exactly reversed for optimal performance.

This chapter presents an alternative micro-ramp design that produces a streamwise vortex pair whose sense of rotation is opposite that of the standard micro-ramp, and that preserves the appealing simplicity and robustness of the standard design. The new design is suitably termed the inverse micro-ramp. Analogous results to those presented in Chapter V are provided, with a number of metrics suggesting considerably improved performance.

6.1 Inverse micro-ramp design

The inverse micro-ramp design is shown schematically in Fig. 6.4 from a projective view (Fig. 6.4*a*) and a downstream vantage looking upstream at the rearward angled faces of the feature (Fig. 6.4*b*). Similar to the standard design, the incoming boundary layer is initially deflected by ramp-like features before passing over two angled dumps. The faces on the outward boundaries of the feature are parallel with the streamwise flow velocity, and the two angled dumps form a "V" in the interior of the geometry. Note that the appealing characteristics of the standard ramps, particularly their simple and robust design, remain intact.

The vortex pair produced by these angled dumps is shown schematically in Fig. 6.4*b*. As a result of their sense of rotation, the vortex-vortex interaction and the effect of the wall force the vortices to remain separated from each other as well as to remain deep in the boundary layer. Thus such a design enables the vortex strength to persist further downstream of the features, with the spanwise region controlled by the individual features being greater than with the standard design.

Therefore, not only is it expected that the inverse micro-ramps will perform their desired function better than the standard ramps, but they should do so with fewer individual elements. Ultimately, this translates to reduced drag-related losses and reduced fabrication expenses for the same influence on the SBLI region.

The nomenclature used for the defining dimensions of the inverse micro-ramp is shown in Fig. 6.5, and is analogous to that used for the standard micro-ramp design. Each half of the inverse ramp has hypotenuse c, interior angle A_p, height h, and inter-feature spacing s. Also as before, the features are located a distance $x_{_R}$ upstream of the inviscid shock impingement location.

It is the goal of this study to provide relevant comparisons to the previously described standard micro-ramp, while also iterating toward an optimal configuration. To do this, we begin by again following the recommendations of Anderson et al. (2006). For purposes of relevant comparison to the findings of the previous chapter as well as to other independent works, three of the defining dimensions are kept constant from the inverse micro-ramp design: the nominal flow deflection angle, the ratio c/h, and the upstream location $x_{_R}$. The flow deflection angle, β, is given by

$$\beta = \sin^{-1}\left(\frac{h}{c\cos A_p}\right), \tag{6.1}$$

thus leaving two free design variables, h and A_p. These are chosen through considerations described in detail in Appendix B and, for the present study, are $A_p = 14$-deg and $h = 3\,\text{mm}$. These choices increase the frontal area of the ramps by 36% as compared to the standard ramps, however they effectively elongate the feature so that the angled dumps are aligned more closely with the streamwise direction. Then by extension, the axes of the vortices created by the dumps are also aligned more closely with the streamwise direction and more effectively perform their intended function.

6.2 Comparison of vorticity

Spanwise imaging planes are again used to visualize the flow field and the streamwise vortices contained therein. Figure 6.6 shows the streamwise vorticity fields $\overline{\omega}_x(y,z)$ produced by the standard micro-ramp (Fig. 6.6*a*) and the inverse micro-ramp (Fig. 6.6*b*) at the same downstream location, in this case upstream of the $\theta = 7.75$-deg interaction at $x/\delta_0 = -2.5$. The inverse micro-ramp design produces streamwise vortices that remain closer to the wall and do not merge together. Those aspects should allow the vortices to survive further downstream and to remain deeper within the boundary layer, making the inverse micro-ramp design more effective than the standard design. In what follows, these inferences are quantitatively assessed.

Figures 6.7–6.9 show the evolution of the streamwise vortex pair through the interaction region for the $\theta = 7.75$-deg, 10.0-deg, and 12.0-deg shock strengths, respectively. The persistence of the vorticity through the interaction is similar to that observed using the standard micro-ramp; while the streamwise vortex pair largely maintains its form throughout the entire $\theta = 7.75$-deg interaction, its vorticity is considerably reduced through the $\theta = 10.0$-deg and 12.0-deg interactions. As before, this is due in part to the three-dimensional effects identified in § 4.2.3. Looking at Fig. 6.9, for example, Position 3 shows strong components of spanwise velocity directed toward the centerline. The streamwise vortices are pushed together and their respective vorticity is mutually canceled. Additional contributions to the spanwise velocity come from the distortion of the impinging shock in the interaction region, and will be discussed in § 6.3.4.

Figures 6.10–6.12 show profiles of the evolution of vorticity through each of the three interactions. As in Figs. 5.7–5.9, the extracted profiles were chosen at locations

corresponding approximately to the centers of the vortices in the streamwise pair, in this case at $z/\delta = \pm 0.4$. Comparing the profiles upstream of the shock with those for the standard micro-ramp, shown previously in Figs. 5.7–5.9, one identifies a factor of 2.3 increase in peak vorticity produced by the inverse design. Furthermore, within the available field-of-view, the circulation Γ produced by the inverse ramps is 1.8 times greater than that produced by the standard micro-ramps. Undoubtedly this is in part due to the increased height of the inverse micro-ramp as compared to the standard micro-ramp. Note, however, the normalized circulation values upstream of the interaction in Fig. 6.13. Here, despite having considerable contributions to the circulation being located outside of the field-of-view (see Fig. 6.6), the measured normalized circulation is equal to or greater than that produced by the standard design.

The persistence of the vorticity through the interaction is shown via the normalized circulation in Fig. 6.13. Here, the pre- and post-interaction circulation is virtually unaltered for both the $\theta = 7.75$-deg and $\theta = 10.0$-deg interactions, while only in the $\theta = 12.0$-deg interaction are the streamwise vortices forced together, negating their associated circulation. This is in contrast to the results from the standard micro-ramp shown in Fig. 5.10, where the vorticity was negated in both the $\theta = 10.0$-deg and 12-deg interactions.

It is apparent from Fig. 6.6, and also from Figs. 6.7–6.12, that the overall vorticity produced by the inverse ramps is situated deeper in the boundary layer and at larger $|z|$ values as compared to the vorticity produced by the standard design. These observations are quantified through calculation of the vorticity centroids, shown in Fig. 6.14 for all three interactions, with solid symbols representing vortices produced by the inverse micro-ramps and open symbols representing vortices produced by the

standard micro-ramp design. The inverse vortices are separated in the spanwise direction by an average of $0.83\delta_0$, compared to $0.37\delta_0$ for those produced by the standard ramps. In the wall-normal direction, the vortex pair produced by the inverse ramps have centroids at $y/\delta_0 = 0.22$, while those produced by the standard ramps have centroids at $y/\delta_0 = 0.37$. Note that the latter average was computed after excluding the highest two points in Fig. 6.14.

Thus the inverse micro-ramp design provides an approximately two-fold increase in both peak vorticity and spreading distance, accompanied by an approximately two-fold decrease in the wall-normal location. These compelling results are summarized in Table 6.1.

6.3 Effect on mean velocity fields

With the sense of vorticity produced by the ramps now reversed, the vortex-induced downwash now occurs along the tunnel centerline. The evolution of the resulting streamwise velocity fields $\overline{u}(y, z)$ are shown in spanwise planes in Figs. 6.15–6.17 for the $\theta = 7.75$-deg, 10.0-deg, and 12.0-deg deflection angles, respectively. The powerful vortex-induced downwash along the centerline convects high velocity air deep into the boundary layer, and enables a core of such high-energy gas to pass through the interaction relatively unaffected by the shock. Conversely, in the vortex-induced upwash regions which occur at larger $|z|$ values, the low velocity gas originally in the boundary layer is convected toward the free stream. One might note, at least qualitatively, that while the effect on the streamwise velocity in the downwash region is considerably greater in the present case as compared to the

standard micro-ramps, the effect in the upwash regions appear comparable.

Further insight into this regard is provided through inspection of the streamwise velocity profiles, offered in Figs. 6.18–6.20 for all three shock strengths. Here, the off-centerline profiles are located at $z/\delta_0 = \pm 0.5$. As was observed in the standard micro-ramp cases in Figs. 5.15–5.17, the centerline and off-centerline profiles have equal velocities at large y/δ_0 values, deviate in the central region of the boundary layer, and then approach equal values in the near wall region. Owing to the two-fold increase in vortex strength, the deviations in the present case are substantially larger than for the standard micro-ramps.

Comparison between the two controlled boundary layers and the uncontrolled boundary layer is offered in Fig. 6.21 at the $x/\delta_0 = -1.1$ location in the $\theta = 10.0$-deg interaction. Caution is suggested when comparing the vortex-induced upwash regions, denoted by the circular points, since in the case of the inverse micro-ramps the full degree of upwash has not been resolved. The flow is relatively unaffected by the method of control for $y/\delta_0 \gtrsim 0.75$, with large variation being observed closer to the wall. Using the standard micro-ramps, the benefit provided by the vortex-induced downwash region is approximately equal to the loss produced by the corresponding upwash region. With much larger vorticity magnitude, as produced by the inverse ramps, the gain in the downwash region of the vortex pair significantly outweighs any loss in the presently resolved upwash region.

6.3.1 Comparison of mean integral relations

These observations are seen more completely through the spanwise measurements of the modified shape factors H^*, introduced previously in §5.3.1. Figures 6.22–6.27

show these measurements for the uncontrolled and controlled boundary layers in locations upstream (Figures 6.22, 6.24, and 6.26) and downstream (Figures 6.23, 6.25, and 6.27) of the interaction for all three shock strengths. Recall that in general a smaller shape factor is indicative of high momentum being located close to the wall and therefore represents a boundary layer that is less susceptible to detachment. Note also that $H^* = 1$ is the lower bound, and describes the case of a uniform velocity profile everywhere equal to the free stream velocity u_∞. Finally, recall from the discussion in §5.3.1 that due to the lack of a uniform free stream, the numerical values of H^* are rendered somewhat moot and therefore comparison between figures is irrelevant. Instead, accurate inferences can only be made through comparisons contained within each individual figure.

These precautions considered, the effect of the inverse micro-ramps is substantial for all shock strengths. The effects on the boundary layer upstream are comparable to the effects of the standard micro-ramp design. Downstream of the interaction, however, the inverse micro-ramps provide a substantial reduction in the shape factor within the available field of view. In addition, while the standard micro-ramp design provides little or no benefit to the shape factor for the $\theta = 10.0$-deg and 12.0-deg interactions, the inverse ramps provide substantial benefit even in these stronger interactions.

6.3.2 Comparison of net displacement thicknesses

As in Chapter V, one quantification of the net effect of the micro-ramps is the spanwise-averaged displacement thickness $\langle \delta^* \rangle$, defined previously in § 5.3.2, which can be investigated as a function of the streamwise coordinate. Figures 6.28, 6.29,

and 6.30 show this for the $\theta = 7.75$-deg, 10.0-deg, and 12.0-deg interactions, respectively, with each figure comparing the uncontrolled and controlled boundary layers. For all incident shock strengths, the net displacement thickness is reduced by the inverse micro-ramps at all streamwise locations, further demonstrating the potential utility of the design. Table 6.2 shows the maximum net displacement thickness for each interaction together with the percent reduction provided by the two boundary layer control techniques. Recall that these maxima have direct implications for supersonic inlet performance, as they are indicative of the reduction in the effective inlet area due to the SBLI. The results suggest the inverse micro-ramp design effectively reduces the peak boundary layer thickness through the SBLI by as much as 34% over the uncontrolled interaction. Even in the strongest interaction a 17% reduction is achieved, demonstrating a four-fold improvement over the reduction produced by the standard micro-ramp design.

6.3.3 Effects on wall-normal velocity

Figure 6.31 gives spanwise visualizations of the wall-normal velocity field $\overline{v}(y, z)$ through the $\theta = 7.75$-deg interaction, and Figs. 6.32–6.34 show profiles of the wall-normal velocity for all three shock strengths. Of particular interest in these is an indication of the strength of the upstream reflected shock wave, C_2, which recall is manifested as positive wall-normal velocity occurring in the boundary layer in the upstream portion of the interaction. Figure 6.32, which shows the $\theta = 7.75$-deg interaction, indicates a much weaker wave than in the uncontrolled case from Fig. 4.10. In fact, there is almost no indication of the upstream reflected wave C_2 until Location 4, which is comparatively much later in the interaction than in the

uncontrolled case. The same observations, albeit to lesser extents, are observed in the stronger two interactions. In Figs. 6.33 and 6.34, the maximum wall-normal velocity occurs upstream of the interaction in the vortex-induced upwash regions, while the wall-normal velocity on the centerline is reduced. Comparing Figs. 6.33 and 6.34 with Figs. 4.11 and 4.12, respectively, the maximum wall-normal velocity in the vortex-induced upwash regions of the controlled interaction is comparable to the levels observed in the uncontrolled interaction. From this, one can infer that the reflected shock C_2 is of comparable strength in the vortex-induced upwash region, and has reduced strength in the downwash region. This at least suggests that the losses associated with wave-drag are reduced through the interaction via the micro-ramp control.

6.3.4 Distortion of reflected shock

One secondary effect that results from the micro-ramp arrays is the distortion of the reflected shock wave. In the vortex-induced downwash region produced by the vortex pair, high velocity gas is convected deep into the boundary layer lowering the sonic line, while in the vortex-induced upwash region low velocity gas is moved toward the free stream, raising the sonic line. When the impinging shock reaches the controlled boundary layer, it is reflected first upon reaching the vortex-induced upwash regions but penetrates closer to the wall in the vortex-induced downwash regions. This is particularly evident in Station 4 of Fig. 6.31, which by happenstance visualizes the shock wave very near to its lowest point. The shock wave assumes a V-like profile across the span and thus is no longer normal to the incident velocity in this dimension. As a result, the distorted shock turns the flow partially in the

z-direction, giving the post-shock velocity a non-zero w-component that is always directed toward the vortex-induced downwash region.

The shock-induced spanwise velocity component can be seen in Fig. 6.35, which shows visualizations of the spanwise velocity component at the six sampling planes through the $\theta = 7.75$-deg interaction. In sampling Planes 1-3, the spanwise velocity component is approximately zero everywhere except where due to the streamwise vortices. From Positions 3 to 4, the incident shock wave becomes distorted and an additional spanwise velocity component is induced, directed toward the centerline. As the shock reflects and leaves the boundary layer, its distortion reduces, and the magnitude of the induced spanwise velocity follows accordingly. Sampling Position 6 provides a unique vantage, showing the nearly decoupled spanwise velocities that result from both the streamwise vortex pair and the shock distortion.

With increasingly strong shock waves this effect is amplified and, together with the overall three dimensionality of the interaction, draws the initially separate vortices together. This can be seen in Fig. 6.36, which shows spanwise visualizations of $\overline{w}$ for the $\theta = 10.0$-deg interaction. As the spanwise vortices are drawn together, their respective vorticity is negated, explaining the post-shock vorticity levels previously observed in Figs. 6.8, 6.9 and 6.13.

6.4 Effects of vortex-induced upwash and downwash

The net effect of any vortex generator design is to produce alternating regions of vortex-induced upwash and downwash regions across the span. In the present study, the standard micro-ramp array produces one such upwash region along the tunnel centerline, while the inverse ramp array produces a downwash region along the

centerline. This provides an opportunity to compare the effects of the upwash and downwash to the uncontrolled interaction through visualizations of the streamwise centerline plane. Figures 6.37–6.41 do this, using the one uncontrolled and two controlled interactions involving the $\theta = 12.0$-deg flow deflection.

Figure 6.37 shows visualizations of the streamwise velocity fields $\overline{u}(x, y)$ from the uncontrolled and controlled interactions, using the vortex-induced upwash region from the standard micro-ramp and the vortex-induced downwash region from the inverse micro-ramp. The effects are consistent with the previous discussions; the downwash leads to a dramatic reduction in the thickening of the boundary layer, while the upwash does not create substantially greater overall thickening as compared to the uncontrolled case.

Visualizations of the spanwise vorticity component fields $\overline{\omega}_z(x, y)$, given in Fig. 6.38, provide somewhat new insight. In the upwash region slow moving fluid originating from deep in the boundary layer is convected toward the free stream. A mild shear layer results where this upwash meets the high speed gas away from the wall, and this is observed upstream of the interaction at $y/\delta_0 \approx 0.5$. Between that shear layer and the wall the vorticity levels are low, indicating the relatively uniform nature of the streamwise velocity in the upwash region. At the intersection point I from Fig. 1.4, the preexisting vorticity in this shear layer couples with the vorticity produced by the C_3 shock and associated expansion fan, producing amplified vorticity levels in this location. In the vortex-induced downwash region, the vorticity is contained in the near wall region below $y/\delta_0 \approx 0.3$, and aside from this minimal thickening the effects of the impinging shock are almost unnoticeable.

Figure 6.39 shows the kinetic energy fields $\overline{k}(x, y)$ for the three regions. As discussed in Chapter V, the $\overline{k}$ fields are rather similar in the uncontrolled and upwash

regions, with the elevated kinetic energy levels being a result of an unsteady free shear layer that exists between the low velocity fluid at the shock foot and the high speed incoming stream. In the vortex-induced downwash region, the kinetic energy is dramatically reduced in the entirety of the field except in the region immediately near the wall. This suggests that the shear layer, no longer unsteady, remains attached to the wall allowing for the overall interaction to be quite steady in this region.

Figures 6.40–6.42 show the shear strain rate fields $\overline{S}_{yy}(x,y)$, $\overline{S}_{xy}(x,y)$ and $\overline{S}_{xx}(x,y)$, respectively, and they again provide dramatic views of the interactions. In the upwash region, the formation of the reflected shock wave C_2 by the progressive coalescence of compression waves can again be seen in the $\overline{S}_{yy}$ field in Fig. 6.40, with the difference between it and the uncontrolled interaction being minimal. In the downwash region, the nature of the reflected shock C_2 is considerably altered, and it appears overall weaker than in the other scenarios.

Similar to the spanwise vorticity fields, Fig. 6.41 illuminates the mild shear layer produced by the upwash region upstream of the interaction, which couples with the shear strain rate produced by the interaction in the region near the intersection point I. Aside from this, the interaction in the uncontrolled and upwash interactions are again comparable. The downwash region, however, is again considerably different. In both Fig. 6.41 and Fig. 6.42, the latter of which shows the normal strain rate fields $\overline{S}_{xx}(x,y)$, all four shock wave branches are clearly evident as highly localized features. In particular, the upstream reflected shock, C_2, and incident shock, C_3, now appear as distinct and highly localized features. This follows directly from the previous observation involving the kinetic energy field in Fig. 6.39, which noted evidence that the vortex-induced downwash causes the otherwise free shear layer to remain attached to the bottom wall. Without the large-scale unsteady motion caused

by the free shear layer, the shock structure remains extremely stable, even below the intersection point I.

6.5 Interpretation of results

As previously noted, vortex generator arrays will produce regions of alternating vortex-induced upwash and downwash across the span. Sections 6.3–6.4, and particularly Figs. 6.22–6.27 and Fig. 6.37, showed that even with relatively strong incident shock waves, the vortex-induced downwash produced by suitably designed micro-ramp vortex generators can dramatically improve the boundary layer profile as it evolves through the SBLI region. In the complementary upwash regions, meanwhile, the effects of the vortex generators are not significantly worse than in an uncontrolled interaction. When these effects are integrated across the span, as is done in Figs. 6.28–6.30, the net effects of the incident shock on the boundary layer can be considerably reduced. Table 6.2 summarizes this quantitatively.

Effects of the micro-ramp vortex generators on the stability of the interaction can also be inferred. Figures 6.39, 6.41, and 6.42 indicate that the fluctuations of the interaction are dramatically reduced in the presence of sufficiently strong downwash. This is substantiated further in Figs. 6.43–6.45, which show profiles of the kinetic energy for the three interactions. In the upwash regions the turbulence levels are comparable to those from the uncontrolled interactions, but in the downwash regions the fluctuation levels are reduced. This is especially true in the $\theta = 12.0$-deg interaction in Fig. 6.45, where the effect of the downwash region is dramatic.

The low fluctuation levels in the downwash regions result from elimination of any

instantaneous recirculation bubbles that might appear in the interaction and thus the otherwise free shear layer is constrained at the bottom wall boundary. Thus, extrapolating this result across a large span, the vortex generator arrays will produce an SBLI with alternating regions of fully attached flow in the vortex-induced downwash regions and intermittent recirculating or detached flow in the vortex-induced upwash regions. By extension, then, the potentially large recirculation structure from Fig. 4.13, which has been demonstrated experimentally many times, should be divided into much smaller cells, and it would be expected that the downstream dimension of such cells would be on the order of their spanwise dimension. Similarly, the previously large-scale oscillations associated with the large recirculation zone should be reduced to localized effects with correspondingly reduced amplitudes.

Chapter VI demonstrates that the beneficial aspects of the micro-ramp vortex generators depend highly on the magnitude of vorticity produced and the sense of the constituent vortices in the vortex pair. The inverse design proposed herein demonstrates approximately two-fold improvements over the standard design in several key metrics; namely the maximum vorticity, spanwise separation, and the wall normal location. The resulting effects on the flow field make the inverse micro-ramps strong candidates for use in augmenting or eliminating the use of active boundary layer control techniques.

	$\max(\omega_x/(u_\infty/\delta_0))$	$\Delta z_{\omega_c}/\delta_0$	y_{ω_c}/δ_0
Standard micro-ramp	0.23	0.37	0.37
Inverse micro-ramp	0.52	0.83	0.22
Factor increase/decrease	**2.3**	**2.2**	**1.7**

Table 6.1: Comparison of magnitudes and locations of the streamwise vortex pairs produced by the standard and inverse micro-ramp designs.

	$\theta = 7.75$-deg	$\theta = 10.0$-deg	$\theta = 12.0$-deg
Blank	2.8	3.9	4.3
Standard micro-ramp	2.2	3.4	4.1
Percent decrease	**22%**	**12%**	**4%**
Inverse micro-ramp	1.9	3.0	3.6
Percent decrease	**34%**	**21%**	**17%**

Table 6.2: Maximum displacement thicknesses through the three interactions, showing also the net reductions produced by the standard and inverse micro-ramps as compared to the uncontrolled interactions.

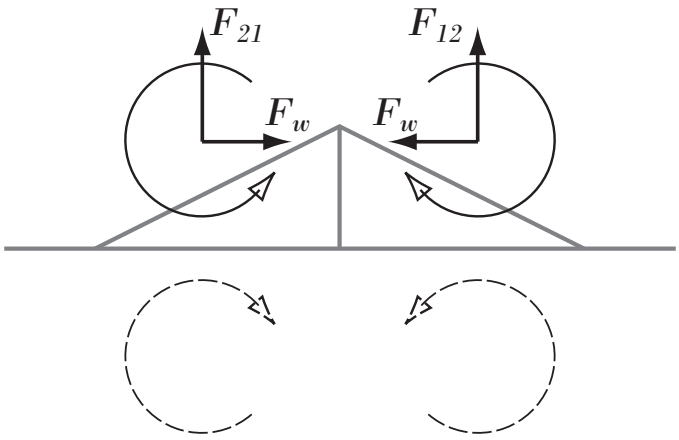

Figure 6.1: Schematic of the standard micro-ramp design are shown looking upstream at the rearward faces of the ramp. The induced streamwise vortices and the forces arising from the vortex-vortex interaction are also shown.

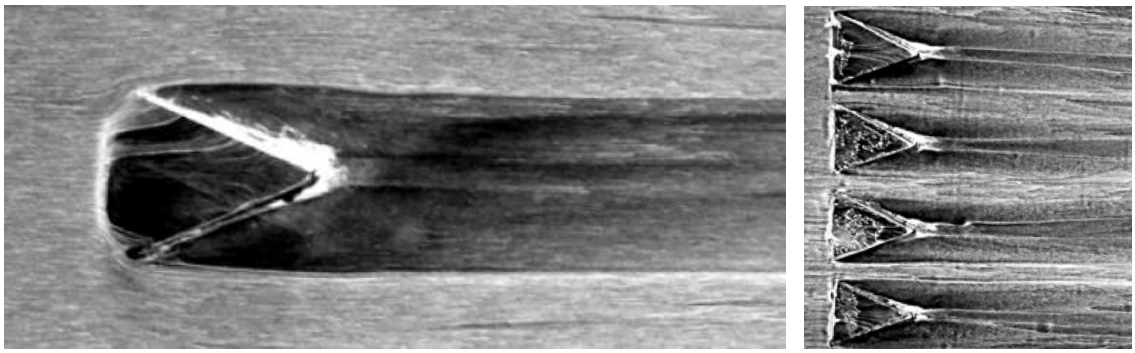

Figure 6.2: Oil streak visualizations around standard micro-ramps are shown from the work of Ford and Babinsky (2007), demonstrating the extremely confined area of influence produced by each micro-ramp in the array.

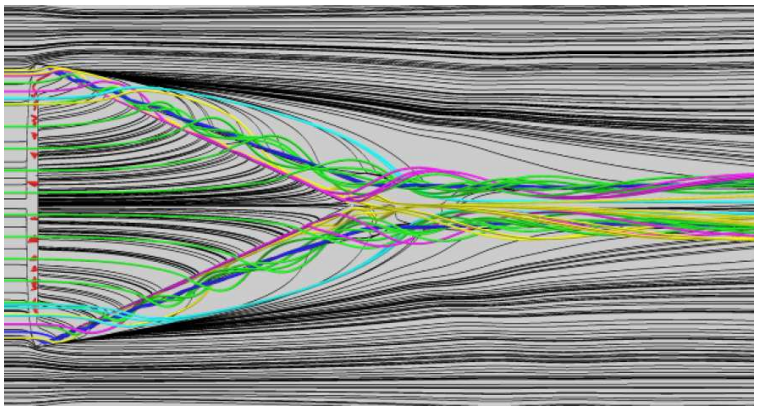

Figure 6.3: Streamlines over the standard micro-ramp produced by the RANS simulation of Galbraith et al. (2009).

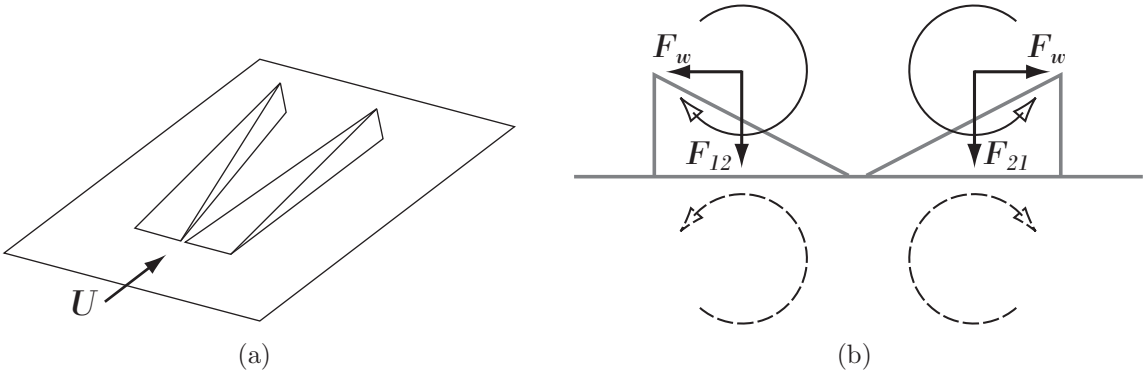

Figure 6.4: Schematics of the inverse micro-ramp design are shown *(a)* from a projection view and *(b)* looking upstream at the rearward faces of the ramp. The induced streamwise vortices and the forces arising from the vortex-vortex interaction are also shown.

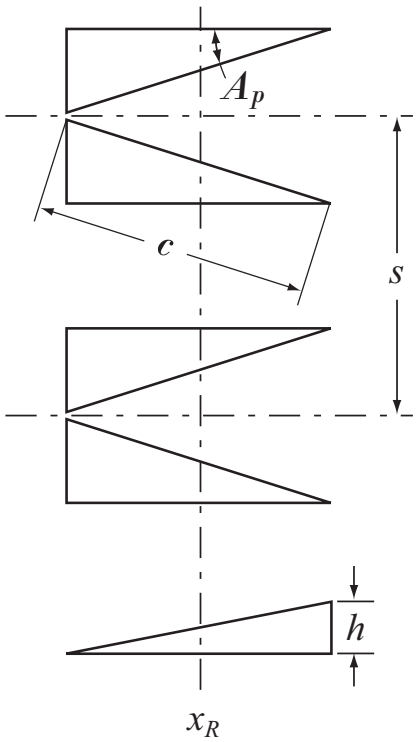

Figure 6.5: The defining dimensions of the inverse micro-ramp are shown, including the ramp angle A_p, side-length c, height h, and ramp spacing s.

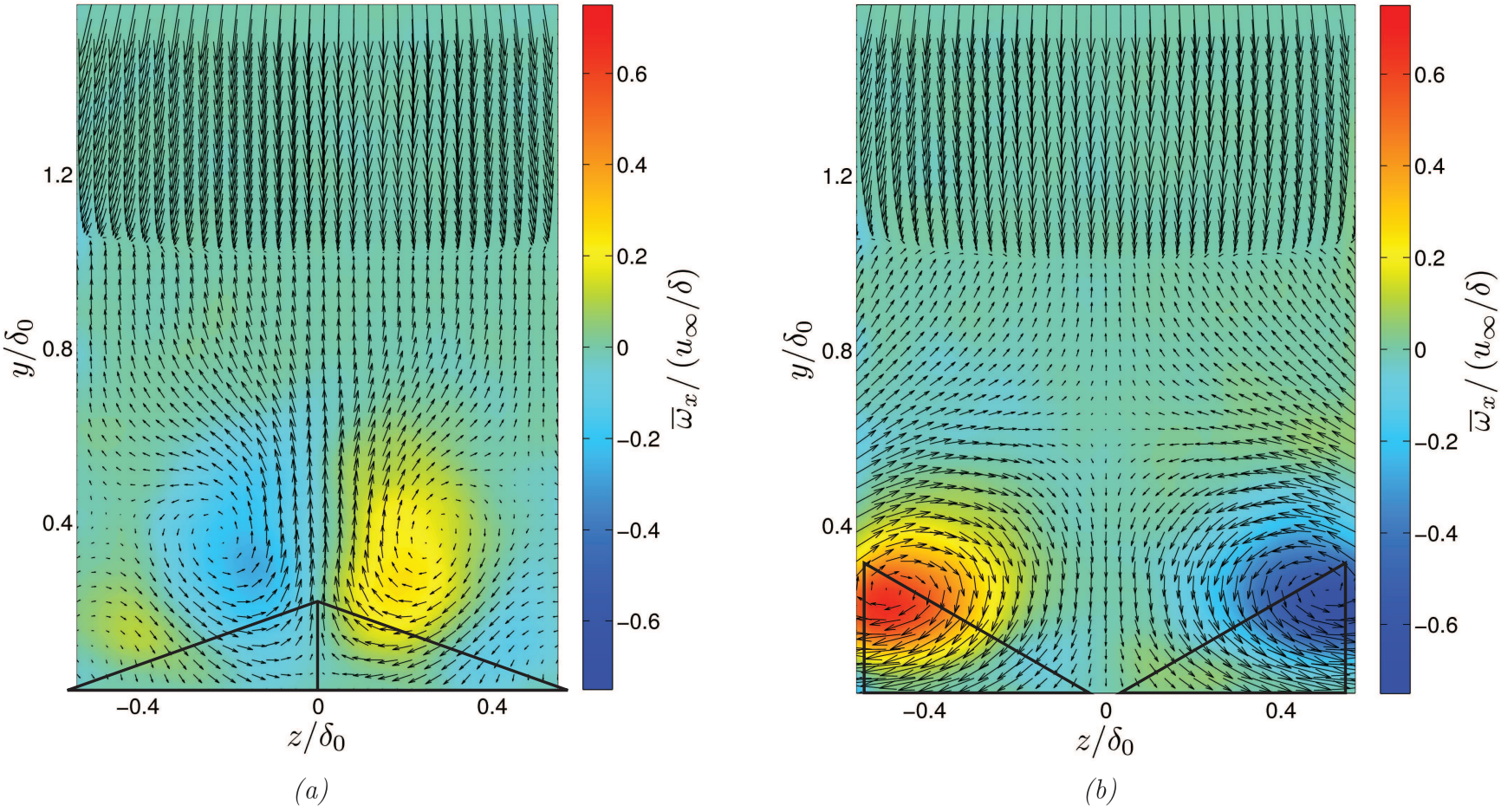

Figure 6.6: Typical mean vorticity fields $\overline{\omega}_x$, in this case located upstream of the interaction at $x/\delta_0 = -2.5$ and with the $\theta = 7.75$-deg flow deflection angle. Figure shows the streamwise vortex pair generated by *(a)* the standard micro-ramp and *(b)* the inverse micro-ramp. Superimposed on the vector fields are scale representations of the ramp outlines.

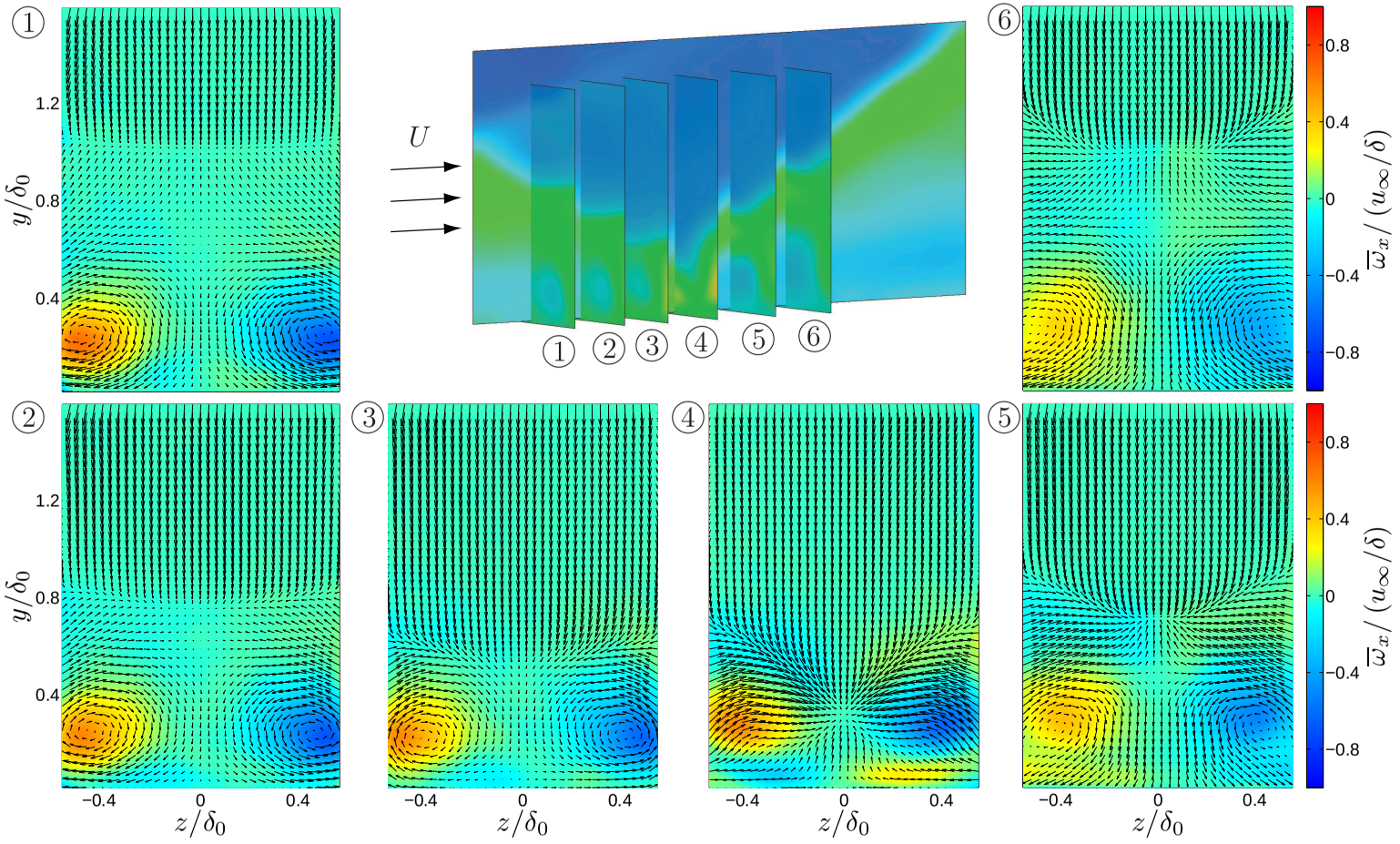

Figure 6.7: Color plots of $\overline{\omega}_x$ show the SBLI region in transverse planes for a flow deflection angle of $\theta = 7.75$-deg and passive control via inverse micro-ramps located at $x/\delta_0 = -8.50$. The averaged in-plane velocity fields ($\overline{v}$,$\overline{w}$) are overlayed as vectors. The six sampling locations correspond to 1: $x/\delta_0 = -2.0$, 2: $x/\delta_0 = -1.55$, 3: $x/\delta_0 = -1.2$, 4: $x/\delta_0 = -0.7$, 5: $x/\delta_0 = -0.2$, and 6: $x/\delta_0 = +0.3$. The central perspective plot shows the relative location of each plane.

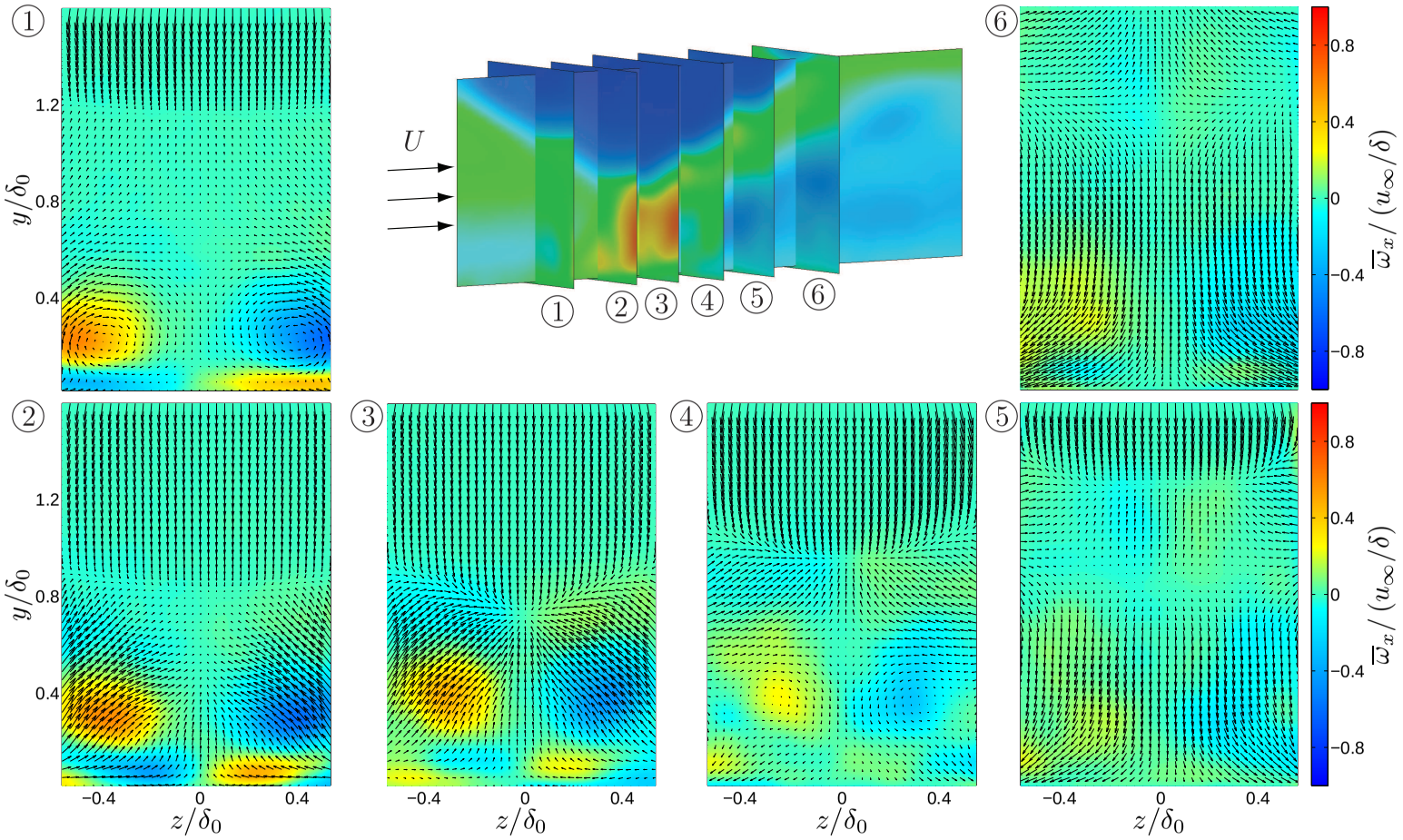

Figure 6.8: Color plots of $\overline{\omega}_x$ show the SBLI region in transverse planes for a flow deflection angle of $\theta = 10.0$-deg and passive control via inverse micro-ramps located at $x/\delta_0 = -9.42$. The averaged in-plane velocity fields ($\overline{v}$,$\overline{w}$) are overlayed as vectors. The six sampling locations correspond to 1: $x/\delta_0 = -2.5$, 2: $x/\delta_0 = -1.9$, 3: $x/\delta_0 = -1.5$, 4: $x/\delta_0 = -1.1$, 5: $x/\delta_0 = -0.6$, and 6: $x/\delta_0 = 0.0$. The central perspective plot shows the relative location of each plane.

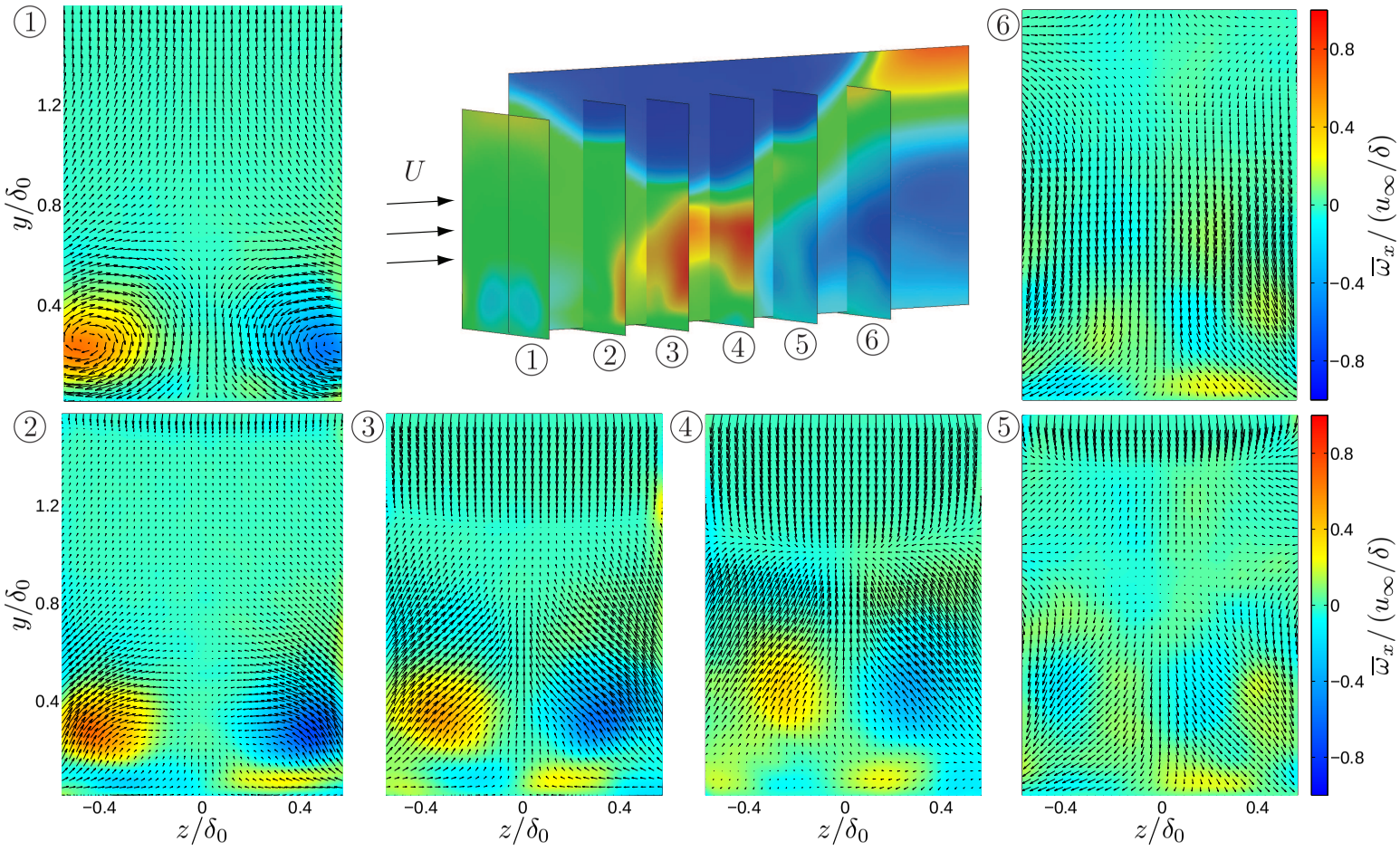

Figure 6.9: Color plots of $\overline{\omega}_x$ show the SBLI region in transverse planes for a flow deflection angle of $\theta = 12.0$-deg and passive control via inverse micro-ramps located at $x/\delta_0 = -9.76$. The averaged in-plane velocity fields ($\overline{v}$,$\overline{w}$) are overlayed as vectors. The six sampling locations correspond to 1: $x/\delta_0 = -3.6$, 2: $x/\delta_0 = -2.9$, 3: $x/\delta_0 = -2.3$, 4: $x/\delta_0 = -1.7$, 5: $x/\delta_0 = -1.1$, and 6: $x/\delta_0 = -0.4$. The central perspective plot shows the relative location of each plane.

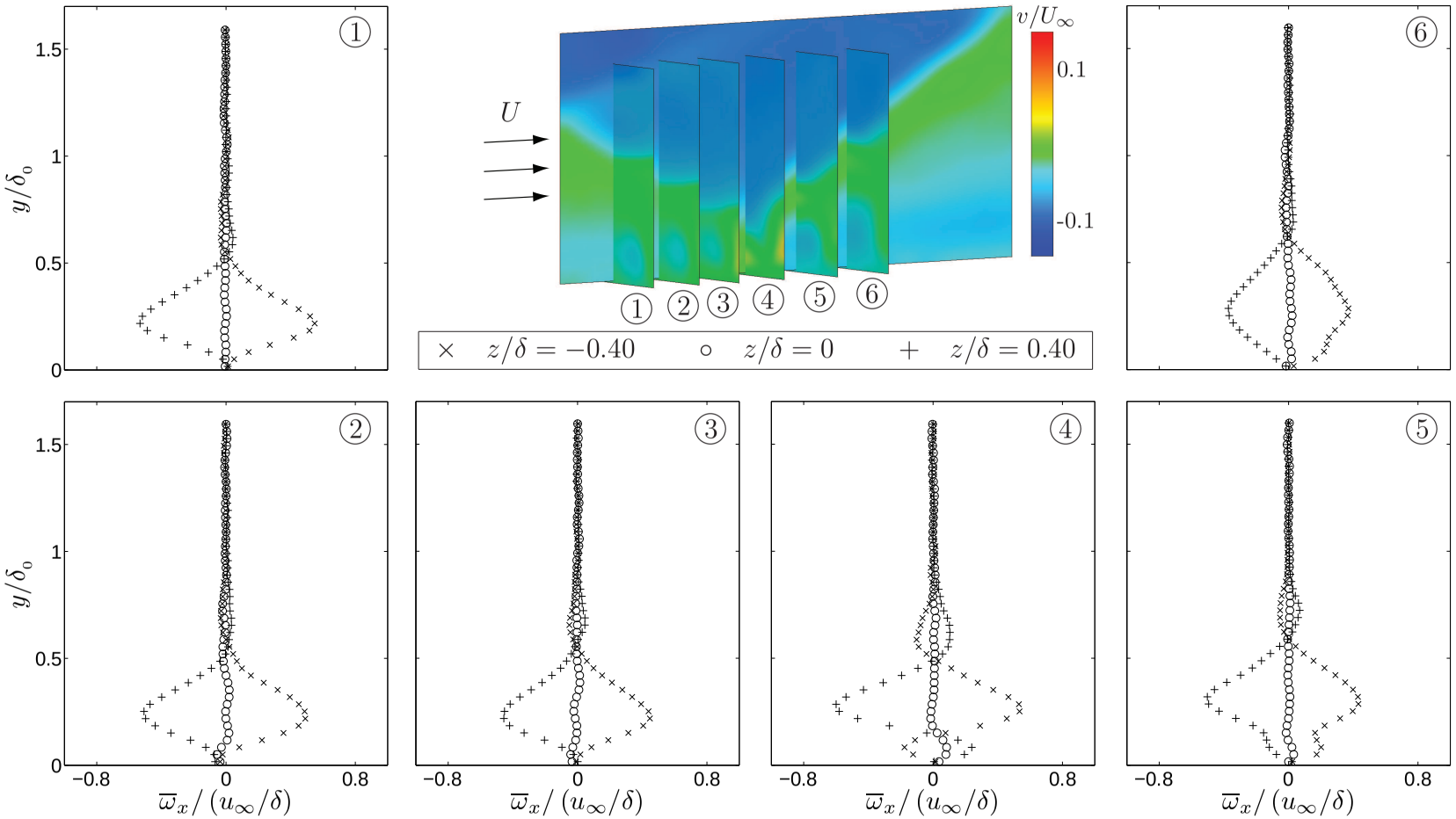

Figure 6.10: The evolution of $\overline{\omega}_x$ through the SBLI region is shown for a flow deflection angle of $\theta = 7.75$-deg and passive control via inverse micro-ramps located at $x/\delta_0 = -8.50$. The six sampling locations correspond to 1: $x/\delta_0 = -2.0$, 2: $x/\delta_0 = -1.55$, 3: $x/\delta_0 = -1.2$, 4: $x/\delta_0 = -0.7$, 5: $x/\delta_0 = -0.2$, and 6: $x/\delta_0 = +0.3$. At top, colors show the $\overline{v}$ field throughout each plane and show the relative location of each plane.

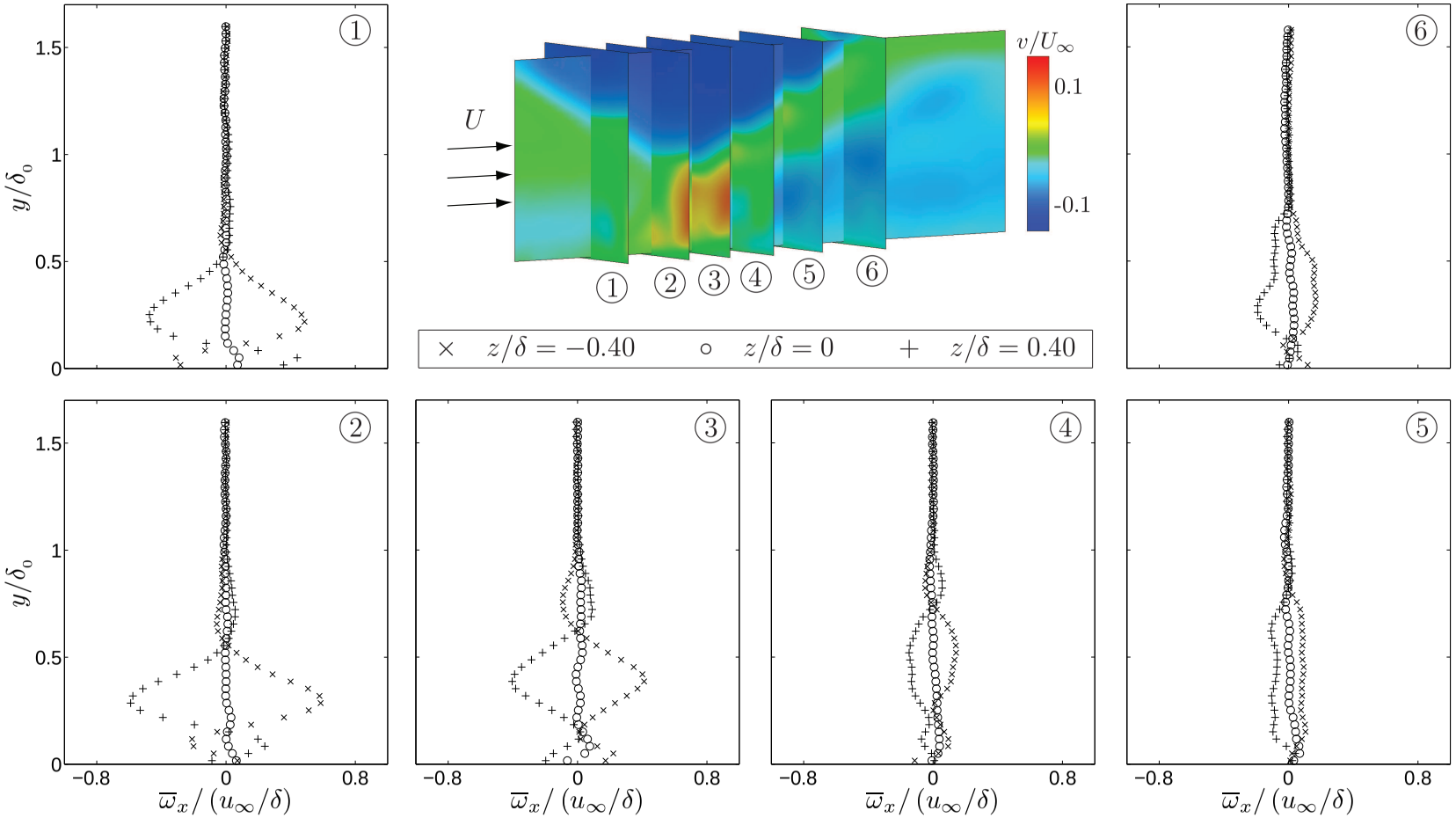

Figure 6.11: The evolution of $\overline{\omega}_x$ through the SBLI region is shown for a flow deflection angle of $\theta = 10.0$-deg and passive control via inverse micro-ramps located at $x/\delta_0 = -9.42$. The six sampling locations correspond to 1: $x/\delta_0 = -2.5$, 2: $x/\delta_0 = -1.9$, 3: $x/\delta_0 = -1.5$, 4: $x/\delta_0 = -1.1$, 5: $x/\delta_0 = -0.6$, and 6: $x/\delta_0 = 0.0$. At top, colors show the $\overline{v}$ field throughout each plane and show the relative location of each plane.

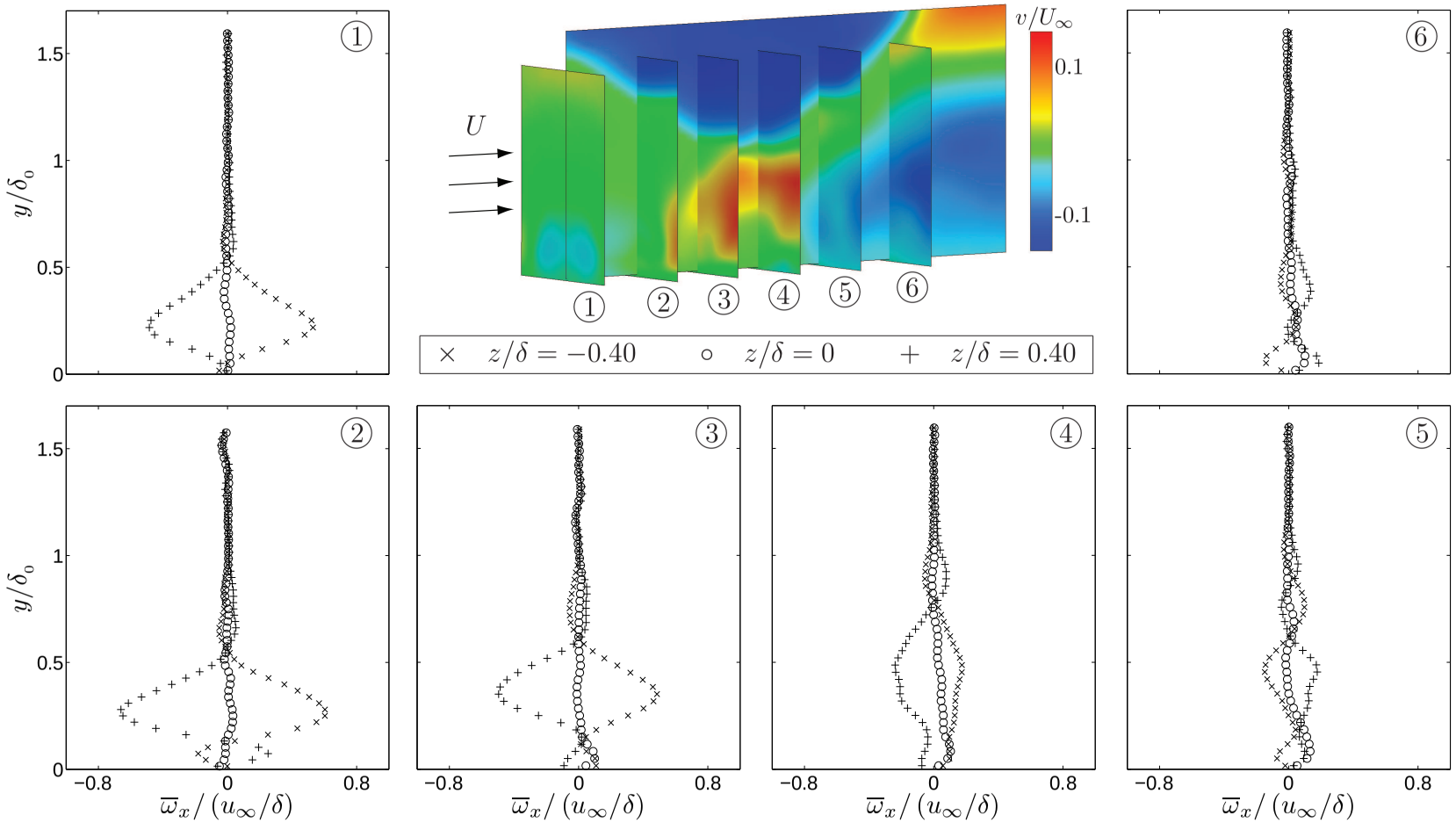

Figure 6.12: The evolution of $\overline{\omega}_x$ through the SBLI region is shown for a flow deflection angle of $\theta = 12.0$-deg and passive control via inverse micro-ramps located at $x/\delta_0 = -9.76$. The six sampling locations correspond to 1: $x/\delta_0 = -3.6$, 2: $x/\delta_0 = -2.9$, 3: $x/\delta_0 = -2.3$, 4: $x/\delta_0 = -1.7$, 5: $x/\delta_0 = -1.1$, and 6: $x/\delta_0 = -0.4$. At top, colors show the $\overline{v}$ field throughout each plane and show the relative location of each plane.

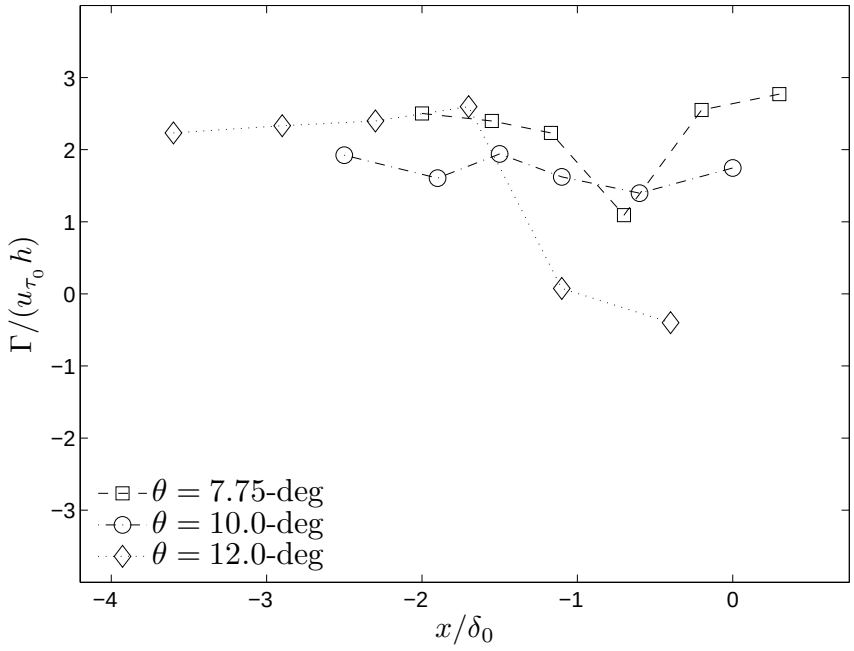

Figure 6.13: Evolution of the circulation Γ generated by the inverse micro-ramps shown as a function of downstream distance x/δ_0 for all three shock strengths.

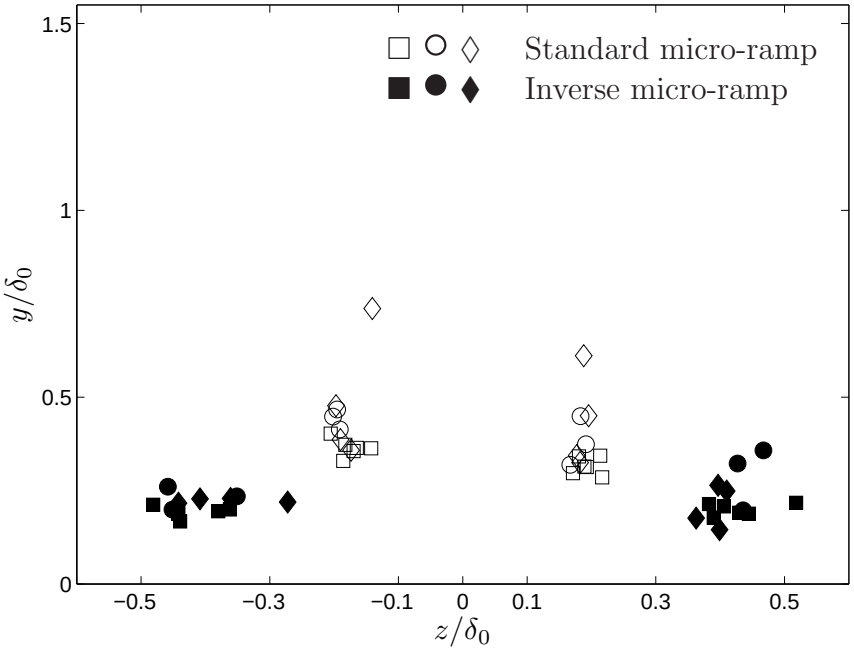

Figure 6.14: The left and right vortex centroids are shown at each x-location and for each shock strength, showing the vortex centroids from the standard micro-ramp (open symbols) and inverse micro-ramps (filled symbols).

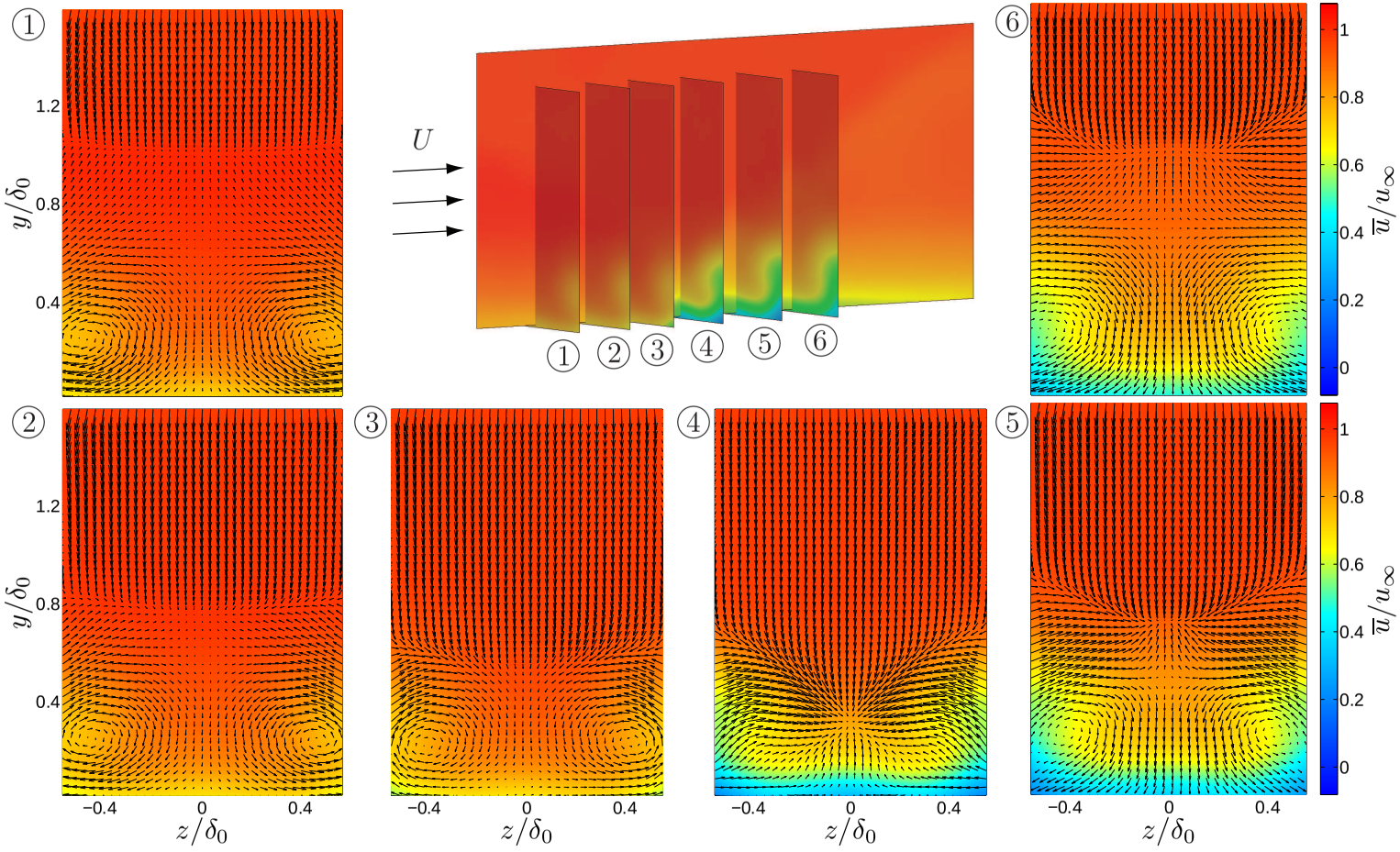

Figure 6.15: Color plots of $\overline{u}$ show the SBLI region in transverse planes for a flow deflection angle of $\theta = 7.75$-deg and passive control via inverse micro-ramps located at $x/\delta_0 = -8.50$. The averaged in-plane velocity fields ($\overline{v}$,$\overline{w}$) are overlayed as vectors. The six sampling locations correspond to 1: $x/\delta_0 = -2.0$, 2: $x/\delta_0 = -1.55$, 3: $x/\delta_0 = -1.2$, 4: $x/\delta_0 = -0.7$, 5: $x/\delta_0 = -0.2$, and 6: $x/\delta_0 = +0.3$. The central perspective plot shows the relative location of each plane.

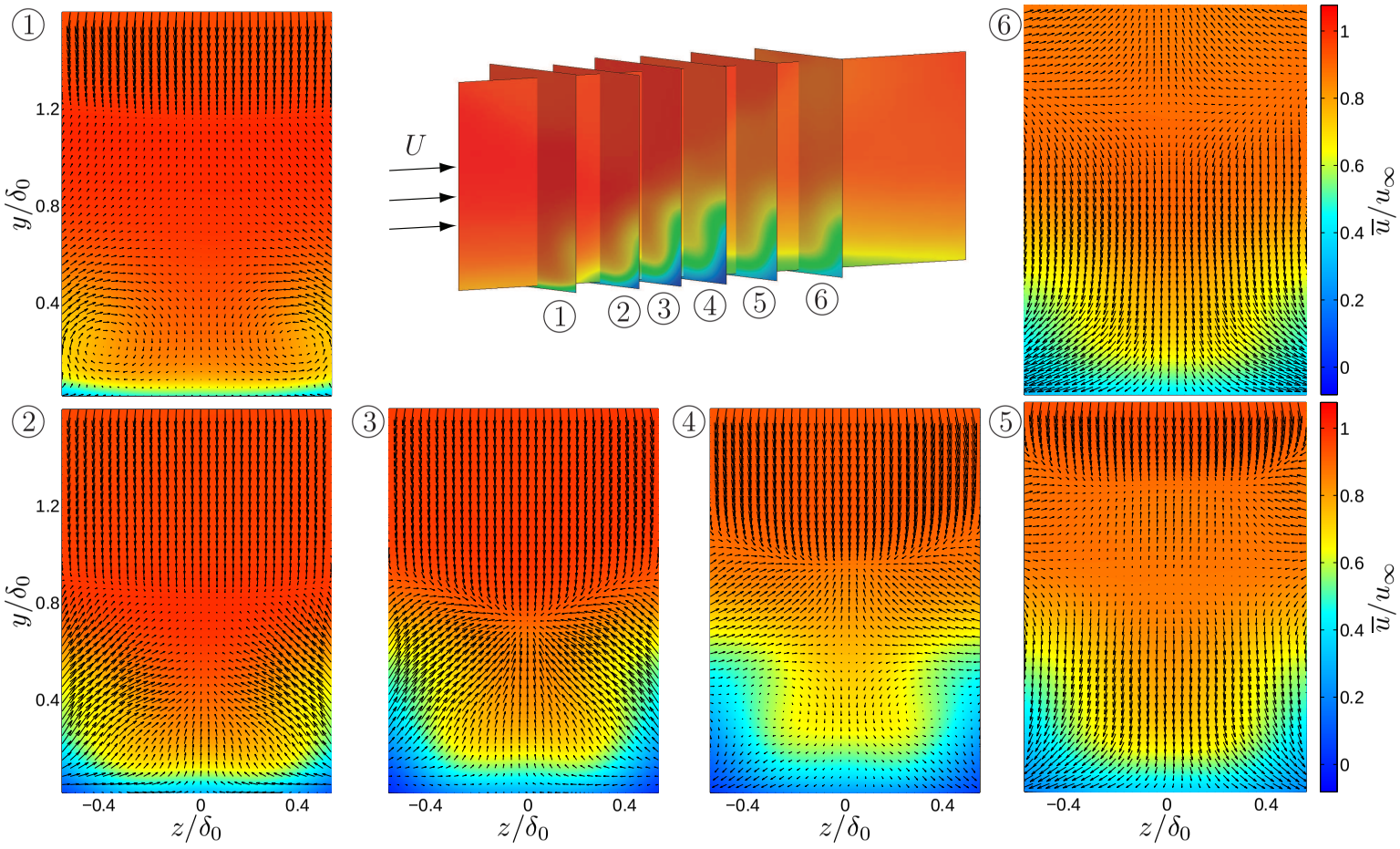

Figure 6.16: Color plots of $\overline{u}$ show the SBLI region in transverse planes for a flow deflection angle of $\theta = 10.0$-deg and passive control via inverse micro-ramps located at $x/\delta_0 = -9.42$. The averaged in-plane velocity fields ($\overline{v}$,$\overline{w}$) are overlayed as vectors. The six sampling locations correspond to 1: $x/\delta_0 = -2.5$, 2: $x/\delta_0 = -1.9$, 3: $x/\delta_0 = -1.5$, 4: $x/\delta_0 = -1.1$, 5: $x/\delta_0 = -0.6$, and 6: $x/\delta_0 = 0.0$. The central perspective plot shows the relative location of each plane.

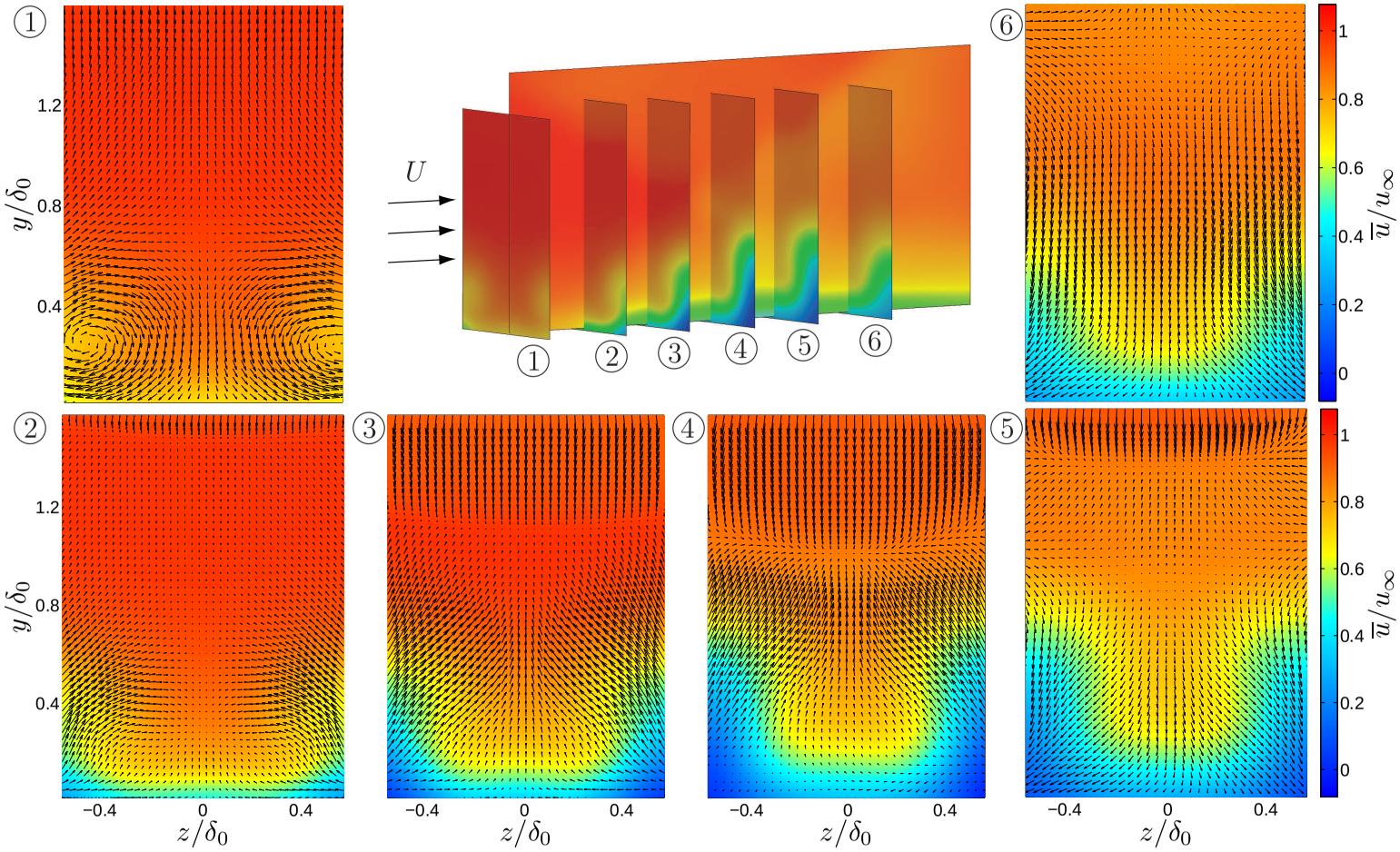

Figure 6.17: Color plots of $\overline{u}$ show the SBLI region in transverse planes for a flow deflection angle of $\theta = 12.0$-deg and passive control via inverse micro-ramps located at $x/\delta_0 = -9.76$. The averaged in-plane velocity fields ($\overline{v}$,$\overline{w}$) are overlayed as vectors. The six sampling locations correspond to 1: $x/\delta_0 = -3.6$, 2: $x/\delta_0 = -2.9$, 3: $x/\delta_0 = -2.3$, 4: $x/\delta_0 = -1.7$, 5: $x/\delta_0 = -1.1$, and 6: $x/\delta_0 = -0.4$. The central perspective plot shows the relative location of each plane.

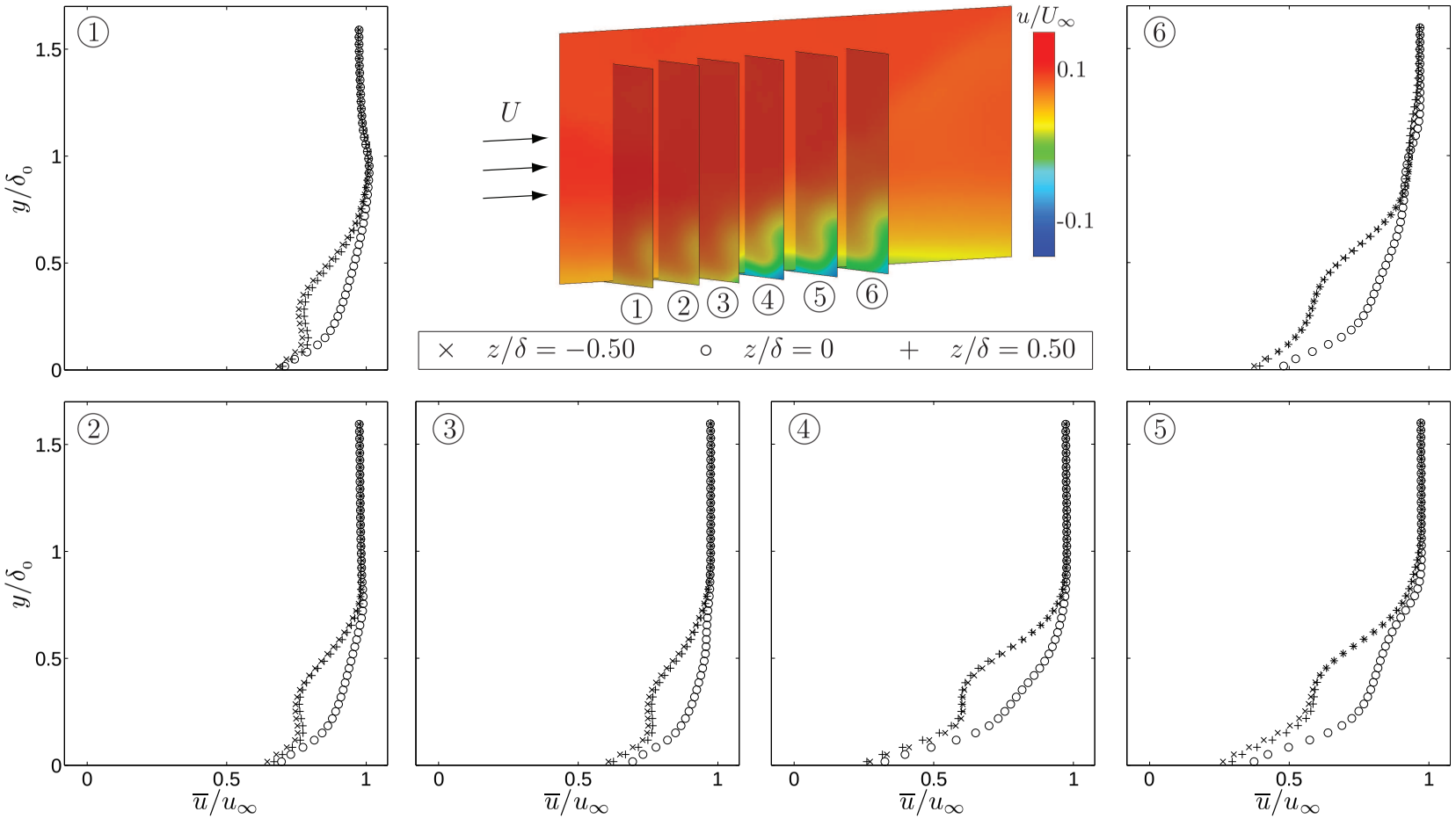

Figure 6.18: The evolution of $\overline{u}$ through the SBLI region is shown for a flow deflection angle of $\theta = 7.75$-deg and passive control via inverse micro-ramps located at $x/\delta_0 = -8.50$. The six sampling locations correspond to 1: $x/\delta_0 = -2.0$, 2: $x/\delta_0 = -1.55$, 3: $x/\delta_0 = -1.2$, 4: $x/\delta_0 = -0.7$, 5: $x/\delta_0 = -0.2$, and 6: $x/\delta_0 = +0.3$. At top, colors show the $\overline{u}$ field throughout each plane and show the relative location of each plane.

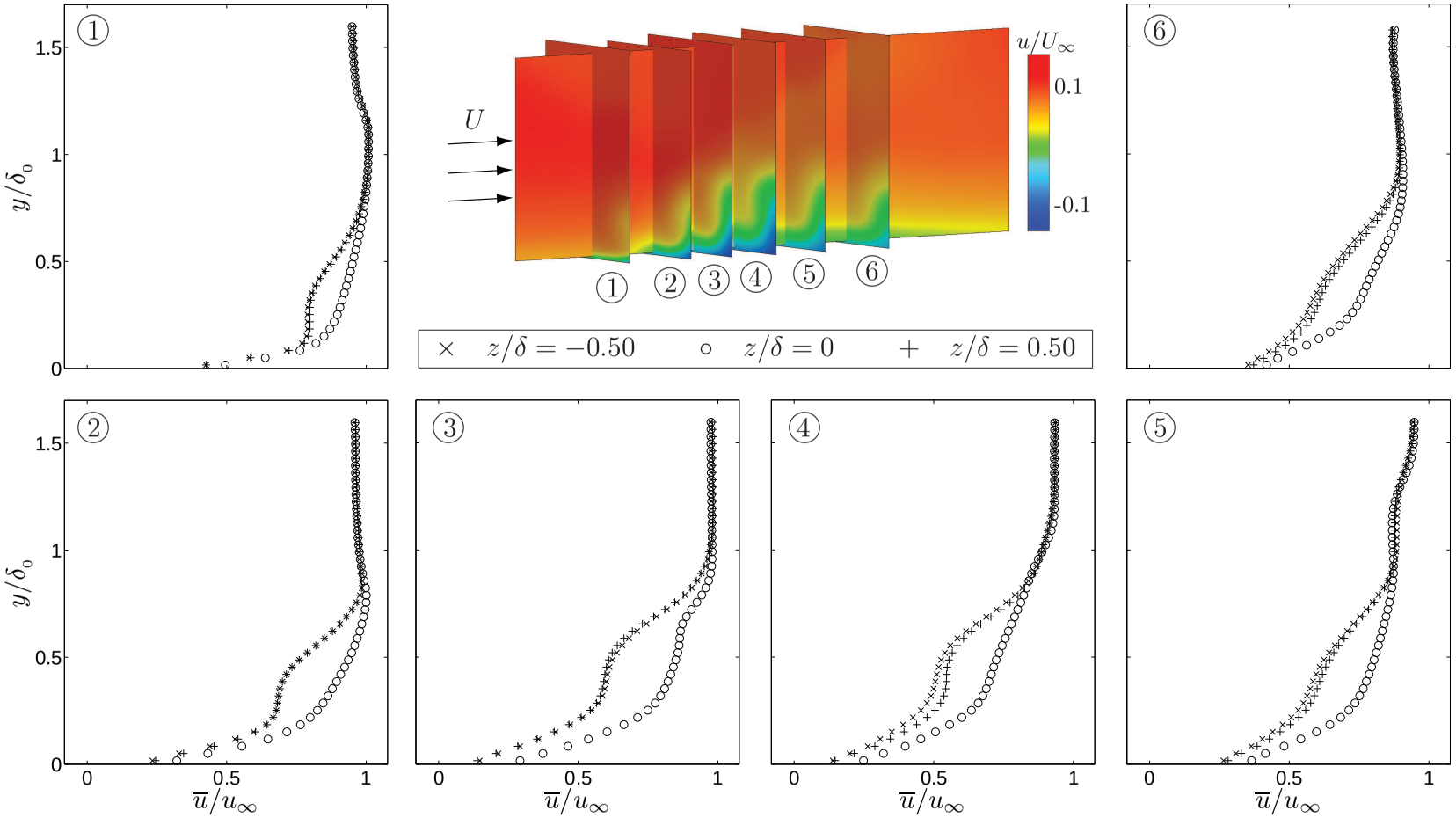

Figure 6.19: The evolution of $\overline{u}$ through the SBLI region is shown for a flow deflection angle of $\theta = 10.0$-deg and passive control via inverse micro-ramps located at $x/\delta_0 = -9.42$. The six sampling locations correspond to 1: $x/\delta_0 = -2.5$, 2: $x/\delta_0 = -1.9$, 3: $x/\delta_0 = -1.5$, 4: $x/\delta_0 = -1.1$, 5: $x/\delta_0 = -0.6$, and 6: $x/\delta_0 = 0.0$. At top, colors show the $\overline{u}$ field throughout each plane and show the relative location of each plane.

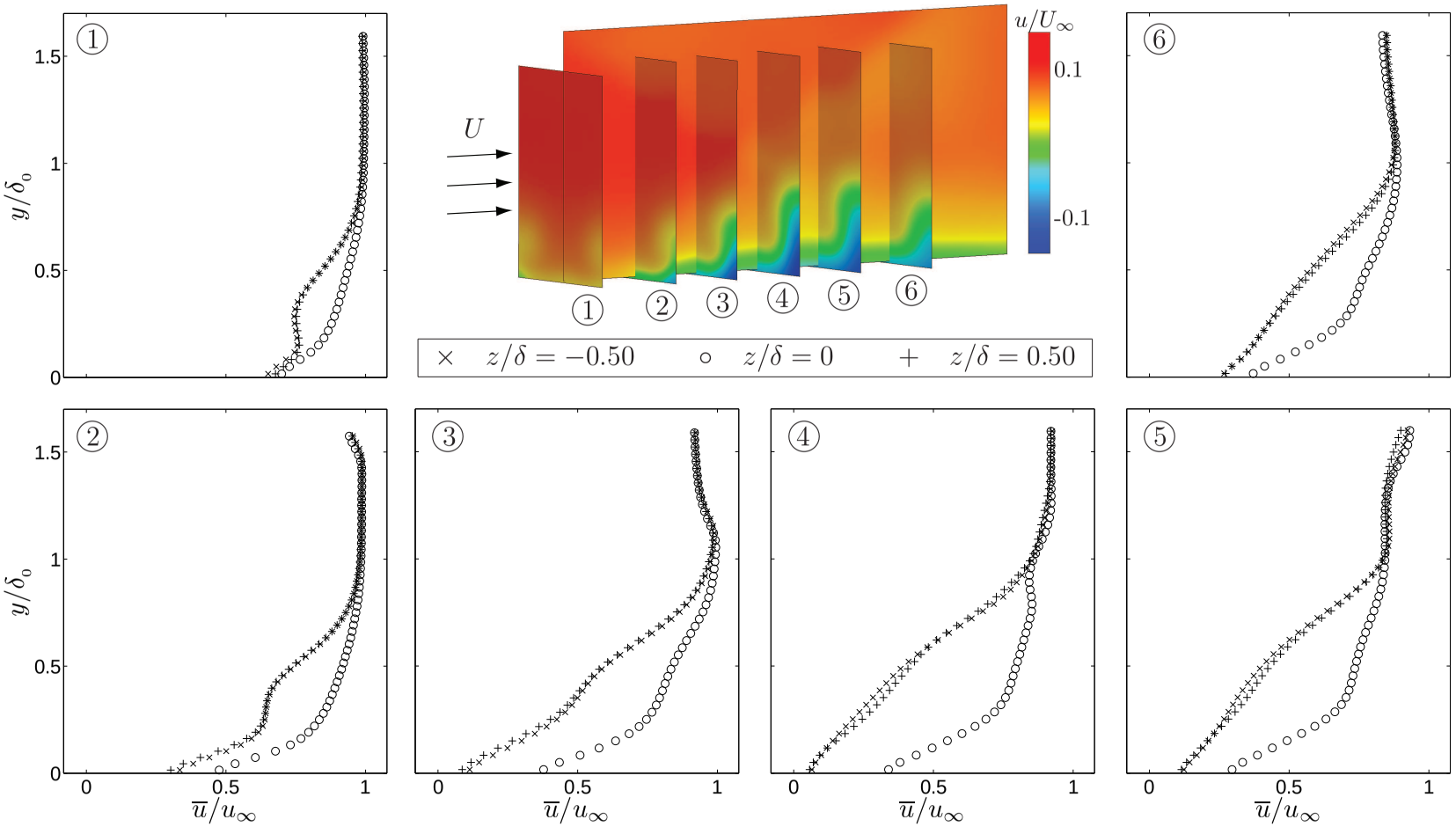

Figure 6.20: The evolution of $\overline{u}$ through the SBLI region is shown for a flow deflection angle of $\theta = 12.0$-deg and passive control via inverse micro-ramps located at $x/\delta_0 = -9.76$. The six sampling locations correspond to 1: $x/\delta_0 = -3.6$, 2: $x/\delta_0 = -2.9$, 3: $x/\delta_0 = -2.3$, 4: $x/\delta_0 = -1.7$, 5: $x/\delta_0 = -1.1$, and 6: $x/\delta_0 = -0.4$. At top, colors show the $\overline{u}$ field throughout each plane and show the relative location of each plane.

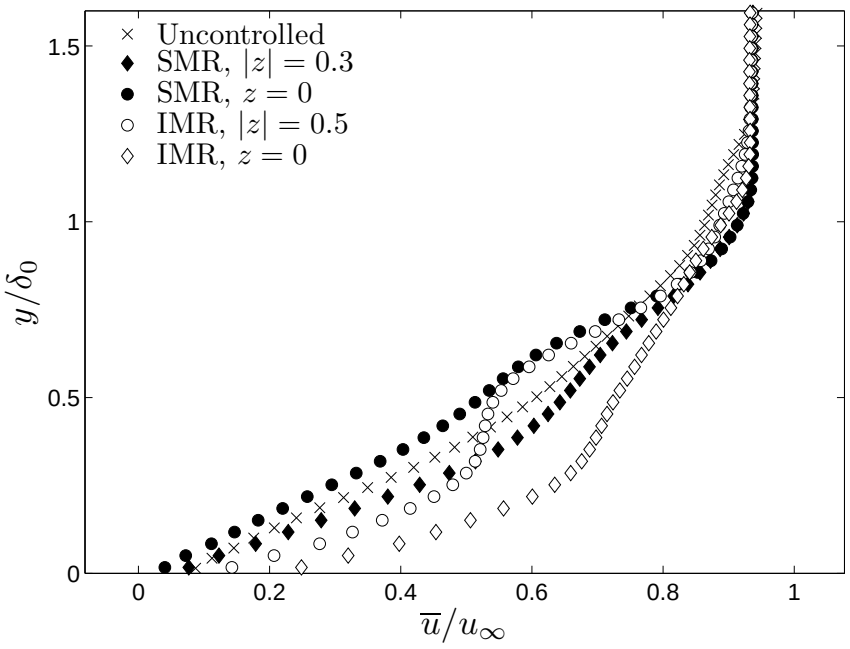

Figure 6.21: Comparison of the controlled boundary layers using the standard micro-ramp (SMR) and inverse micro-ramp (IMR) to uncontrolled boundary layer at the $x/\delta_0 = -1.1$ location of the $\theta = 10.0$-deg interaction. Circles denote vortex-induced upwash regions, and diamonds represent vortex-induced downwash regions.

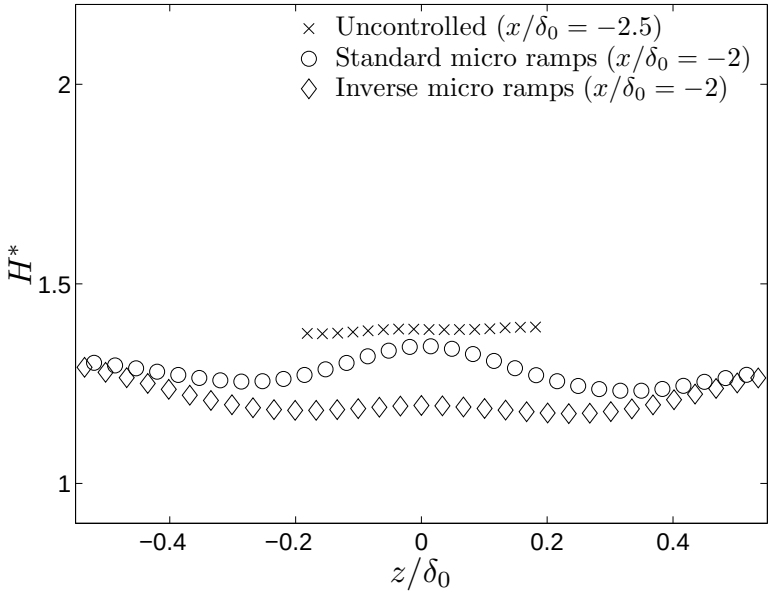

Figure 6.22: Modified shape factor H^* shown upstream of the $\theta = 7.75$-deg interaction as a function of the spanwise coordinate, comparing the uncontrolled boundary layer with those controlled by the standard and inverse ramps.

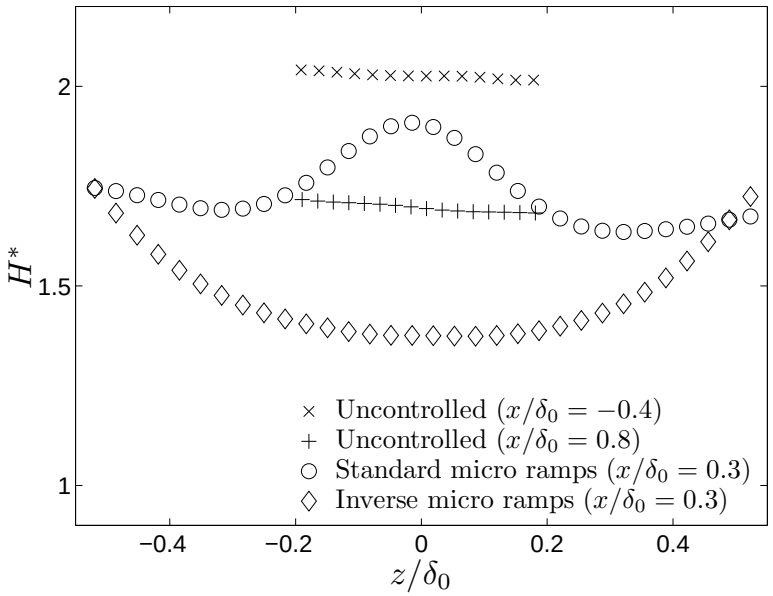

Figure 6.23: Modified shape factor H^* shown downstream of the $\theta = 7.75$-deg interaction as a function of the spanwise coordinate, comparing the uncontrolled boundary layer with those controlled by the standard and inverse ramps.

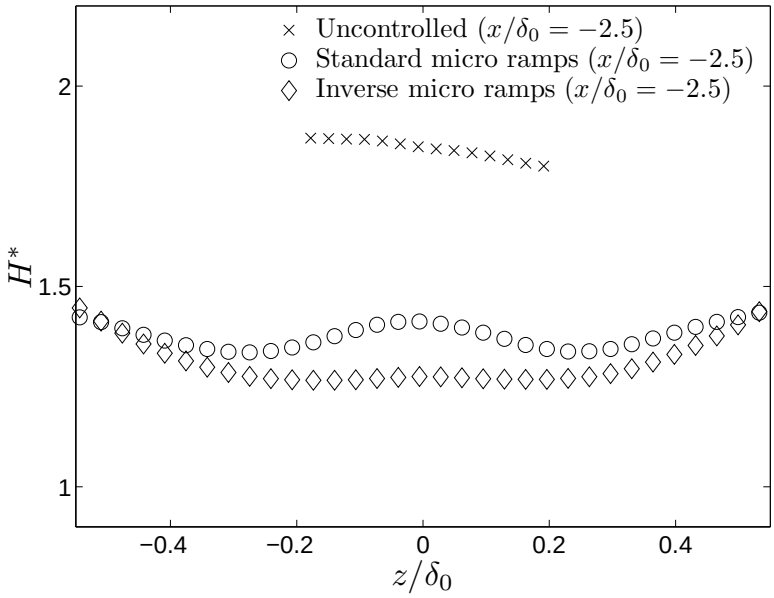

Figure 6.24: Modified shape factor H^* shown upstream of the $\theta = 10.0$-deg interaction as a function of the spanwise coordinate, comparing the uncontrolled boundary layer with those controlled by the standard and inverse ramps.

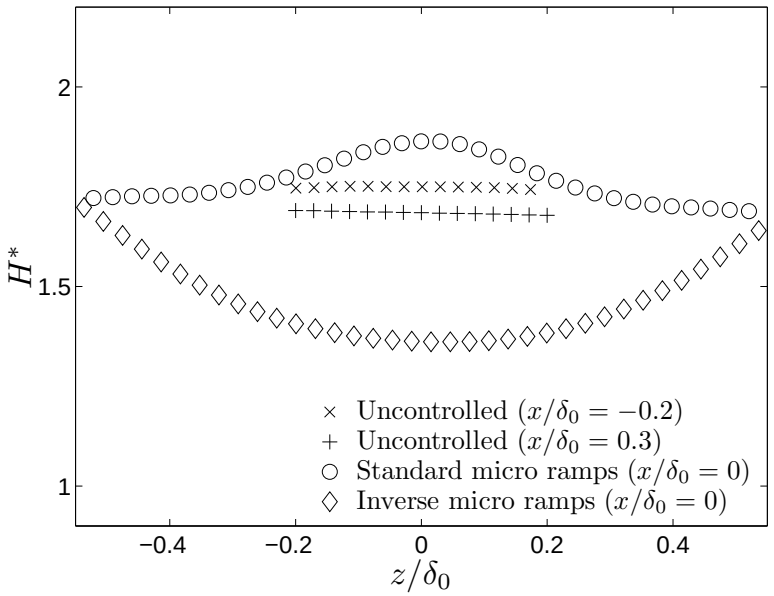

Figure 6.25: Modified shape factor H^* shown downstream of the $\theta = 10.0$-deg interaction as a function of the spanwise coordinate, comparing the uncontrolled boundary layer with those controlled by the standard and inverse ramps.

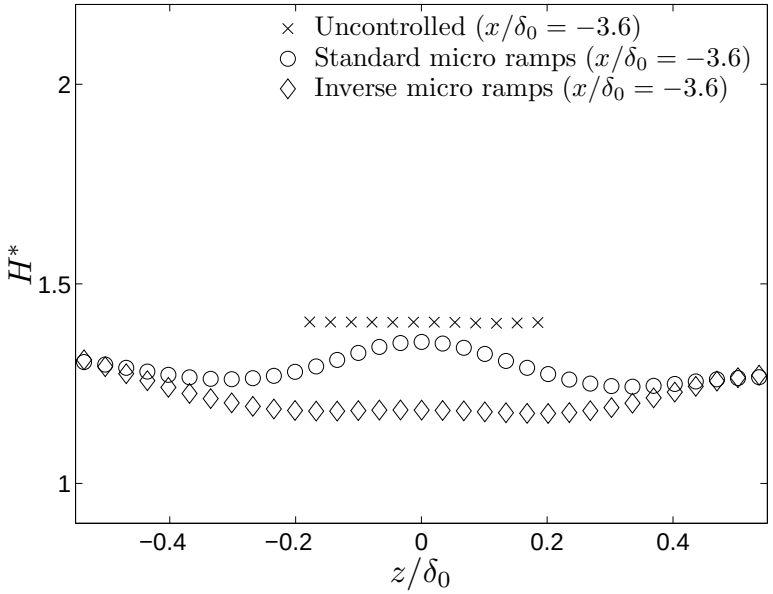

Figure 6.26: Modified shape factor H^* shown upstream of the $\theta = 12.0$-deg interaction as a function of the spanwise coordinate, comparing the uncontrolled boundary layer with those controlled by the standard and inverse ramps.

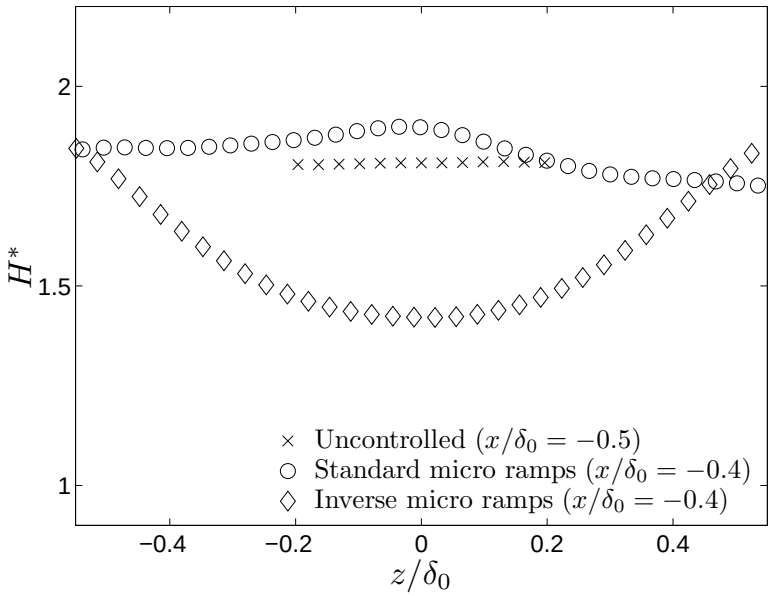

Figure 6.27: Modified shape factor H^* shown downstream of the $\theta = 12.0$-deg interaction as a function of the spanwise coordinate, comparing the uncontrolled boundary layer with those controlled by the standard and inverse ramps.

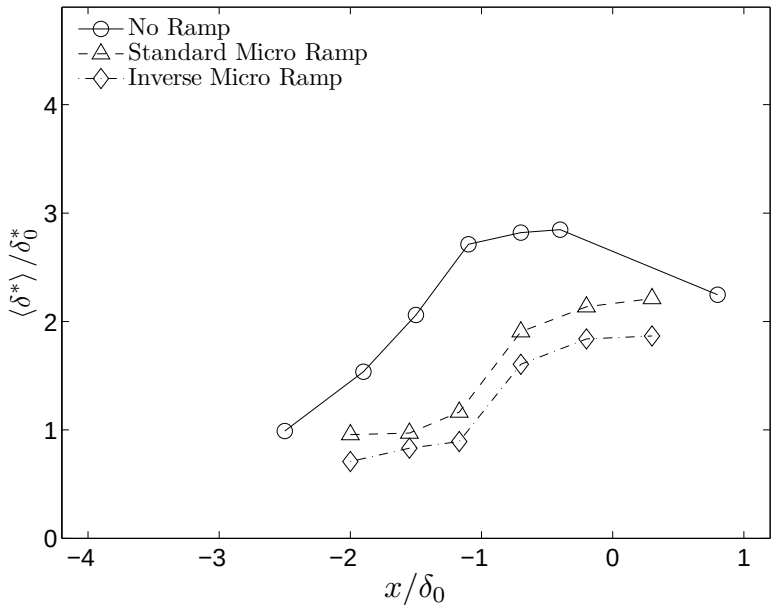

Figure 6.28: The net displacement thickness $\langle\delta^*\rangle$ as a function of the downstream distance x for the $\theta = 7.75$-deg flow deflection angle. The figure compares the interaction controlled by the inverse micro-ramp array to those using the standard micro-ramps and the uncontrolled interaction, demonstrating a 34% reduction in the peak value.

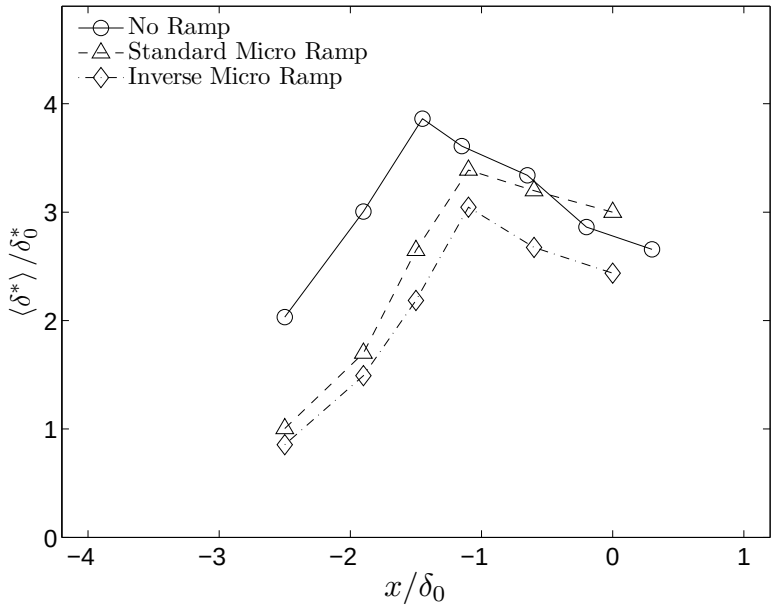

Figure 6.29: The net displacement thickness $\langle\delta^*\rangle$ as a function of the downstream distance x for the $\theta = 10.0$-deg flow deflection angle. The figure compares the interaction controlled by the inverse micro-ramp array to those using the standard micro-ramps and the uncontrolled interaction, demonstrating a 21% reduction in the peak value.

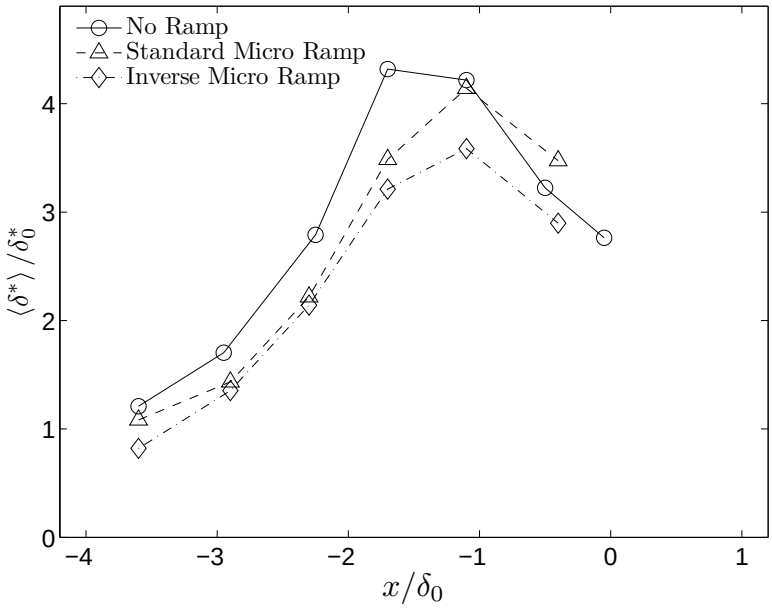

Figure 6.30: The net displacement thickness $\langle \delta^* \rangle$ as a function of the downstream distance x for the $\theta = 12.0$-deg flow deflection angle. The figure compares the interaction controlled by the inverse micro-ramp array to those using the standard micro-ramps and the uncontrolled interaction, demonstrating a 17% reduction in the peak value.

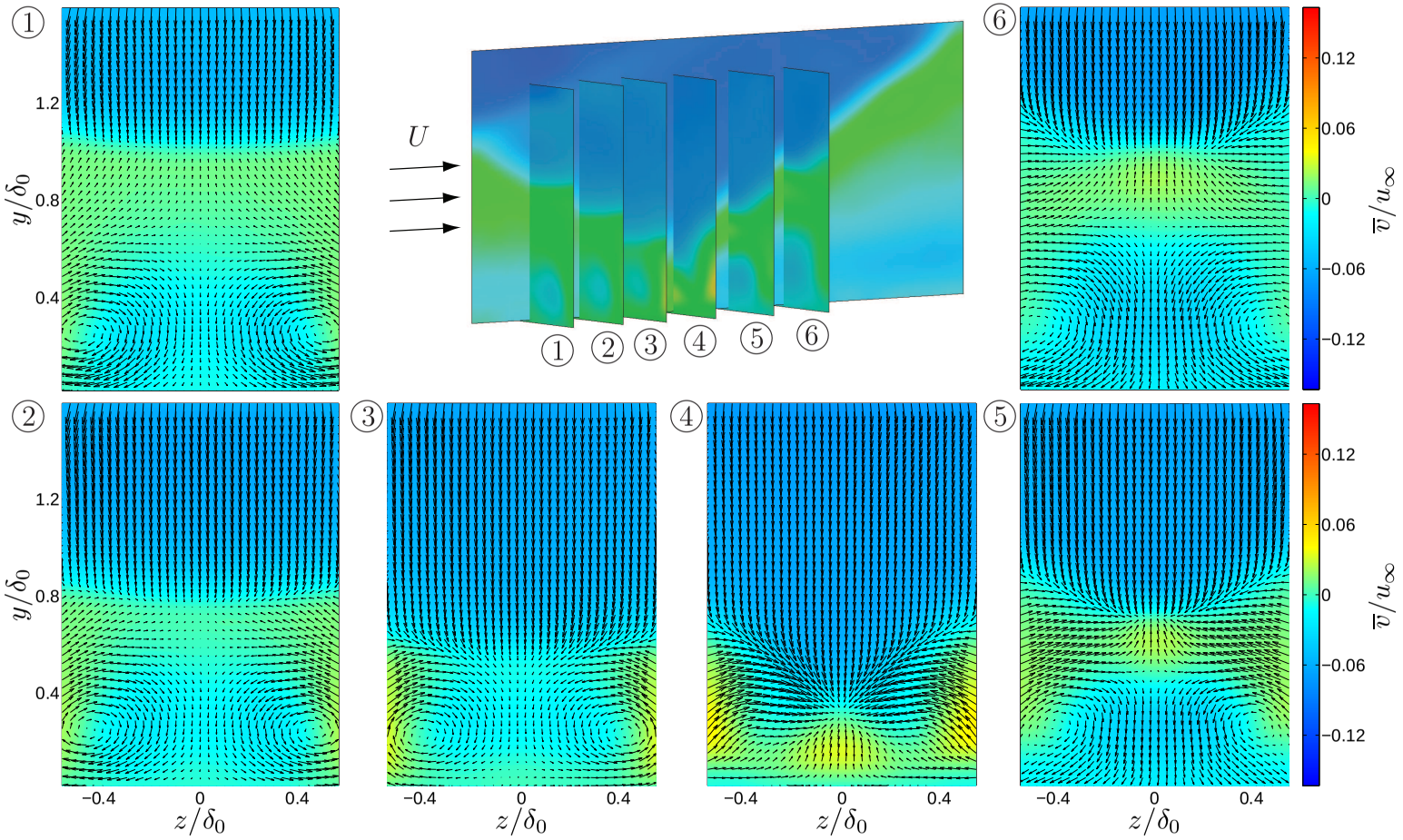

Figure 6.31: Color plots of $\overline{v}$ show the SBLI region in transverse planes for a flow deflection angle of $\theta = 7.75$-deg and passive control via inverse micro-ramps located at $x/\delta_0 = -8.50$. The averaged in-plane velocity fields ($\overline{v}$,$\overline{w}$) are overlayed as vectors. The six sampling locations correspond to 1: $x/\delta_0 = -2.0$, 2: $x/\delta_0 = -1.55$, 3: $x/\delta_0 = -1.2$, 4: $x/\delta_0 = -0.7$, 5: $x/\delta_0 = -0.2$, and 6: $x/\delta_0 = +0.3$. The central perspective plot shows the relative location of each plane.

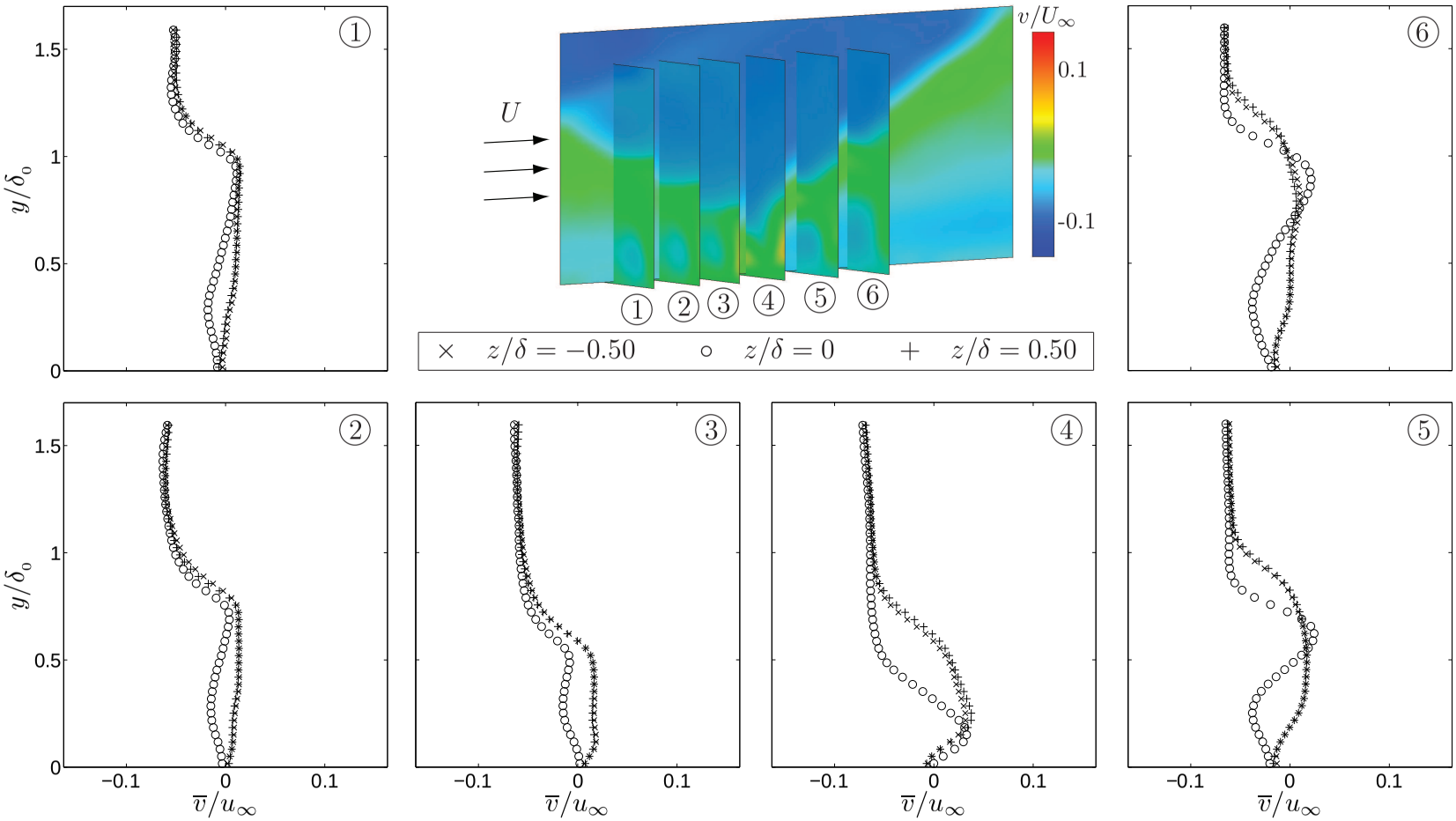

Figure 6.32: The evolution of $\overline{v}$ through the SBLI region is shown for a flow deflection angle of $\theta = 7.75$-deg and passive control via inverse micro-ramps located at $x/\delta_0 = -8.50$. The six sampling locations correspond to 1: $x/\delta_0 = -2.0$, 2: $x/\delta_0 = -1.55$, 3: $x/\delta_0 = -1.2$, 4: $x/\delta_0 = -0.7$, 5: $x/\delta_0 = -0.2$, and 6: $x/\delta_0 = +0.3$. At top, colors show the $\overline{v}$ field throughout each plane and show the relative location of each plane.

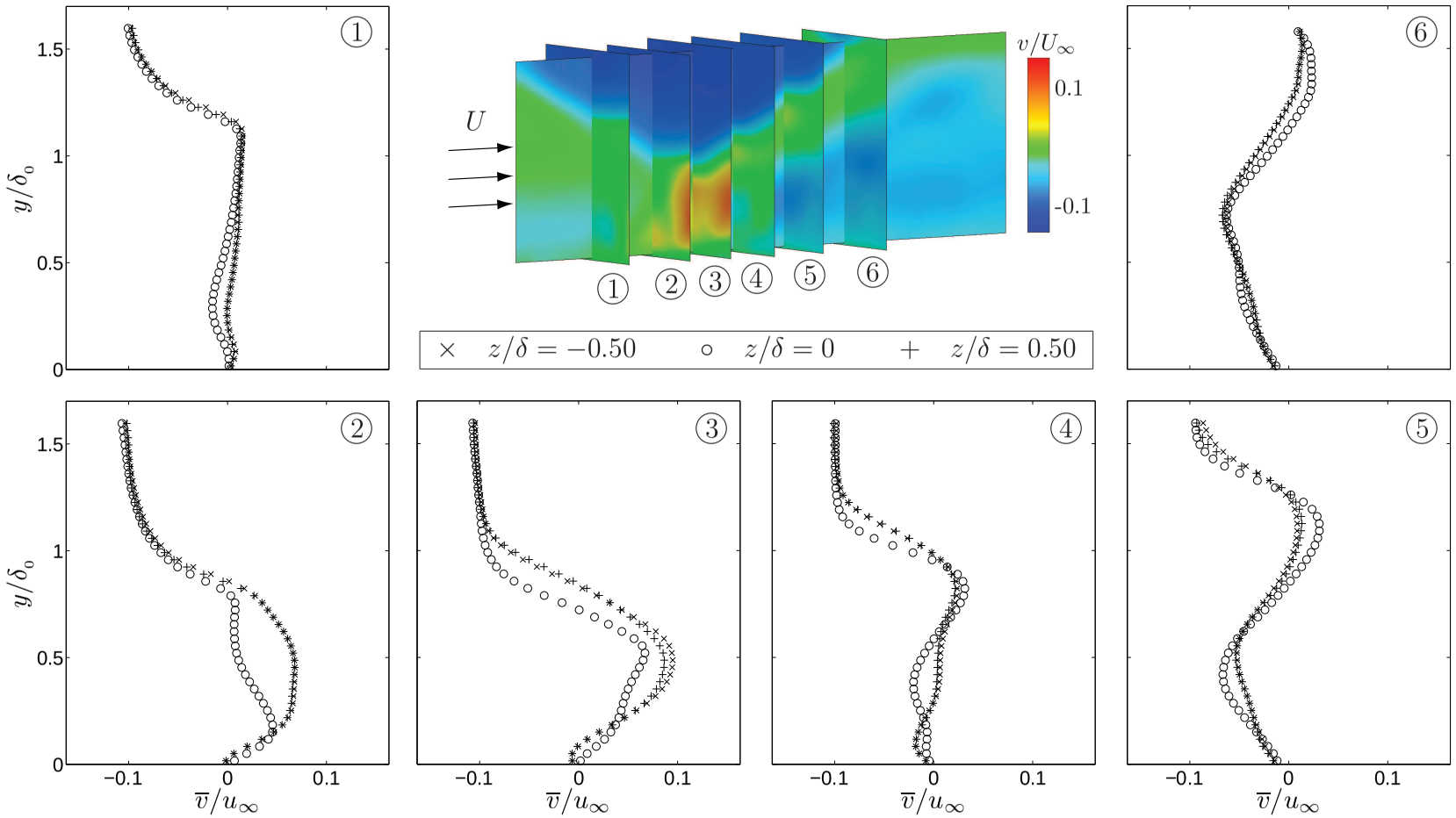

Figure 6.33: The evolution of $\overline{v}$ through the SBLI region is shown for a flow deflection angle of $\theta = 10.0$-deg and passive control via inverse micro-ramps located at $x/\delta_0 = -9.42$. The six sampling locations correspond to 1: $x/\delta_0 = -2.5$, 2: $x/\delta_0 = -1.9$, 3: $x/\delta_0 = -1.5$, 4: $x/\delta_0 = -1.1$, 5: $x/\delta_0 = -0.6$, and 6: $x/\delta_0 = 0.0$. At top, colors show the $\overline{v}$ field throughout each plane and show the relative location of each plane.

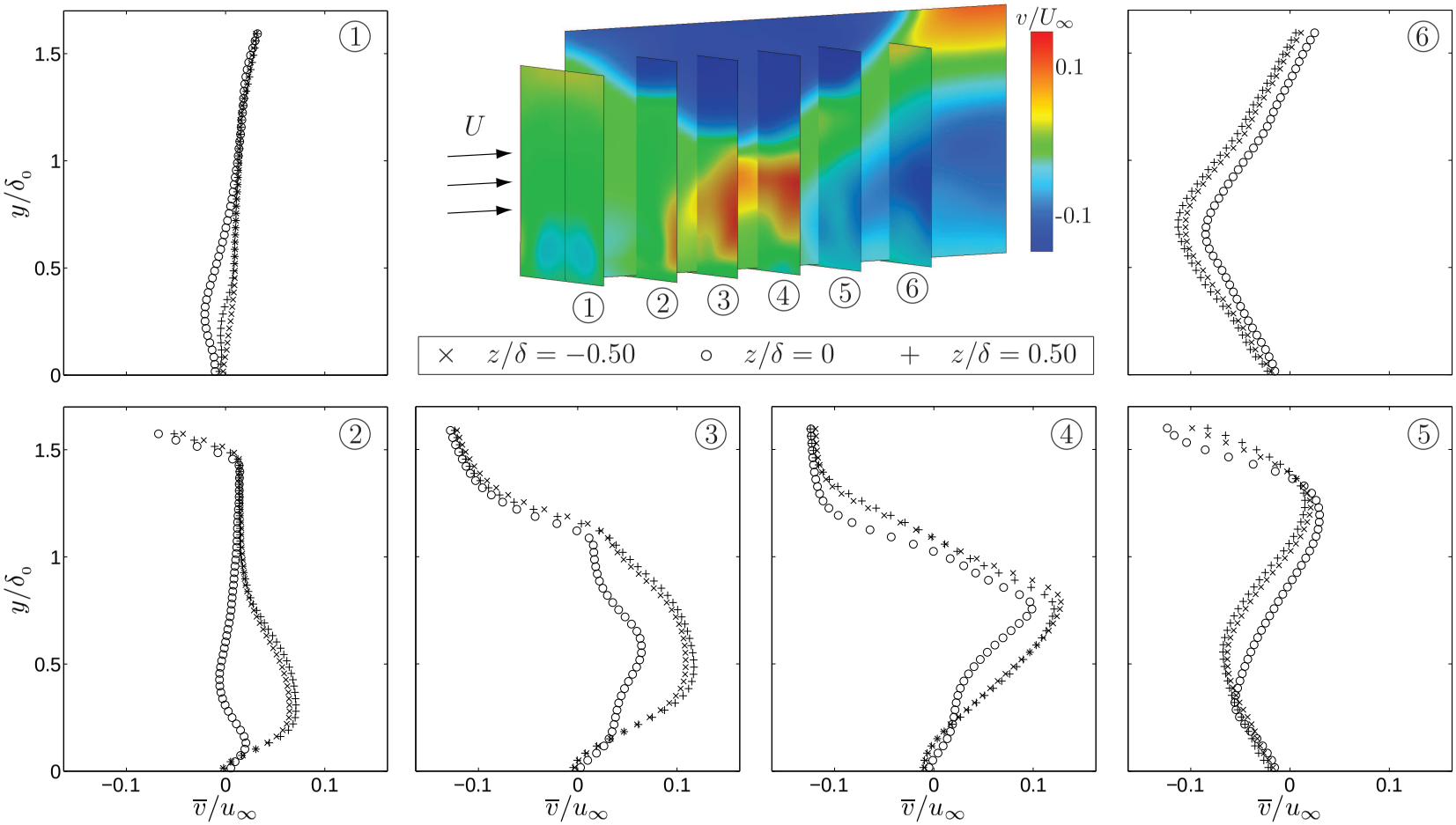

Figure 6.34: The evolution of $\overline{v}$ through the SBLI region is shown for a flow deflection angle of $\theta = 12.0$-deg and passive control via inverse micro-ramps located at $x/\delta_0 = -9.76$. The six sampling locations correspond to 1: $x/\delta_0 = -3.6$, 2: $x/\delta_0 = -2.9$, 3: $x/\delta_0 = -2.3$, 4: $x/\delta_0 = -1.7$, 5: $x/\delta_0 = -1.1$, and 6: $x/\delta_0 = -0.4$. At top, colors show the $\overline{v}$ field throughout each plane and show the relative location of each plane.

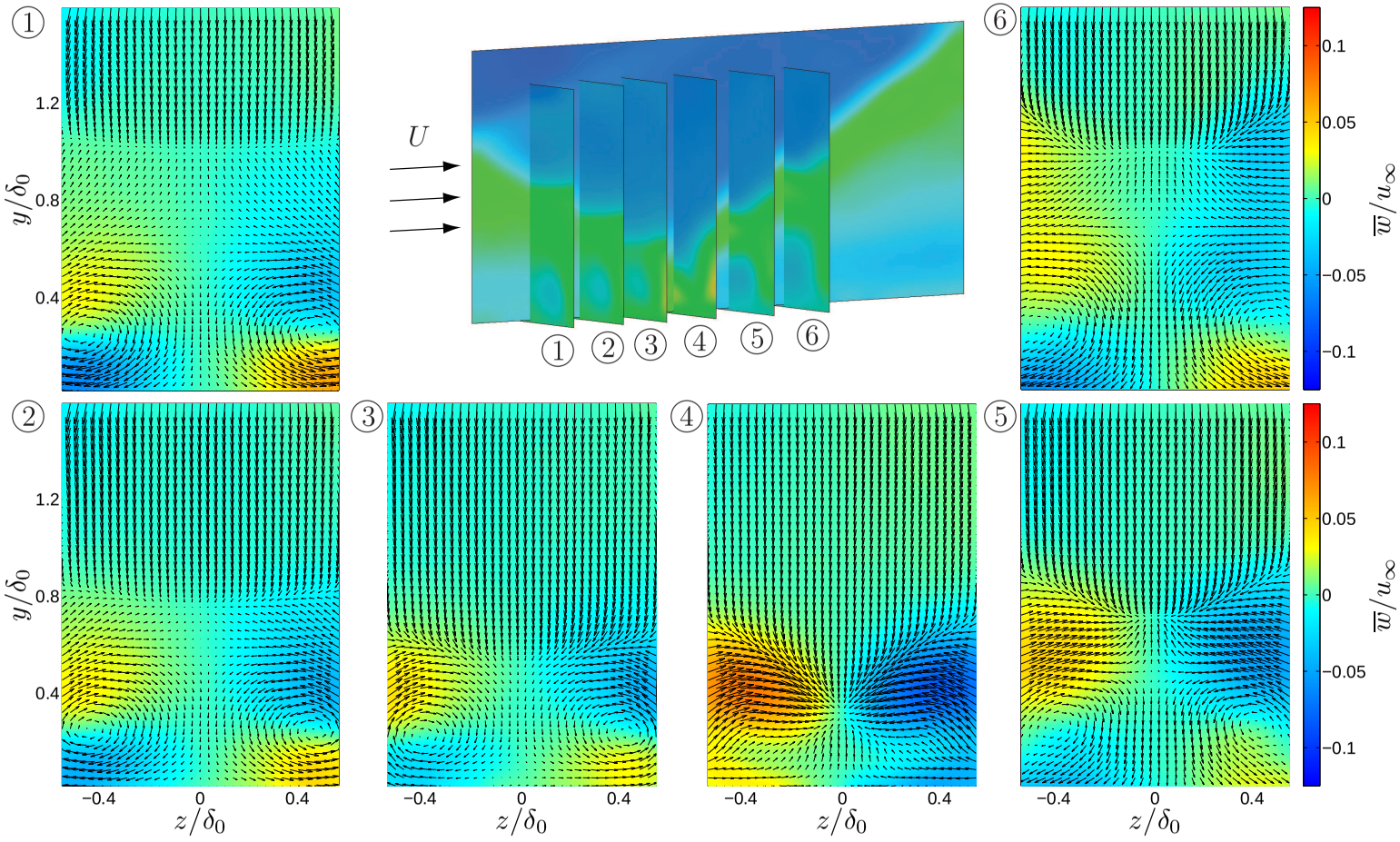

Figure 6.35: Color plots of $\overline{w}$ show the SBLI region in transverse planes for a flow deflection angle of $\theta = 7.75$-deg and passive control via inverse micro-ramps located at $x/\delta_0 = -8.50$. The averaged in-plane velocity fields ($\overline{v}$,$\overline{w}$) are overlayed as vectors. The six sampling locations correspond to 1: $x/\delta_0 = -2.0$, 2: $x/\delta_0 = -1.55$, 3: $x/\delta_0 = -1.2$, 4: $x/\delta_0 = -0.7$, 5: $x/\delta_0 = -0.2$, and 6: $x/\delta_0 = +0.3$. The central perspective plot shows the relative location of each plane.

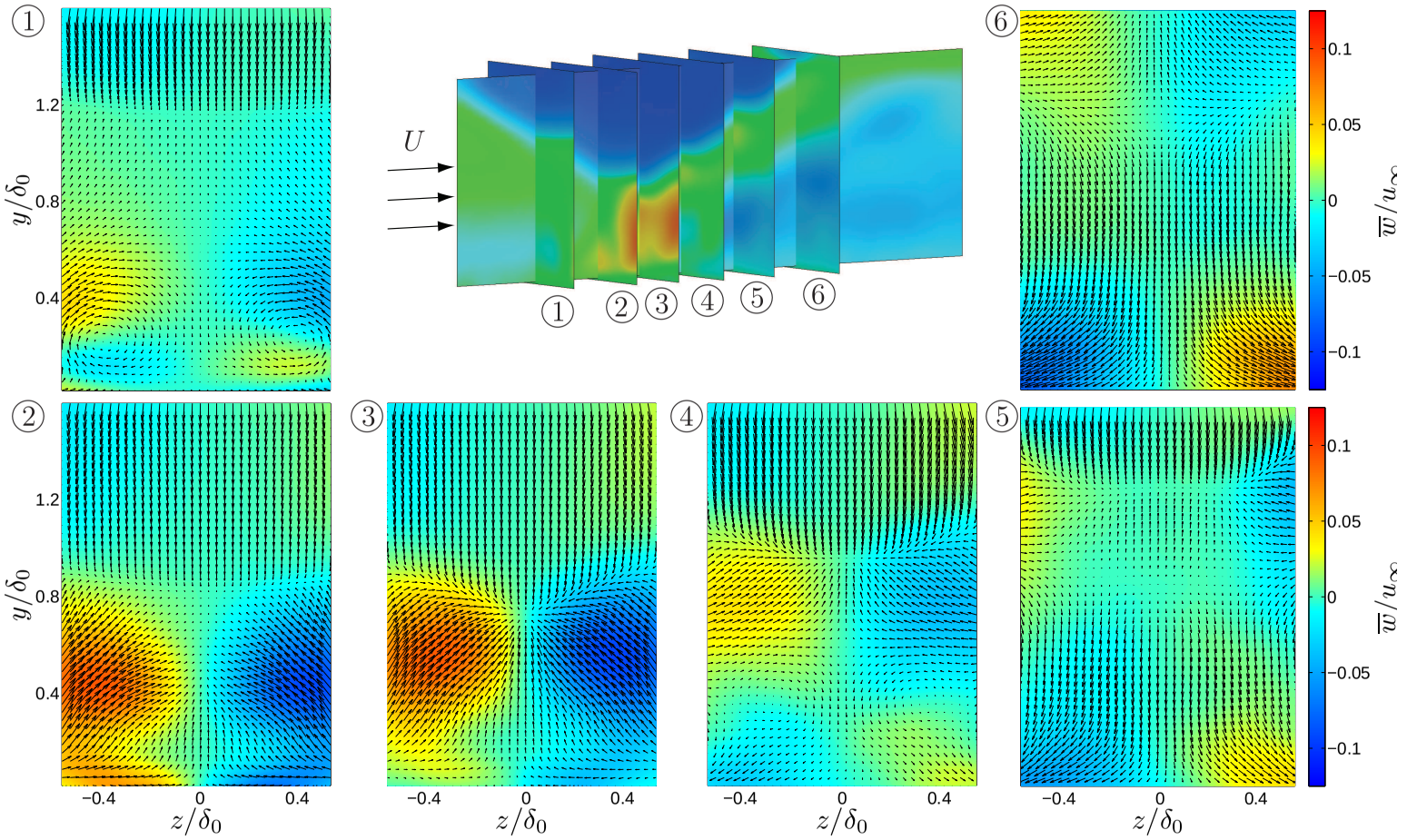

Figure 6.36: Color plots of $\overline{w}$ show the SBLI region in transverse planes for a flow deflection angle of $\theta = 10.0$-deg and passive control via inverse micro-ramps located at $x/\delta_0 = -9.42$. The averaged in-plane velocity fields ($\overline{v}$,$\overline{w}$) are overlayed as vectors. The six sampling locations correspond to 1: $x/\delta_0 = -2.5$, 2: $x/\delta_0 = -1.9$, 3: $x/\delta_0 = -1.5$, 4: $x/\delta_0 = -1.1$, 5: $x/\delta_0 = -0.6$, and 6: $x/\delta_0 = 0.0$. The central perspective plot shows the relative location of each plane.

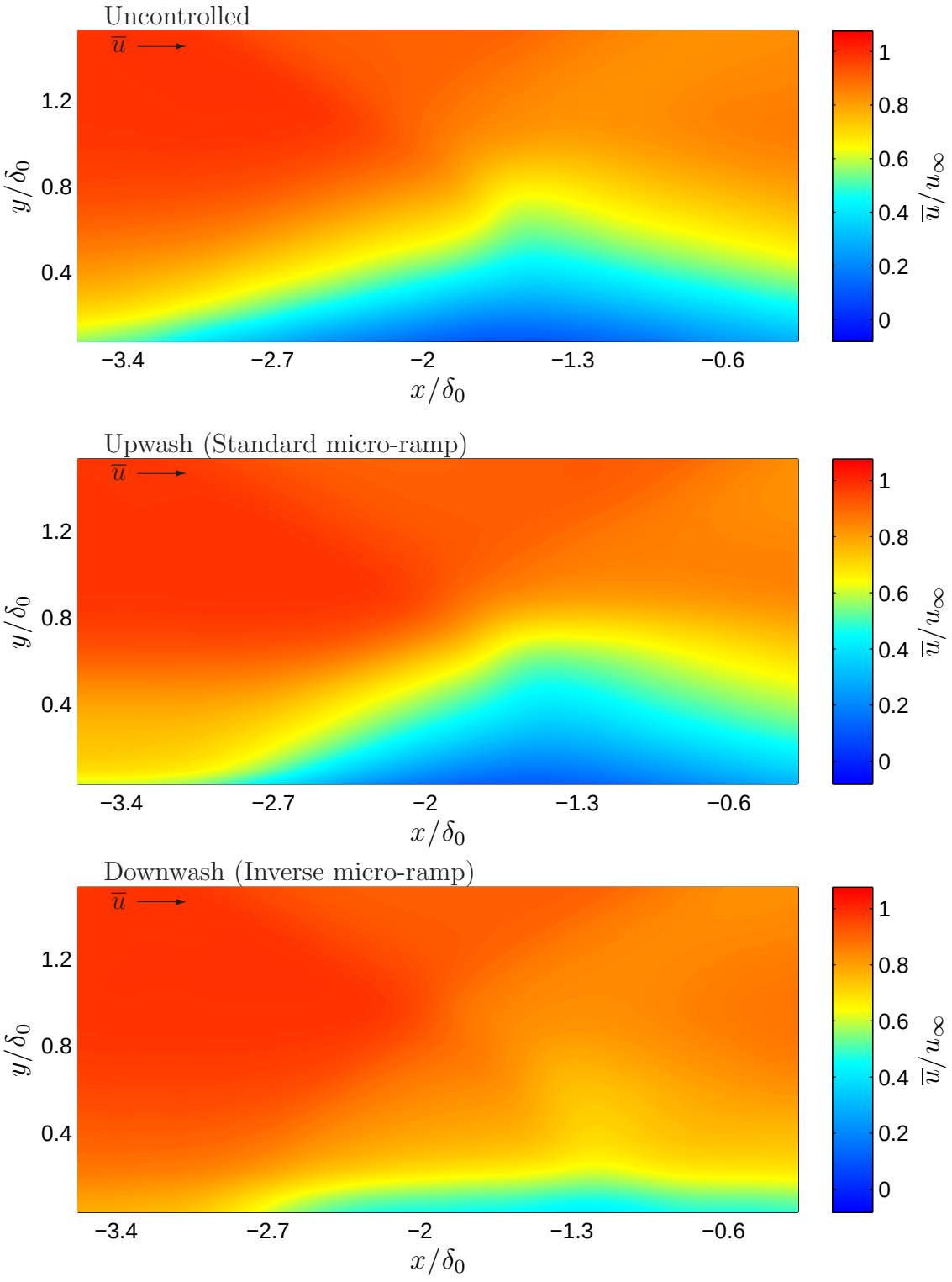

Figure 6.37: The mean streamwise velocity $\overline{u}$ fields are shown along the tunnel centerline from the uncontrolled interaction, the vortex-induced upwash region produced by the standard micro-ramp, and the vortex-induced downwash region produced by the inverse micro-ramp. All visualizations involve the $\theta = 12.0$-deg flow deflection angle.

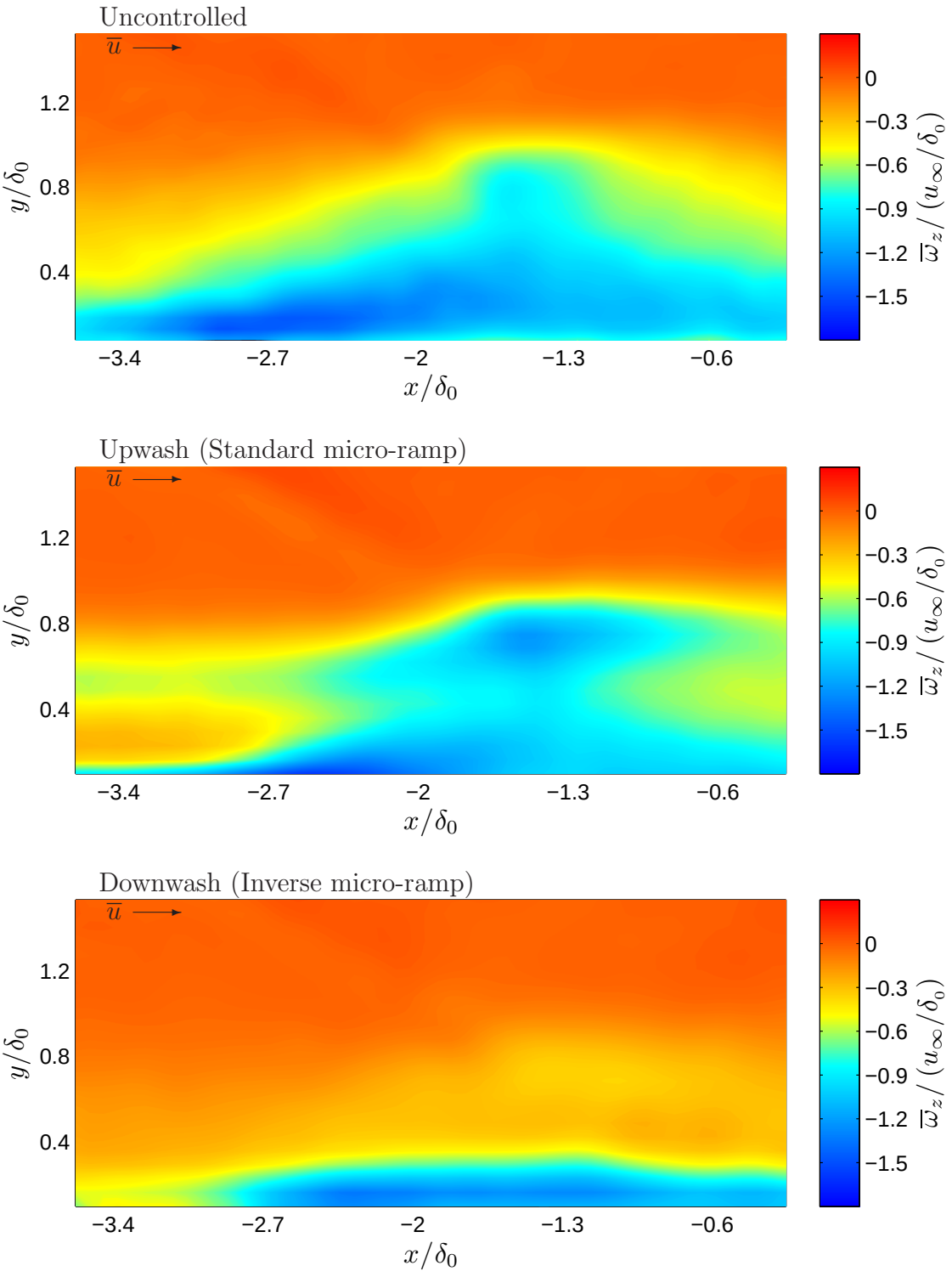

Figure 6.38: The mean spanwise vorticity component $\overline{\omega}_z$ fields are shown along the tunnel centerline from the uncontrolled interaction, the vortex-induced upwash region produced by the standard micro-ramp, and the vortex-induced downwash region produced by the inverse micro-ramp. All visualizations involve the $\theta = 12.0$-deg flow deflection angle.

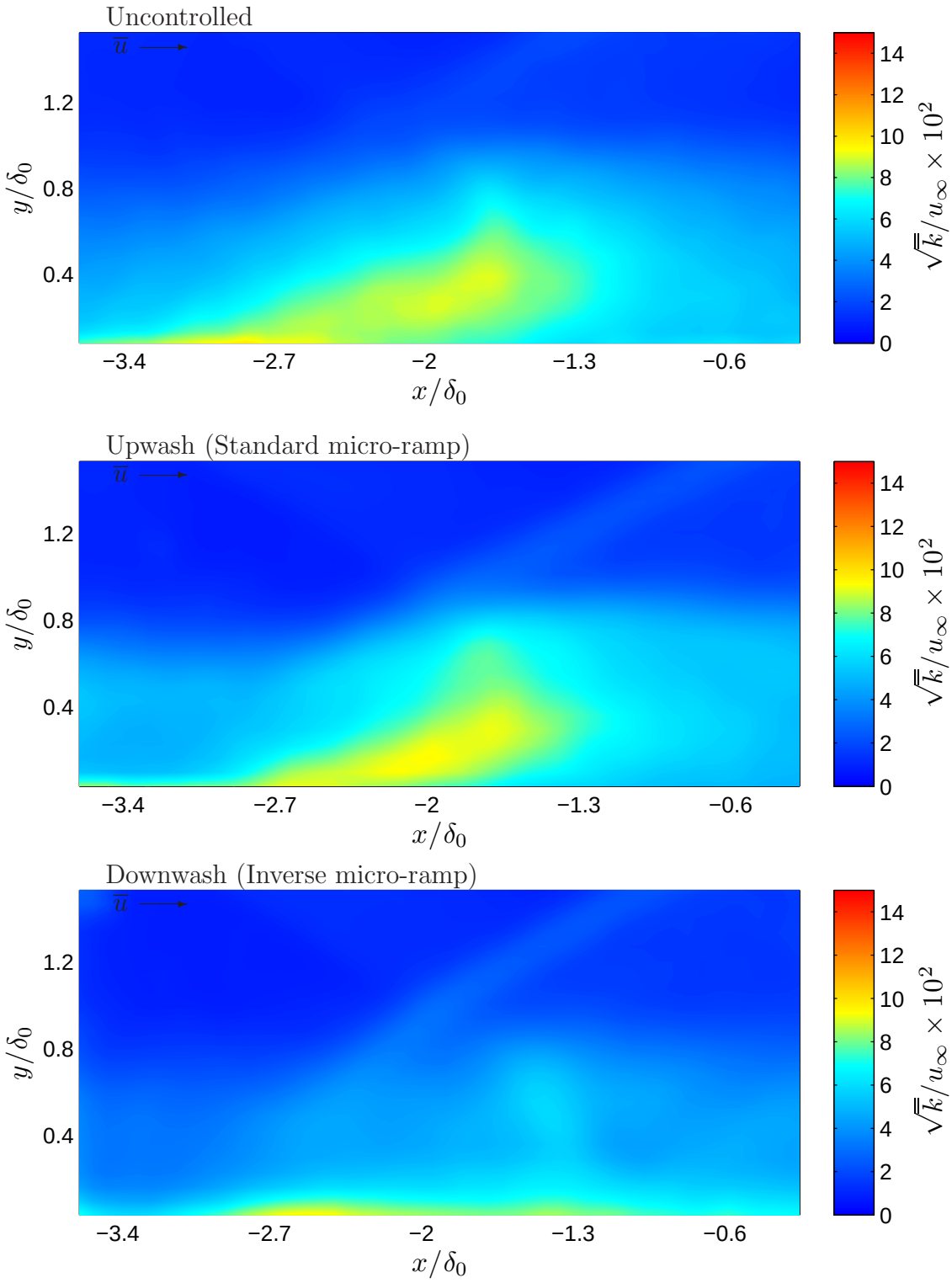

Figure 6.39: The mean turbulence kinetic energy $\overline{k}$ fields are shown along the tunnel centerline from the uncontrolled interaction, the vortex-induced upwash region produced by the standard micro-ramp, and the vortex-induced downwash region produced by the inverse micro-ramp. All visualizations involve the $\theta = 12.0$-deg flow deflection angle.

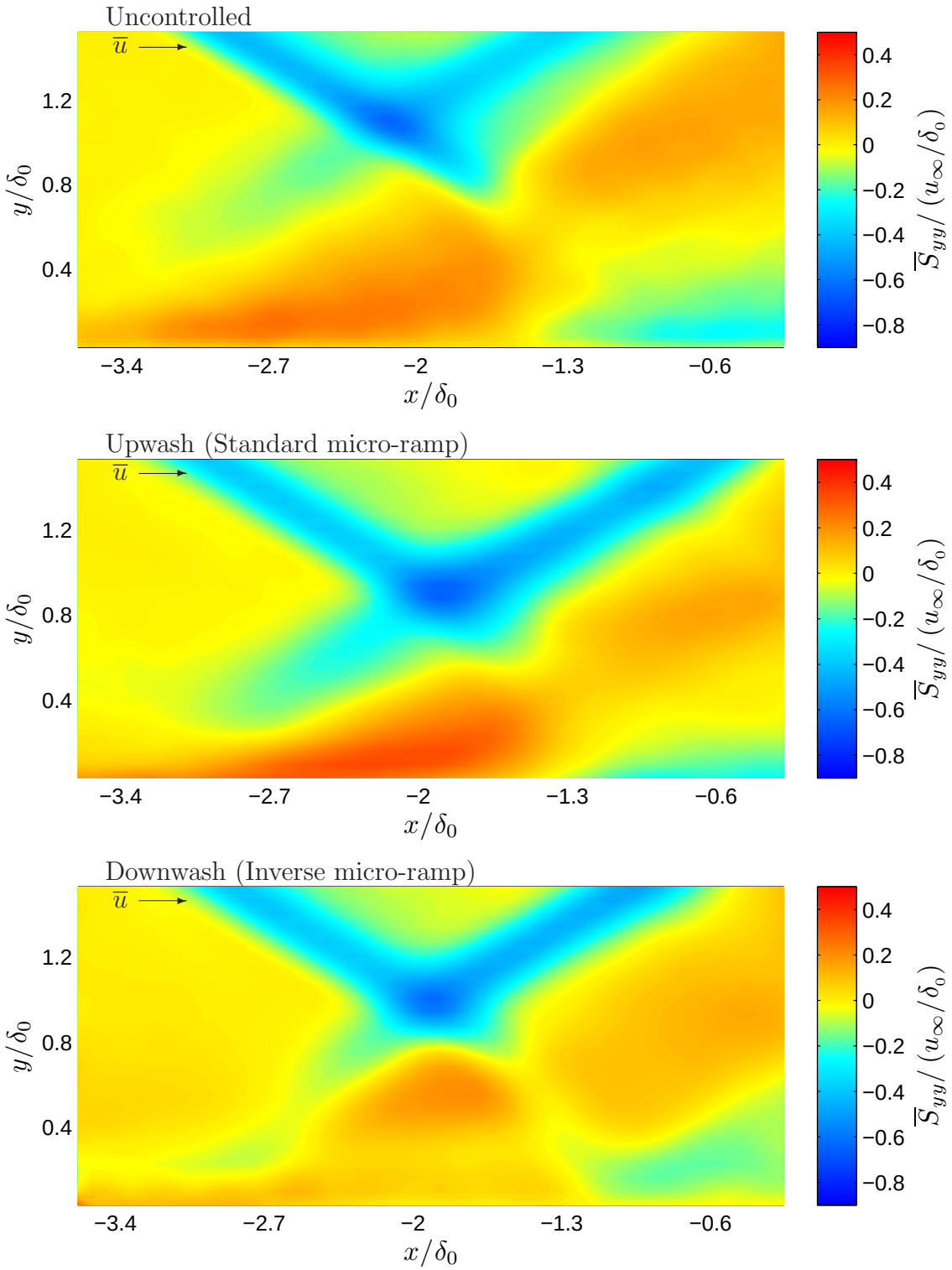

Figure 6.40: The mean normal strain rate $\overline{S}_{yy}$ fields are shown along the tunnel centerline from the uncontrolled interaction, the vortex-induced upwash region produced by the standard micro-ramp, and the vortex-induced downwash region produced by the inverse micro-ramp. All visualizations involve the $\theta = 12.0$-deg flow deflection angle.

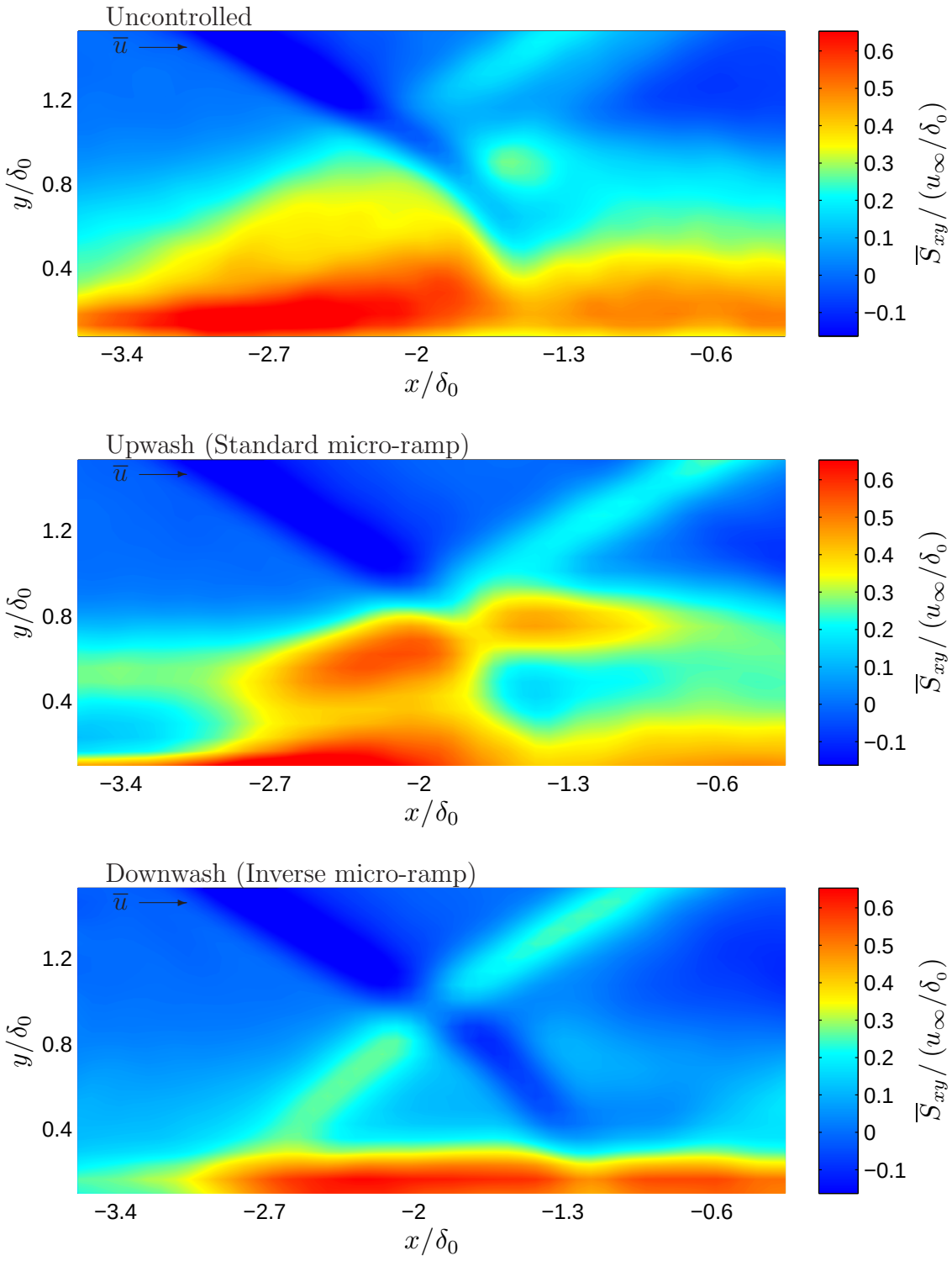

Figure 6.41: The mean shear strain rate $\overline{S}_{xy}$ fields are shown along the tunnel centerline from the uncontrolled interaction, the vortex-induced upwash region produced by the standard micro-ramp, and the vortex-induced downwash region produced by the inverse micro-ramp. All visualizations involve the $\theta = 12.0$-deg flow deflection angle.

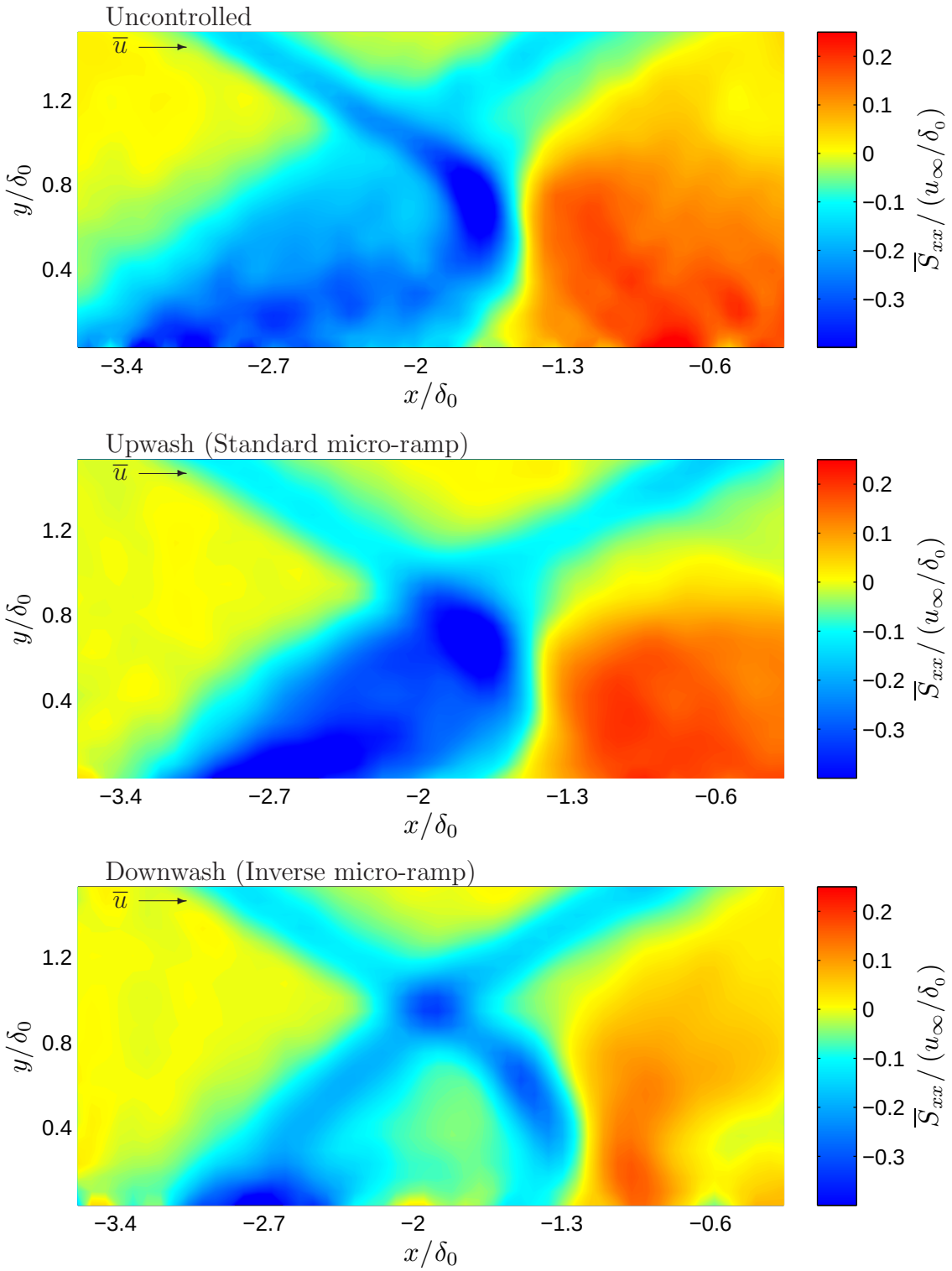

Figure 6.42: The mean normal strain rate $\overline{S}_{xx}$ fields are shown along the tunnel centerline from the uncontrolled interaction, the vortex-induced upwash region produced by the standard micro-ramp, and the vortex-induced downwash region produced by the inverse micro-ramp. All visualizations involve the $\theta = 12.0$-deg flow deflection angle.

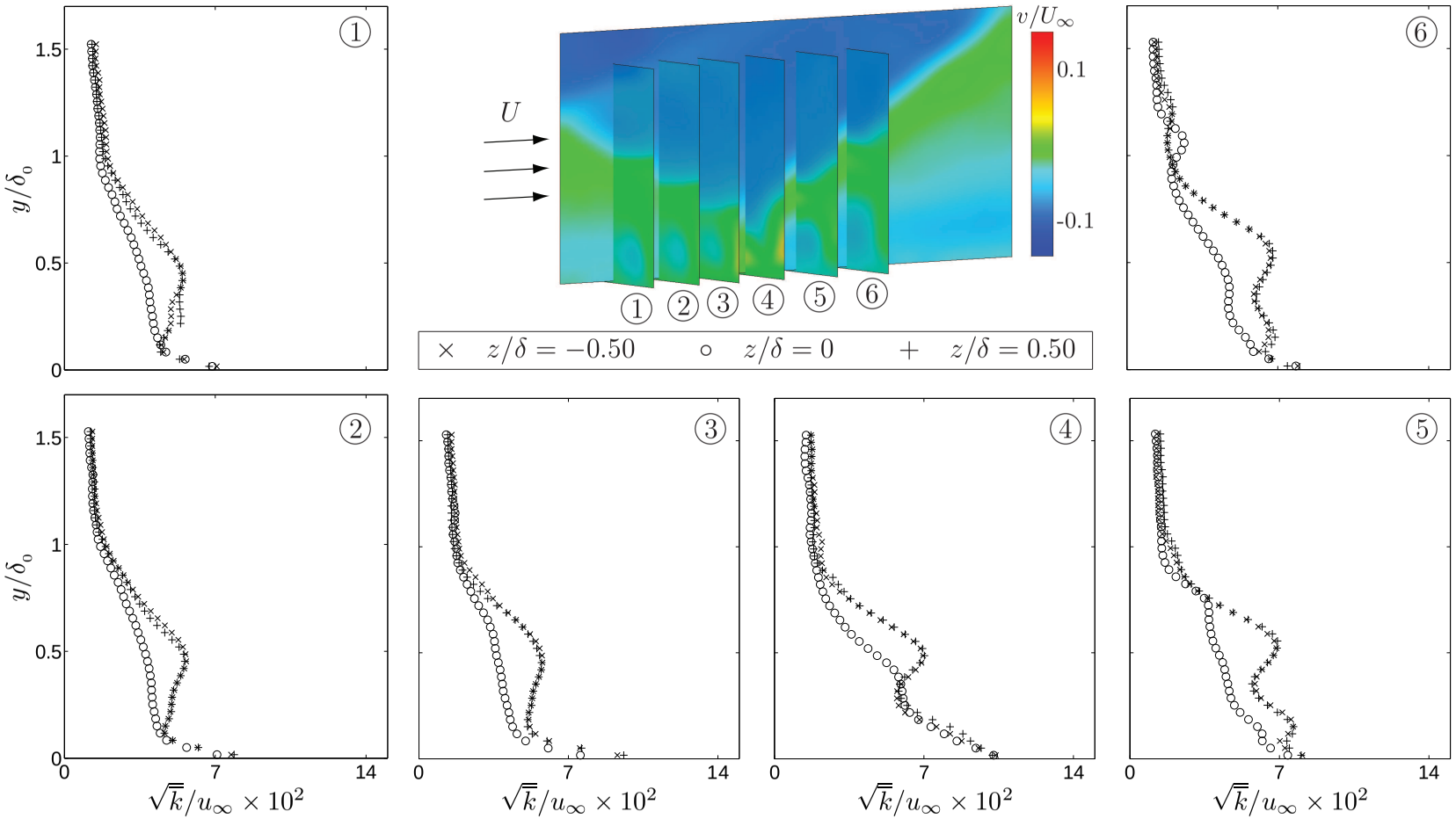

Figure 6.43: The evolution of $\overline{k}$ through the SBLI region is shown for a flow deflection angle of $\theta = 7.75$-deg and passive control via inverse micro-ramps located at $x/\delta_0 = -8.50$. The six sampling locations correspond to 1: $x/\delta_0 = -2.0$, 2: $x/\delta_0 = -1.55$, 3: $x/\delta_0 = -1.2$, 4: $x/\delta_0 = -0.7$, 5: $x/\delta_0 = -0.2$, and 6: $x/\delta_0 = +0.3$. At top, colors show the $\overline{v}$ field throughout each plane and show the relative location of each plane.

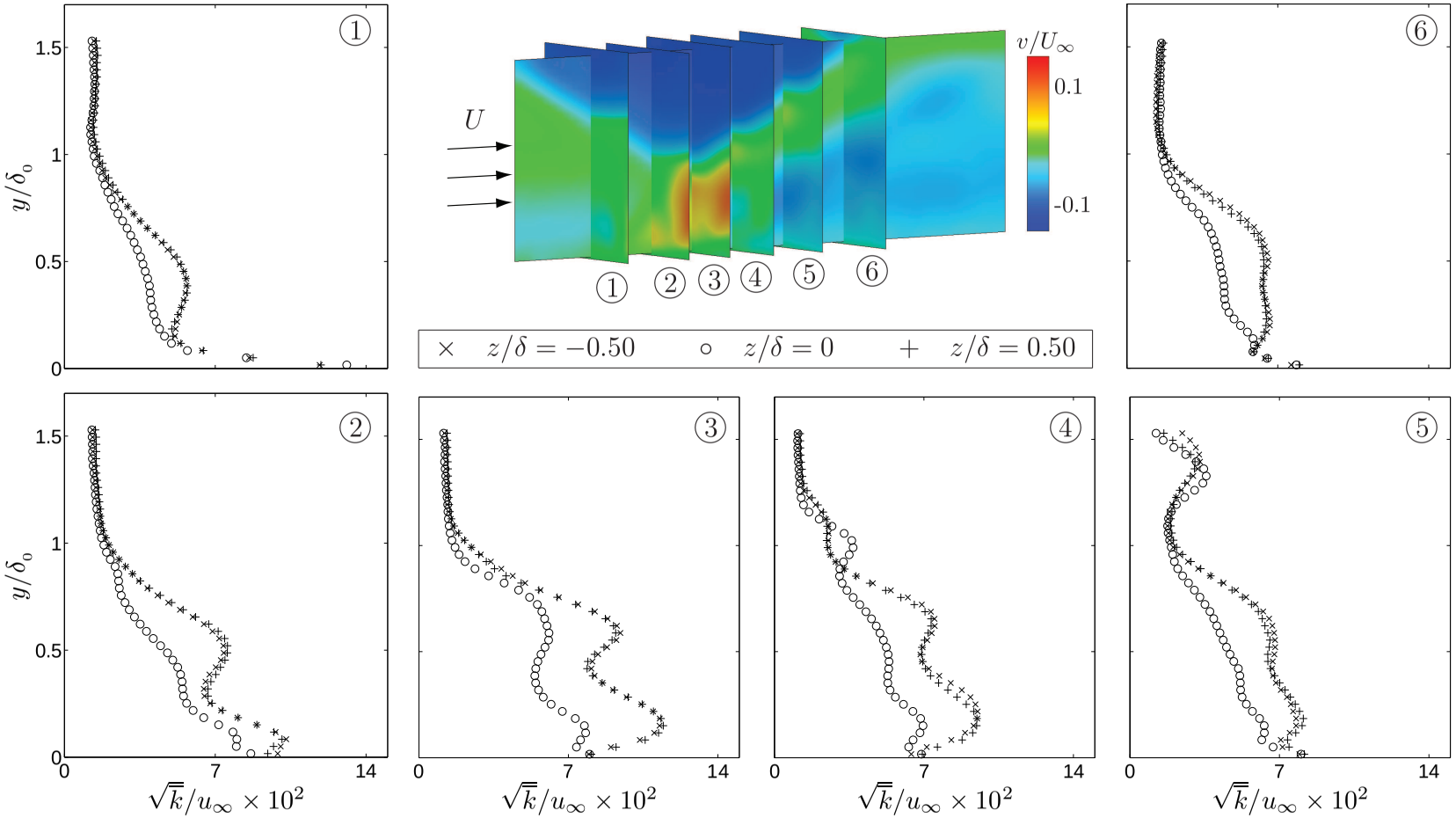

Figure 6.44: The evolution of $\overline{k}$ through the SBLI region is shown for a flow deflection angle of $\theta = 10.0$-deg and passive control via inverse micro-ramps located at $x/\delta_0 = -9.42$. The six sampling locations correspond to 1: $x/\delta_0 = -2.5$, 2: $x/\delta_0 = -1.9$, 3: $x/\delta_0 = -1.5$, 4: $x/\delta_0 = -1.1$, 5: $x/\delta_0 = -0.6$, and 6: $x/\delta_0 = 0.0$. At top, colors show the $\overline{v}$ field throughout each plane and show the relative location of each plane.

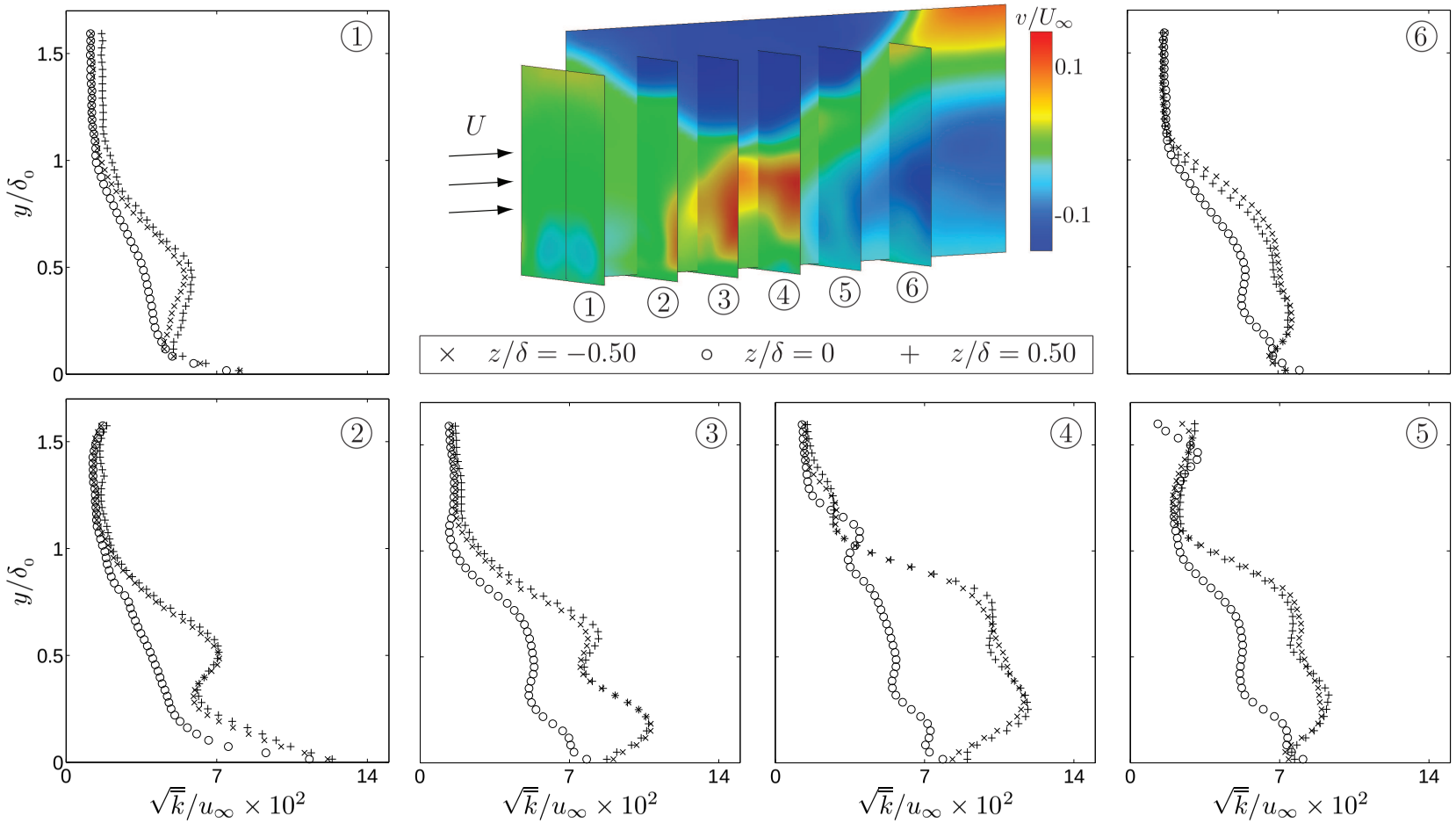

Figure 6.45: The evolution of $\overline{k}$ through the SBLI region is shown for a flow deflection angle of $\theta = 12.0$-deg and passive control via inverse micro-ramps located at $x/\delta_0 = -9.76$. The six sampling locations correspond to 1: $x/\delta_0 = -3.6$, 2: $x/\delta_0 = -2.9$, 3: $x/\delta_0 = -2.3$, 4: $x/\delta_0 = -1.7$, 5: $x/\delta_0 = -1.1$, and 6: $x/\delta_0 = -0.4$. At top, colors show the $\overline{v}$ field throughout each plane and show the relative location of each plane.

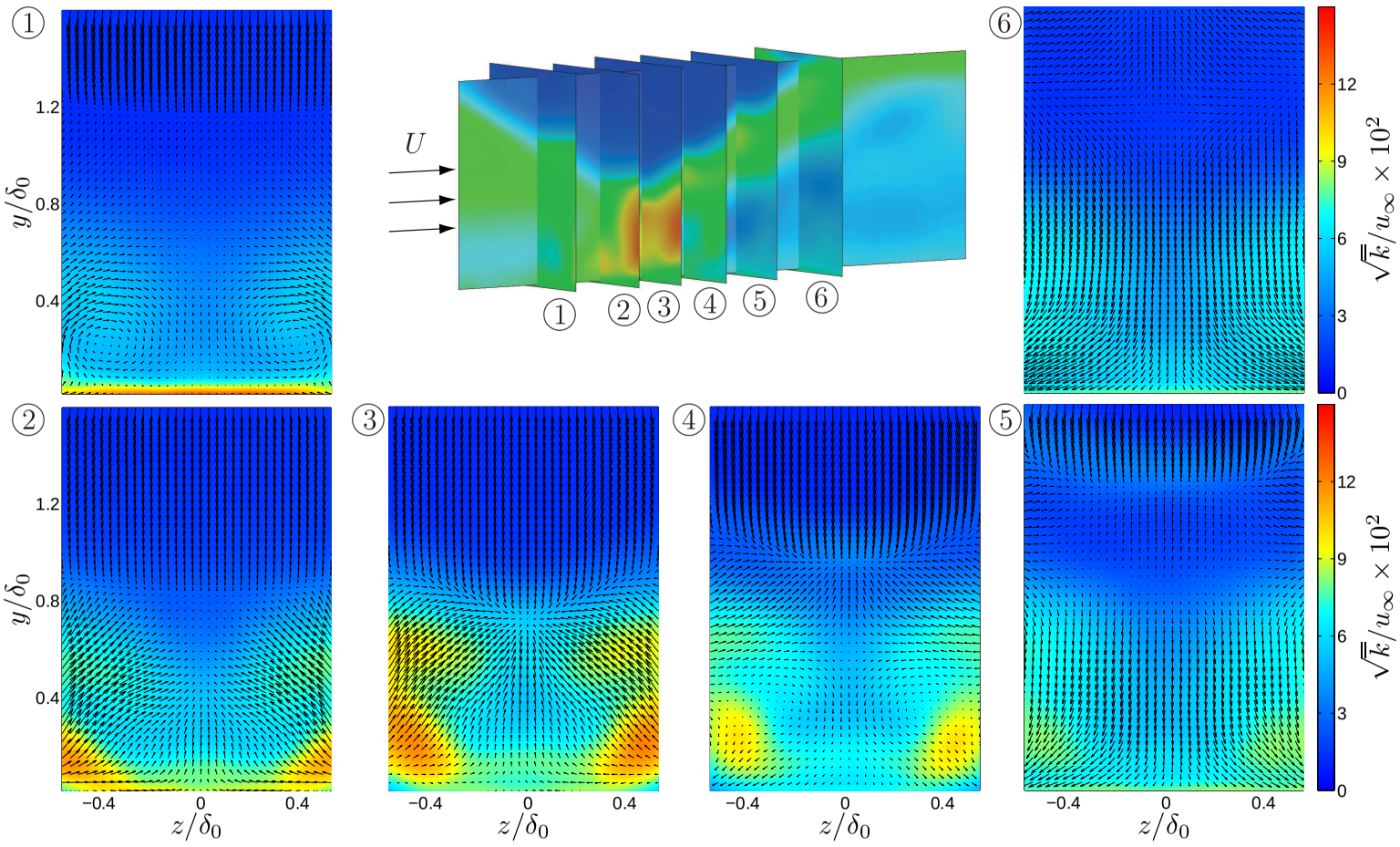

Figure 6.46: Color plots of $\overline{k}$ show the SBLI region in transverse planes for a flow deflection angle of $\theta = 10.0$-deg and passive control via inverse micro-ramps located at $x/\delta_0 = -9.42$. The averaged in-plane velocity fields ($\overline{v}$,$\overline{w}$) are overlayed as vectors. The six sampling locations correspond to 1: $x/\delta_0 = -2.5$, 2: $x/\delta_0 = -1.9$, 3: $x/\delta_0 = -1.5$, 4: $x/\delta_0 = -1.1$, 5: $x/\delta_0 = -0.6$, and 6: $x/\delta_0 = 0.0$. The central perspective plot shows the relative location of each plane.

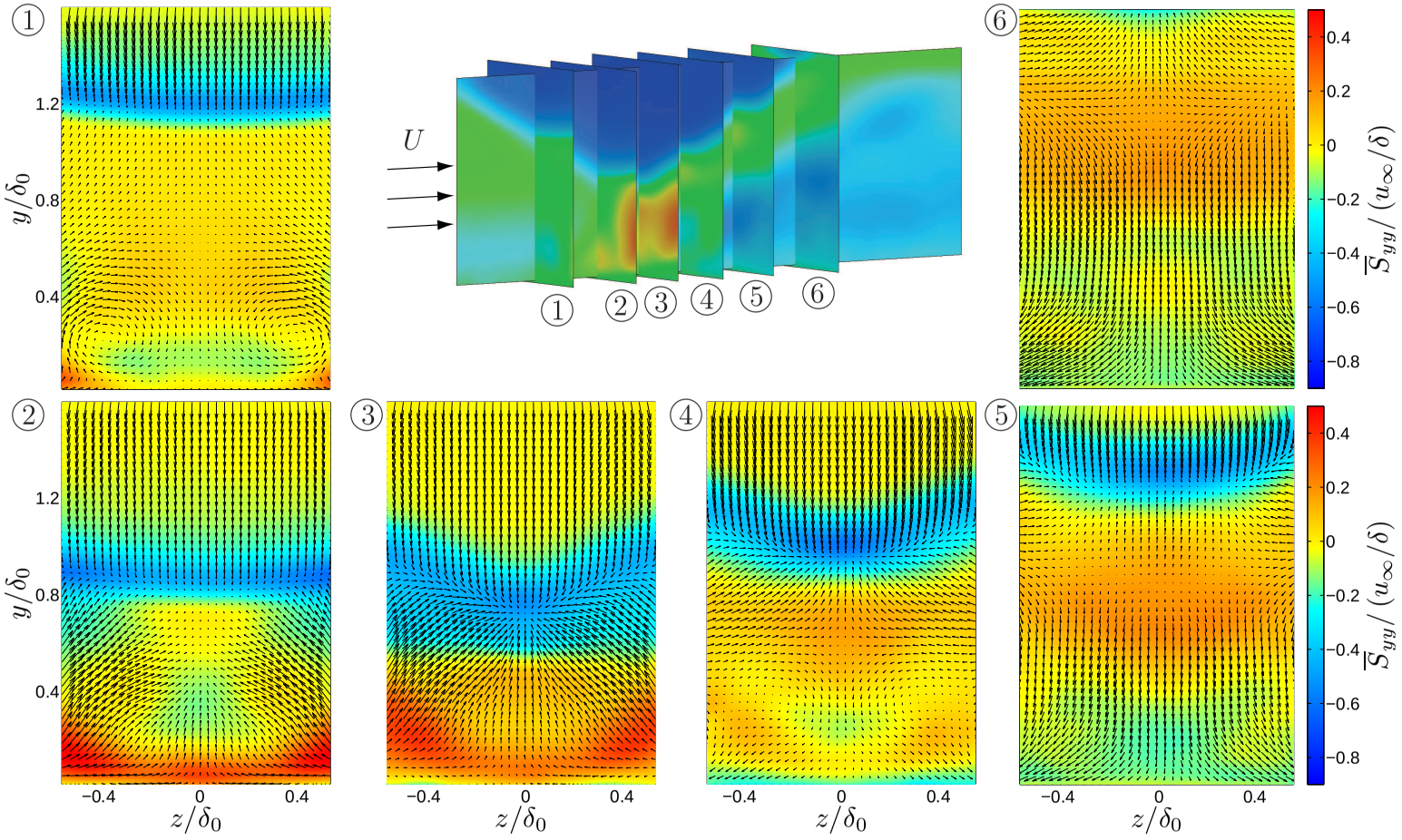

Figure 6.47: Color plots of $\overline{S}_{yy}$ show the SBLI region in transverse planes for a flow deflection angle of $\theta = 10.0$-deg and passive control via inverse micro-ramps located at $x/\delta_0 = -9.42$. The averaged in-plane velocity fields ($\overline{v}$,$\overline{w}$) are overlayed as vectors. The six sampling locations correspond to 1: $x/\delta_0 = -2.5$, 2: $x/\delta_0 = -1.9$, 3: $x/\delta_0 = -1.5$, 4: $x/\delta_0 = -1.1$, 5: $x/\delta_0 = -0.6$, and 6: $x/\delta_0 = 0.0$. The central perspective plot shows the relative location of each plane.

CHAPTER VII

Conclusions

The potential effectiveness of ramp-like streamwise vortex generators for passive control of incident oblique shock–boundary layer interactions (SBLI) has been investigated using highly resolved stereo particle image velocimetry (SPIV) measurements. An "inverse" micro-ramp design is introduced which, according to multiple metrics, demonstrates a two-fold improvement over the standard design in the ability to generate streamwise vortices. The effects of the resulting stronger vortices on the control of SBLI are similarly improved over those produced by the standard design. Thus a simple, passive, and physically robust method for SBLI control is proposed to supplement or replace other active techniques in practical applications.

The dissertation separately investigates undisturbed compressible boundary layers, uncontrolled shock–boundary layer interactions, SBLI controlled by standard micro-ramps, and SBLI controlled by the new inverse micro-ramps. High fidelity non-intrusive measurements of the undisturbed boundary layer provide the first- and second-order mean, fluctuation, and gradient quantities needed for rigorous evaluation of computational models. Major findings relating to uncontrolled shock–boundary layer interactions include:

(1) The thickening of the boundary layer through the SBLI region is quantified

via the mean spanwise vorticity component $\overline{\omega}_z$, which additionally uncovers aspects of the interaction structure. One such aspect is a protuberance that can comprise a significant portion of the overall boundary layer height. The protuberance results from the fluctuating interaction and the resulting space between the incident shock wave, C_3, and its reflection from the sonic line. The same feature is observed by inspection of the $\overline{u}(x, y)$ and $\overline{S}_{xy}(x, y)$ fields, and its prevalence increases with increasing incident shock strength.

(2) The upstream penetration distance of the reflected shock wave grows linearly with the incident shock strength. Additionally, the x and y coordinates of the intersection point I also vary approximately linearly with the incident shock strength.

(3) A thin layer of high shear, anchored by the impingement of the reflected shock wave, C_2, is identified and visualized in the upstream portion of the interaction region. Results show compelling evidence that this free shear layer is highly unstable and is likely fundamental to the large-scale low-frequency oscillations preeminent in strong shock–boundary layer interactions.

(4) The effect of the SBLI on the turbulence state is investigated via the two non-zero invariants of the anisotropy tensor. As a result of the interaction, the near-wall turbulence state transitions from having one dominant fluctuation component to a state much closer to isotropic.

The effects of the standard micro-ramp design on SBLI are compared to the effects of the new inverse micro-ramp design. Major findings relating to the effects of these passive control devices include:

(5) Streamwise vortex generator arrays produce regions of alternating vortex-induced upwash and downwash across the span. Preferential entrainment of high-velocity gas means that the effects of the downwash regions generally outweigh the effects of the upwash regions.

(6) Sufficiently strong streamwise vortices locally eliminate recirculation zones from forming in the vortex-induced downwash regions. This also forces the shear layer identified in Conclusion 3 to remain fixed to the bottom wall boundary.

(7) Large-scale fluctuations of the interaction structure are dramatically reduced in the vortex-induced downwash regions as a result of the shear layer remaining attached to the wall.

(8) Extrapolating Conclusions 6 and 7 across the entire span suggests that well-designed micro-ramp arrays will reduce large scale recirculation zones to much smaller structures whose sizes are on the order of the micro-ramp spacing. The associated instabilities will be similarly localized.

(9) The magnitudes of the wall-normal velocity indicate that the upstream reflected shock wave is weakened in the vortex-induced downwash regions but is of comparable strength to the uncontrolled case in the vortex-induced upwash regions. This indicates a potential reduction in the net wave drag associated with the SBLI.

(10) The magnitude and locations of the streamwise vortices are critical to their effectiveness, and the sense of vorticity in the vortex pair are key determinants of these factors. The new inverse micro-ramp design provides a factor of 2.3 increase in peak vorticity, a factor of 1.8 increase in total circulation, a factor

of 2.2 increase in spanwise extent, and a factor of 1.7 decrease in wall-normal location over the standard micro-ramp design.

(11) Due to the improvements noted in Conclusion 10, the inverse micro-ramp design dramatically reduces the boundary layer shape factor in its vortex-induced downwash region as compared to the uncontrolled boundary layer and those resulting from control by the standard micro-ramp design.

(12) The effects of the inverse micro-ramp design on the boundary layer shape factor persist downstream of the SBLI, even for strong incident shock strengths, while the effects of the standard micro-ramp design become largely mitigated downstream of the interactions.

(13) The net effect of the micro-ramps is evaluated by integrating the displacement thickness across the span to include regions of both vortex-induced downwash and vortex-induced upwash. The standard micro-ramp design reduces the peak displacement thickness through the $\theta = 7.75$-deg, 10.0-deg, and 12.0-deg interactions by 22%, 12%, and 4%, respectively, while the inverse micro-ramp design reduces the net displacement thickness by 34%, 21%, and 17%, respectively.

The results cumulatively demonstrate the favorable effects of appropriately designed streamwise vortex generators for passive boundary layer control of shock–boundary layer interactions. Reduced shape factors and displacement thicknesses prevent boundary layer separation and can improve flow rates through supersonic inlets, for example, while reduced fluctuations ease dynamic loading on constituent parts. In these regards, a new micro-ramp design demonstrates considerable improvements over the standard design, while still maintaining the latter's appealing characteristics.

Direction for future work

The present study focuses on developing and evaluating the effectiveness of ramp-like passive vortex generators for SBLI control. Optimization of these designs through experimentation is likely inefficient, with simulation techniques being better-suited for this purpose. Instead, readily conductible experiments focussing on the physics of SBLI can advance the science in at least two key ways.

Simultaneous measurements of the instantaneous density and velocity fields can be achieved by combining the present SPIV technique with Rayleigh scattering. Such measurements would enable computation of the Favre averaged mean and fluctuation statistics, and therefore more directly account for the effects of compressibility. Coupling these measurements with static wall-pressure measurements would furthermore enable good approximations of the thermodynamic state variables and transport quantities throughout the SBLI. In turn, these will enable more accurate accounts of the dissipation rate, for example, and can be used to more rigorously assess the validity of the popular Boussinesq hypothesis as well as the improvements provided by non-equilibrium RANS models presently under development.

Definitive conclusions regarding the cause for the unsteady nature of SBLI can also be approached. For example, if an acoustics-related mechanism, such as the one proposed by Pirozzoli and Grasso (2006), is indeed the source of the large fluctuations, then the associated frequencies should be altered by the presence of sufficiently strong streamwise vortices. Specifically, the characteristic frequencies should increase when the characteristic size of the recirculation zones are decreased via the mechanism described in Conclusion 8. If instead the large scale fluctuations are instead due to pre-existing boundary layer features or the boundary layer burst frequency, as proposed by Ganapathisubramani et al. (2007), then the associated frequencies

should be unchanged by the presence of micro-ramps. Furthermore, high-speed static pressure measurements made at or above the Nyquist frequency of the dominant oscillation mode can be made readily. While hardware limits the sampling rate of the SPIV technique, concurrent measurements would enable computation of conditional statistics. Correlations between the instantaneous pressure, location of the unstable shear layer, and location of the reflected shock wave should all be possible. Combining these measurements with instantaneous density field measurements should enable conclusive evaluation of an acoustics-related mechanism for the unsteadiness.

APPENDICES

APPENDIX A

Defining test section dimensions

The critical dimensions necessary to model or reproduce the present experiment are offered in this section. Figure A.1*a* shows a streamwise-oriented cross-sectional view of the test section. The bulk flow moves from left to right and is deflected by an angle θ via a wedge mounted to the top boundary of the test section by an 0.90-in tall strut. The height of the wedge is 0.388-in, and its downstream face is formed at an 11-deg angle. The leading edge of the wedge, which extends a distance of x_{LE} upstream of the leading edge of the 3.75-in long strut, produces an oblique shock wave which propagates at angle β. The inviscid extension of the shock wave impinges on the opposite boundary at x_0. Three dovetail inserts are located at distances x_{R1}, x_{R2}, and x_{R3} upstream of this point, and these lengths correspond with the upstream locations of any micro-ramp arrays used in the facility. These lengths are consistent with the definitions given in Figs. 5.2 and 6.5. In the present study only the x_{R1} location is used. The unspecified dimensions, namely θ, β, x_{R1}, x_{R1}, x_{R1}, and x_{R1}, are given for the three deflection angles in Table A.1.

Figure A.1*b* gives the corresponding dimensions in the spanwise-oriented cross-section, showing in particular the 1.25-in spanwise extent of the shock-generating wedge which is mounted by the 0.135-in wide strut. As previously noted, the test

section has a 2.25×2.75-in cross-section.

The geometry of the converging-diverging nozzle is also potentially critical for computational simulation of the present geometry. An under-sampled array of 163 defining coordinates are given in Table A.2. In this, the $x = 0$ location corresponds to the nozzle throat, which is located 21.185-in upstream of the strut leading edge, $x_{_{SLE}}$, from Fig. A.1. The throat has height 0.742-in, giving a total expansion ratio of $A/A^* = 3.706$. As discussed in § 2.1.2, the supersonic nozzle contour is determined using the NOZCS code and additionally considers the growth of the displacement thickness.

θ (deg)	β (deg)	x_{R1} (cm)	x_{R2} (cm)	x_{R3} (cm)	x_{LE} (cm)
7.75	27.4	8.50	14.00	19.50	4.705
10.0	29.4	9.42	14.92	20.42	3.055
12.0	31.3	9.76	15.26	20.76	2.103

Table A.1: Defining dimensions for the three flow deflection angles used in the present study, corresponding to Fig. A.1.

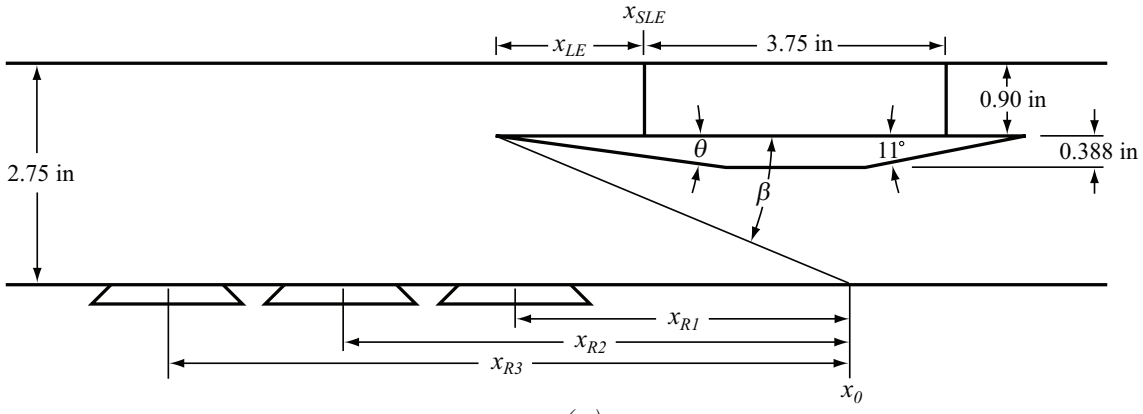

(a)

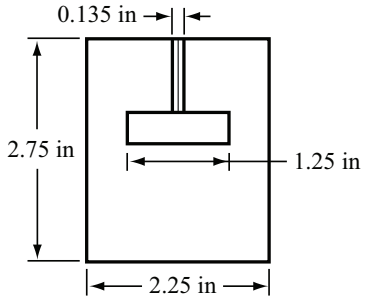

(b)

Figure A.1: Defining test section dimensions in *(a)* a streamwise-oriented cross-section and *(b)* a spanwise-oriented cross-section.

Nozzle Coordinates ($M = 2.75$)									
x (in)	y (in)	x (in)	y (in)	x (in)	y (in)	x (in)	y (in)	x (in)	y (in)
-12.215	10.000	-1.164	0.977	2.584	1.661	5.995	2.407	9.406	2.709
-11.664	9.992	-1.003	0.915	2.684	1.692	6.095	2.421	9.506	2.713
-11.343	9.968	-0.843	0.863	2.784	1.723	6.196	2.435	9.607	2.717
-11.022	9.925	-0.682	0.821	2.885	1.753	6.296	2.448	9.707	2.721
-10.701	9.865	-0.522	0.788	2.985	1.782	6.396	2.461	9.807	2.724
-10.380	9.787	-0.361	0.764	3.085	1.810	6.497	2.474	9.908	2.727
-10.059	9.689	-0.201	0.749	3.186	1.838	6.597	2.486	10.008	2.730
-9.738	9.571	-0.040	0.742	3.286	1.866	6.697	2.498	10.108	2.733
-9.417	9.432	0.000	0.742	3.386	1.892	6.798	2.510	10.209	2.735
-9.095	9.269	0.075	0.745	3.487	1.918	6.898	2.521	10.309	2.738
-8.774	9.081	0.176	0.758	3.587	1.944	6.998	2.532	10.409	2.740
-8.453	8.865	0.276	0.779	3.687	1.969	7.098	2.543	10.510	2.742
-8.132	8.616	0.376	0.810	3.788	1.993	7.199	2.553	10.610	2.744
-7.811	8.330	0.477	0.848	3.888	2.017	7.299	2.563	10.710	2.745
-7.490	7.997	0.577	0.892	3.988	2.040	7.399	2.573	10.811	2.746
-7.139	7.583	0.677	0.935	4.089	2.063	7.500	2.582	10.911	2.747
-6.732	7.089	0.778	0.978	4.189	2.085	7.600	2.591	11.011	2.748
-6.324	6.612	0.878	1.021	4.289	2.107	7.700	2.600	11.112	2.749
-5.916	6.126	0.978	1.063	4.390	2.128	7.801	2.608	11.212	2.749
-5.509	5.640	1.079	1.106	4.490	2.149	7.901	2.617	11.312	2.750
-5.101	5.154	1.179	1.148	4.590	2.169	8.001	2.625	11.413	2.750
-4.693	4.668	1.279	1.189	4.691	2.189	8.102	2.633	11.513	2.750
-4.286	4.182	1.380	1.230	4.791	2.208	8.202	2.640	11.613	2.750
-3.878	3.697	1.480	1.269	4.891	2.227	8.302	2.647	11.714	2.750
-3.470	3.211	1.580	1.309	4.992	2.246	8.403	2.654	11.814	2.750
-3.063	2.725	1.681	1.347	5.092	2.264	8.503	2.661	11.914	2.750
-2.655	2.239	1.781	1.385	5.192	2.281	8.603	2.667	12.015	2.750
-2.288	1.801	1.881	1.422	5.293	2.298	8.704	2.673		
-2.127	1.627	1.982	1.459	5.393	2.315	8.804	2.679		
-1.967	1.477	2.082	1.494	5.493	2.332	8.904	2.685		
-1.806	1.347	2.182	1.529	5.594	2.347	9.005	2.690		
-1.646	1.234	2.283	1.563	5.694	2.363	9.105	2.695		
-1.485	1.136	2.383	1.596	5.794	2.378	9.205	2.700		
-1.324	1.050	2.483	1.629	5.895	2.393	9.306	2.704		

Table A.2: Sampled coordinates for $M = 2.75$ nozzle.

APPENDIX B

Sizing for inverse micro-ramps

This section discusses the design considerations used for sizing the inverse micro-ramps, which were motivated in § 6.1. The nomenclature is consistent with Fig. 6.5. Following from the recommendations of Anderson et al. (2006), and for purposes of relevant comparison to the findings of the previous chapter as well as independent works, three of the defining dimensions are kept constant in the inverse micro-ramp design: the nominal flow deflection angle, the ratio c/h, and the upstream location $x_{_R}$. The flow deflection angle, β, is given by

$$\beta = \sin^{-1}\left(\frac{h}{c\cos A_p}\right), \tag{B.1}$$

leaving two free design variables, h and A_p.

To evaluate a reasonable first-order estimate for these values, it is instructive to first estimate the growth rate of the vortical structures issuing from the passive control elements. The growth rate of such vortical structure is scarcely studied. Shear layers, however, are well-studied canonical flows with perhaps analogous growth behavior. Dimotakis (1986) gives the growth rate of such a layer to be:

$$\frac{\delta_v}{x} = \varepsilon\left(\frac{1-r}{1+s^{1/2}r}\right)\left[1+s^{1/2}-\frac{1-s^{1/2}}{1+2.9(1+r)/(1-r)}\right], \tag{B.2}$$

where δ_v is the characteristic diameter of the vortical structure, x is the distance downstream of the control element, ε is an empirical constant, s is the density ratio, and r is the velocity ratio. For simplicity $s \approx 1$ is assumed, although in actuality the density ratio will be non-unity due to compressibility effects. Equation B.2 then becomes

$$\frac{\delta_v}{x} = 2\varepsilon \left(\frac{1-r}{1+r} \right). \tag{B.3}$$

The correct value for ε is somewhat open to debate, however $\varepsilon \approx 0.17$ is typical. Assuming a velocity ratio of $r \approx 0.75$, which seems intuitively reasonable, the growth rate of the vortex is approximately

$$\frac{\delta_v}{x} \approx 0.05. \tag{B.4}$$

It is furthermore assumed that the size of the vortex at the downstream boundary of the control element is approximately $\delta_{v_0} \approx h$, and the two vortices issuing from each side of the feature pair are initially separated by a distance of $2c \sin A_p$. It is desirable for the influences of these vortices to meet at the interaction location, x_R, and thus

$$\delta_v = 2c \sin A_p \approx 0.05 x_R + \delta_{v_0}. \tag{B.5}$$

Since the flow deflection angle β remains unchanged we can write c in terms of the free variables h and A_p, so that

$$c = \frac{h}{\sin\beta \cos A_p}, \tag{B.6}$$

and thus

$$x_p = \frac{\frac{2h}{\sin\beta} \tan A_p - h}{0.05}. \tag{B.7}$$

Then finally

$$h = c \sin\beta \cos A_p = \frac{0.05 x_R}{\frac{2}{\sin\beta} \tan A_p - 1}. \tag{B.8}$$

Appropriate choice of the ramp height can follow from consideration of the desired interaction between the primary vortices and the boundary layer. For example it is reasonable to expect good performance from the passive micro elements if the size of the vortices are one boundary layer thickness in diameter. In this case, to first order, the vortex pairs will pull high energy gas from the free stream into the inner regions of the boundary layer. Using this as an additional design criterion, we can deduce h:

$$\begin{aligned} \delta_v &= \delta_{v_0} + 0.05 x_R \\ &\approx h + 0.05 x_R = \delta, \end{aligned} \tag{B.9}$$

and thus

$$h = \delta - 0.05 x_R. \tag{B.10}$$

Anderson et al. (2006) recommend $x_R/\delta = 14$, and using this we find $h = 0.3\delta$. For the present facility, where $\delta = 10.0\,\text{mm}$, equation B.7 gives $A_p = 14^\circ$.

BIBLIOGRAPHY

BIBLIOGRAPHY

Adams, N., 2000. Direct simulation of the turbulent boundary layer along a compression ramp at $m = 3$ and $re_\theta = 1685$. Journal of Fluid Mechanics 420, 47–83.

Anderson, B., Tinapple, J., Surber, L., 2006. Optimal control of shock wave turbulent boundary layer interactions using micro-array actuation. In: 3rd AIAA Flow Control Conference.

Andreopoulos, J., Muck, K., 1987. Some new aspects of the shock-wave boundary layer interaction. Journal of Fluid Mechanics 180, 405–428.

Andreopoulos, Y., Agui, J., Briassulis, G., 2000. Shock wave-turbulence interactions. Annual Review of Fluid Mechanics 32, 309–345.

Bardina, J., Huang, P., Coakley, T., 1980. Turbulence modeling validation, testing, and development. NASA Technical Memorandum 110446.

Barter, J., Dolling, D., 1993. Experimental study of the use of vortex generators to reduce fluctuating pressure loads in shock wave turbulent boundary layer interactions. In: 15th AIAA Aeroacoustics Conference. AIAA-93-4335.

Beresh, S., Clemens, N., Dolling, D., 2002. Relationship between upstream turbulent boundary-layer velocity fluctuations and separation shock unsteadiness. AIAA Journal 40 (12), 2412–2422.

Bookey, P., Wyckham, C., Smits, A., 2005a. Experimental investigations of Mach 3 shock-wave turbulent boundary layer interactions. In: 35th AIAA Fluid Dynamics Conference and Exhibit. AIAA 2005-4899.

Bookey, P., Wyckham, C., Smits, A., Martin, M., 2005b. New experimental data of STBLI at DNS/LES accessible Reynolds numbers. In: 43rd AIAA Aerospace Sciences Meeting and Exhibit. AIAA 2005-309.

Brusniak, L., Dolling, D., 1996. Engineering estimation of fluctuating loads in shock wave/turbulent boundary-layer interactions. AIAA Journal 34 (12), 2554–2561.

Bur, R., Corbel, B., Délery, J., 1998. Study of passive control in a transonic shock wave/boundary-layer interaction. AIAA Journal 36 (3), 394–400.

Chapman, D., Kuehn, D., Larson, H., 1958. Investigation of separated flows in supersonic and subsonic streams with emphasis on the effect of transition. Tech. rep., NACA Report 1356.

Clemens, N., Mungal, M., 1991. A planar mie scattering technique for visualizing supersonic mixing flows. Experiments in Fluids 11, 175–185.

Coles, D., 1953. Measurements in the boundary layer on a smooth flat plate in supersonic flows. Tech. rep., J.P.L. CalTech, reports 20-69, 20-70, 20-71.

Coles, D., 1954. Measurements of turbulent friction on a smooth flat plate in supersonic flows. Journal of Aeronautical Sciences 21, 433–448.

Coles, D., Hirst, E., 1968. Computation of turbulent boundary layers — 1968 AFOSR-IFP Stanford Conference. Proceedings of the 1968 Conference 2, Stanford University, Stanford, CA.

Couldrick, J., Gai, S., Milthorpe, J., Shankar, K., 2005. Active control of swept shock wave/turbulent boundary-layer interactions. The Aeronautical Journal 109, 577–583.

Croker, B., Meicenheimer, H., Kutschenreuter, P., 2007. On the design of hypersonic inward-turning inlets. In: 3rd Interational Symposium on Integrating CFD and Experiments in Aerodynamics.

Delery, J., 2001. Handbook of Shock Waves. Vol. 2. Academic Press.

Delery, J., Marvin, J., 1986. Shock-wave boundary layer interactions. Tech. rep., Advisory Group for Aerospace Research & Development (AGARD), aGARD-AG-280.

Dimotakis, P. E., 1986. Two-dimensional shear-layer entrainment. AIAA Journal 24 (11), 1791–1796.

Dolling, D., 2001. Fifty years of shock-wave/boundary-layer interaction research: what's next? AIAA Journal 39 (8), 1517–1531.

Dolling, D., Murphy, M., 1983. Unsteadiness of the separation shock wave structure in a supersonic compression ramp flowfield. AIAA Journal 21, 1628–1634.

Donaldson, C., 1950. Investigation of a simple device for preventing separation due to shock and boundary-layer interaction. NACA RM L50302A.

Driest, E. V., 1951. Turbulent boundary layer in compressible fluids. Journal of the Aeronautical Sciences 18 (3), 1012–1028.

Dupont, P., Haddad, C., Debiève, J., 2006. Space and time organization in a shock-induced separated boundary layer. Journal of Fluid Mechanics 559, 255–277.

Dupont, P., Piponniau, S., Sidorenko, A., Debiève, J., 2008. Investigation by particle image velocimetry measurements of oblique shock reflection with separation. AIAA Journal 46 (6), 1365–1370.

Dussauge, J., Dupont, P., Debiève, J., 2006. Unsteadiness in shock wave boundary layer interactions with separation. Aerospace Science and Technology 10, 85–91.

Dussauge, J., Fernholz, H., Smith, R., Finley, P., Smits, A., Spina, E., 1996. Turbulent boundary layers in subsonic and supersonic flows. Tech. rep., Advisory Group for Aerospace Research & Development (AGARD).

Eléna, M., Lacharme, J., 1988. Experimental study of a supersonic turbulent boundary layer using a laser doppler anemometer. Journal de Mécanique Théorique et Appliqueé 7, 175–190.

Erm, L., Smits, A., Joubert, P., 1985. Low Reynolds number turbulent boundary layers on a smooth flat surface in a zero pressure gradient. In: Proceedings of the Fifth Symposium on Turbulent Shear Flows. Cornell University.

Fernholz, H., Finley, P., 1980. A critical commentary on mean flow data for two-dimensional compressible turbulent boundary layers. AGARDograph 253.

Ford, C. P., Babinsky, H., 2007. Micro-ramp control for oblique shock wave/boundary layer interactions. In: 37th AIAA Fluid Dynamics Converence and Exhibit. AIAA 2007-4115.

Galbraith, M., Orkwis, P., Benek, J., 2009. Multi-row micro-ramp actuators for shock wave boundary-layer interaction control. In: 47th AIAA Aerospace Sciences Meeting. AIAA 2009-321.

Ganapathisubramani, B., Clemens, N., Dolling, D., 2006. Large-scale motions in supsersonic turbulent boundary layer. Journal of Fluid Mechanics 556, 271–282.

Ganapathisubramani, B., Clemens, N., Dolling, D., 2007. Effects of upstream boundary layer on the unsteadiness of shock-induced separation. Journal of Fluid Mechanics 585, 369–394.

Garnier, E., Sagaut, P., Deville, M., 2002. Large eddy simulation of shock/boundary-layer interaction. AIAA Journal 40 (10), 1935–1944.

Gatski, T., Erlebacher, G., 2002. Numerical simulation of a spatially evolving supersonic turbulent boundary layer. Tech. rep., NASA/TM-2002-211934.

Gefroh, D., Loth, E., Dutton, C., McIlwain, S., 2002. Control of oblique shock/boundary-layer interaction with aeroelastic mesoflaps. AIAA Journal 40 (12), 2456–2466.

Gerolymos, G., Sauret, E., Vallet, I., 2004. Oblique-shock-wave/boundary-layer interaction using near-wall Reynolds stress models. AIAA Journal 42 (6), 1089–1100.

Green, J., 1970. Interactions between shock waves and turbulent boundary layers. Progress in Aerospace Sciences 11, 253–340.

Guarini, S., Moser, R., Shariff, K., Wray, A., 2000. Direct numerical simulation of a supersonic turbulent boundary layer at mach 2.5. Journal of Fluid Mechanics 414, 1–33.

Hamed, A., Shang, J., 1991. Survey of validation data base for shockwave boundary-layer interactions in supersonic inlets. Journal of Propulsion and Power 7 (4), 617–625.

Hamlington, P., Dahm, W., 2007. A new physically-based fully-realizable nonequilibrium Reynolds stress closure for turbulent flow RANS modeling. In: 43rd Joint Propulsion Conference & Exhibit. AIAA-2007-5573.

Hamlington, P., Dahm, W., 2008. Reynolds stress closure for nonequilibrium effects in turbulent flows. Physics of Fluids 20, 115101.

Hamlington, P., Dahm, W., 2009. Computational validation of new Reynolds stress closure for nonequilibrium effects in turbulent flows. In: 47th AIAA Aerospace Sciences Meeting. AIAA-2009-1323.

Hayakawa, H., Squire, L., 1982. The effect of the upstream boundary-layer state on the shock interaction at a compression corner. Journal of Fluid Mechanics 122, 369–394.

Holden, H., Babinsky, H., 2007. Effect of microvortex generators on separated normal shock/boundary layer interactions. Journal of Aircraft 44 (1), 170–174.

Hou, Y., Clemens, N., Dolling, D., 2003. Wide-field PIV study of shock-induced turbulent boundary layer separation. In: 41st Aerospace Sciences Meeting and Exhibit. AIAA-2003-0441.

Humble, R., Elsinga, G., Scarano, F., van Oudheusden, B., 2009. Three-dimensional instantaneous structure of a shock wave/turbulent boundary layer interaction. Journal of Fluid Mechanics 622, 33–62.

Humble, R., Scarano, F., van Oudheusden, B., 2007. Particle image velocimetry measurements of a shock wave/turbulent boundary layer interaction. Experiments in Fluids 43, 173–183.

Kim, J., Moin, P., Moser, R., 1987. Turbulence statistics in fully developed channel flow at low reynolds number. Journal of Fluid Mechanics 177, 133–166.

Knight, D., Yan, H., Panaras, A., Zheltovodov, A., 2003. Advances in cfd prediction of shock wave turbulent boundary layer interactions. Aerospace Science and Technology 39, 131–184.

Kuethe, A., 1971. Boundary layer control of flow separation and heat exchange. U.S. Patent 3,578,264.

Kuethe, A., 1973. Boundary layer control of flow separation and heat exchange. U.S. Patent 3,741,285.

Kumar, V., Alvi, S., 2006. Use of high-speed microjets for active separation conrol of diffusers. AIAA Journal 44 (2), 273–281.

Lawson, N., Wu, J., 1997. Three-dimensional particle image velocimetry: experimental error analysis of a digital angular stereoscopic system. Measurement Science & Technology 8, 1455–1464.

Lee, S., Loth, E., Wang, C., Kim, S., 2007. LES of supersonic turbulent boundary layers with μvg's. In: 25th AIAA Applied Aerodynamics Conference. AIAA 2007-3916.

Lin, J., 2002. Review of research on low-profile vortex generators to control boundary-layer separation. Progress in Aerospace Sciences 38, 389–420.

Lin, J., Howard, F., 1989. Turbulent flow separation control through passive techniques. In: AIAA 2nd Shear Flow Conference. AIAA-89-0976.

Lina, L., Reed, W., 1950. A preliminary flight investigation of the effects of vortex generators on separation due to shock. NACA RM L50J02.

Loginov, M., Adams, N., Zheltovodov, A., 2006. Large-eddy simulation of shock-wave/turbulent-boundary-layer interaction. Journal of Fluid Mechanics 565, 135–169.

Maeder, T., Adams, N., Kleiser, L., 2001. Direct simulation of turbulent supersonic boundary layers by an extended temporal approach. Journal of Fluid Mechanics 429, 187–216.

Maise, G., McDonald, H., 1968. Mixing length and kinematic eddy viscosity in a compressible boundary layer. AIAA Journal 6 (1), 73–80.

McCormick, D., 1993. Shock/boundary-layer interaction conrol with vortex generators and passive cavity. AIAA Journal 31 (1), 91–96.

Melling, A., 1997. Tracer particles and seeding for particle image velocimetry. Measurement Science & Technology 8, 1406–1416.

Meyer, M., Buter, T., Bowersox, R., 1997. Compressible turbulence measurements in a supersonic boundary layer with impinging shock wave interaction. In: 35th Aerospace Sciences Meeting and Exhibit. AIAA-97-0427.

Modarress, D., Johnson, D., 1976. Investigation of shock-induced separation of a turbulent boundary layer using laser velocimetry. In: 9th Fluid and Plasma Dynamics Conference. AIAA-76-374.

Morkovin, M., 1962. Effects of compressibility on turbulent flows. In: The Mechanics of Turbulence (ed. A. Favre). CNRS, pp. 367–380.

Pirozzoli, S., Bernardini, M., Grasso, F., 2008. Characterization of coherent vortical structures in a supersonic turbulent boundary layer. Journal of Fluid Mechanics 613, 205–231.

Pirozzoli, S., Grasso, F., 2006. Direct numberical simulation of impinging shock wave/turbulent boundary layer interaction at M=2.25. Physics of Fluids 18.

Pirozzoli, S., Grasso, F., Gatski, T., 2004. Direct numerical simulation and analysis of a spatially evolving supersonic turbulent boundary layer at M=2.25. Physics of fluids 16, 530–545.

Prasad, A., Jensen, K., 1995. Scheimpflug stereocamera for particle image velocimetry in liquid flows. Applied Optics 34, 7092–7099.

Raffel, M., Willert, C., Kompenhans, J., 1998. Particle Image Velocimetry: A Practical Guide. Springer.

Raghunathan, S., 1989. Passive control of shock-boundary layer interaction. Progress in Aerospace Sciences 25 (3), 271–296.

Ringuette, M., Wu, M., Martin, M., 2008. Coherent structures in direct numerical simulation of turbulent boudnary layers at mach 3. Journal of Fluid Mechanics 594, 56–69.

Rizzetta, D., Visbal, M., Gaitonde, D., 2001. Large-eddy simulation of supersonic compression-ramp flow by high-order method. AIAA Journal 39 (12), 2283–2292.

Robinet, J., 2007. Bifurcations in shock-wave/laminar-boundary-layer interaction: global instability approach. Journal of Fluid Mechanics 579, 85–112.

Rose, W., Johnson, D., 1975. Turbulence in a shock-wave boundary-layer interaction. AIAA Journal 13 (7), 884–889.

Roshko, A., Thomke, G., 1976. Flare-induced interation lengths in supersonic, turbulent boundary-layers. AIAA Journal 14, 873–879.

Samimy, M., Elliott, G., 1990. Effects of compressibility on the characteristics of free shear layers. AIAA Journal 28, 439–445.

Samimy, M., Lele, S., 1991. Motion of particles with inertia in a compressible free shear layer. Physics of Fluids 3, 1915–1923.

Scarano, F., 2008. Particle Image Velocimetry: New Developments and Recent Applications. Springer-Verlag.

Selig, M., Andreopoulos, J., Muck, K., Dussauge, J., Smits, A., 1989. Turbulence structure in a shock-wave turbulent boundary-layer interaction. AIAA Journal 27, 862–869.

Settles, G., Bogdonoff, S., Vas, I., 1976. Incipient separation of a supersonic turbulent boundary-layer at moderate to high Reynolds numbers. AIAA Journal 14, 50–56.

Settles, G., Perkins, J., Bogdonoff, S., 1981. Upstream influence scaling of 2D & 3D shock/turbulent boundary layer interactions at compression corners. In: AIAA 19th Aerospace Sciences Meeting. AIAA-1981-0334.

Sinha, K., Mahesh, K., Candler, G., 2003. Modeling shock unsteadiness in shock/turbulence interaction. Physics of Fluids 15 (8), 2290–2297.

Sinha, K., Mahesh, K., Candler, G., 2005. Modeling the effect of shock unsteadiness in shock/turbulent boundary-layer interactions. AIAA Journal 43, 586–594.

Smith, A., Babinsky, H., 2004. Shock-wave/boundary-layer interaction control using streamwise slots in transonic flows. Journal of Aircraft 41 (3), 540–546.

Smith, M., Smits, A., 1995. Visualization of the structure of supersonic turbulent boundary layers. Experiments in Fluids 18, 288–302.

Smits, A., Dussauge, J., 2006. Turbulent shear layers in supersonic flow. Springer.

Smits, A., Muck, K., 1987. Experimental study of 3 shock-wave turbulent boundary-layer interactions. Journal of Fluid Mechanics 182, 291–314.

Spalart, P., 1988. Direct simulation of a turbulent boundary layer up to $re_\theta = 1410$. Journal of Fluid Mechanics (187), 61–98.

Spalding, D., 1961. A single formula for the law of the wall. Transactions of the ASME, Series E: Journal of Applied Mechanics 28, 455–458.

Spina, E., Smits, A., Robinson, S., 1994. The physics of supersonic turbulent boundary layers. Annual Review of Fluid Mechanics 26, 287–319.

Teramoto, S., 2005. Large-eddy simulation of transitional boundary layer with impinging shock wave. AIAA Journal 43 (11), 2354–2363.

Thomas, F., Putman, C., Chu, H., 1994. On the mechanism of unsteady shock oscillation in shock/wave turbulent boundary layer interaction. Experiments in Fluids 18, 69–81.

Ünalmis, O., Dolling, D., 1998. Experimental study of causes of unsteadiness of shock induced turbulent separation. AIAA Journal 36, 371–378.

Wheeler, G., 1984. Means for maintaining attached flow of a flowing medium. U.S. Patent 4,455,045.

Wheeler, G., 1991. Low drag vortex generators. U.S. Patent 5,058,837.

White, F., 1991. Viscous Fluid Flow, 2nd Edition. McGraw-Hill, Inc.

Wu, M., Bookey, P., Martin, M., Smits, A., 2005. Analysis of shockwave/turbulent boundary layer interaction using dns and experimental data. In: 43rd AIAA Aerospace Sciences Meeting and Exhibit. AIAA 2005-310.

Wu, M., Martin, M., 2007. Direct numerical simulation of supersonic turbulent boundary layer over a compression ramp. AIAA Journal 45 (4), 879–889.

Yanta, W., Collier, A., Spring, W., Boyd, C., McArthur, J., 1990. Experimental measurements of the flow in a scramjet inlet at Mach 4. Journal of Propulsion and Power 6 (6), 784–790.

Zucrow, M., Hoffman, J., 1976. Gas Dynamics. John Wiley & Sons.